University of Alberta

Lead Antimony Sulfides as Potential Solar Absorbers
for Thin-film Solar Cells

by

Matthieu Versavel   ©

A thesis submitted to the Faculty of Graduate Studies and Research
in partial fulfillment of the requirements for the degree of

Doctor of Philosophy

Department of Chemistry

Edmonton, Alberta
Spring 2007

Library and
Archives Canada

Published Heritage
Branch

395 Wellington Street
Ottawa ON K1A 0N4
Canada

Bibliothèque et
Archives Canada

Direction du
Patrimoine de l'édition

395, rue Wellington
Ottawa ON K1A 0N4
Canada

NOTICE:
The author has granted a non-
exclusive license allowing Library
and Archives Canada to reproduce,
publish, archive, preserve, conserve,
communicate to the public by
telecommunication or on the Internet,
loan, distribute and sell theses
worldwide, for commercial or non-
commercial purposes, in microform,
paper, electronic and/or any other
formats.

The author retains copyright
ownership and moral rights in
this thesis. Neither the thesis
nor substantial extracts from it
may be printed or otherwise
reproduced without the author's
permission.

AVIS:
L'auteur a accordé une licence non exclusive
permettant à la Bibliothèque et Archives
Canada de reproduire, publier, archiver,
sauvegarder, conserver, transmettre au public
par télécommunication ou par l'Internet, prêter,
distribuer et vendre des thèses partout dans
le monde, à des fins commerciales ou autres,
sur support microforme, papier, électronique
et/ou autres formats.

L'auteur conserve la propriété du droit d'auteur
et des droits moraux qui protège cette thèse.
Ni la thèse ni des extraits substantiels de
celle-ci ne doivent être imprimés ou autrement
reproduits sans son autorisation.

In compliance with the Canadian
Privacy Act some supporting
forms may have been removed
from this thesis.

While these forms may be included
in the document page count,
their removal does not represent
any loss of content from the
thesis.

Conformément à la loi canadienne
sur la protection de la vie privée,
quelques formulaires secondaires
ont été enlevés de cette thèse.

Bien que ces formulaires
aient inclus dans la pagination,
il n'y aura aucun contenu manquant.

Canada

Abstract

This thesis reports the thin film synthesis and the optical characterization of several lead antimony sulfide films as potential light absorbers for thin-film solar cells and the efforts to combinatorially investigate the Hf-Zr-Sb phase diagram. Cells based on direct band gap semiconductors, such as $CuInS_2$ and $Cu(In,Ga)Se_2$, that absorb light strongly are promising alternatives to Si-based solar cells. Although the efficiencies of these cells are excellent, the toxicity of cadmium and the availability of indium and tellurium will ultimately limit their use and their electricity generation capacity. Our approach is to develop new semiconductor thin films that contain only cost effective, abundant, and relatively less toxic materials. Most of the lead antimony sulfides exhibit suitable optical band gaps for thin film photovoltaic applications. The preparation of amorphous and polycrystalline antimony sulfide thin films from RF-sputtering of an Sb_2S_3 target and subsequent annealing at 400°C in sulfur vapor yielded smooth and compact semiconductor thin films. In an effort to prepare polycrystalline films of lead antimony sulfides, sputtered metallic Pb-Sb precursor films were annealed in sulfur vapor. It was observed that the inevitable initial formation of PbS was detrimental to the product film morphology and control of the film composition. A more successful approach was to react sulfur-containing precursor films composed of crystalline PbS and amorphous (Sb,S) layers prepared by cycled sputtering of Sb_2S_3 and Pb under sulfur vapor. The sulfur-containing layered precursor films were essential to prepare phase-pure ternary films with good morphology. Moreover, films of the plagionite group phases were preferentially obtained, indicating that the presence of hydrogen is not

necessary for the occurrence of the plagionite phases, and suggesting their metastability. Despite a lack of precise control over the as-deposited Sb:Pb ratio, sulfurization of the unique crystalline PbS and amorphous (Sb,S) layered precursor films yielded smooth, continuous and phase-pure films of the four plagionite group phases with appropriate optical properties: strong absorption coefficients and direct band gaps ranging from 1.5 eV to 1.9 eV.

Acknowledgements

I would first like to thank the Ecole Nationale Supérieure de Chimie de Montpellier in France, more particularly Mme Jacqueline Raymond, and the department of Chemistry of the University of Alberta, more particularly Profs. Josef Takats and Joel A. Haber for their assistance that allowed me to begin graduate studies at the University of Alberta and the opportunity to study away from my home country. That experience abroad has been truly enriching scientifically, culturally and personally.

My sincere thanks go to my supervisor, Professor Joel A. Haber, who has offered me the opportunity to work in his research group, and provided his support and advice throughout the research projects we started from ground zero. I would also like to thank him for letting me attend two great international conferences: the 20th European Photovoltaic Solar Energy Conference and Exhibition in Barcelona, Spain and the symposium on thin film chalcogenide photovoltaic materials of the E-MRS 2006 Spring Meeting in Nice, France, for which I also received travel assistance provided by the Mary Louise Imrie Graduate Student Award.

I would like to thank NRC-NINT and especially Mr. Steve Launspach for access to XRD facilities, ACSES for TOF-SIMS data collection, Prof. Mark McDermott for access to the UV-VIS spectrometer, Dr. Sergei Matveev for WDX data collection, and Mr. George Braybrook for SEM/EDX data collection. I would like to thanks the Chemistry department staff, especially Mr. Roman Lipiecki for his precise and

meticulous manufacturing of combinatorial masks, and Mrs. Ilona Baker for her administrative assistance. Lastly, I would also like to thank Dr. Tim D. Hatchard for his insights about the deposition processes.

Among the friendly persons I have met in Edmonton, I would like to thank Nathan D. Jones, Genaro and Laura Gelves, and Dolores Martinez for their friendships that made life in Edmonton more enjoyable, thanks to fruitful and never boring conversations…

Lastly, I would like to thank and dedicate my thesis to the persons that always offered me their unconditional support and love, regardless of how hard being separated has been. I name my mother, my father, my sister Aude and my very dear Delphine. *"Sans votre soutien rien n'aurait été possible, et je tiens très sincèrement et simplement à vous dire Merci…"*

Table of Contents

Chapter 5:   Pb-Sb-S Thin-films Obtained from Reactive Annealing of

Sb-Pb Metal Precursor Films   184

Chapter 6:   Pb-Sb-S Plagionite Phase Thin-films by Reactive Annealing

of Layered Amorphous (Sb,S) and Crystalline PbS Precursor

Films   225

List of Tables

List of Figures

Chapter 1: Development of Pb-Sb-S Semiconductor Thin-films as Potential Solar Absorbers

General, technological and scientific backgrounds concerning photovoltaic research and the development of thin-film solar cells are the subjects of this introductory chapter. First, the need for photovoltaic electricity and its feasibility is assessed. Next, an overview of the major historical milestones will describe the development of photovoltaic research and technologies. Reviews of the fundamental properties of semiconductors and of the physical principles underlying the operation of solar cells will then be given. Further in this chapter, the different technologies available to harvest the sunlight and reasons for the need for new solar absorber materials for thin-film solar cells will be presented. As our research work is closely related to the chalcopyrite compound-based thin-film solar cells, some of the manufacturing techniques that are currently employed will be described. Finally, specifics about the properties and the crystal structure of Pb-Sb-S ternary phase will be given.

1.1   The need for solar energy

Approximately 80 % of the world energy and 65 % of the world electricity are currently produced by burning fossil fuels – natural gas, coal and oil – as shown in Figures 1.1.a and 1.1.b [1]. Moreover, if the global electricity production continues to grow at 3 % per year as during the period 1985-1995, then five times more electricity will be required in 2050 than in 1995 [2].

1

a)

b)
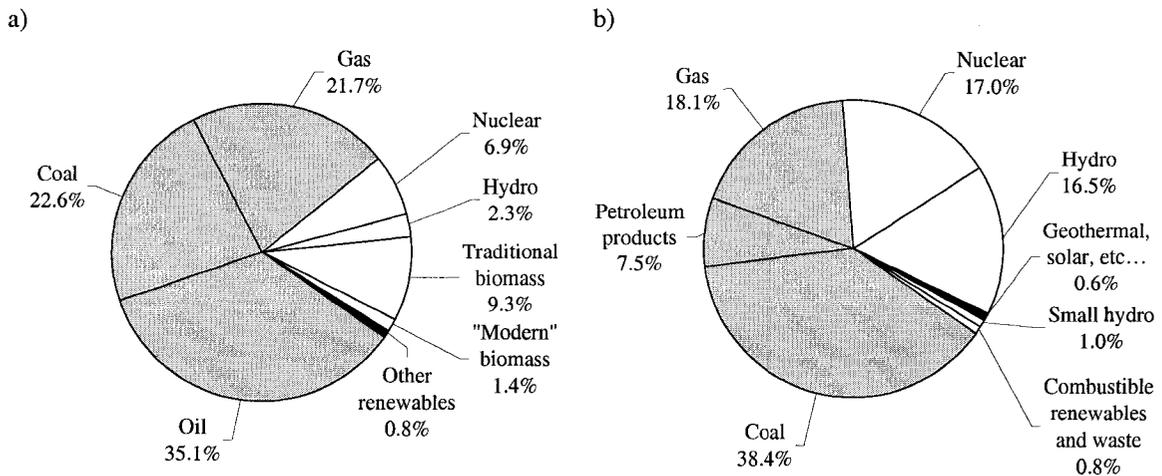
Figure 1.1. a) World primary energy use by energy source in 2001 (shares of 10.2 Gtoe = 428.4 EJ) and b) world electricity production by energy source in 2001 (shares of 15,476 TWh = 56 EJ) (adapted from [1]).

The fossil fuel-dominated energy system and the ever-increasing demand for energy and electricity are raising major global issues: socially, economically, geo-politically and environmentally. First, more than two billion people cannot access affordable energy services, limiting their opportunities for economic development and improvement of living conditions. Moreover, as one can expect, there are wide disparities in accessibility between the industrialized countries and undeveloped countries, even more acute disparities exist with rural areas in undeveloped countries. These disparities and the poor accessibility run counter to the concept of human development and threaten social stability. Furthermore, the dependence on imported fuels leaves many countries vulnerable to disruption in supply that could cause physical and economic hardships. Moreover, the weight of fossil fuels imports on the balance of payments is unbearable for many poorer countries. Thus, the limited availability and the geographical concentration of the fossil fuels in a few regions of the world may increasingly create geopolitical conflicts to control the resources and to secure sufficient

2

supply. Finally, as mentioned earlier, a large portion of energy and electricity production is achieved by burning fossil fuel. Thus, emissions of fine particulates and acid rain precursors contribute to local and regional air pollution and ecosystem degradation that constitute a threat for human health. Between 1973 and 2003, the CO_2 emissions have increased from 16 Gt to 25 Gt [3], which represents a rapid 70 % increase. Emissions of greenhouse gases, such as CO_2, are altering the atmosphere, contributing to the global warming and subsequent climate changes that will have a significant impact on the global economy and human development [1].

In this context, finding ways to expand the quality and the quantity of energy services while simultaneously addressing the environmental impacts associated with energy use represents a critical challenge to humanity – commonly called *sustainable development*. This will require major changes in the current global energy system, which would, because of lower cost, remain dominated by fossil fuels for decades, unless firm incentives and policy changes occur. Both physical and technological resources exist to meet the challenges of sustainable development. The possible options include more efficient use of energy, accelerated development and deployment of new cleaner fossil fuel and nuclear energy technologies, and finally, the increased reliance on renewable energies, that currently only account for approximately 1 % of global electricity production (excluding hydroelectricity).

Thus, increasing electricity demand and the environmental and availability related issues associated with fossil fuels call for new and more sustainable long-term

3

energy solutions. In that perspective, one of the most attractive alternatives for future large-scale electricity production is solar energy conversion. Indeed, photovoltaics address in rather positive ways the issues and challenges described earlier; for the most part, advantages and disadvantages of traditional fossil fuels and photovoltaics are opposite, as shown in Table 1.1 which gathers both technical and non-technical advantages and disadvantages of photovoltaics.

Table 1.1. Advantages and disadvantages of photovoltaics (adapted from [4])

Advantages of photovoltaics	Disadvantages of photovoltaics
Fuel source is vast and essentially infinite. It does not contribute perceptibly to global climate change or pollution: no emissions or radioactive waste for disposal.	Fuel source is diffuse (relatively low-density energy).
It has **low operating costs**: no fuel is required, it operates at ambient temperature (no high temperature corrosion or safety issues), it has no moving parts (no wear).	**High installation costs** and lack of economically efficient energy storage.
Modules have high **reliability** (>20 years).	Reliability of auxiliary (balance of system) elements, including battery for energy storage, is still poor.
Installation is quick and may be done at nearly any point-of-use and into new or existing building structures. Moreover, it may be done in small or large increments due to the modular nature of PV systems.	Lack of widespread commercially available system integration and installation.
It has a high public acceptance and an excellent safety record.	

The energy supply from the Sun is obviously enormous (1.2×10^{17} W): in one hour the energy supplied to the Earth is equivalent to the entire energy demand of the human population over the whole year [5]. More importantly, the technical potential of solar energy is estimated to be over 1,575 EJ (Exa=10^{18}) per year [6,7], which is about 3.6 times the world energy supply of 443 EJ for the year 2003 [3]. Thus, global electricity demand (60 EJ in 2003 [7]) could be met exclusively by photovoltaic

4

systems, requiring only an area equivalent to a few percent of the world's desert area [8]. Other quick calculations have demonstrated as well that the yearly electricity need of a family can be generated by a 5 by 10 meters solar module area, which is roughly the area of a house roof [4]. Finally, it is important to mention that photovoltaic electricity generation can be achieved all around the globe, eliminating issues related to the geographical concentration of fossil fuels.

Solar modules are easy to install and use, moreover, their reliability and long operational lifetimes reduces the need for continuous maintenance [8], contributing to the fast growth rate of the global photovoltaic market: 15 % per year until 1996 and closer from 30 % per year nowadays [6]. Also, photovoltaic systems are modular in small or large increments, and therefore are equally well suited for both centralized and non-centralized electricity productions. Thus, solar module applications are really diverse, from simple consumer electronics to large power plants, and more commonly, systems installed on rooftops and facades of buildings. Rooftop solar modules may be connected to the commercial grid and surplus electricity may be sold, reducing consumers' dependence on the availability and price of the commercial electricity. Also, in remote areas, it is more cost-effective to install rooftop solar modules than to extend the grid by just 500 meters [8]. In this perspective, solar energy has already contributed to the improvement of living conditions of several isolated African villages by powering pumps and well systems [9].

5

Despite its environmental and technical advantages and its wide public acceptance, photovoltaic electricity production remains far from meeting its technical potential and nowadays only contributes 0.01 EJ per year, less than 0.02 % of the global electricity production of 2003 [7]. The major barrier preventing more rapid expansion in photovoltaic use in today's energy market is that the cost of the electricity produced by photovoltaics remains too high to compete with conventional methods, as shown in Table 1.2.

Table 1.2. Electricity production, technical potential and cost of renewable sources (adapted from [7])

Renewable energy sources	World electricity production in 2003 (TWh)	World technical potential production (10^3 TWh)	Electricity generation costs in 2003 (€cents/kWh)
Hydroelectricity	2,631	14	2 - 8
Bio-energy	175	> 77	5 - 6
Wind energy	75	178	4 - 12
Geothermal power	50	1400	2 - 10
Marine energy	0.8	32	~ 8 - 15
Photovoltaics	2.5	> 440	25 - 65
Solar thermal energy	0.5		12 - 18
Total renewable energy	2969	>2100	
Total world electricity	~16,700		
Total world primary energy:	~120,000		

Ambitious PV programs have been implemented in Japan and Europe, especially, and in the U.S.A., with the goal of generating 4 % of the worldwide electricity by photovoltaics, by 2030 [7]. These programs regroup tax incentives for installation, guaranteed feed-in tariffs, large R&D programs and favorable regulations. Their aim is to create a sustainable PV market by reducing costs; solutions include improvement of the solar cells efficiencies and reduction of the production costs of solar modules. Thus, both technological (see section 1.4) and processing improvements are necessary.

6

1.2   A brief history of photovoltaics

The history of photovoltaics takes us back over 160 years, when, in 1839, Alexandre-Edmond Becquerel discovered the photogalvanic effect in liquid electrolytes: he measured small a voltage and current across two metal plates that were immersed in appropriate electrolytes exposed to sunlight [10]. Only several decades later, photoconductivity of solid Se was discovered and, shortly after, the first functional PV device was made by Fritts, melting Se into a thin sheet on a metal substrate and using a gold leaf as the top contact [4,11].

The modern era of photovoltaics started in 1954 when researchers at Bell Labs in the U.S.A. accidentally discovered that pn junction diodes generated a voltage when the room lights where on [12]. Within a year, a 6 % efficient Si pn junction solar cell was produced. Shortly after, a 6 % thin-film heterojunction solar cell based on Cu_2S/CdS and a 6 % GaAs pn junction solar cell were reported by a Wright Patterson Air Force Base research group [13] and by RCA Lab [14], respectively; in 1963, a 6 % thin-film heterojunction solar cell based on CdTe/CdS was reported [15]. Key papers explaining the fundamentals of pn junction solar cell were published by 1960: Prince [16], Loferski [17], Rappaport and Wysoski [18], Shockley and Queisser [19], reported the theoretical relation between band gap, incident spectrum, temperature, thermodynamics, and efficiency [4]. The initial applications were on a small scale, and the first real impact of solar cells came with the advent of space exploration, when the U.S.A. space program used Si PV cells for powering satellites. Because of their high efficiency and high

7

resistance to the ionizing radiation in outer space, GaAs and hetero-interface GaAlAs/GaAs solar cells were then used for space applications [4].

Interest arose in solar cells as an alternative energy source for terrestrial applications in the mid-1970s, as efficiency improvements and political awareness occurred. In 1973, several PV researchers and heads of US government scientific organizations met to evaluate the scientific merit and potential of photovoltaics. Shortly after this meeting (Cherry Hill Conference), the world's first government agency – the US Energy Research and Development Agency (now named the US Department of Energy) – was created to foster research on renewable energies. Finally, in October 1973, Persian Gulf oil producers imposed a global embargo on oil, obliging most governments of the industrialized countries to develop new energy policies and to encourage renewable energy, especially solar energy.

In the 1980s, the industry began to mature and manufacturing facilities for Si wafer pn junction based solar cells and modules were built in the U.S.A., Japan, and Europe. The thin-film PV technologies like amorphous-Si and $CuInSe_2$ achieved very promising efficiencies (> 10 %) for small area laboratory devices but attempts to scale up failed, as this was far more complicated than just scaling up the size of the equipment. Moreover, lacking both private or government financial support, most of the American semiconductor companies gave up their R&D efforts and sold their technologies to European and Japanese companies in the 1990s. Thus, the 1990 world's largest solar manufacturer Arco Solar (CA, U.S.A.), that had crystalline-Si and thin-film

8

amorphous-Si in production and thin-film $CuInSe_2$ in pre-commercialization, was sold to Siemens and renamed Siemens Solar, now owned by Shell Solar since 2001. Other examples include the Japanese Company Canon, the German Company ASE and the British Company BP Solar. Meanwhile, the Japanese PV industry developed large-scale production of crystalline-Si modules. Moreover, in Japan, strong research incentives led to advances in thin-film technology, device designs and materials processing, building Japanese leadership in photovoltaics.

In the early years, the maturing of the solar cell industry was strongly helped by the development of PV cells, especially the one based on amorphous-Si for consumer-sized, small-scale power applications, such as portable electronics and outdoor lightening. Another source of income for the PV industry arose from international aid agency programs for electrification of rural villages with small PV systems (100 times smaller than required for a "modern" home). Despite the high reliability of the solar modules, these programs were conducted with varying success rates because of short-comings in educational, technical and financial planning for the long-term functioning of the PV systems. On the opposite end, MW-size PV plants were installed by utilities in developed countries in the 1980s to evaluate their potential to provide additional power to meet peak demand during the afternoon and as generators to reduce transmission and distribution losses. Although American utilities lost interest in PV in the late 1990s due to deregulation, grid-connected applications in Europe and Japan began to grow rapidly, primarily owing to strong government support for both small- and large-scale grid connected PV installations. The total PV powers installed in Europe and Japan at the end

9

of 2003 were 575 MW and 700 MW, respectively [7]. The other PV systems components, such as DC to AC inverters, were not improved as fast as the solar module technology. Inverters were often responsible for the lack of reliability of the PV systems and of the AC power quality.

As mentioned previously, governmental support directed towards the PV industry and research, especially strong in Japan and Europe, help the field to reduce the cost of photovoltaic electricity by reducing production cost and by improving cell efficiencies. For these later advances, one must mention key efficiency breakthroughs in 1985 for Si solar cells (> 20 %) [20], in 1994 for GaInP/GaAs multijunction cell (> 30 %) [21] and in 1998 for $Cu(In,Ga)Se_2$ thin-film solar cells (19 %)[22]. Cost reductions for the 1st (Si wafer) and 2nd (thin-film) generation mostly include the use of alternative sources of silicon and the use of more cost-effective materials and processes, respectively. Despite being necessary for near-future commercial applications, these will be limited and therefore proposals for a 3rd generation of photovoltaics for terrestrial applications have already been published [23], this generation should be ultra-high efficiency (> 30 %) at a low-cost (~US$ 0.20 per W) to meet the long term demands of the energy market.

1.3   Photovoltaic effect and principle of solar cell operation

To understand the physical principles underlying the operation of solar cells, it is necessary to briefly review some of the fundamental properties of semiconductors.

10

1.3.1 Fundamental properties of semiconductors

The physical way in which atoms are arranged in a material determines its properties. Materials can be single crystalline, polycrystalline or amorphous. In a single crystal, the lattice periodicity extends throughout the material, as in wafers. This is an ideal case. More commonly, materials such as as-grown crystalline thin-films are polycrystalline: boundaries exist between crystalline grains, the periodicity extends over a few nanometers to a few microns. Lastly, an extreme case is when the periodic structure does not exist or extends for only a few atoms, such materials having no or very short order, such materials are called amorphous materials.

a)   Band diagram, band-gap

Electronic properties of crystalline materials/semiconductors are determined by their crystal structure. Indeed, an electron moving in a semiconductor material sees the lattice of atomic cores as a periodic potential. Therefore, the dynamic behavior of the electrons can be established by solving the time-dependent Schrödinger equation for a periodic potential. F. Bloch demonstrated that the wave-functions that are solutions of this equation must be the product of a plane wave times a function of the lattice periodicity [24]. A careful physical and mathematical treatment of the Bloch functions shows that the periodic potentials arising from the atoms of the lattice limits the allowed energies of the electron to energy bands separated by energy gaps. The allowed electron energies are plotted against the crystal momentum or the reciprocal-space $\mathbf{k}$ vector: this plot is commonly called a band diagram, an example is shown in Figure 1.2. For clarity, in the illustrations that follow, only the valence and the conduction bands are usually

11

represented: indeed, energy bands below the valence band are presumed to be fully occupied by electrons and those above the conduction band are presumed to be empty. When a minimum of the conduction band occurs at the same value of the **k** vector as the maximum of the valence band, the semiconductor has a direct band gap. When they occur at different values of the **k** vector, the semiconductor has an indirect band gap. Figure 1.2 shows that $CuGaSe_2$ is a direct band gap semiconductor.
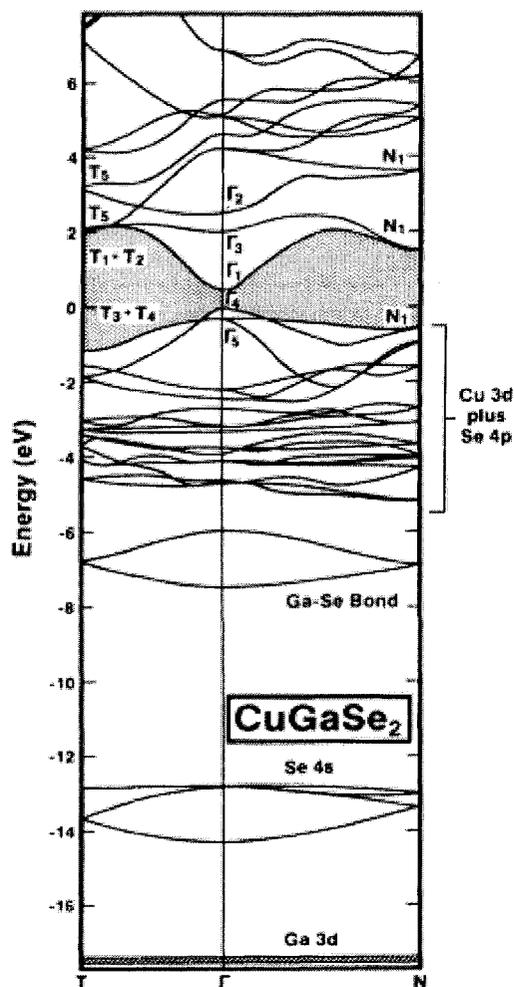
Figure 1.2. Electronic band structure of $CuGaSe_2$, the optical band gap is represented by the shaded area (from reference [25]).

12

In amorphous semiconductors (*e.g.* a-Si, a-Sb_2S_3), over short distances, the atoms are arranged in a periodic manner and an electron wave function can be defined. The wave functions from these small regions overlap in a way that a mobility gap can be established with electrons above the mobility gap defining the conduction band and electrons below the mobility gap defining the valence band. Contrary to crystalline semiconductors, there is a large number of localized energy states or trap states within the mobility gap, yielding a band edge tail. This will be discussed in Chapter 4 in the case of amorphous-Sb_2S_3.

b)   Intrinsic and extrinsic semiconductors

In semiconductors, the valence and conduction bands are separated by a small to moderate energy gap: smaller than 3 eV. As shown in Figure 1.3, thermal energy is sufficient to excite some electrons above the band gap at room temperature. Electrons fill the states from bottom to top and the states near the top of the valence band are empty due to the electrons thermally excited to the conduction band. These empty states can conveniently be regarded as positively charged carriers of current, called holes. At 0 K, the Fermi level is the energy below which all available energy states are occupied and above which no states are occupied. At temperature above 0 K, some electrons are thermally excited to higher energy level, the Fermi level is then the energy at which an energy state has a 50 % probability of being occupied based on the Fermi-Dirac distribution. An intrinsic semiconductor is pure: for instance, pure Si or stoichiometric semiconductor compounds. In an intrinsic semiconductor in thermal equilibrium, the number of electrons in the conduction band equals the number of holes in the valence

13

band. The intrinsic carrier concentration (holes or electrons) is typically very small

($10^{10} - 10^{13}$ cm^{-3} at room temperature) and therefore intrinsic semiconductors behave

very much like insulators.
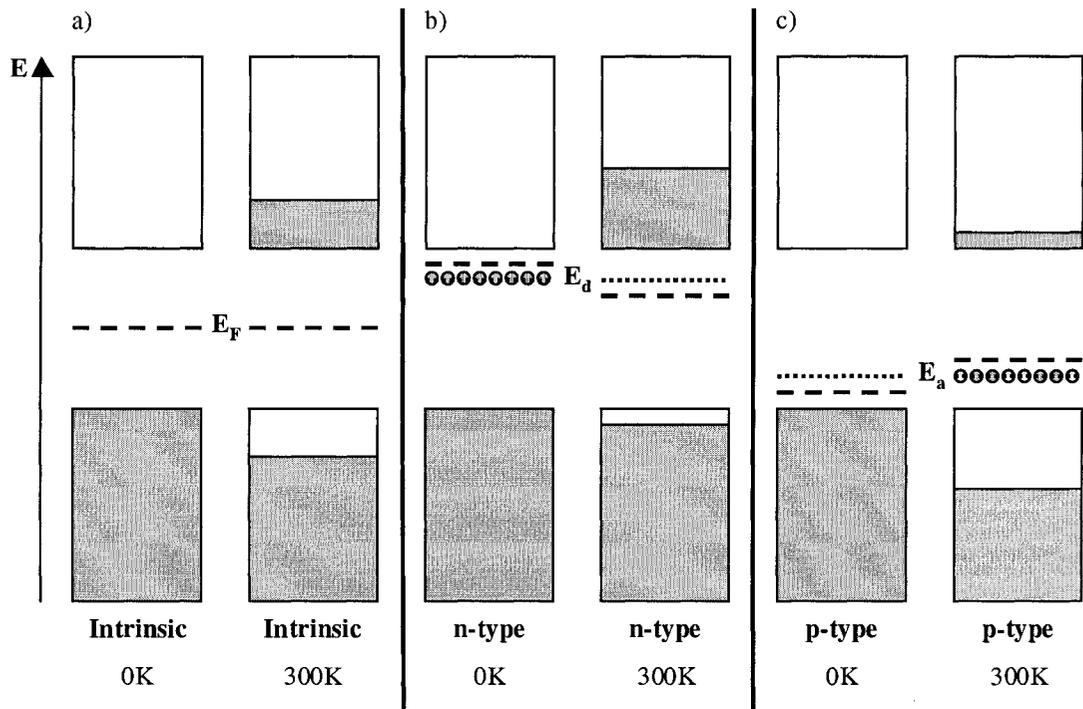
Figure 1.3. Schematic of semi-conductor band diagrams: a) for an intrinsic semiconductor at 0K and room temperature, b) for an extrinsic p-type semiconductor at 0K and room temperature, and c) for an extrinsic p-type semiconductor at 0K and room temperature. The bottom and top rectangles represent the valence and the conduction bands, respectively. E$_F$ stands for the Fermi level, they are represented by the bolder dash lines. E$_d$ stands for the donor level and E$_a$ stands for the acceptor level, they are represented by the thinner dash lines. Lastly, the shaded area represents electrons, while the blank areas represents holes.

The electrical conductivity of semiconductors can nevertheless be controlled through the introduction of specific impurities, or dopants, called donors or acceptors. Such materials are called extrinsic or doped semiconductors. If the semiconductor is electron-rich, *i.e.* electrons are the majority carriers, the semiconductor is n-type; if the semiconductor is electron-poor, *i.e.* holes are the majority carriers, the semiconductor is p-type. Donor impurities (n-type semiconductor) introduce filled energy levels close to

14

the conduction band. At room temperature, these donor levels are ionized promoting electrons to the conduction bands. Acceptor impurities (p-type semiconductor) introduce empty energy levels close to the valence band. At room temperature, electrons from the valence band are promoted to these acceptor energy states, leaving holes behind in the valence band. As an example, for solar cell applications, p-type Si wafers are usually doped with boron with concentrations in the range of 10^{16} cm^{-3}, yielding resistivity values on the order of 1 Ω.cm.

c)   *Absorption processes*

The creation of electron-hole pairs via the absorption of sunlight is fundamental to the operation of solar cells. The excitation of an electron directly from the valence band (which leaves a hole behind) to the conduction band is called the fundamental absorption. It is characterized by a rapid rise of the absorption coefficient $\alpha(h\nu)$, that for a given photon energy $h\nu$ is proportional to:

- the probability for the transition from the initial state to the final state,

- the density of electron in the initial states,

- and the density of available (empty) states in the final sates.

The absorption coefficient is used to determine the energy gap. However, the estimation of the energy gap from the "absorption edge" is not straight forward as transitions should obey certain selection rules. Indeed, both the total energy and momentum of all particles involved in the absorption process should be conserved. Because the momentum of the photon (h/λ, λ is the light wavelength, thousands of $\mathring{A}$) is very small

15

compared to the crystal momentum (h/a, a is the lattice constant, a few Å), the photon

absorption process must conserve the momentum of the electron.

Direct band gap semiconductors

Indirect band gap semiconductors

$$E_g = \frac{hv_2 + hv_1}{2}$$

$$E_{ph} = \frac{hv_2 - hv_1}{2}$$
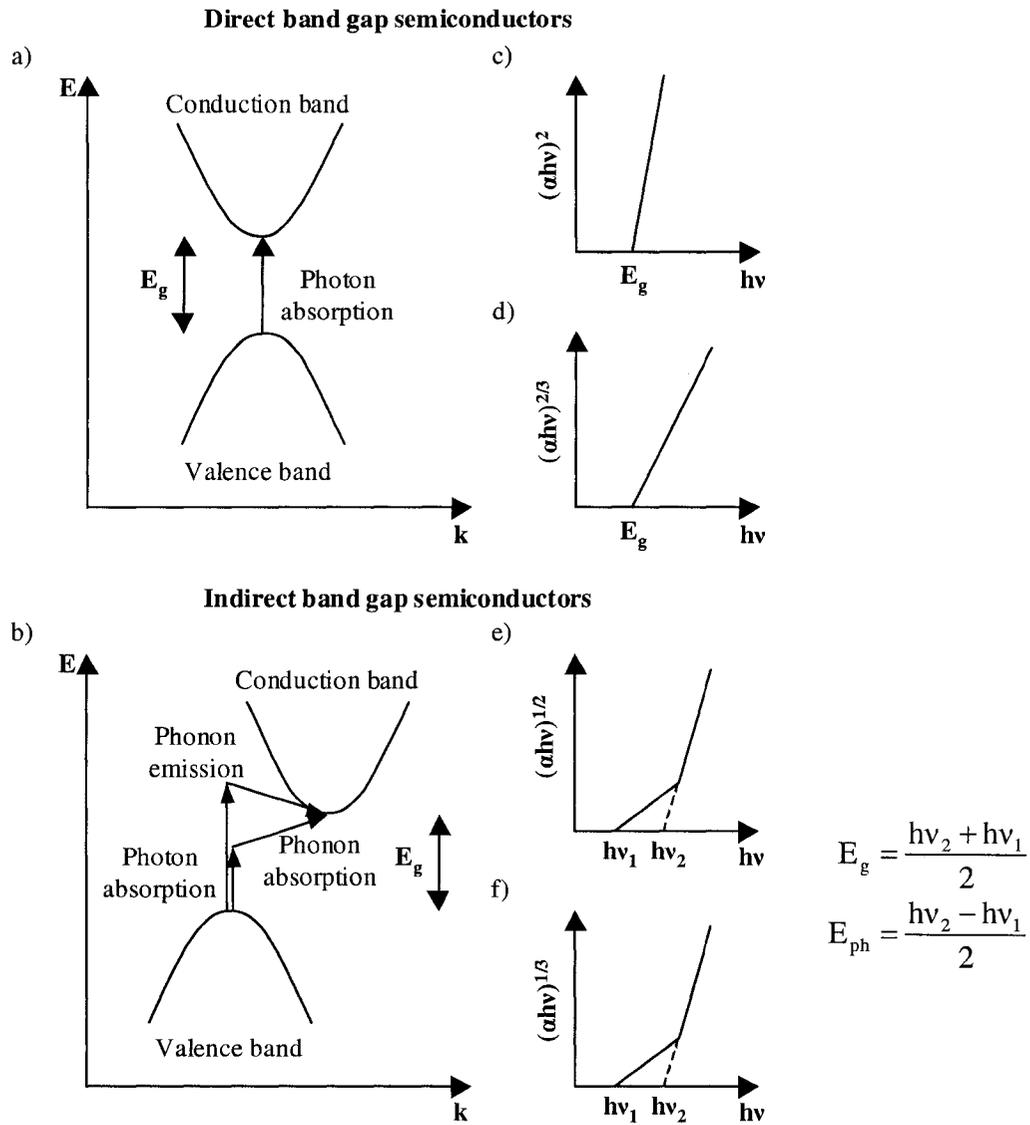
Figure 1.4. Schematic band diagrams for a) direct band gap and b) indirect band gap semi-conductors. Schematics of optical data processing for c) a direct allowed transition, d) a direct forbidden transition, e) an indirect allowed transition and f) an indirect forbidden transition. For the indirect transitions, the band gap energy (E_g) and the phonon energy (E_{ph}) are calculated according to the equations written above. k is the crystal momentum (adapted from references [26-28]).

16

Thus, four different types of transitions should be considered as shown in Figure 1.4: allowed direct transition, forbidden direct transition, allowed indirect transition, and forbidden indirect transition. In direct band gap semiconductors, transition occurs between the valence band and the conduction band at a given crystal momentum, the electron momentum is therefore conserved. From the conservation of energy, one can derive that for allowed direct transitions, the absorption coefficient $\alpha(h\nu)$ is proportional to $(h\nu - E_g)^{1/2}$, where E_g is the energy of the band gap [27]. Moreover, in some semiconductor materials, quantum selection rules forbid transitions at k=0 but allow them for k≠0, then, the transition is a forbidden direct transition and $(\alpha h\nu)$ is proportional to $(h\nu - E_g)^{3/2}$ [28]. In indirect band gap semiconductors, the valence band and the conduction band have extrema that are located at different crystal momentum, thus conservation of the electron momentum necessitates that the photon absorption process involve the absorption or emission of an additional particle, called phonon or lattice vibration. They are low energy (0.3 eV) and high momentum particles. The absorption coefficient $\alpha(h\nu)$ is then proportional to $(h\nu \pm E_{ph} - E_g)^2$, where E_{ph} is the energy of the emitted (− sign) or absorbed (+ sign) phonon, or to $(h\nu \pm E_{ph} - E_g)^3$ for indirect allowed and indirect forbidden transitions, respectively. Since both a phonon and an electron are required for indirect transitions, the absorption coefficient also depends on the availability of phonons with the required momentum. Thus, compared to direct transitions, indirect transitions have a lower probability and the absorption coefficient for indirect transitions is relatively small. As a result, light penetrates more deeply into indirect band gap semiconductors than into direct band gap semiconductors. In both indirect and direct band gap semiconductors, other photon absorption processes

17

exist: including phonon assisted direct transition, and absorption aided by localized states in the forbidden gap (impurity levels).

d)   *Recombination processes*

When a semiconductor is taken out of thermal equilibrium, for instance by illumination, the concentrations of electrons and holes tend to relax back toward their equilibrium values through a process called recombination, in which an electron falls from the conduction band to the valence band, thereby eliminating a valence band hole.
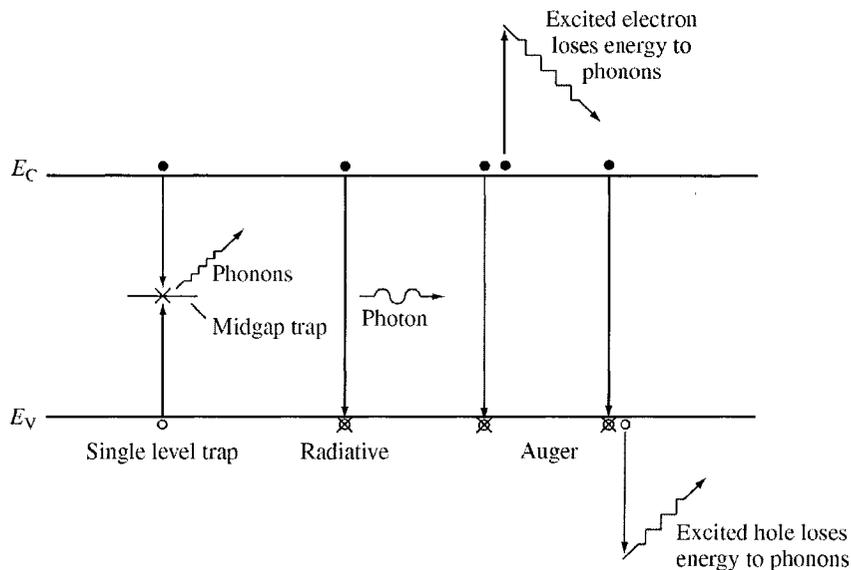
Figure 1.5. Recombination processes in semiconductors (from reference [27]).

There are several recombination mechanisms important to the operation of solar cells: recombination through trap states (defects) in the forbidden gap, radiative (band-to-band) recombination and Auger recombination, as shown on Figure 1.5. The net recombination rate per unit volume per second through a single level trap with energy within the forbidden gap is known as Shockley-Read-Hall recombination [27]. This rate depends on the carrier lifetime, which is inversely proportional to the trap cross-section,

18

the thermal velocity of the carriers, and the concentration of trap. If the material is of a certain type (p-type, for instance) and in low injection conditions ($n_0 < n \ll p_0 \approx p$, where p_0 and n_0 are the carrier concentration at thermal equilibrium), the recombination rate depends only on the minority carrier, also called limiting carrier. Radiative (band-to-band) recombination is the inverse of the optical absorption process by which an electron returns to the valence band and its energy is given to a photon. This process is much more efficient in direct band gap semiconductors than in indirect band gap semiconductors. Lastly, Auger recombination is somewhat similar to radiative recombination, except that the energy of the electron is given to another carrier in the conduction (electron) or the valence (hole) bands. Auger recombination is the inverse process of impact ionization. Moreover, interfaces between two dissimilar materials have a high concentration of defects due to the termination of the crystal lattice; it yields a continuum of traps in the forbidden gap at the surface. Electron-hole pair recombination processes are phenomena that can be detrimental to the operation of solar cells.

e) *Electron and hole motions*

Electrons and holes are subject to the classical processes of drift and diffusion. Drift is the response of a charged particle to an electric field. When an electric field is applied across a uniformly doped semiconductor, the bands bend upward in the direction of the applied electric field, as shown in Figure 1.6. Electrons in the conduction band move in the opposite direction of the applied electric field, whereas holes in the valence band move in the direction of the electric field. In other words, electrons sink and holes

19

float. Therefore, on a macroscopic scale, the carriers appear to move at a constant velocity since their motions are restrained by the semiconductor atoms, lattice vibrations (phonons), dopant ions, crystal defects and even other electrons and holes. The most significant scattering mechanisms in semiconductors are lattice (phonon) and ionized impurity scattering. Then, a drift velocity can be determined: it is proportional to the carrier mobility and the electric field. Moreover, electrons and holes in semiconductors tend, as a result of their random thermal motion, to diffuse from regions of high concentration to regions of low concentration. Hole and electron diffusion coefficients are then defined.
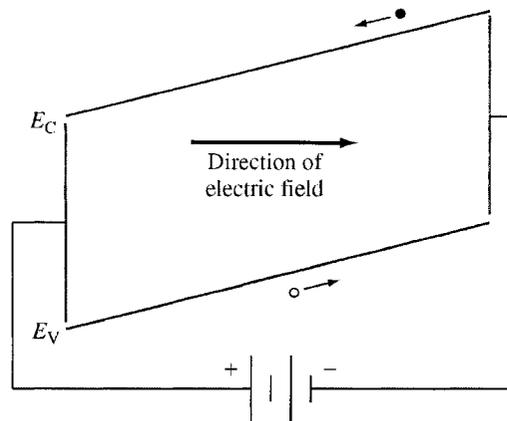
Figure 1.6. Illustration of the concept of drift in a semiconductor: electrons and holes move in opposite directions in the electric field created by an externally applied bias voltage (from reference [27]).

In thermal equilibrium, there can be no net hole or electron current: the drift and diffusion current should exactly balance. In intrinsic semiconductors, this leads to the Einstein relationship [27]:

$$\frac{D}{\mu} = \frac{kT}{q}$$ (1.1)

20

where D, μ, q are the diffusion coefficient, the mobility, and the charge of the carrier (electron or hole), respectively; and where k and T are the Boltzmann constant and the temperature (in K), respectively. This Einstein formula and its generalized forms (extrinsic semiconductors) allow for determination of the diffusion coefficients from the carrier mobilities, that are usually obtained from resistivity and photoconductivity measurements.

1.3.2 Solar cells operation

As the ultimate goal of this thesis was originally a combinatorial discovery of thin film solar cell architectures based on new light absorber materials, the basics of solar cell operation will be briefly reviewed. More detailed and comprehensive reviews of solar cell operations may be found in the references [5,8,10,27,29,30]. Solar cells convert sunlight directly into electricity, the power generating part of a solar cell consists of a rectifying junction: p-n or p-i-n junctions (i- standing for intrinsic region where the semiconductor is not doped and is therefore quite insulating). p-n junctions may be homojunctions or heterojunctions according to whether the semiconductor material on one side of the junction is the same or different from that on the other side. It is interesting to mention that a metal-semiconductor junction may form a rectifying junction named a Schottky barrier that allows charge separation, or an ohmic contact that can be used to extract electrical current from the device. Polycrystalline thin film solar cells are usually p-n junctions and therefore only this type of junctions will be discussed in this section. However, before this discussion, it is useful to describe the solar radiation.

21

a) *Solar spectrum*
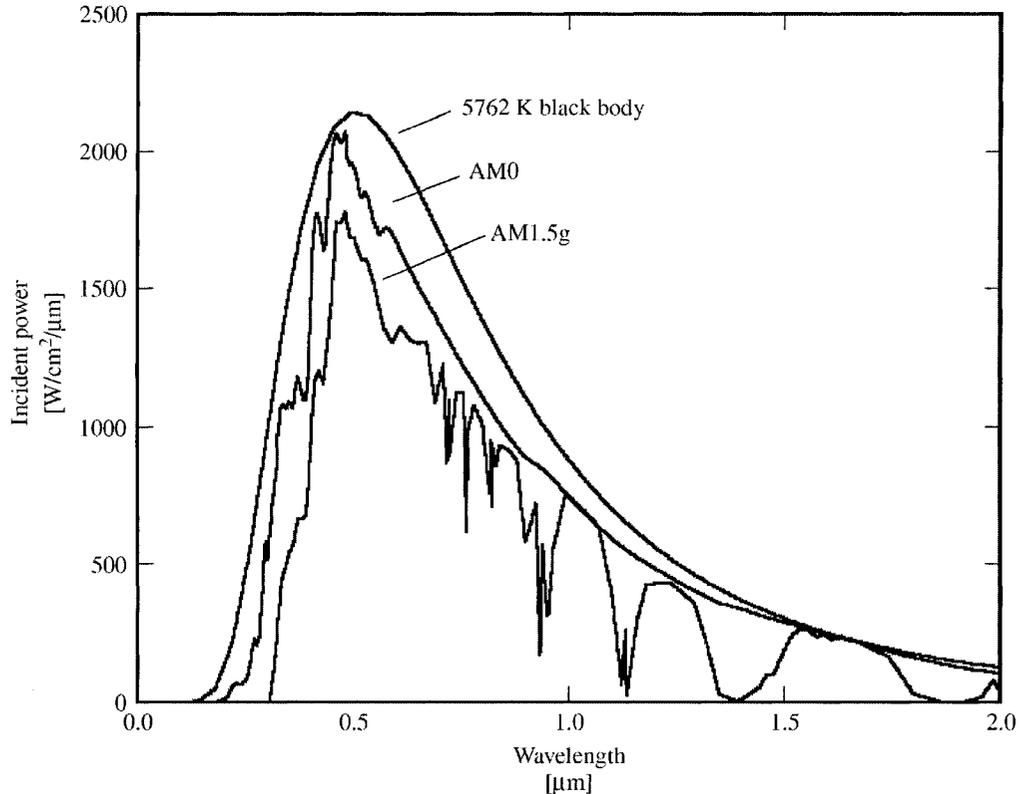
Figure 1.7. The radiation spectrum for a black body at 5762 K, an AM0 spectrum, and an AM1.5 global spectrum (from reference [27]).

The sun has a surface temperature of 5762 K and its spectrum can be approximated by a blackbody radiator at that temperature [27]. Only the photons emitted directly in the direction of the Earth contribute to the solar spectrum as observed from earth. Just above the Earth's atmosphere, the irradiance or radiation intensity is about 1.353 kW/m² and the spectral distribution is referred to as an air mass zero (AM0) radiation spectrum. The air mass is a measure of how the atmosphere affects the irradiance and the spectrum of the solar radiation reaching the earth's surface. A widely used standard for comparing solar cell performances is the AM1.5 solar spectrum normalized to an irradiance of 1 kW/m² (= 100 mW/cm²) at 25°C for cell areas larger

22

than 1 cm^2. Figure 1.7 shows the spectrum for blackbody radiation at 5762 K, an AM0

spectrum and an AM1.5 spectrum (global) that includes the diffuse component of the

solar radiation.

b)   *p-n junction formation*
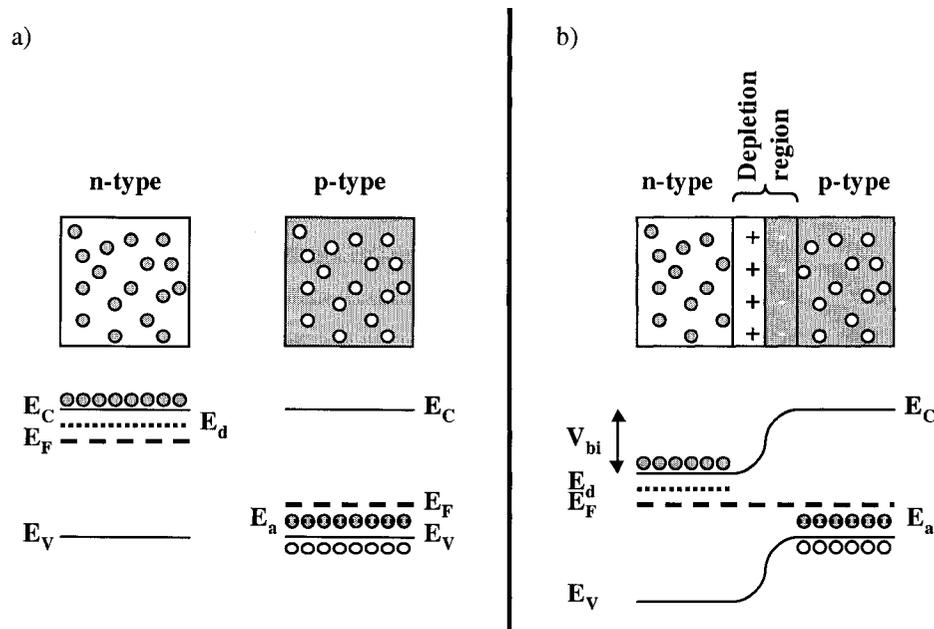
Figure 1.8. Band diagrams a) before and b) after the p-n junction formation. E_c, E_v, E_F, E_a, E_d stands for conduction, valence, Fermi, acceptor, donor energy level, respectively. V_{bi} is the built-in potential. Shaded areas and circles represent electrons; blank areas and circles represent holes (adapted from reference [5]).

When an n-type semiconductor and a p-type semiconductor are brought in

contact, a pn-junction is formed. Before contact, the n-type and p-type semiconductors

have different Fermi energy levels. After contact and in thermal equilibrium, the two

materials must share a common Fermi level. Thus, as the Fermi level positions must

remain the same relative to the valence and the conduction bands in the bulk of the

semiconductor, the relative band edge positions are adjusted at the junction to achieve a

common Fermi level, as shown in Figure 1.8. This phenomenon is called band bending.

23

In thermal equilibrium, since there is a concentration difference of holes and electrons between the two types of semiconductors, holes diffuse from the p-type to the n-type region, and electrons diffuse from the p-type to the n-type region. Therefore, at the junction, a positively charged region is created in the n-type material and a negatively charged region is created in the p-type material, this creates a potential difference that prevents further diffusion. These regions constitute a space-charge or depletion region practically free of any mobile charges (*i.e.* charge carrier). This phenomenon is illustrated in Figure 1.8.b. The electrostatic potential difference resulting from the junction formation is called the built-in voltage (V_{bi}).

c)   p-n junction under illumination

Figure 1.9 presents schematic energy band diagrams for a p-n heterojunction solar cell under different conditions: a) at thermal equilibrium in dark, b) under a forward bias, c) under a reverse bias, and d) under illumination, open circuit conditions. In Figure 1.9, subscripts 1 and 2 refer to an n-type and a p-type semiconductor, respectively. E_{Ci} and E_{Vi} refer to the conduction and valence band energies; E_{gi} and E_{Fi} refer to the band gap energies and Fermi levels, respectively. In the absence of an applied potential and in thermal equilibrium (Figure 1.9.a), the Fermi levels of the semiconductors coincide, and there is no current flow, as the diffusion and the drift currents for the each carrier type exactly balance. Figure 1.9.b shows the effect of a forward bias, V_f (*i.e.* applying a positive voltage to the p-side). It shifts the Fermi level of the n-type semiconductor upward and that of the p-type semiconductor downward, thus lowering the potential energy barrier of the junction, and facilitating the current

24

flow across it. A net current flows from the p-side to the n-side (conventionally positive current).
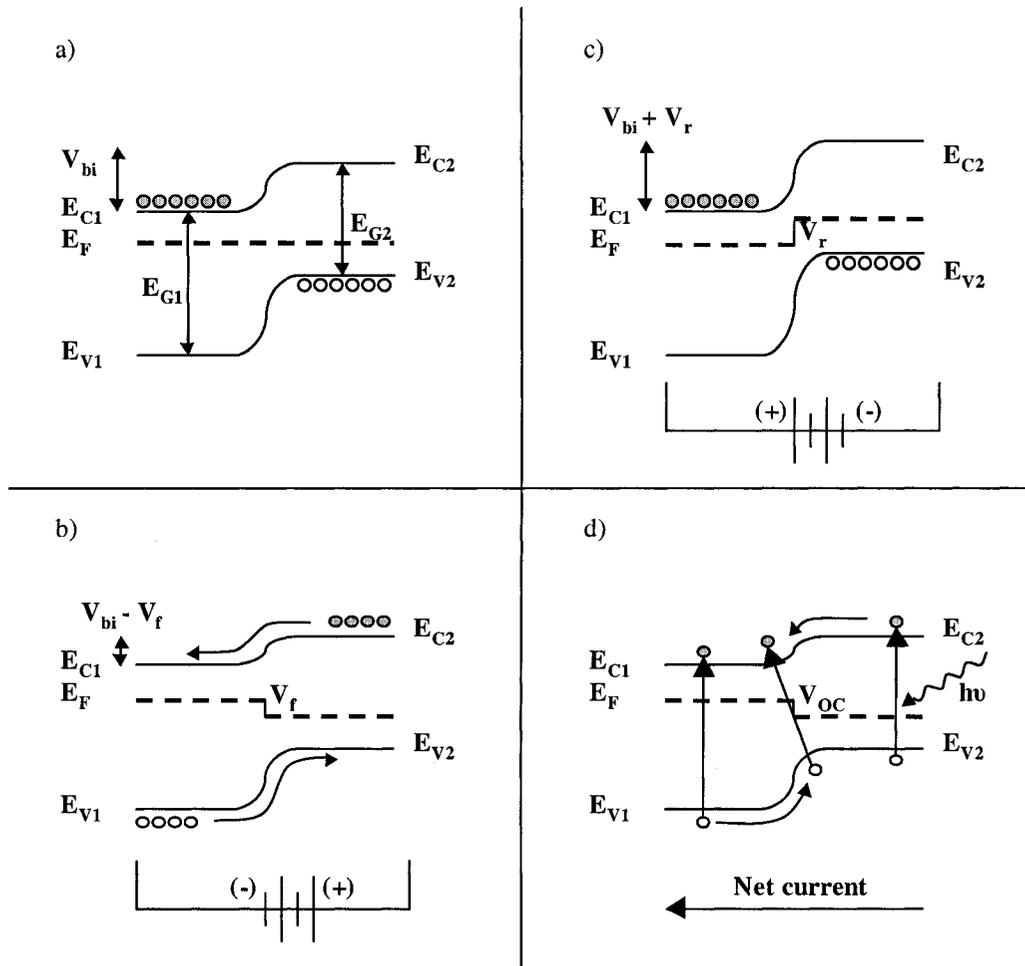
Figure 1.9. A simplified band diagram of a p-n heterojunction solar cell a) at thermal equilibrium, b) under a forward bias (V_f), c) under a reverse bias (V_r) and d) under illumination, open circuit conditions (V_{OC}) (adapted from reference [8]).

As shown in Figure 1.9.c, the effect of a reverse bias, V_r (*i.e.* applying a positive voltage to the n-side) is opposite: it increases the potential barriers and thus impedes the current flow; only a tiny current I_o from the n-side to the p-side is produced, it is called the dark saturation current (herein conventionally negative current). In the dark, a solar cell is similar to a diode. However, illumination of the junction, as shown in Figure 1.9.d,

25

creates electron-hole pairs; indeed, photons with energy hv larger than that of the band gap of the semiconductor excite electrons into the conduction band, leaving a hole in the valence band. The internal field of the junction separates electron-hole pairs, also named excitons: electrons drift ("sink") to the n-side and holes drift ("float") to the p-side. Therefore, a photovoltage V_{OC} (open circuit voltage or photovoltage under open circuit conditions) is generated across the junctions.

d)   Solar cell I-V curve, fill factor and efficiency

In a simple approach, the I-V characteristic of a solar cell is equivalent to the one of a current generator, representing the light-induced current (*i.e.* photocurrent) in parallel with a diode, representing the p-n junction; this is clearly shown in Figures 1.10.a and 1.10.b. Therefore, the output current is then equal to the difference between the photocurrent and the diode current, as shown in figure 1.10.d. The current-voltage (I-V) characteristics of a solar cell in the dark and under illumination are shown in Figure 1.10.c. The most important parameters that describe the performances of a solar cell are derived from its I-V characteristic (Figure 1.10.d) under standard illumination, simulating the sunlight. These parameters are the open-circuit voltage V_{OC}, the short circuit current I_{SC} and the fill-factor FF.

The open circuit voltage, V_{OC}, is limited by the band gap energy E_g of the absorber material, and its maximum value is calculated by dividing the band gap energy by the charge of an electron (E_g/e). Because of electron-hole pair recombination, the open circuit voltages of real solar cells are considerably below their maximum limits.

26

a)

c)

$$I = I_{ph} - I_D$$

Current I

b)

n-type   p-type

E_C

E_F —————— V ————

E_V

d)

Current:

$$I = I_{ph} - I_o\left(\exp\left(\frac{qV}{kT}\right) - 1\right)$$

Fill factor:

$$FF = \frac{V_{mp}I_{mp}}{V_{OC}I_{SC}}$$

Maximum power:

$$P_{max} = V_{mp}I_{mp}$$

Efficiency:

$$\eta = \frac{P_{max}}{P_{input}}$$
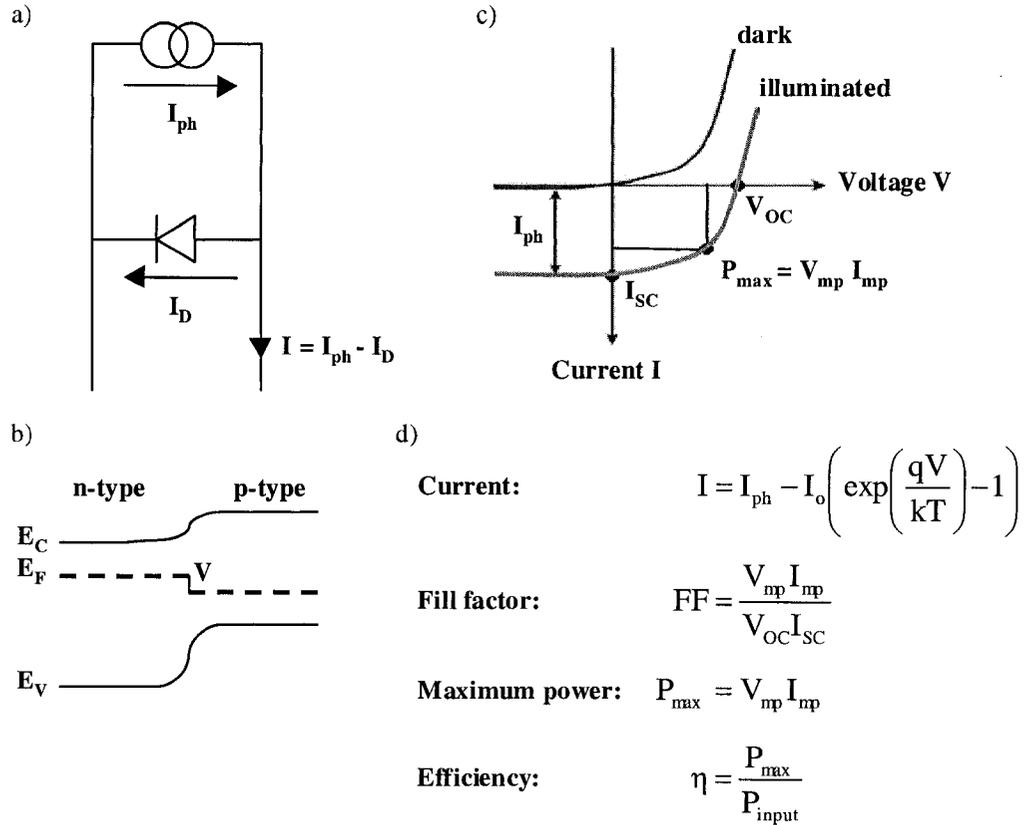
Figure 1.10. I-V characteristic of a solar cell: a) equivalent circuit under illumination, b) corresponding band diagram, c) I-V curve in the dark and under illumination and d) parameters determined from the I-V curve. I_{ph}, I_D are the photocurrent and the diode current, respectively. V_{mp} and I_{mp} are the maximum power voltage and current, respectively; V_{oc} and I_{SC} the open circuit voltage and short circuit current, respectively (adapted from references [5,8]).

The maximum value of a short circuit current density, j_{SC}, is limited by the photogenerated current density, j_{ph}, that depends on the amount of absorbed light. As mentioned earlier, to be absorbed photons must have energies larger than the band gap energy of the semiconductor. Therefore, the maximum value of a short circuit current density equals exN, where e is the charge of an electron and N is the number of photons with $E > E_g$, N may be determined from the AM1.5 spectrum. Because every photon with $E > E_g$ does not necessarily generate an electron-hole pair, the short circuit current densities of real solar cells are considerably below their maximum limits. The fill factor,

27

FF, encapsulates all of the internal power losses; high efficiency cells usually have fill factor values of 75 % to 85 % [31]. Lastly, the conversion efficiency η of a solar cell is the ratio of the maximum power output that can be extracted from the device to the input power (sunlight).

e)   *Power losses*

Several power losses in solar cells exist. First, there are fundamental losses related to the band gap energy: indeed, most of the absorbed photons have energies larger than the band gap energy, and the extra energy is dissipated as heat. In addition, a considerable part of the solar spectrum is not utilized because of the inability of a semiconductor to absorb photons with energy smaller than the band gap. More efficient collection of the solar spectrum may be achieved with tandem cells (also known as multijunction cells), containing two (several) absorbers with different band gaps [23]. Based on these considerations, the band gap value is one of the most important properties of the absorber material of a solar cell. The dependency of the conversion efficiency with the band gap energy may be found in [32]. There is an optimum band gap value for the absorber material of a single-junction solar cell, as the V_{OC} and FF increase and j_{SC} decreases while the band gap increases. This theoretical maximum efficiency (~30 %) is obtained for a band gap value of 1.5 eV [32].

As mentioned in Section 1.3.1.d, recombination is the opposite process of electron-hole pair generation. Recombination is most common at impurities or defects of the crystal structure, or at the semiconductor junctions and surfaces, where energy levels

28

maybe introduced inside the band gap. Recombination phenomena mostly result in a net loss of the cell current. These levels act as stepping stones for the electrons to fall back into the valence band and recombine with holes. Important sites of recombination are also the ohmic metal-semiconductor contacts. In addition, the transmission of electric current produced by the solar cell involves ohmic losses as the materials involved have non-zero resistivities; these losses are called series resistance and mostly reduces the fill factor, which in turn decreases the maximum power point value and therefore the efficiency of the cell. Lastly, other sources of power losses should be mentioned and include surface reflection, shadowing, absorption by contacts and incomplete light absorption. Therefore, manufacturing thin-film solar cells is a challenging process that involves engineering of the band edges of the different device layers (front contact, window layer, buffer layer, absorber layer and back contact) and requires careful control of the bulk layers and of interfaces between them in order to limit the power losses.

1.4   The different technologies and the need for new solar absorbers

As was previously mentioned, several technologies are available for terrestrial photovoltaic applications; it includes: single crystalline and polycrystalline silicon solar cells, amorphous silicon solar cells, CdTe solar cells, and Cu-chalcopyrite solar cells. amorphous-Si and crystalline-Si thin films, CdTe and CIS (CIGS) solar cells are types of thin film solar cells.

29
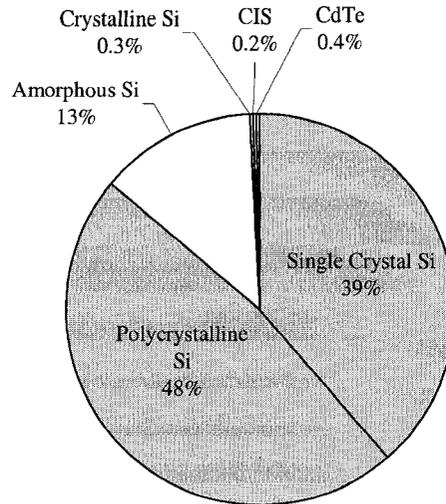
Figure 1.11. Market shares of the different PV technologies for terrestrial applications, blank sectors are thin film solar cells (adapted from reference [32]).

a)   *Crystalline silicon based solar cells*

As shown in Figure 1.11, most commercial solar cells of today are made of single crystalline (39 %) or polycrystalline silicon (48 %). Abundant, available at relatively low cost, of high quality and with well-known properties, silicon has attracted a lot of attention for photovoltaic applications, especially because of synergies with the microelectronics industry. Indeed, the knowledge of the material properties and the development of manufacturing techniques for the microelectronics industry have largely contributed to the rapid growth of silicon solar cells. As shown in Figure 1.12, in polycrystalline and single crystalline Si solar cells, the bulk of the cell (wafer or cast) is p-type Si with a thin, highly doped layer of n-type Si; the cell top surface is usually textured to produce light trapping and reduce reflectance. Anti-reflective coating (ARC) is made of a thin layer of a non-absorbing material with a lower refraction index, it decreases the reflectance. Finally metal back contacts and fingers are deposited. A comprehensive review about crystalline silicon solar cell may be found in reference [33].

30
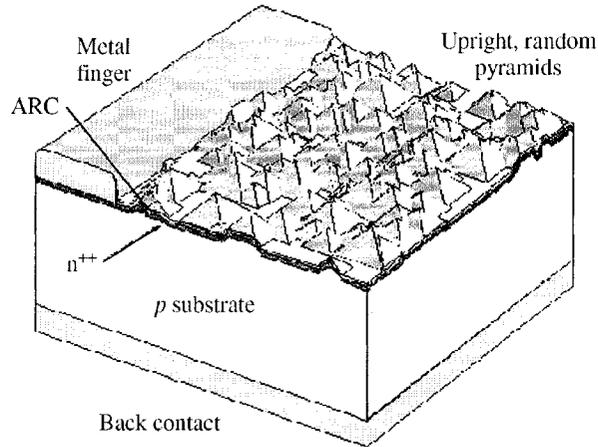
Figure 1.12. Typical structure of a single crystalline Si solar cell (from reference [33]).

Despite high efficiencies for cells (> 20 %) and modules (> 15 %) [31] based on crystalline silicon, silicon is not an ideal absorber material for solar cells. Silicon is an indirect semiconductor and therefore does not absorb light as efficiently as a direct semiconductor. Consequently, thick layers of material are required to achieve sufficient light absorption. Thus, 100 μm of crystalline silicon is needed for 90 % light absorption in comparison with 1 μm of GaAs (which is a direct band gap semiconductor). Because of the large thickness required, the silicon used in solar cells must be of high quality to minimize recombination of the photogenerated charge carriers. Thus, for crystalline Si thin film solar cells, not only the amount of material required is larger, but also the requirements on the film crystallinity are more stringent. These strict requirements increase production costs. In addition, for single crystalline (wafer) silicon solar cells, the manufacturing process of silicon ingots is very energy consuming; moreover, the current production technologies suffer from high material losses during the dicing of ingots (single crystalline silicon) or casts (polycrystalline silicon). Several alternative processes, such as fabrication of Si ribbon, have been developed to decrease material

31

losses. However, the cost of production of silicon cells remain high and their energy payback time too long (duration required for solar cell to produce as much energy as was required for its fabrication). Fortunately, the high production costs of crystalline silicon solar cells are compensated by their high efficiencies, with a record efficiency for a small area crystalline Si solar cell of 25 %, which is close to the theoretical maximum [31]. One should note that other, even more expensive, high-efficiency materials, such as GaAs and InP are used for space applications where efficiency is the main requirement and cost is not such an issue.

b)   *Thin-film solar cells*

The limitations and cost of crystalline silicon based solar cells have encouraged the development of other types of solar cells for terrestrial applications: namely thin film solar cells. Those based on direct band gap semiconductors are of particular interest because of their high absorption coefficients. Thus, the required thicknesses of the active absorber material are only 1 to 2 μm, reducing both material consumption and requirements for film crystallinity. Indeed, higher concentrations of impurities and crystalline defects may be tolerated, as charge carrier transport distances are shorter. In addition, thin film solar cells enable a greater flexibility in terms of processing, as thin-films can be deposited by a variety of vacuum and non-vacuum methods on various substrates – inexpensive such as glass or curved and/or flexible such as polymer substrates. In addition, during the thin film processing, cells can be connected in series in an integral manner on large area substrates by appropriate patterning/scribing of the different functional layers. Main candidates for low-cost thin film solar cell materials are

32

amorphous hydrogenated silicon (a-Si:H), Cadmium telluride (CdTe) and Cu-chalcopyrite compounds: CuInS$_2$ (CIS) and Cu(In,Ga)(S,Se)$_2$ (CIGS). Schematics of these cells architecture are shown in Figure 1.13.
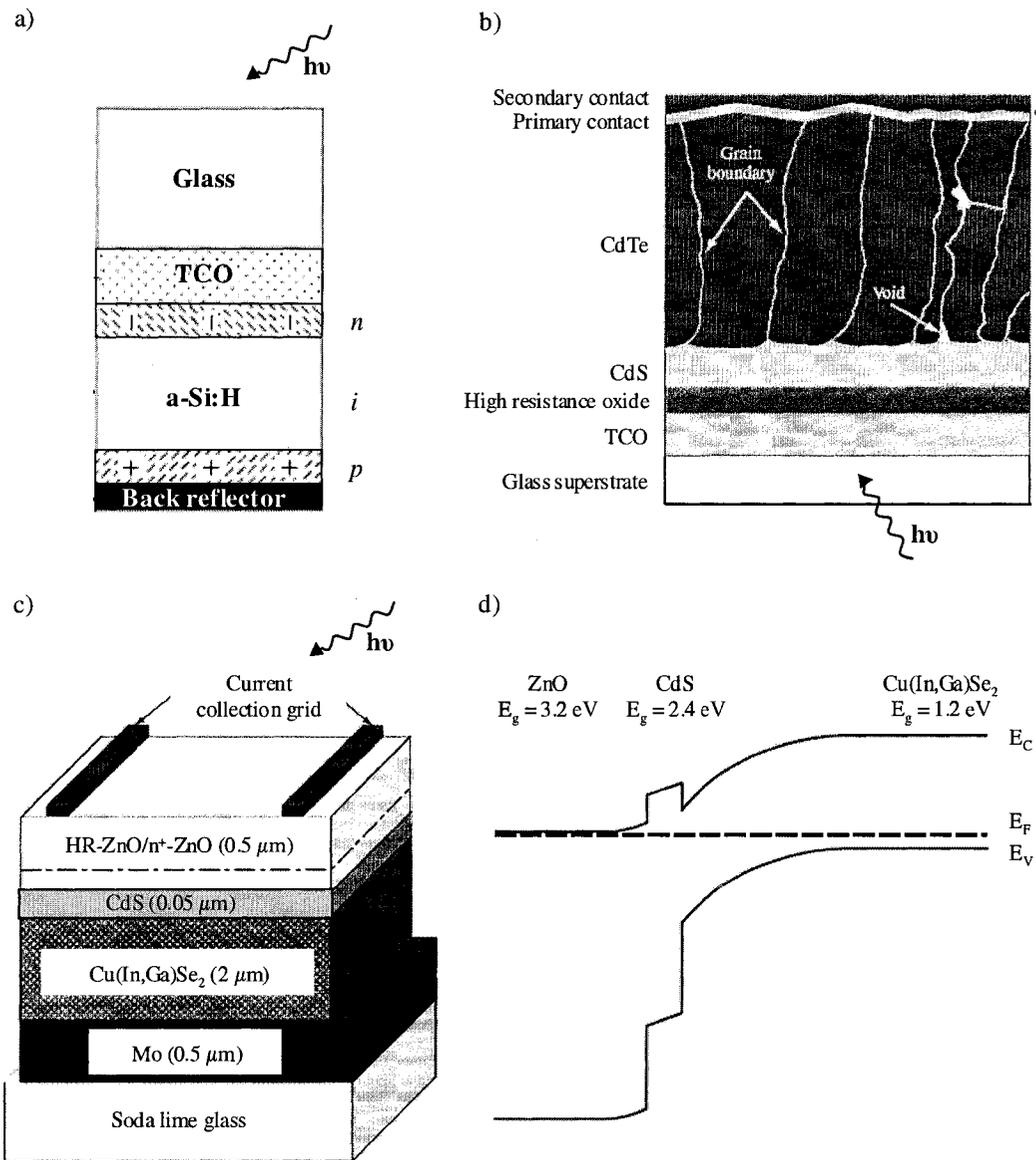
Figure 1.13. Schematics of thin film solar cells based on: a) a-Si (adapted from reference [32,34]), b) CdTe (adapted from reference [35]) and c) Cu(In,Ga)Se$_2$ (from reference [36]). d) Schematic of the band diagram of a Cu(In,Ga)Se$_2$ thin film solar cell (adapted from reference [36]). TCO stands for transparent conductive oxide.

33

Amorphous hydrogenated silicon (a-Si:H) solar cells are quite cost effective to produce and represent most of the thin-film PV market, as shown in Figure 1.10. It accounts for 13 % of the PV market while CdTe and Cu-chalcopyrite compound solar cells account only for 0.4 % and 0.2 % of the PV market. The high absorption coefficient of amorphous silicon compared to crystalline silicon enables its use in thin film form; in addition, its band gap is close to the ideal value of about 1.5 eV, potentially enabling a high efficiency solar cell. In a-Si thin film solar cell, because of low carrier mobility, a high electric field is required, this is achieved by depositing thin p-i-n layers, of the order of a few hundred nanometers. A typical a-Si:H cell architecture is shown in Figure 1.13.a. Light-induced degradation of a-Si solar cells is, however, detrimental and causes a drop in conversion efficiency from the initial value. This is known as the Staebler–Wronski effect: defects, such as dangling bonds are generated by illumination and act as recombination centers for electron-hole pairs. Stabilized (light soaking) amorphous silicon solar cells feature efficiencies only around 10 % [31]. Comprehensive reviews about amorphous-Si solar cell include references [32,34].

The polycrystalline compound semiconductor materials (CdTe, $CuInS_2$ and $Cu(In,Ga)(S,Se)_2$) are the other materials that are under intensive investigation and development for use as solar absorbers in thin film solar cells. Figures 1.13.b and 1.13.c show typical thin film cell architectures and their functional layers:

- front contact and window layer are made of an n-type transparent conductive oxide (*e.g.* ITO, ZnO); a second, highly resistive, transparent oxide layer is deposited to avoid the possibility of local shunting or excessive forward current due to the thin, polycrystalline CdS layer,

- a thin layer of CdS is used as the n-type semiconductor for the p-n junction (it is also called buffer layer),

- a thicker (1 to 2 μm) absorber layer of chalcopyrite or CdTe is used as the p-type semiconductor, this is the area were most of the photons are absorbed and generate electron-hole pairs,

- lastly, a metal layer ensures the contact between the absorber layer and the outside world.

As, one can see, these thin film solar cells, especially the Cu-chalcopyrite based-ones, involve a large number of rather complex layers. Thus, making a fully functional device requires optimization of the structural, optical and electrical properties not only of the various materials involved, but also of the interfaces between these materials. Indeed, interfaces are regions where the defect levels (recombination centers) are particularly critical and where the band edge matching occurs; interfaces are therefore crucial to the cell operation and performance. Optimization of the layers and their interfaces strongly depend on the manufacturing processes used to make the thin film solar cell: both main deposition techniques and post-deposition treatments (*e.g.* dopant introduction) should be carefully established. These polycrystalline thin film solar cells

have been under intensive investigation and lead to a rich literature; comprehensive reviews may be found in references [32,35-39].

c)   *The need for new solar absorbers: issues related to the availability and toxicity of materials*

Despite high efficiencies for CIGS and CdTe cells, up to 18.4 % and 16.5 % for a small-size laboratory cell [31], some limitations may arise from the materials and elements used in these cells. Indeed, as shown in Table 1.3, cadmium, indium, gallium, selenium and tellurium are rare or geochemically scarce and are, therefore, mostly recovered as by-products of refining other ores. Cadmium and indium are recovered from zinc ore, gallium from bauxite (Al) ore, while selenium and tellurium are recovered from copper ores [2]. Despite its relative abundance in the earth's crust, gallium is a very expensive element, since it is not recovered efficiently from bauxite. Cadmium is about as abundant in the earth's crust as are antimony and indium. Cadmium is never found as a native metal, and only three cadmium minerals are known, none of which is found in sufficient concentration to be mined alone as an ore; however, it may be effectively recovered from zinc ore refining and therefore its price is reasonable. Selenium is quite rare in the earth's crust with a crustal abundance in the range of 0.05 ppm [40] to 0.1 ppm [2]. Perhaps more importantly, it is quite scattered in the crust and may only be enriched from copper ores by a factor of 30 [2]. Although, tellurium may be enriched quite efficiently by a factor of 300 from copper ores, tellurium is the rarest of all the elements considered herein, with only a 0.005 ppm by weight abundance in the earth's crust [2]. Lastly, indium is also a rare element with an estimated 0.24 ppm by weight

36

[41]; despite this somewhat higher overall crustal abundance, indium is not efficiently recovered from zinc ores, with only an enrichment factor of 80 [2], as the usual content of indium in ores is smaller than 0.05 ppm [41]. Elemental In, Ga, Se and Te are all expensive materials due to their limited availability, as shown in Table 1.3. Lastly, it is interesting to note that the availability of tellurium and indium will ultimately limit the electricity generation capacity of CdTe and CIGS thin film solar cells to 4 % and 1 % of the current global electricity production, respectively [2], calling for alternative materials.

Table 1.3. Geological and economical characteristics of selected elements

Element	Crustal abundance (ppm by weight)	Availability [1]	Price [2] (USD / kg)
S	~ 350	Native	0.04
Cu	25 [2]	Native and ore	3.65
Ga	15 [2]	Recovered from bauxite (E.F. = 3)	250
Pb	~ 14	Recovered from galena (PbS)	0.95
In	0.24 [41]	Recovered from copper ore (E.F. = 80)	810
Sb	0.20 [42]	Recovered from stibnite (Sb_2S_3)	3.20
Cd	0.16 [43]	Recovered from zinc ore (E.F. = 2000)	3.30
Se	0.05 [2]	Recovered from copper ore (E.F. = 30)	115
Te	0.005 [2]	Recovered from copper ore (E.F. = 300)	210

Notes: (1) ore from which the element is recovered; the enrichment (E.F.) factor indicates the efficiency of the recovery, values were obtained from [2].

(2) prices (for ~99.9 % materials) were calculated from USGS Mineral Commodity Summaries 2006 [42].

In addition, the toxicity of elemental tellurium, selenium, cadmium and their compounds will raise important environmental issues, both at the production and the recycling levels if widely used. Despite well-controlled emissions during manufacturing

37

and recycling of the photovoltaic modules [44,45], these elements and compounds may impede the wide acceptance of photovoltaic technology. European, U.S. federal and California environmental regulations regarding spent PV modules and European restrictions on the use of certain hazardous substances will impact the cost of current thin film solar cell technologies and may decrease their feasibility.

d)   *Pb-Sb-S phases as potential candidates for the light absorber*

As just shown, it is not surprising that a lot of effort is still going into the search for new thin film solar cell materials. The requirements for an ideal solar cell material would be [32]:

- band gap between 1.1 and 1.7 eV (close to 1.5 eV),

- direct band gap structure (high absorption coefficient),

- consisting of readily available, non-toxic materials,

- easy, reproducible synthesis suitable for large area deposition technique,

- good photovoltaic conversion efficiency,

- long-term stability.

Such a material has not yet been found...

Despite some toxicity-related issues, lead and antimony are quite cost effective materials, as shown in Table 1.3. Indeed, their respective abundance and availability should not be an issue as these elements are readily recovered from sulfide ores: galena (PbS) for lead and stibnite (Sb_2S_3) for antimony. Containing only cost effective and abundant elements, Pb-Sb-S compounds are potential light absorbers for thin-film solar

38

cells. Indeed, as shown in Table 1.4, with energies close to 1.4 eV, their bandgaps are appropriate for efficient solar to electrical energy conversion. Moreover, a recent investigation of the potential of many mineralogical compounds for photovoltaic applications indicated that $Pb_9Sb_8S_{21}$ (semseyite) displayed "device quality" properties [46]. Dittrich et al. also reported preliminary thermal evaporation and subsequent characterization of multiphase Pb-Sb-S thin films [47]. Thus, Pb-Sb-S compounds are promising potential light absorbers for thin-film solar cells.

Table 1.4. Band gap energies of some Pb-Sb-S ternary phases

Phase	Composition	Band gap (eV)	Ref.
Boulangerite	$Pb_5Sb_4S_{11}$	1.43, 1.34	[48],[49]
Zinckenite	$Pb_9Sb_{22}S_{42}$	1.48	[49]
Semseyite	$Pb_9Sb_8S_{21}$	1.50	[49]
Heteromorphite	$Pb_7Sb_8S_{19}$	1.41	[48]
Plagionite	$Pb_5Sb_8S_{17}$	1.53	[49]
Fülöppite	$Pb_3Sb_8S_{15}$	1.63	[49]

1.5 Cu-chalcopyrite thin film solar cell manufacturing and processing

As mentioned earlier, polycrystalline thin-film solar cells, based on chalcogenide compound semiconductors, such as Cu-chalcopyrites and cadmium telluride, are important for terrestrial applications because of their high efficiency, long-term stability and potential for low-cost production [39]. Because, $Cu(In,Ga)(Se,S)_2$ (CIGS) and $CuInS_2$ (CIS) are well-developed and conceptually close to the Pb-Sb-S ternary phases, it is interesting and relevant to review some of the current solar cell manufacturing processes for these compounds.

39

The system of copper chalcopyrites, with $CuInSe_2$ and its alloys with Ga [50], Al [51] and S [52] is of particular interest as it covers the visible spectrum over a wide range of band-gap energies from 1.04 eV for $CuInSe_2$ up to 2.7 eV for $CuAlSe_2$. As any desired alloys between these compounds can be produced [38,53], they offer a wide range of possibilities for optoelectronic properties improvement. Thus, the research interest has expanded from $CuInSe_2$, to $CuGaSe_2$, $CuInS_2$ and their multinary alloys $Cu(In,Ga)(Se,S)_2$ [32]. A wide range of thin-film deposition techniques have been employed to synthesized these compounds [8]: including vacuum techniques such as single source evaporation, co-evaporation, DC and RF sputtering and reactive sputtering, or non vacuum techniques such as spray pyrolysis, electrodeposition [54], and chemical bath deposition [55]. Precursor film deposition is usually followed by an annealing stage in the 450°C – 600°C temperature range in the presence of Se or S. Chalcogenization reactants can either be selenium or sulfur hydrides or elemental selenium or sulfur vapor. For non-vacuum deposition methods, a heat treatment in a reducing atmosphere (H_2) is required to improve crystallinity and purity before the recrystallization / chalcogenization step [39].

As $Cu(In_{1-x},Ga_x)Se_2$ (x = 0.2 to 0.3) yielded, to date, the most efficient laboratory scale thin-film solar cell [22,56] in the traditional ZnO/CdS/CIGS/Mo device architecture, the synthesis of these compounds attracted considerable interest. For large-scale applications, two approaches are of particular interest: multi-source thermal evaporation or reactive annealing of precursor films. During the multi-source thermal evaporation process, a precise control of the metal deposition rates is required while Se

40

is always evaporated in excess. Several preparation sequences have been developed to improve the film composition and morphology, yet, all of them include a Cu-rich stage during the growth process and aim at an In-rich overall composition in order to combine the large grain growth regime of the Cu-rich phase with the more favorable electronic properties of the In-rich composition [38]. Moreover, variation of the Ga/In ratio during deposition with a larger Ga content towards the back of the cell, allows the design of graded-bandgap absorbers [39]. Co-evaporation can be realized easily on relatively small areas, however it is challenging to control evaporation rates over large areas.

Reactive annealing of metal precursor films is more suitable for large-area film deposition; for instance, large-area solar modules up to 60×120 cm^2 yielding maximum efficiencies of 13 % on 30×30 cm^2 modules were fabricated via DC-magnetron sputtering [57,58]. Reactive annealing of metal precursor films involves a two-stage process: in a first step, Cu and In metals are co-deposited or stacked and in a second step the precursor film is annealed in a H$_2$Se/Ar atmosphere at temperatures around 500°C for about one hour. Although co-deposited metal precursor films yielded higher device performances, layered precursors attracted greater attention, as their fabrication is believed to be more easily scalable for large area deposition [59]. Variations of this absorber-formation technique include cases where Cu/(In,Ga)/Se or InSe$_x$/Cu thin film structures are used as precursors and are annealed via a rapid thermal process in Se vapor or inert atmosphere, avoiding the use of toxic H$_2$Se [38,59]. On the laboratory scale, cells obtained from selenization processes usually demonstrate efficiencies 3 % smaller than the record values, yet, on the module level, efficiencies of cells with co-

41

evaporated and sequentially prepared absorbers are comparable [38]. Despite the stack structure of the precursor films, the distribution of the elements within the film grown during the selenization process is fortunately almost optimal. Indeed, because of their higher reactivity with Se, Cu and In diffuse preferentially to the surface forming $CuInSe_2$ [59]. Because the formation of the ternary chalcopyrites phase starts at the reaction front with the Se from the surface, and because the formation of $CuGaSe_2$ is slower, Ga is concentrated toward the back surface of the film. As it has been mentioned earlier, this creates a graded-bandgap with a larger bandgap at the back of the film, it not only improves carrier collection but also minimizes back-surface recombination.

Lastly, for both approaches, deposition or annealing in a S-containing atmosphere seems beneficial, as sulfur is incorporated at the front surface of the film, reducing recombination losses and increasing the band gap at the heterojunction [38,59]. Because of the film growth mechanism, where $Cu_{2-y}Se$ acts as a flux agent during co-evaporation or Cu_xSe mediates the growth of crystallites during selenization, a Cu-rich phase segregates preferentially at the surface of the absorber film [38]. The metallic nature of this phase prevents the formation of an efficient heterojunction and should be removed via an aqueous potassium cyanide (KCN) etch. Finally, the role of sodium incorporation in the CIGS absorber, although not fully explained, should also be mentioned. Indeed, a 0.1 % atomic sodium incorporation is necessary for optimum film preparation and high device efficiency [38]. Sodium incorporation is usually achieved by Na diffusion from the Mo-coated soda-lime glass used as a substrate, or by controlled incorporation of Na from precursors such as Na_2Se or Na_2S [39].

42

For CuInS$_2$, reactive sputtering have also been implemented, Cu and In target are sputtered in a H$_2$S/Ar plasma, this approach remains rare as it requires a H$_2$S proof deposition chamber [60,61]. More common approaches include the deposition of Cu and In metallic precursors (evaporation [62], co-evaporation [62,63], sputtering [64], and co-sputtering [65]) followed by sulfurization. Several sulfurization methods have been attempted: annealing in H$_2$S/Ar [63,66], annealing in sulfur vapor generated from elemental sulfur [64,65], and thermal evaporation of sulfur (effusion cell at ~180°C) onto heated precursor films [62]. Currently, pilot and commercial production of CuInS$_2$ based thin film solar modules is under development at Sulfurcell Solartechnik GmbH, using co-sputtered Cu/In metallic precursor films rapidly (<5 min) annealed in elemental sulfur vapor [67,68].

Evaporation, sputtering and co-sputtering of metal precursor followed by annealing under H$_2$S or under sulfur vapor generated from elemental sulfur are processes we can performed to prepare thin films of Pb-Sb-S with our UHV deposition system and our laboratory equipment.

1.6 Pb-Sb-S ternary phases: synthesis, phase diagram and crystal structure

As previously mentioned, because they contain only cost effective, abundant and relatively less toxic materials, Pb-Sb-S ternary phases are potential candidates for thin-film solar cells. The only reports of thin films of Pb-Sb-S ternary phases were brief. Deposition methods that were employed are chemical bath deposition of PbSb$_2$S$_4$ (zinkenite) [69], and thermal evaporation of amorphous and multiphase Pb-Sb-S thin

films [47]. Ternary films of Pb-Sb-S were prepared via vacuum thermal co-evaporation of sulfur, metal or binary compounds. The substrate temperature proved to be important for the growth and structure of the deposited films; indeed, from 30°C to ~150°C films were amorphous, from 150°C to ~250°C films were polycrystalline with a tendency to be oriented, and finally above 250°C films were polycrystalline with random orientations. One should mention that, while definite determinations of crystalline phases are not achieved, the films are believed to be multi-phase. Furthermore, to our knowledge, no H_2S or S vapor sulfurization of lead, antimony or lead-antimony metal precursor films has been reported. Our challenge is then to prepare device quality-like thin films of Pb-Sb-S phases with suitable crystalline and morphological properties. Single-phase, dense, and smooth films with large crystallites (>1 μm) are the target.

Despite a lack of materials science and thin film literature concerning the preparation of Pb-Sb-S phases, mineralogy and solid state chemistry literature maybe found on traditional solid state and hydrothermal syntheses, phase diagram evaluation and crystal structure determination. Thus, lead antimony sulfides have attracted the interest of numerous mineralogists, because of their chemical and mineralogical complexity, as well as their common association with ore-forming sulfides. Among the numerous lead antimony sulfide phases (at least 18 such phases have been identified), most belong to the so-called acicular (needle-like crystal) phases, which may be synthesized in the laboratory using conventional solid state methods. However, four phases known as the plagionite group are distinct and adopt tabular crystal habits; until

44

now, they have been exclusively synthesized in the laboratory under hydrothermal conditions.

a) *Acicular phases*

Acicular phases may be obtained using traditional dry synthesis methods, by mixing and heating elemental sulfur, lead and antimony in sealed silica tubes. Some of these phases belong to the thermodynamic Pb-Sb-S phase diagram, and more specifically to the $PbS-Sb_2S_3$ binary join that is shown in Figure 1.14. Studies of the phase diagram include references [70-73].
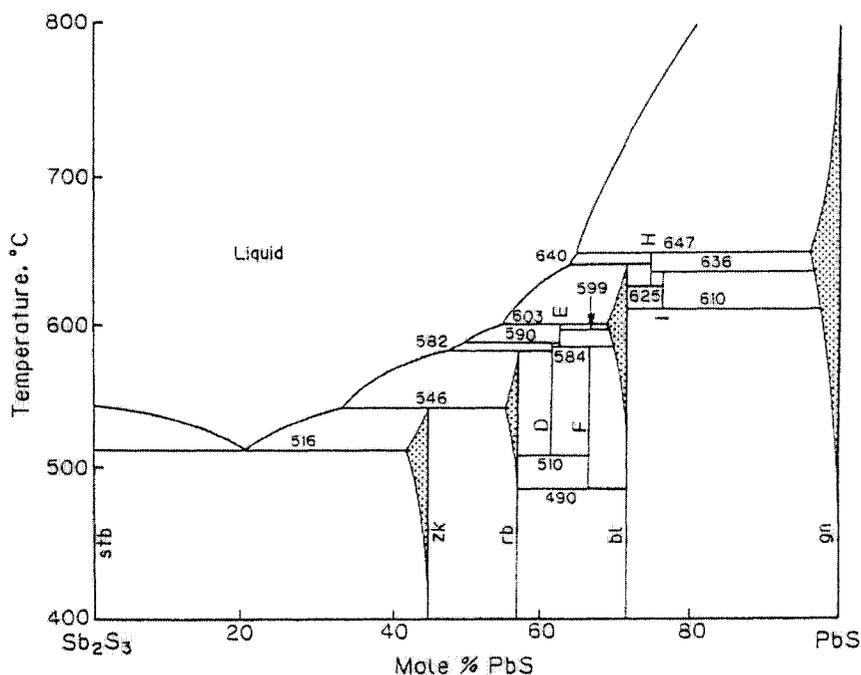
Figure 1.14. Phase relation on the $PbS-Sb_2S_3$ join. stb: stibnite (Sb_2S_3), zk: zinkenite, rb: robinsonite, bl: boulangerite, gn: galena (PbS), D, E, F, H, I: synthetic phases D ($5PbS:3Sb_2S_3$), E ($7PbS:4Sb_2S_3$), F ($2PbS:Sb_2S_3$), H ($3PbS:Sb_2S_3$) and I ($16PbS:5Sb_2S_3$), (adapted from reference [72]).

Structures of these phases may be described according to an homologous series. The homologous series contains different phases that have the same ribbon arrangement

45

but different ribbon sizes. The ribbons (building blocks) are derived from the PbS (100) sheets by substituting Pb^{2+} by Sb^{3+} and a vacancy. The bonding between ribbons occurs between Pb^{2+} and S^{2-}. Details about homologous series may be found in references [74,75]. Due to our processing temperatures (<500°C), the phases that are most likely to be obtained are the lower temperature phases, *i.e.* zinkenite, robinsonite, and boulangerite. These phases belong to three different homologous series, their crystal structures are given in Table 1.5.

Table 1.5. Crystal structure of selected Pb-Sb-S phases

Phase	Formula	System	S.G.	a (Å)	b (Å)	c (Å)	β (°)	Z	Ref.
Boulangerite	$Pb_5Sb_4S_{11}$	Orthorhombic	Pnam	23.49	21.25	4.02	-	4	[76]
Robinsonite	$Pb_4Sb_6S_{13}$	Monoclinic	I2/m	23.70	3.98	24.47	93.9	4	[77]
Zinckenite	$Pb_9Sb_{22}S_{42}$	Hexagonal	P6$_3$	22.13	22.13	4.32	-	1	[78]
Stibnite	Sb_2S_3	Orthorhombic	Pnma	11.30	3.83	11.22	-	4	[79]
Galena	PbS	FC Cubic	Fm$\bar{3}$m	5.93	5.93	5.93	-	4	[80]

Notes: S.G. = Space Group, Z = number of motif per lattice

b) *Tabular phases: the plagionite group*

Another group of phases has been obtained very frequently during thin film syntheses of Pb-Sb-S phases. The plagionite group phases are fülöppite, plagionite, heteromorphite and semseyite. These phases failed to appear in the thermodynamic phase diagram obtained from dry solid state syntheses. The four plagionite phases are distinct from the acicular phases; indeed, they adopt tabular crystal habits [71] and share common crystallographic features [81-84]. Table 1.6 presents a summary of the

46

plagionite crystal structure. They all crystallize in the monoclinic C2/c space group with

4 motifs of $Pb_{3+2n}Sb_8S_{15+2n}$ (with n = 0 to 3) per unit cell [81].

Table 1.6. Crystal structure of plagionite group phases (adapted from reference [84])

Phase	Formula	n	a (Å)	b (Å)	c (Å)	β (°)	c×sin β (Å)	Ref.
Semseyite	$Pb_9Sb_8S_{21}$	3	13.60	11.94	24.44	106.0	23.5	[85]
Heteromorphite	$Pb_7Sb_8S_{19}$	2	13.63	11.94	21.29	90.6	21.3	[86]
Plagionite	$Pb_5Sb_8S_{17}$	1	13.49	11.87	19.98	107.2	19.1	[87]
Fülöppite	$Pb_3Sb_8S_{15}$	0	13.44	11.73	16.93	94.7	16.9	[88]

As shown in Table 1.6, the lattice parameters **a** and **b** do not vary significantly from one member of the series to another. However, the lattice parameter **c** increases with **n** (*i.e.* with the number of Pb and S atoms in the motif); and more significantly c×sinβ increases quite linearly with **n** [81]. Figure 1.15 is the projection of a half of the lattice along the **b** axis of the plagionite phase. Here, it is particularly interesting to notice that four Pb octahedra located along the **c**-axis are linked by lead polyhedra (dash lines in Figure 1.15), this forms a continuous lead polyhedron chain along [10$\bar{1}$] direction. In addition, each successive member of the plagionite group contains eight additional lead and eight additional sulfur atoms per unit cell, as Z = 4. This change in composition, as well as the invariance of all the lattice constants except c×sinβ, which increases quite linearly with **n**, may be explained by the addition of two Pb octahedra in the chain parallel to the **c**-axis, for a total of eight Pb and S atoms considering the entire unit cell [82,84].

47
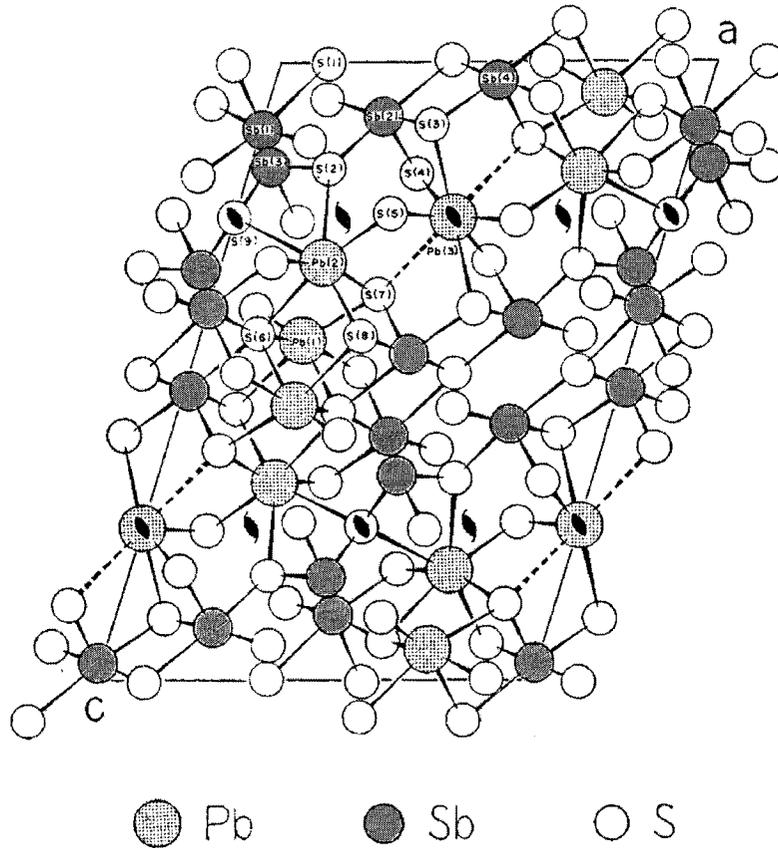
Figure 1.15. Projection along b of the coordination polyhedra contained between y = 0 and y = ½ for plagionite, the second member of the series (adapted from reference [82]).

Lastly, the plagionite phases are relatively rare in nature, and as mentioned previously, have, until now, been exclusively synthesized under hydrothermal conditions at temperatures near 400°C. Indeed, Robinson produced semseyite, plagionite, and fülöppite from aqueous solutions at temperatures between 340°C and 435°C [71,89]; whereas Garvin investigated the phase diagram to temperatures as low as 300°C using dry synthesis, and KCl-LiCl and NH₄Cl-LiCl fluxes and obtained none of the plagionite group phases [71]. The plagionite phases, both natural and synthetic in origin, decompose into phases stable in the "dry" system upon heating at temperatures above 425°C [71,89]. Garvin hypothesized that formation of the plagionite group compounds

48

depended upon an additional essential volatile component, probably hydrogen, that would be liberated upon heating [71]. Thus, for over 30 years, the plagionite compounds have been regarded as not existing on the pure Pb-Sb-S phase diagram.

1.7   Conclusions

Production of electricity via photovoltaic solar cells will play an increasingly important role in the energy sector, encouraged by the rising awareness of global warming and the rising cost of oil, calling for new alternative renewable sources of energy. Solar energy has now proved its feasibility and economic viability thanks to the continual improvement of photovoltaic devices; in particular, devices based on crystalline and amorphous silicon. Although the efficiencies of crystalline silicon cells are very close to the theoretical maximum, their cost remains too high to really compete on the open energy market. Cells based on direct band gap semiconductors that absorb light more strongly seem a promising alternative, as stronger light absorption not only reduces the amount of material required, but also reduces the requirements for film crystallinity. For historical reasons, the current thin film cells are based on CdTe and Cu-chalcopyrite compounds. Although the efficiencies of the cells are excellent (15 to 20 % for a small-size laboratory cell), issues related to price, availability and, perhaps to a lesser extent, toxicity of some of the materials will ultimately limit their electricity generation capacity to few percents of the current global electricity production. Our approach is to build new thin film device architectures with ~5 % efficiency that contain only cost effective, abundant, and relatively less toxic materials. In this context, lead antimony sulfides are potential solar absorbers, since, for instance, they have band gap

49

energies close to the optimal 1.4 eV. Goals of this thesis include the preparation of crystalline materials to be used as solar absorbers in thin film solar cells. Thus, preparation of thin films of Pb-Sb-S phases have been undertaken via techniques that are compatible with the current solar cell manufacturing technologies: namely vacuum deposition (sputtering) and annealing in H_2S and elemental sulfur vapor environments. To our knowledge, this thesis and related publications are the first reports of extensive development of thin film preparations of Pb-Sb-S phases as potential light absorber material in thin film solar cells.

1.8 References

[1]   U.N. Development Program, World Energy Assessment: Overview 2004 Update, United Nation, New York, NY, 2004.

[2]   B.A. Andersson, Progress in Photovoltaics 8 (2000) 61.

[3]   International Energy Agency, Key World Energy Statistics 2005, International Energy Agency, Paris, 2005.

[4]   S.S. Hegedus, A. Luque, in: S.S. Hegedus, A. Luque (Eds.), Handbook of Photovoltaic Science and Engineering, John Wiley and Sons Ltd., Chichester, UK, 2003.

[5]   T. Markvart, Solar Electricity - 2nd Edition, John wiley and Sons Ltd., Chichester, UK, 2000.

[6]   J. Luther, in: S.S. Hegedus, A. Luque (Eds.), Handbook of Photovoltaic Science and Engineering, John Wiley and Sons Ltd., Chichester, UK, 2003.

[7] Photovoltaic Technology Research Advisory Council, A Vision for Photovoltaic Technology, European Commission, Luxembourg, 2005.

[8] M. Kemell, M. Ritala, M. Leskelä, Crit. Rev. Solid State Mater. Sci. 30 (2005) 1.

[9] J.M. Huacuz, L. Gunaratne, in: S.S. Hegedus, A. Luque (Eds.), Handbook of Photovoltaic Science and Engineering, John Wiley and Sons Ltd., Chichester, UK, 2003.

[10] H.J. Möller, Semiconductors for Solar Cells, Artech House Inc., Norwood, MA, 1993.

[11] C. Fritts, Proc. Am. Assoc. Adv. Sci. 33 (1883) 97.

[12] D.M. Chapin, C.S. Fuller, G.L. Pearson, J. Appl. Phys. 25 (1954) 676.

[13] D.C. Reynolds, G. Leies, L.L. Antes, R.E. Marburger, Phys. Rev. 96 (1954) 533.

[14] D.A. Jenny, J.J. Loferski, P. Rappaport, Phys. Rev. 101 (1956) 1208.

[15] D.A. Cusano, Solid-State Electron. 6 (1963) 217.

[16] M.B. Prince, J. Appl. Phys. 26 (1955) 534.

[17] J.J. Loferski, J. Appl. Phys. 27 (1956) 777.

[18] J.J. Wysocki, P. Rappaport, J. Appl. Phys. 31 (1960) 571.

[19] W. Shockley, H. Queisser, J. Appl. Phys. 32 (1961) 510–519.

[20] M.A. Green, in: the Conference Record of the 18th IEEE Photovoltaic Specialists Conference, Las Vegas, U.S.A., October 21-25, 1985, p.39.

[21] D.J. Friedman, S.R. Kurtz, K.A. Bertness, A.E. Kibbler, C. Kramer, J.M. Olson, D.L. King, B.R. Hansen, J.K. Snyder, Progress in Photovoltaics 3 (1995) 47.

[22] M.A. Contreras, B. Egaas, K. Ramanathan, J. Hiltner, A. Swartzlander, F. Hasoon, R. Noufi, Progress in Photovoltaics 7 (1999) 311.

51

[23] M.A. Green, Progress in Photovoltaics 9 (2001) 123.

[24] C. Kittel, Introduction to Solid State Physics, John Willey and Sons Inc., New York, NY, 1996.

[25] J. Jaffe, A. Zunger, Phys. Rev. B 28 (1983) 5822.

[26] R.H. Bube, Electrons in Solids - an Introductory Survey, Academic Press Inc., San Diego, CA, 1988.

[27] J.L. Gray, in: S.S. Hegedus, A. Luque (Eds.), Handbook of Photovoltaic Science and Engineering, John Wiley and Sons Ltd., Chichester, UK, 2003.

[28] J.I. Pankove, Optical Processes in Semiconductors, Prentice-Hall Inc., Englewood Cliffs, NJ, 1971.

[29] T. Markvart, L. Castañer, Practical Handbook of Photovoltaics: Fundamentals and Applications, Elsevier Science Ltd., Kidlington, UK, 2003.

[30] S.S. Hegedus, A. Luque (Eds), Handbook of Photovoltaic Science and Engineering, John Wiley and Sons Ltd., Chichester, UK, 2003.

[31] M.A. Green, K. Emery, D.L. King, Y. Hishikawa, W. Warta, Progress in Photovoltaics 14 (2006) 455–461.

[32] A. Goetzberger, C. Hebling, H.-W. Schock, Mater. Sci. Eng., R 40 (2003) 1 .

[33] I. Tobías, C. del Cañizo, J. Alonso, in: S.S. Hegedus, A. Luque (Eds.), Handbook of Photovoltaic Science and Engineering, John Wiley and Sons Ltd., Chichester, UK, 2003.

[34] X. Deng, E.A. Schiff, in: S.S. Hegedus, A. Luque (Eds.), Handbook of Photovoltaic Science and Engineering, John Wiley and Sons Ltd., Chichester, UK, 2003.

[35] B.E. McCandless, J.R. Sites, in: S.S. Hegedus, A. Luque (Eds.), Handbook of Photovoltaic Science and Engineering, John Wiley and Sons Ltd., Chichester, UK, 2003.

[36] W.N. Shafarman, L. Stolt, in: S.S. Hegedus, A. Luque (Eds.), Handbook of Photovoltaic Science and Engineering, John Wiley and Sons Ltd., Chichester, UK, 2003.

[37] S.K. Deb, in Y. Hamakawa (Ed.) Thin-Film Solar Cell: Next Generation Photovoltaics and its Applications, Springer - Verlag, Berlin, 2004.

[38] H.-W. Schock, in Y. Hamakawa (Ed.) Thin-Film Solar Cell: Next Generation Photovoltaics and its Applications, Springer - Verlag, Berlin, 2004.

[39] A. Romeo, A. Terheggen, D. Abou-Ras, D.L. Batzner, F.J. Haug, M. Kalin, D. Rudmann, A.N. Tiwari, Progress in Photovoltaics 12 (2004) 93.

[40] W.C. Butterman, R.D.Jr. Brown, U.S. Department of the Interior, U.S. Geological Survey, Denver, CO, 2004, report no. 2003-18.

[41] J.D. Jorgenson, M.W. George, U.S. Department of the Interior, U.S. Geological Survey, Denver, CO, 2005, report no. 2004-1300.

[42] U.S. Department of Interior, U.S. Geological Survey, Reston, VA, 2006, http://minerals.usgs.gov/minerals/pubs/commodity/.

[43] W.C. Butterman, J. Plachy, U.S. Department of the Interior, U.S. Geological Survey, Denver, CO, 2004, report no. 2002-238.

[44] V.M. Fthenakis, Renewable & Sustainable Energy Reviews 8 (2004) 303.

[45] V.M. Fthenakis, W. Wang, Progress in Photovoltaics 14 (2006) 363.

53

[46] H. Dittrich, D.J. Vaughan, R.A.D. Pattrick, S. Graeser, M. Lux-Steiner, R. Kunst, D. Lincot, in: W. Freiesleben (Ed.), Proceedings of the 13th European Photovoltaic Solar Energy Conference, Nice, France, October 23-27, 1995, p.1299.

[47] H. Dittrich, K. Herz, in: R.D. Tomlinson, A.E. Hill, R.D. Pilkington (Eds.), Ternary and Multinary Compounds: Proceedings of the 11th International Conference on Ternary and Multinary Compounds, Salford, UK, September 8-12, 1997 Inst. Phys. Conf. Ser. 152 (1997) 293.

[48] T.F. Lomelino, G. Mozurkewich, Am. Mineral. 74 (1989) 1285.

[49] S.I. Boldish, W.B. White, Am. Mineral. 83 (1998) 865.

[50] W.N. Shafarman, R. Klenk, B.E. McCandless, J. Appl. Phys. 79 (1996) 7324.

[51] P.D. Paulson, M.W. Haimbodi, S. Marsillac, R.W. Birkmire, W.N. Shafarman, J. Appl. Phys. 91 (2002) 10153.

[52] M. Engelmann, B.E. McCandless, R.W. Birkmire, Thin Solid Films 387 (2001) 14.

[53] K.L. Chopra, P.D. Paulson, V. Dutta, Progress in Photovoltaics 12 (2004) 69.

[54] D. Lincot, Thin Solid Films 487 (2005) 40.

[55] H.M. Pathan, C.D. Lokhande, Appl. Surf. Sci. 245 (2005) 328.

[56] M.A. Green, K. Emery, D.L. King, S. Igari, W. Warta, Progress in Photovoltaics 13 (2005) 387.

[57] F.H. Karg, Sol. Energy Mater. Sol. Cells 66 (2001) 645.

[58] K. Kushiya, M. Ohshita, I. Hara, Y. Tanaka, B. Sang, Y. Nagoya, M. Tachiyuki, O. Yamase, Sol. Energy Mater. Sol. Cells 75 (2003) 171.

[59] R.W. Birkmire, E. Eser, Annual Review of Materials Science 27 (1997) 625.

[60] T. Watanabe, M. Matsui, Jpn. J. Apll. Phys. 35 (1996) 1681.

[61] K. Ellmer, J. Hinze, J. Klaer, Thin Solid Films 413 (2002) 92.

[62] R. Klenk, U. Blieske, V. Dieterle, K. Ellmer, S. Fiechter, I. Hengel, A. JagerWaldau, T. Kampschulte, C. Kaufmann, J. Klaer, M.C. LuxSteiner, D. Braunger, D. Hariskos, M. Ruckh, H.W. Schock, Sol. Energy Mater. Sol. Cells 49 (1997) 349.

[63] M. Gossla, H. Metzner, H.-E. Mahnke, Thin Solid Films 387 (2001) 77.

[64] K. Siemer, J. Klaer, J. Bruns, R. Klenk, D. Bräunig, Sol. Energy Mater. Sol. Cells 67 (2001) 159.

[65] J. Alvarez-Garcia, B. Barcones, A. Romano-Rodriguez, L. Calvo-Barrio, A. Perez-Rodriguez, J.R. Morante, R. Scheer, R. Klenk, J. Electrochem. Soc. 150 (2003) G400.

[66] T. Nakabayashi, T. Miyazawa, Y. Hashimoto, K. Ito, Sol. Energy Mater. Sol. Cells 49 (1997) 375.

[67] R. Klenk, J. Klaer, R. Scheer, M.C. Lux-Steiner, I. Luck, N. Meyer, U. Ruhle, Thin Solid Films 480 (2005) 509.

[68] R. Scheer, R. Klenk, J. Klaer, I. Luck, Solar Energy 77 (2004) 777.

[69] A. Nunez, P.K. Nair, M.T.S. Nair, Mod. Phys. Lett. B 15 (2001) 605.

[70] J.R. Craig, L.L.Y. Chang, W.R. Lees, Can. Mineral. 12 (1973) 199.

[71] P.L. Garvin, Neues Jahrb. Mine. Abh. 118 (1973) 235.

[72] A. Kitakaze, A. Sugaki, H. Shima, Mineralogical Journal 17 (1995) 282.

[73] B. Salanci, Neues Jahrb. Mine. Abh. 135 (1979) 315.

[74] A. Skowron, I.D. Brown, Acta Crystallogr., Sect. B: Struct. Sci. B50 (1994) 524.

[75] E. Makovicky, Neues Jahrb. Mine. Abh. 160 (1989) 269.

[76] A. Skowron, I.D. Brown, Acta Crystallogr., Sect. C: Cryst. Struct. Commun. C46 (1990) 531.

[77] A. Skowron, I.D. Brown, Acta Crystallogr., Sect. C: Cryst. Struct. Commun. C46 (1990) 527.

[78] A. Kitakaze, A. Sugaki, Scientific Report Tohoku University, Tohoku University, Sendai, Japan, 1988.

[79] D.O. McKee, J.T. McMullan, Z. Kristallogr. 142 (1975) 447.

[80] Y. Noda, K. Masumoto, S. Ohba, Y. Saito, K. Toriumi, Y. Iwata, I. Shibuy, Acta Crystallogr., Sect. C: Cryst. Struct. Commun. C43 (1987) 1443.

[81] J.L. Jambor, Mineral. Mag. 37 (1969) 443.

[82] S.-A. Cho, B.J. Wuensch, Nature 225 (1970) 444.

[83] B.J. Wuensch, Acta Crystallogr., Sect. B: Struct. Sci. B30 (1974) 2935.

[84] B.J. Wuensch, in: J.M. Cowley (Ed.) International Conference on Modulated Structures, Kailua Kona, Hawaii, U.S.A., 1979, AIP Conference Proceedings 53 (1979) 337.

[85] J.J. Kohatsu, B.J. Wuensch, Am. Mineral. 59 (1974) 1127.

[86] A. Edenharter, Z. Kristallogr. 151 (1980) 193.

[87] S.-A. Cho, B.J. Wuensch, Z. Kristallogr. 139 (1974) 351.

[88] E.W. Nuffield, Acta Crystallogr., Sect. B: Struct. Sci. B31 (1975) 151.

[89] S.C. Robinson, Econ. Geol. 43 (1948) 293.

Chapter 2: Techniques: Thin -film Deposition and Characterization

2.1 Thin-film deposition techniques

Several deposition techniques have been developed for the preparation of thin films of various materials, among them physical vapor deposition (PVD) techniques are very common. PVD techniques include a broad range of methods designed to deposit a thin solid film on a chosen substrate. These techniques are based on the ejection of atoms from a target material under vacuum or in low-pressure plasma, and their subsequent adhesion on a substrate, forming a film. Evaporation or bombardment of energetic particles or photons may be used to eject the atoms from the target/source material. In evaporation processes, heating of the material source yields ejection of the atoms by vaporization. With techniques using bombardment with particles or photons, the target atoms are ejected by momentum transfer.

2.1.1 Evaporation

a)   *Main characteristics of evaporation deposition*

Studies of Hertz, Knudsen and Langmuir on evaporation phenomena showed that the evaporation rates are not limited by insufficient heat supply to the surface of the molten evaporant, since they are proportional to the difference between the equilibrium pressure of the evaporant at the given temperature and the hydrostatic pressure acting on the surface (*i.e.* deposition system pressure) [1]. Thus, the lower the pressure of the deposition system, the greater the evaporation rate is. Equilibrium pressures of the evaporant at given temperatures are estimated from thermodynamic data: indeed vapor-

57

pressures of metals and compounds can be estimated and conveniently represented as a function of temperature, as shown in Figure 2.1. Two modes of evaporation can be distinguished, depending on whether the vapor effectively emanates from a liquid or a solid source. As a rule of thumb, elements with vapor pressures smaller than 10^{-3} Torr at the melting point will require a melt [1]. This is the case for most metals, such as zirconium, hafnium and lead, meaning that effective film deposition is achieved only when the source is heated into the liquid phase. Other elements, such as antimony, have sufficiently high vapor pressures below the melting point and, therefore, sublime.
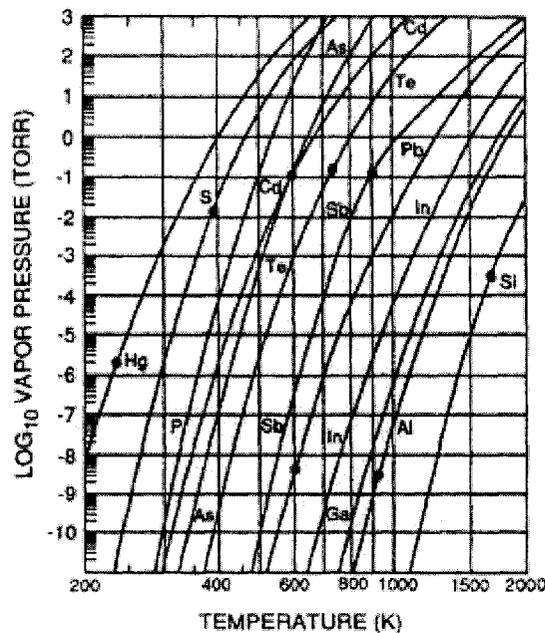
Figure 2.1. Vapor pressures of elements employed in semiconductor materials. Dots correspond to melting points (from reference [1]).

In absence of collisions in the gas phase, which is the case for vacuum evaporation, the materials travel in a straight line between the source and the substrate. Thus, the material from a point source deposits on a surface with a distance and substrate orientation dependence given by a the cosine distribution [2]; Figure 2.2 shows

58

the distribution of atoms vaporized from a point source and the thickness distribution of the film formed on a planar surface above the point source. Concerning the distribution of the evaporated film, our deposition system was designed to yield uniform deposition across the 5 cm × 5 cm substrate. Indeed, the source crucible is located at ~36 cm from the substrate that has a diagonal of ~3.5 cm, therefore, the maximum angle from the normal is 2.8° which, according to Figure 2.2, means that the entire substrate width is located in the central area where the thickness is uniform.
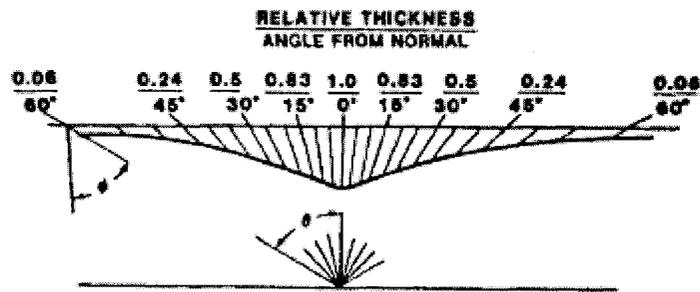
Figure 2.2. Distribution of atoms vaporized from a point source and the thickness distribution of the film formed on a planar surface above the source (from reference [2]).

Deposition rates for vacuum deposition processes can vary greatly, ranging from less than one monolayer per second, i.e. < 3 Å/s, to more than 3 μm/s. Rates depend mostly on the thermal power input to the source, the system geometry, and the deposited material. Since the vaporization rate can change during the deposition process, the power input to the source is generally controlled by monitoring the deposition rate. Our system does not possess that capability. A film thickness monitor (FTM) however, once calibrated, allows us to pre-set the desired thickness to be deposited. The film thickness monitor uses a quartz crystal oscillator to give in-situ, real-time deposition rates and deposited thicknesses. The quartz single crystal is a piezoelectric material, in which

59

volume changes by applying a voltage. If the voltage is applied at a high frequency (typically 5 MHz range) the movement will resonate with a frequency that depends on the crystalline orientation of the quartz crystal slab and its thickness. Thus, quartz crystal deposition monitors measure the change in resonant frequency that is proportional to the deposited mass (film). The frequency change is related to the deposited mass after a careful calibration. The frequency change of the oscillation allows the detection of a change of mass of about 0.1 $\mu g/cm^2$, which is equivalent to less than a monolayer of deposited film material [2]. The quartz crystal is usually cut with a crystalline orientation that has a low temperature dependence of its resonant frequency near room temperature. The crystal diameter is 1.9 cm for a probe area of 1.3 cm. The crystal is coated with gold on the front side (exposed to the evaporation source) and patterned on the back side to provide electrical contact with the electrodes for applying the voltage. Moreover, the crystal is also water cooled to avoid large temperature changes. Lastly, the film thickness monitor should be located, as much as possible, in a position similar to the one of the substrate. It is therefore necessary to relate the probe readings to the actual film thickness deposited. A tooling factor can then be determined and implemented so that the probe readings are reliable from run-to-run, as long as the system geometry and vaporization flux distribution stays constant. Thus, in our deposition chamber, the desired total thickness can be implemented, and once it is reached, a shutter is activated to block the evaporated material flux. In addition, the total residual film stress may change as the film thickness increases and, consequently the elastic properties of the crystal and thus the frequency calibration. The major concerns with the use of quartz crystal monitors are, as mentioned earlier, the system geometry,

the film stress, the limited lifetime of the crystal (only 10 μm) and perhaps more significantly the necessary assumption of a density for the as-deposited film to calculate a thickness from the measured frequency (*i.e.* mass). Other film thickness monitors are commercially available but are not commonly used: ionization rate monitors, optical atomic adsorption spectrometer, or optical monitor measuring the interference fringes arising from the optical film thickness.

Lastly, due to large power dissipation at the source, significant radiative heat transfer occurs to the substrate and the film; for instance an evaporant at 1000 °C generates a blackbody radiation at $\lambda = 0.6$ to 6 μm, that the substrate and film will absorb, causing heating of the substrate. Other sources of heat for the substrate come from the condensation of the vaporized atoms on the surface: heat of vaporization or sublimation (given up, a few eV per atom which includes the kinetic energy of the particle), energy to cool to ambient (depends on heat capacity and temperature change), and also the energy associated with chemical reaction or alloying. The condensation energy can produce appreciable substrate heating, especially at high deposition rates [2] and therefore may affect the deposited film morphology, as much as involving complete re-evaporation of the film.

b) *Several evaporation techniques*

Thermal vaporization requires that the surface and, generally, a large volume of material must be heated to temperatures where there is an appreciable vapor pressure. Heating of the material is achieved by resistive heating of boats or crucibles, by

61

inductive (RF) heating or by focussed electron or laser beams. Thus, the most common way of heating materials that vaporize below 1500 °C is by contact with a hot surface that is heated by passing a current through it (resistively heated). Evaporation sources must contain the molten liquid without leaks and extensive reaction. This is achieved using containers such as crucibles, boat or baskets (used for chips of evaporant that do not melt but sublimate) or heated surfaces in the form of wires (the evaporant is in form of thin wires wounded around the helix, upon melting the evaporant wets the filament and is held by surface tension). Typically, the resistive heater materials are made of W, Ta, Mo, C, and BN/TiB_2 composite ceramics. Resistive heating of electrically conductive sources is usually achieved using low voltage (< 10 volts) and very high current (> several hundreds of amperes) AC transformer supplies [2]. Except for the crucibles, only a few grams of evaporant can be held. Crucibles are usually heated by RF induction heating: RF energy is directly inductively coupled into an electrical conductor such as metals or carbon. Disadvantages of resistively heated evaporation sources include possible contamination by crucibles, heaters or support materials, and limitations related to the low input power levels.

c) *Electron-beam evaporation*

Electron-beam heating eliminates these disadvantages and has consequently become the most widely used vacuum evaporation technique for preparing highly pure films [1]. Our system does not contain any resistively heated sources, but hosts a 4-pocket electron beam evaporation source. Focused high-energy electron-beams allow the evaporation of refractory materials for which temperatures greater than 1500 °C are

62

required, and allow the evaporation of large quantities of materials. Figure 2.3 shows the schematic of a focussed e-beam evaporation system similar to the one contained in our system.
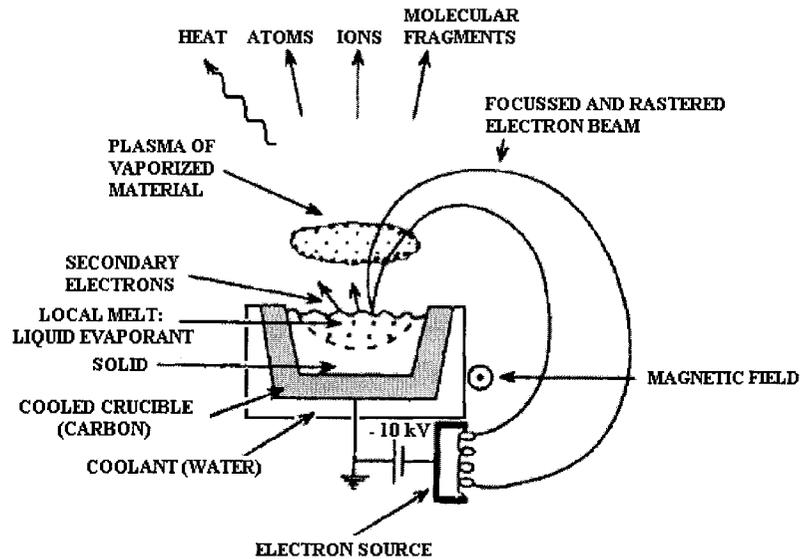
<u>Figure 2.3.</u> Focussed electron beam (e-beam) evaporation (adapted from reference [2]).

As shown in Figure 2.3, the evaporant charge is placed in a crucible located in the depression of a water-cooled copper hearth. The absence of contamination is ensured as only a small amount of the charge melts or sublimes so that the effective crucible is the unmelted material between the local melt and the crucible (typically made of graphite to ensure thermal and electrical conductivity). The electron gun generates a high-energy electron beam by thermionic emission from a heated filament, which are shielded from direct line of sight of the evaporant charge and substrate to eliminate contamination from the heated electron source. The filament cathode is biased negatively anywhere from 4 to 20 kV, and this serves to accelerate the electrons. In addition, a transverse magnetic field is applied, it deflects the electron beam in a 270° circular arc and focuses it at the center of the evaporation material, that is grounded

63

through the crucible and the body of the crucible liner. The electron beam can be rastered over the surface to produce heating over a large area. The high-energy electron bombardment produces secondary electrons, which are magnetically deflected to the ground. Moreover, the electron beam ionizes a portion of the vaporized material creating a plasma of the vaporized material. Thus, the source material is mostly evaporated as atoms, ions and to a lesser extent as molecular fragments [2]. Lastly, due to large power dissipation at the source, significant radiative heat transfer to the substrate and the film occurs.

d)   *Deposition of alloys and compounds*

Deposition of alloys or compounds via evaporation is not an easy task. As evaporation is an atom-by-atom deposition process, atomically dispersed mixtures can be formed. Thus, if the vapor pressures of the constituents are nearly the same, alloys may be deposited directly by the vaporization of the alloy. However, if the vapor pressures differ appreciably (*e.g.* lead and antimony), then the composition of the film will change as the deposition proceeds and the composition of the melt changes. In this latter case, alloy films may be formed by depositing alternating layers of the different materials from different sources; the stacked layers are then interdiffused, forming the alloy film. Other techniques include rod-fed, electron-beam evaporation system that ensure identical compositions for the vapor and the incoming feedstock by precise control of the temperature and the volume of the molten pool [2]. Another very common technique is the combination of multiple sources with individual deposition rate controllers. The deposition of compounds from compound sources is very difficult as

64

very few inorganic compounds (examples include SiO, MgF_2 or CaF_2 where fluorine atoms are tightly bonded) evaporate without molecular change. Indeed, the free energy of evaporation of the compound may very well be on the order of the heat of dissociation: causing what is known as evaporation with dissociation or even decomposition. Evaporation with dissociation – $e.g.$ $MX_{(s)} \rightarrow M_{(g)} + \frac{1}{2} X_{2(g)}$ – occurs when components of the compounds dissociate into gaseous species, this is usually the case for chacogenides, such as CdS, CdSe, CdTe, or for oxides such as SiO_2, ZrO_2. Since the gaseous species may have different sticking coefficients and recombination rates at the substrate, the stoichiometry of the film may be different than that of the evaporant. For example, the vaporization of SiO_2 results in an oxygen-deficient (SiO_{2-x}) film that is yellowish in color; therefore, reactive deposition in an oxygen environment or post-deposition heat treatments in oxygen are required for stoichiometric SiO_2 thin film growth [2]. Evaporation with decomposition – $e.g.$ $MX_{(s)} \rightarrow M_{(s\ or\ l)} + \frac{1}{2} X_{2(g)}$ – occurs when a compound melts incongruently, meaning that the compound dissociates into liquid or solid species and gaseous species. Both the stoichiometry of the source material and the film are therefore affected. Unfortunately, evaporation with decomposition is quite common and therefore prevents deposition of compound films from compound sources of Ag_2S or GaAs, for instance. The deposition of compounds should be formed by co-depositing materials and then having them react with each other or by depositing a "metal" precursor film and then performing a reactive annealing step.

e)   *Conclusion*

As a conclusion, it is useful to give some of the advantages and disadvantages of evaporation processes. The advantages include:

- large-area sources can be used for some materials,

- high deposition rates can be obtained and monitored easily,

- vaporization source material can be in many forms such as chunks, powder, wire, chips, etc… and of high purity for relatively low cost,

- high purity films are easily deposited from high purity source material since the deposition environment can be made as non-contaminating as is desired,

- it is a relatively inexpensive PVD technique.

However, the disadvantages include:

- point sources provide poor deposit uniformity over large surface areas,

- poor ability to deposit many alloys and compounds,

- high radiant heat loads during processing,

- poor utilization of vaporized material,

- few processing variables available for film property control,

- process variability requires in-situ monitoring of the deposition (rate, thickness).

2.1.2 Sputtering

a)   *Introduction and general considerations*

Sputtering is a process where-by material is dislodged and ejected from the surface of a solid due to the momentum exchange associated with surface bombardment

66

by energetic particles. It is a very robust form of PVD offering the possibility of depositing nearly any target material, such as metals, insulators and refractory materials (high melting point), under a wide range of conditions onto nearly any substrate. In addition, the deposited films characteristics can also be tuned by adjusting different sputtering characteristics such as the energy of the bombarding particles, pressure of the process gas and the geometry of the system.
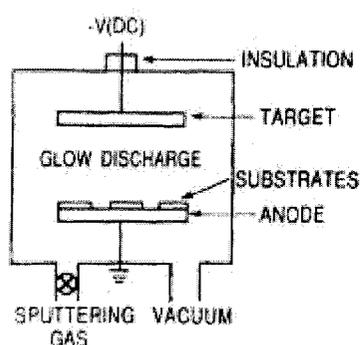
Figure 2.4. Schematic of a simplified DC sputtering system (adapted from reference [1]).

A simplified schematic of a typical sputtering chamber is shown in Figure 2.4. The target is kept at a high negative potential by a power supply, forming the cathode of the system, while the substrate and the rest of the chamber are kept at ground and are therefore the positive electrode or anode for the system. The substrate can be biased either positively or negatively, creating an ion gas bombardment and/or its incorporation into the growing film. In addition, the substrate may be heated, cooled and/or rotated as desired. The bombarding ions are generated from a plasma, which is usually formed from an inert gas – typically Ar. Alternatively, more reactive gases such as N_2, O_2 and H_2S may be used if these elements are desired in the film, this is known as reactive sputtering. The electric field established when the target is energized induces acceleration of the positive ions (*e.g.* Ar^+) towards the target, these very energetic ions

67

strike the target and eject atoms from it. During that process, secondary electrons are also ejected from the target, which can then strike Ar atoms and create more ions, sustaining the plasma.
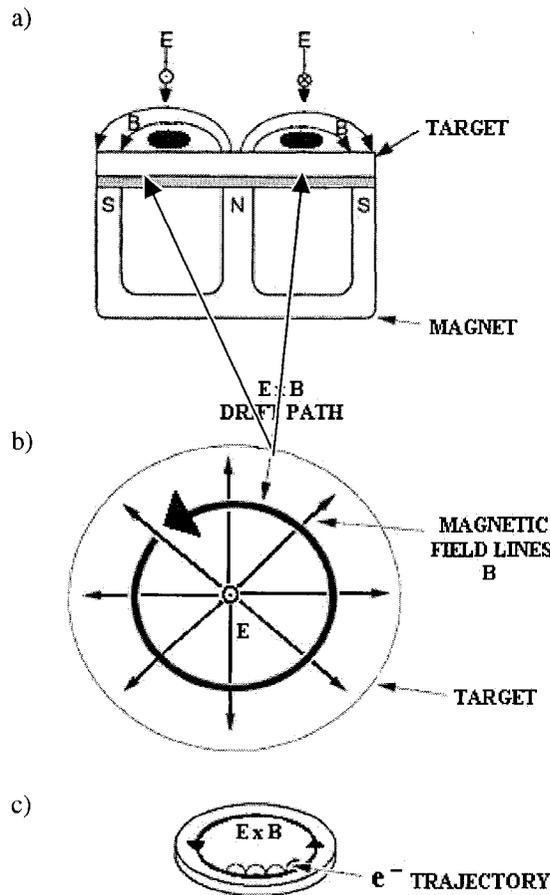
Figure 2.5. The magnetic field configuration for a circular planar magnetron cathode, a) exploded cross-section, b) top view of the target, and c) the electron drift in the E×B direction, actually executing a cycloidal path (adapted from reference [1,3,4]).

Most sputtering systems incorporate magnets in the sputtering source, the sputtering is then referred to as magnetron sputtering. The main purpose of the magnets is to increase the sputtering rates by enhancing the plasma near the target. Indeed, by the suitable application of a magnetic field, the electrons can be constrained to a closed path near the target surface. Our system possesses, exclusively, three annular magnetron guns

68

with a geometry similar to the one presented in Figure 2.5. In that arrangement, the secondary electrons are constrained to what is named a racetrack where the electrons hop around at high speed, increasing the likelihood that they will collide with gas atoms and create more ions in that region located very close to the target surface. Thus, the ionization efficiency is increased, offering the possibility for lower pressure or voltage conditions while allowing higher deposition rates. In addition, because of secondary electron confinement, there is no electron bombardment of the film, yielding lower substrate temperature and avoiding any damage to the growing film. Despite, enhanced erosion of the target beneath the racetrack and a subsequent low usage of the target, magnetron sputtering is commercially the most widely used sputtering method, presently.

One of the most critical parameters in the sputtering process is the sputtering yield. This is the number of target atoms ejected per bombarding ion. It determines the sputtering rate of the target and how fast the deposited film grows. This is an important consideration for the deposition of films with specific compositions or range of compositions from multiple targets. Several parameters influence the sputtering yield: indeed, the sputtering yield depends on the mass and the energy of the incident plasma ions (*e.g.* Ar^+), the incident angle, and the mass and the surface binding energy of the target atoms. In addition, the sputtering yield depends on a parameter measuring the efficiency of the momentum transfer; this parameter increases monotonically from 0.17 to 1.4 as the ratio of the target atom mass to the incident ion mass increases from 0.1 to 10 [1]. Moreover, there is a threshold energy below which the incident ion cannot eject

69

atoms from the target, regardless of flux. This threshold energy is related to the target surface binding energy and typically ranges from 15 to 30 eV for most elements under Ar^+ bombardment. Above this threshold energy, the sputtering yield increases with the energy of the incoming ions and reaches a maximum at high energies (< 10 keV), when the incident ions penetrate more deeply into the target and lose energy by stripping away electrons instead of knocking atoms from their lattice sites. In the film deposition regime, a sputter yield of approximately 1 is used, this usually corresponds to incident ion energies of approximately 1 keV. Sputtering yields (number of ejected atoms per incident Ar^+ ion) for selected elements under bombardment of Ar^+ is presented in Table 2.1.

Table 2.1. Sputter yields of selected elements for various bombarding Ar^+ energies

Element	100 eV	300 eV	500 eV	600 eV	1 keV	Ref.
Zr	0.12	0.41	-	0.75	-	[4]
Hf	0.16	0.48	-	0.83	-	[4]
Sn	-	0.6	0.9	-	1.4	[3]
Pb	-	2.5	3.2	-	4	[3]
Sb	-	-	-	-	1.4	[5]

Depending on the energy regime, the momentum transfer involved in the sputtering process can be classified into three categories [6], as shown in Figure 2.6:

- at low energies: single knock-on regime,

- at intermediate energies: linear cascade regime and,

- at high energies: spike regime.

70

a)   b)   c)
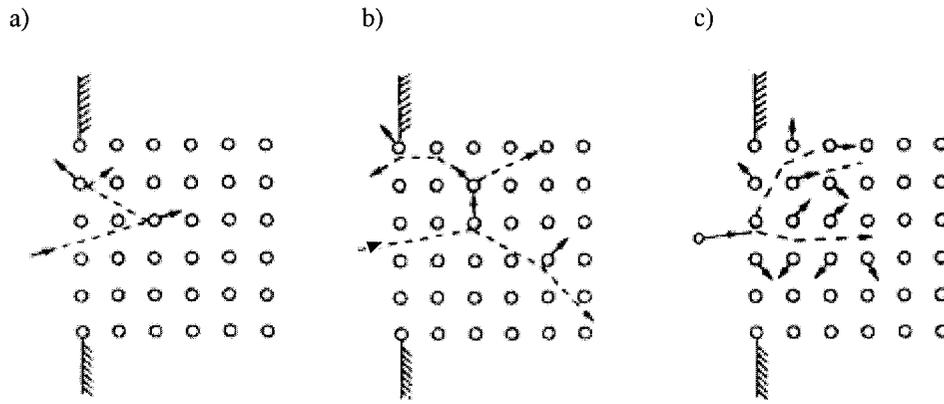
Figure 2.6. Three energy regimes of sputtering: a) Single knock-on (low energy), b) linear cascade, and c) spike (high energy), (from reference [6]).

At low energies, the momentum transfer process occurs in the single knock-on regime, meaning that the incident ion will generally interact with one stationary target atom. At high energies, the momentum transfer process occurs in the spike regime, also called the non-linear regime. In this mode most of the atoms in the target surface region are in motion; atoms can be seen as a vapor. As atoms are also thermally emitted, the sputtering yield can increase very rapidly with a small increase in energy. More interestingly, the common mode for sputtering occurs in the linear cascade regime, where the sputtering yield is proportional to the energy density incident at the surface of the target. In this mode, the incident particle may interact with several target atoms although most collisions still involve one moving and one stationary atom. The transfer of momentum occurs from the incident ion to the top 10 to 50 Å of the target, named the cascade region. This energy transfer is inefficient: only 1 % of incident energy reappears as the energy of the sputtered atoms, therefore the target gets hot and water cooling of the target is necessary.

71

Lastly, for sputtering, as well as for evaporation, heat transfer to the substrate and the film occurs. The principal contributions are heat of condensation, kinetic energy of incident atoms and "plasma heating", arising from the bombardment with neutrals and electrons. Despite usually larger kinetic energies for the incident atoms, sputtering usually causes less substrate/film heating than evaporation. The radiant heating coming from the evaporation source is significantly larger than the plasma heating in normal deposition conditions (low pressures, moderate rates).

b)   *DC Sputtering*

Direct Current (DC) sputtering may be used for depositing materials from low resistivity targets (typically $\rho < 10^6$ Ω.cm). Thus, DC sputtering can be used for metals and even some semi-conductors. The target, acting as the cathode, is kept at a constant negative potential with respect to the substrate and chamber walls, using a high voltage DC power supply. Current flow depends on the creation of populations of free electrons and ions, these particles, in the case of sputtering discharges, are generated by electron impact ionization of neutrals (*e.g.* Ar atoms) and by secondary electron emission when ions strike the cathode. The schematic of the applied voltage as a function of the current for a typical DC discharge is shown in Figure 2.7. Six different regions based on the functional form of the voltage/current curve must be distinguished [7]: A) ohmic conduction and saturation, B) Townsend discharge, C) breakdown, D) normal glow, E) abnormal glow and F) arc.

72
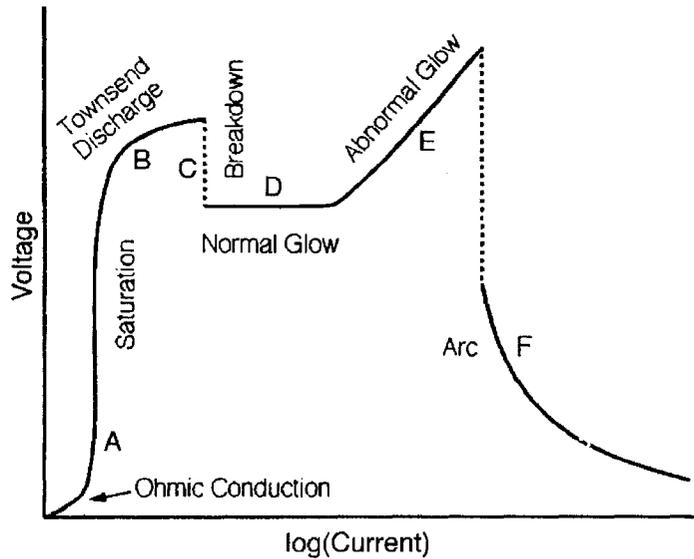
Figure 2.7. Schematic of applied Voltage versus current for a DC discharge (from reference [7]).

At low voltage, in the ohmic conduction region, the free electron density is very small, as it is essentially due to external agent, and therefore only low fluctuating currents are found. At higher voltages, but still a very low current, the above-mentioned current saturates as the applied field removes all the free electrons out of the volume between the electrodes as fast as they are generated. At this stage, the discharge is quite far from a sputtering plasma. Further increasing the applied potential will eventually cause the current to rise as additional free electrons and some ions are generated by impact ionization of the neutral gas atoms (*e.g.* Ar) by electrons that have sufficient kinetic energy while accelerated towards the anode. The discharge is not yet self-sustaining, it is known as Townsend discharge.

Once the potential is increased sufficiently, the ions begin to have enough kinetic energy to create charged particle by knocking free electrons out of the cathode material. The bulk of the ions is now created by these secondary electrons as they impact neutrals

73

(*e.g.* Ar) in transit to the anode. At this point, called breakdown, the voltage drop at constant current as the density of charge particle increases; in other words, the voltage does not need to be nearly as high to maintain the same current. This is when the plasma becomes self-sustaining. Then, the DC discharge enters the normal glow regime, where the potential is nearly constant over a range of currents. In this regime, the generation of secondary electrons is mostly localized at irregularities of the cathode, as the electric field is locally enhanced there. Therefore, the current density at the cathode is not uniform but concentrated at irregularities. The current then increases as ion bombardment spreads over the surface of the entire cathode at nearly constant potential. Once the entire cathode surface is used, the current must then increase if the potential is increased. This regime is called the Abnormal Glow and it is practically the regime where most sputtering processes are performed, since it affords the highest possible sputtering rates under practical conditions [7]. For DC magnetron, the current is proportional to the n power of the voltage: $I \propto V^n$, where n is related to the efficiency of electron trapping near the target. The potential is typically several hundred volts, while current densities typically range from 1 to 100 mA/cm^2 with voltages less than 800 V.

Thus, increasing the power from the power supply will produce increased voltage and current density. At a certain point (j > ~100 mA/cm^2), the ion bombardment involves extreme heating of the target, causing thermal emission of electrons. The increased number of emitted electrons leads to an avalanche of ion production in the plasma, causing an arc discharge: the voltage drops dramatically as it does not need to be nearly as high to maintain the same current due to the greatly increased density of

74

charged particles (Ar$^+$). The plasma is then no longer sustained, as ions do not have enough kinetic energy.

c)   *RF Sputtering*

Radio Frequency (RF) sputtering was invented in order to deposit films from insulating targets, *e.g.* the growth of SiO$_2$ thin films from SiO$_2$ targets. Indeed, the DC glow discharge can not be used for insulating targets with resistivities exceeding 10^6 Ω.cm, because of the positive charge (*e.g.* Ar$^+$ ions) accumulation on the target surface.

a)

b)
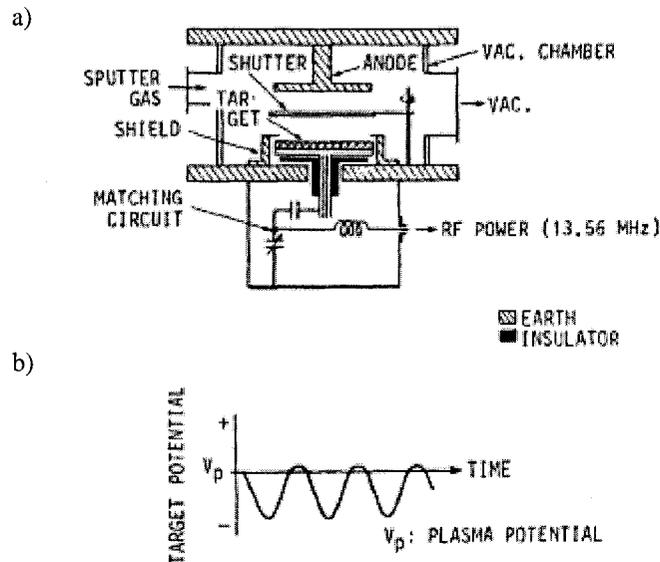
Figure 2.8. a) A schematic of a RF sputtering system, and b) a graph of the target potential, showing the negative self-bias of the target (from reference [4]).

At frequencies below 50 kHz, the ions are sufficiently mobile to establish a complete discharge at each electrode on each half-cycle; therefore, DC sputtering conditions prevail at both electrodes, which alternatively behave as cathodes and anodes [1]. However, at frequencies above 50 kHz, the ions do not have enough mobility to

respond to the fast AC signal, and, therefore, behave as if they were in a DC glow discharge, bombarding the target. Typical Radio Frequencies ($f < 1$ GHz) employed for RF sputtering range from 5 to 30 MHz; however, 13.56 MHz is very widely used, as it is the frequency reserved for plasma processing by the U.S.A. Federal Communications Commission. A simplified schematic of a typical RF sputtering chamber is shown in Figure 2.8.a.

At frequencies above 50 kHz, the power supply (*i.e.* the RF voltage) may be capacitively coupled to the target by a series capacitor. This capacitor allows the target to self-bias to a negative potential, causing the target to behave like a DC target bombarded by positive ions (Ar^+). Thus, Figure 2.9 shows how the self-bias is established through the difference in mobility of Ar^+ and e^-. As shown in Figure 2.9.a, during the first positive half of the RF voltage, the high mobility of the e^- in the plasma generates a large electron current. It is drawn to the target and flows to the capacitor. Then, during the following negative half of the RF voltage, the lower mobility of the Ar^+ ions in the plasma generates a smaller ion current. Therefore, over a few cycles, the target will build up a negative bias, leading to a zero net current through the capacitor over an entire cycle, as shown in the Figure 2.9.b. Thus, the Ar^+ ions can not respond to the fast radio frequency variations, but respond to the negative DC bias of the target, creating a situation similar to DC sputtering, where the ions are continuously accelerated in the plasma towards the target.
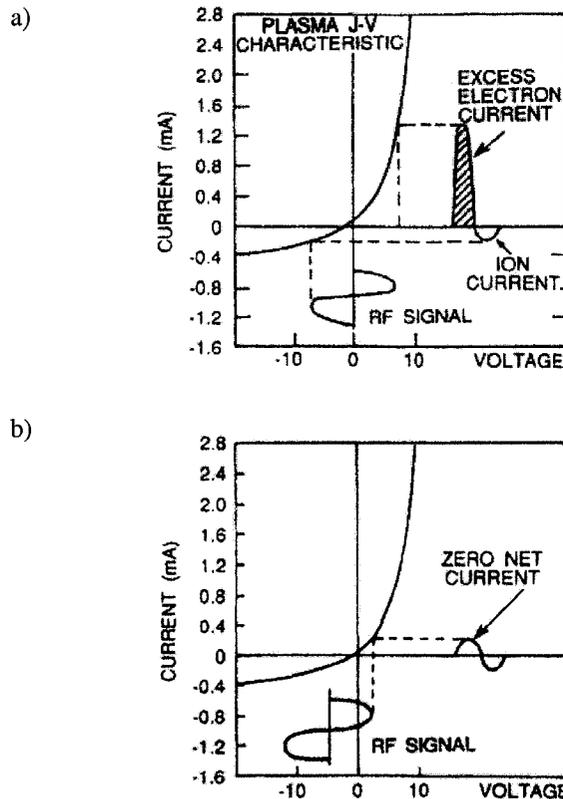
Figure 2.9. Formation of negative DC self-bias in a capacitively coupled RF discharge. a) During the first cycle, before a DC bias is developed, there is an excess electron current. b) After a first few cycles, a DC bias is formed so the sum of electron and ion currents would be zero over a full cycle (from reference [1]).

To optimize power transfer from the power supply to the plasma, the RF sputtering system requires an impedance-matching network between the power supply and the discharge chamber (*i.e.* plasma). The RF power supply is usually designed to see a 50 Ω load [3]. However, the impedance of the plasma is much higher, on the order of 1 to 10 kΩ and is capacitive in nature [4]. The matching circuit consists of a tunable LC circuit that transforms the plasma impedance to 50 Ω. In a simplistic approach, tuning is achieved by varying the distance between the plates of the matching circuit capacitor; this may be done manually or automatically. This latter option was used to ensure a

77

quick response of the matching network to any plasma impedance changes, thereby providing the most efficient power transfer possible.

d)   Plasma Characteristics

A plasma can be defined as a partially ionized gas, as it contains mainly neutral atoms along with some ionized atoms and free electrons: indeed, there are about 10^4 to 10^7 neutral atoms per ion in a weakly ionized plasma (~1 mTorr) [7]. In the plasma, the collisions between neutral atoms and energetic electrons not only generates ions, but may also excite atoms that will emit a photon upon relaxation to their ground state, causing the plasma to glow. One then talk about a glow discharge.
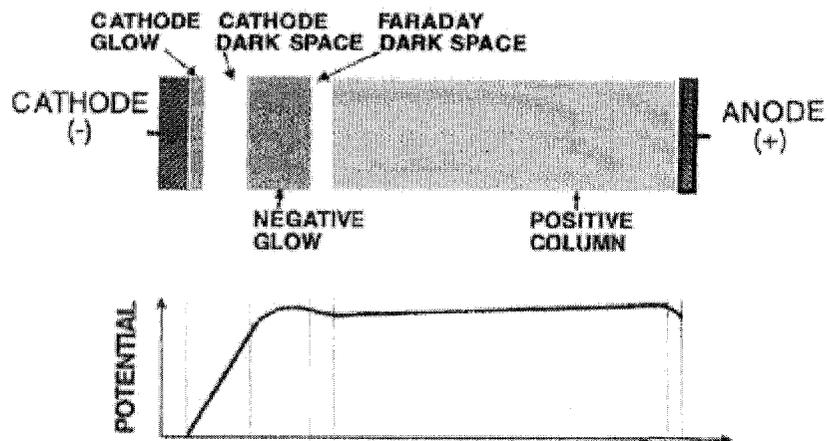
Figure 2.10. Structure of a DC glow discharge with its corresponding potential (adapted from reference [6]).

Figure 2.10 shows a schematic of a DC glow discharge and its corresponding potential and current as a function of position in the plasma. In a first approach, five areas may be distinguished: the cathode glow, the cathode dark space (or sheath), the negative glow, the Faraday dark space and the positive column.

78

- The cathode glow occurs when the bombarding ions are neutralized and lose energy in the collision cascade process after they hit the cathode. Indeed, some of the energy is released in the form of light from decaying exited states. This phenomenon is hard to see in low-pressure discharge.

- The cathode dark space (or sheath) arises from the difference in mobility of the Ar^+ and the e^-. Indeed, low mobility positive ions (heavy) accelerate slowly across the sheath, whereas electrons (light) traverse this region quickly as they are repelled from the cathode, yielding a positively charged region. This region is dark, since electrons do not collide with Ar atoms until they have traveled one mean free path, and therefore the width of this region ($\sim$1 cm) is inversely proportional to the plasma pressure.

- The negative glow is the region where the electrons impact the neutrals, thereby exiting argon atoms that will emit a photon upon relaxation to their ground state, causing the discharge to glow. Gases have their own characteristic glow colors: for instance, Ar and O_2 yield purple and white plasmas, respectively. The substrate is generally placed inside this region, before the Faraday dark space [1].

- The Faraday dark space is essentially an electric field-free region where electrons have lost all their kinetic energy.

- Lastly, the positive column is a region with a weak glow, arising from the collision between gas atoms and the electrons that are slowly accelerated towards the anode.

79

As shown on Figure 2.10, except for the cathode dark space, the remainder of the plasma is approximately equipotential; because of the lower mobility of the positive ions, the body of the plasma is left at a slightly positive potential compared to the ground anode. This potential is usually quite low, approximately 10 V [7]. The maximum energy of a particle bombarding the cathode will consequently be that of a charged particle accelerated across the potential difference between the plasma potential and the cathode potential. Nevertheless, the ion energy may be altered when the ions traverse the cathode sheath, as it may collide with neutrals and undergo a "symmetric" charge transfer: $Ar^+ + Ar \rightarrow Ar + Ar^+$. The result of this charge transfer is an energetic neutral atom (formerly the ion, it has a kinetic energy proportional to the distance that has been crossed in the sheath before charge exchange) and a "cold" ion that will now be accelerated towards the cathode. Overall, the bombarding particles arrive with energies somewhat reduced compared to the maximum expected, decreasing the sputtering yield.

e)   *Sputtering of alloys and compounds*

To sputter alloys and compounds, several methods related to sputtering are available. For instance, to prepare alloy films one might directly sputter a target of the alloy or a pie-like target made with distinct areas corresponding to each of the alloy element. With careful manufacturing of the target – target composition or sector width, respectively – control of the stoichiometry of the deposited film may be achieved. In the case of alloy targets, the target composition will be maintained and deposited since the material is removed layer-by-layer. In the case of a pie-like target, careful design of the sector width should be designed according to the relative sputtering yields of the

80

elements. With multi-sputtering source deposition systems, other methods to prepare alloy films include co-sputtering or cycled sputtering of the required element targets. This respectively yields atomically mixed alloy films or layered films that require post-deposition interdiffusions. These methods require careful calibration of the co-sputtered and elemental deposition rates.

The preparation of compound thin films has been accomplished using a tremendous number of different sputtering methods. Methods include the direct RF sputtering of a sintered or pressed target of the material to be deposited. Despite slight stoichiometry changes due to the atomic nature of sputtering processes, this technique is quite simple to implement, providing that targets can be manufactured with the appropriate quality. Similar to evaporation, oxides and nitrides are usually deposited oxygen or nitrogen poor: to compensate for these deficiencies, O_2 or N_2 gases might be introduced directly into the plasma (this technique is called reactive RF sputtering) or into the environment of the post-deposition annealing process. Because RF sputtering is somewhat slower than DC sputtering, other methods include the reactive DC sputtering of metal target in Ar, O_2, N_2 or H_2S gas mixtures, or post-deposition reactive annealing of DC sputtered metal precursor films (layered or co-sputtered). In addition, substrate biasing, heating, cooling or rotation can tune film structures and compositions. The deposition of compound thin films is an extremely challenging task that involves several process parameters and has therefore yielded many empirical recipes; some are reviewed in a comprehensive handbook [4]. Several of them were employed in the present thesis.

81

f) *Conclusion*

To summarize, some of the advantages of sputtering processes include:

- any material can be sputtered and deposited (*e.g.* element, alloy or compound),

- the single-block solid sputtering targets yield low geometrical constraints: targets can be oriented in any direction, can have large areas (disk up to 30.5 cm in diameter or blocks up to 2.9 m wide, *c.f.* Kurt J. Lesker Co.) with specific geometries (*e.g.* line source),

- sputtering conditions can easily be reproduced from run-to-run,

- there is little radiant heating in the system compared to vacuum evaporation,

- in reactive deposition, the reactive species can be activated or dissociated within the plasma.

Disadvantages include:

- sputtering is not energy efficient: most of the input energy heats the target, which should therefore be cooled,

- sputtering targets are often expensive and have to be custom made for most alloys and compounds; targets, particularly those of insulators, may be fragile and easily broken in handling or by non-uniform heating; lastly utilization of the target material may be low (< 30 % in our system configuration),

- sputter vaporization rates are low compared to those that can be achieved by thermal vaporization,

- substrate heating from electron bombardment can be high in some configurations and can be detrimental to the film structure,

82

■ contaminants on the deposition chamber surfaces are easily desorbed by heating and ion scrubbing, and may be activated in the plasma and incorporated into the film.

2.1.3 Description of our UHV system

The deposition system used was custom designed by Kurt J. Lesker Company. As shown in Figure 2.11, the deposition system has four independently pumped chambers: an annealing chamber, a load/lock chamber, a distribution chamber, and a multi sources combinatorial deposition chamber.
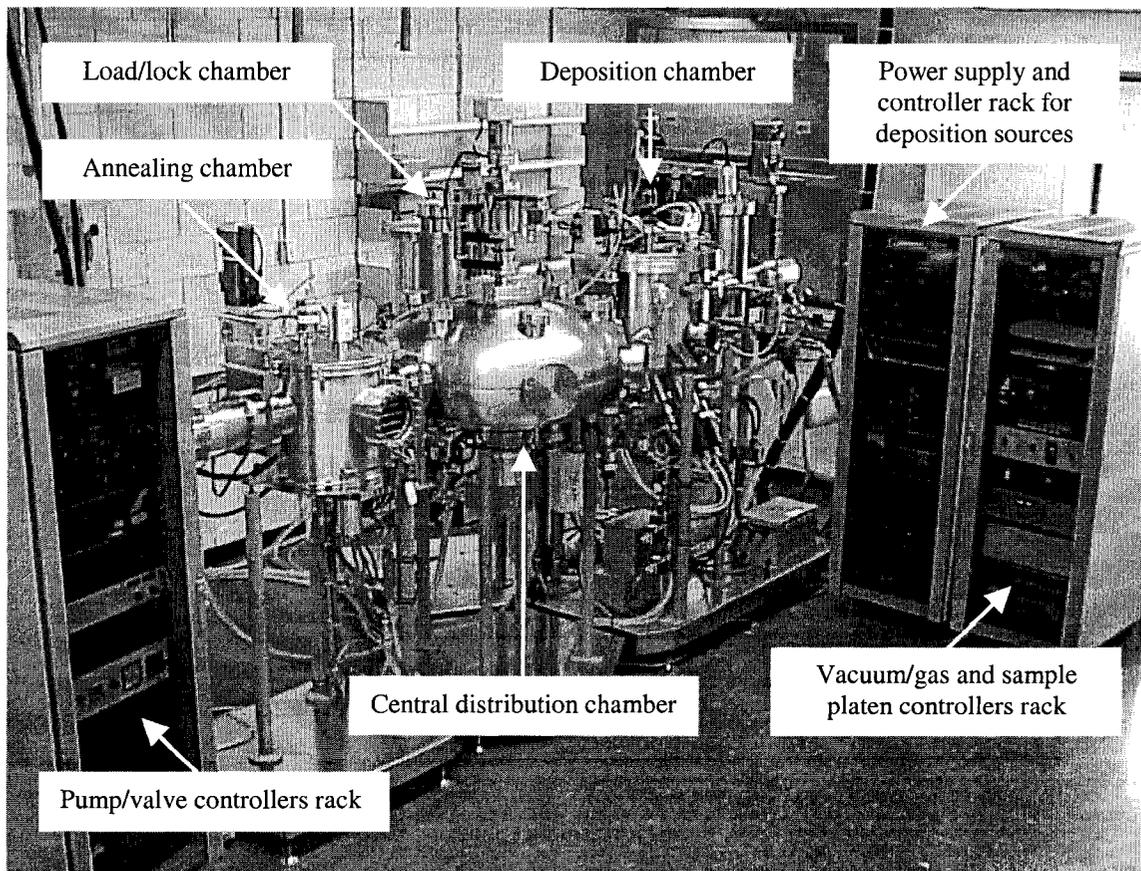
Figure 2.11. Picture of the UHV deposition system used.

83

a)   *The load/lock and distribution chambers*

The load/lock and distribution chambers allow for mask and/or sample transfer from one chamber to another under a UHV environment. These two chambers are separated by a gate valve that allows preservation of the UHV environment in the central distribution chamber at all times and for faster pump-down of the load/lock chamber. The load/lock chamber is first roughed by a dry mechanical pump (BOC EDWARDS XDS10 scroll pump – 11 $m^3.h^{-1}$) and then pumped down via the central distribution chamber. UHV conditions (10^{-9} Torr) for the central distribution chamber are achieved thanks to a turbomolecular pump with mechanical rotor suspension (LEYBOLD TURBOVAC TW700 – 700 $L.s^{-1}$), which is backed by a mechanical pump (LEYBOLD TRIVAC D 16 B rotary vane pump – 15 $m^3.h^{-1}$) equipped with an exhaust filter (LEYBOLD ARS 16-25 exhaust filter with oil return). Located in the central deposition chamber, a fork system is used to transfer mask and substrate holders from one chamber to another.

b)   *The deposition chamber*

It is the heart of our system. The deposition chamber has a UHV environment with a base pressure ranging from high 10^{-10} to low 10^{-8} Torr (measured with an ion gauge). The deposition chamber is roughed with a dry mechanical pump (BOC EDWARDS XDS10 scroll pump – 11 $m^3.h^{-1}$). Once a base pressure of 0.1 mbar (75 mTorr) is reached, the chamber is then connected to a cryopump (CTI CRYOGENICS CRYO-TORR 8F cryopump – 1200 $L.s^{-1}$ for Ar) where gases are trapped on condensed-He cooled high surface area sorbants (T ~ 15 K).

84

a)

Pressure gauges and gas controller

E-beam controller

RF sputtering power supply

Wedge tool and deposition platen control

Magnetron #1

Shutter controllers

DC sputtering power supply

RF match box

Gas flow controllers

b)

FTM

c)

Wedge tool

Glass substrate

Substrate holder

Mask holder

3" Magnetron sputter sources
Pb, Sb: DC-sputtering
Sb_2S_3: RF-sputtering

Knudsen effusion cell

E-beam evaporation sources
Zr, Hf sources

Figure 2.12. The deposition chamber: pictures of a) the outside of the chamber and its control racks and b) the inside of the chamber (one can particularly see the film thickness monitor (FTM) and the three sputter sources and their shutters) and c) schematic.

85

The deposition chamber allows combinatorial deposition of thin films and gathers several deposition sources: Knudsen effusion cell, e-beam evaporation source, and three magnetrons as shown in Figures 2.12.b and 2.12.c. As mentioned and described earlier, a 4-pocket electron beam evaporation source (TELEMARK MODEL 568-02 four pocket 7cc electron beam source) enables the evaporation of any kind of compatible evaporant. The evaporation source is powered with a 5.5 kW (725 mA at 7.5 kV) power supply equipped with an XY sweep to allow for e-beam positioning and rastering on the evaporant surface (TELEMARK MODEL TT-6 power supply and XY sweep). Film thickness and deposition rate can be monitored during growth using a quartz crystal microbalance film thickness monitor (INFICON XTM/2). This device can automatically close the substrate shutter once the desired thickness has been reached. This device requires calibration, as mentioned earlier in Section 2.1.2.a.

The deposition chamber also contains three 30° off-normal axis magnetrons, located 20 cm away from the substrate. Magnetrons provide an annular magnetic field as shown in Figure 2.5. The magnetrons can host 3 in. (7.6 cm) wide and up to ¼ in. (6.4 mm) thick targets. The magnetrons are water-cooled to dissipate heat generated by sputtering, as demagnetization is a risk if the magnets warm up. The central part of the magnetron assembly is kept at the applied sputtering potential, while the outer part of the magnetron is kept at ground, and extended with a ground-shield cap that exposes only the target to the plasma and protects the magnetron body from sputtering. Each magnetron and the substrate are protected with shutters that are manually controlled and compressed air actuated. During target conditioning, shutters are kept closed, just before

86

actual deposition the desired target shutters are opened and finally the substrate shutter is opened and a timer is started. Lastly, magnetrons may be powered by two DC power supplies and one RF power supply. The DC power supplies are ADVANCED ENERGY MDX-500, which can supply up to 500 W (1 A at 500 V). The RF power supply is an ADVANCED ENERGY RFX-600 RF power supplies with a frequency of 13.56 MHz, it can supply up to 600 W. Powers are generally kept below 200 W. The RF supply is equipped with an automatic tuner (ADVANCED ENERGY ATX 600) that controls the matching network that accommodates the source impedance with that of the plasma, in order to optimize power transfer. The reflected power is generally less than 5 W (5 %), with Sb_2S_3, sputtered at 100 W.

Gas flow is controlled through two MKS type 1179A Mass-Flow controllers; one is used for the process gas, 99.998 % pure Argon (PRAXAIR), the other is for a reactive gas, such as oxygen or nitrogen. Gas flow is measured in standard cubic centimeters per minute (sccm). Typical pressures during sputtering are from ~1.5 – 5 mTorr. Plasma pressure was usually maintained at 5.00 ± 0.01 mTorr, requiring 2 – 5 sccm of Argon. The pressure is measured with a capacitance manometer (MKS 627B Absolute Capacitance Manometer).

A computer controls the wedge tool and the sample platen, which hosts the substrate and mask holders. The sample platen can host at the same time a mask holder and a substrate holder. The relative position of the mask holder with respect to the substrate holder can be 0°, 90°, 180° or 270°. This positioning is key for selective area

87

deposition, necessary for mask-based combinatorial deposition strategies. The angle is controlled via Kurt J. Lesker custom-made software. This software also enables the control of the continuous rotation of the sample platen during deposition, as well as control of the wedge tool position with respect to the substrate. Both sample platen and wedge tool are moved with stepper motors. Moreover, the substrate can be heated controllably to temperatures up to 550 °C using a system of quartz heating lamps. However, there is no cooling capability, meaning that because of heat transfer to the substrate during PVD processes, substrate may warm up; this mostly limits the deposition rates that can be achieved without detrimental substrate heating.

c)   The annealing chamber

The annealing chamber is pumped by a turbomolecular pump with mechanical rotor suspension (LEYBOLD TURBOVAC 360 – 360 L.s^{-1}), which is backed by a mechanical pump (LEYBOLD TRIVAC D 16 BCS rotary vane pump – 15 m^{3}h^{-1}) equipped with an exhaust filter (LEYBOLD ARS 16-25 exhaust filter with lubricant return) and a pump lubricant (PFPE) chemical filter (LEYBOLD CFS 16-25 chemical filer). The annealing chamber enables to control the substrate temperature between room temperature and 1000 °C under different gaseous environments from pressures of 100 to 10^{-8} Torr. Thanks to lubricant, pump and seal upgrades, the annealing chamber is H$_2$S-compatible; while purging the chamber, the H$_2$S is scrubbed through a bleach solution. 5 cm × 5 cm samples are placed on top of a circular graphite heating element; temperature programmer and power controller enable control of the substrate temperature.

88

2.1.4 Sulfur vapor annealing set-up

a)
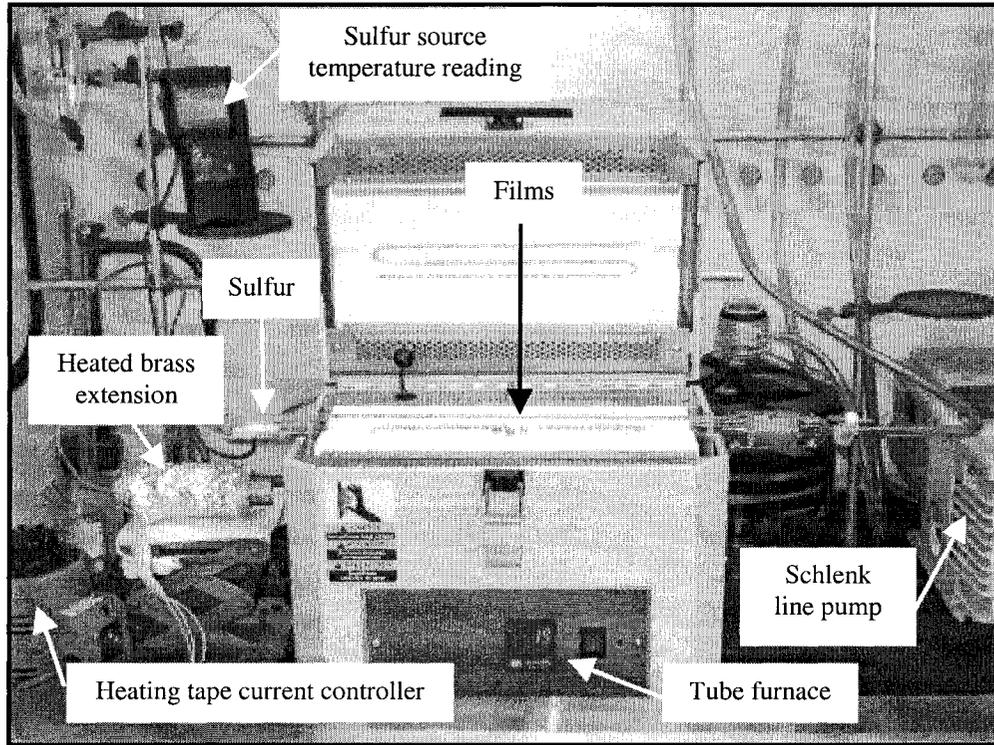
b)
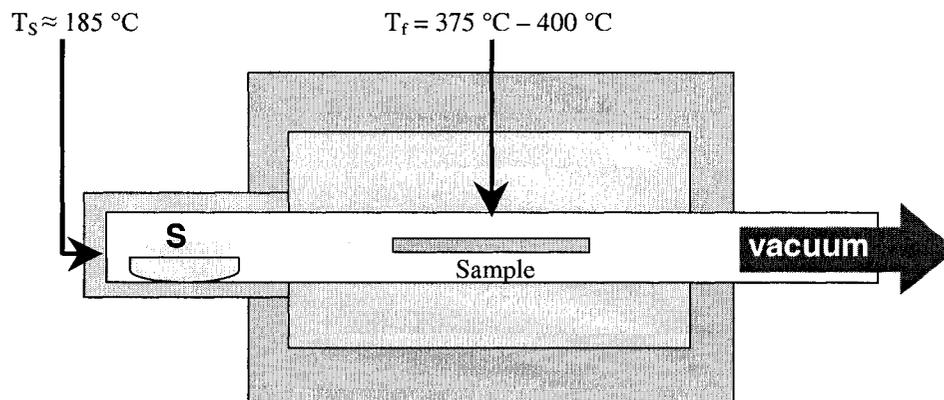
Figure 2.13. Two-zone tube furnace annealing in sulfur vapor set-up: a) picture and b) schematic.

In order to perform annealings in sulfur vapor, a two-zone tube furnace has been assembled. As shown in Figure 2.13, this assembly is made of a resistively heated brass extension and a LINDBERG/BLUE M tube furnace that can host a 2.5 cm OD tube.

89

Solid yellow sulfur was used as a sulfur source, it was freshly removed from a glove box and packed in a quartz boat. Both the sulfur-containing boat and the samples were placed in a 2.5 cm OD quartz tube in a way that the boat is located at the closed end of the tube at the brass extension and the samples are located at the center of the tube furnace. Samples were usually 1 cm^2 pieces of deposited films, up to six different samples could be loaded per run. After loading, the tube is connected to a Schlenk line; the tube is evacuated to ~1 mTorr and subsequently back-filled with N_2. This procedure was performed five times to ensure that no significant amount of oxygen is present. A final 10 minute evacuation was performed to have a tube base pressure of ~1 mTorr. The tube is then closed and the annealing program started. Films were heated to temperatures up to 400 °C, while the elemental sulfur was maintained at ~185 °C (± 5 °C) at one end of the tube, whereas the other end of the tube remained at room temperature, creating a sulfur flux through the tube. The sulfur temperature was monitored with a thermocouple located on the tube surface at the end of it; the current passing through the heating tape was manually adjusted in order to have a ramp rate of ~6 °C/min and maintain a temperature of 185 °C while the film is at temperatures above 300 °C. The sample temperature is controlled thanks to the furnace thermocouple and temperature controller. Specific rate, temperature and duration will be described latter in Chapters 4, 5 and 6, as conditions have been varied in order to determine optimal annealing conditions. Once the sample annealing temperature dwell is finished, the brass extension is removed. The temperature ramp down of the film therefore occurs without generation of sulfur vapors. To avoid air intake as the gas contracts in the tube upon cooling, an N_2 (atmospheric pressure) flow is started right at the end of the high temperature dwell. Once the film

90

reaches a temperature below 100 °C, the furnace is opened and the tube is removed, allowing for a rapid (~20 minutes) cool down to room temperature.

2.2 Thin-film characterization techniques

2.2.1 X-ray diffraction (XRD)

Goals of this thesis include the preparation of crystalline materials to be used as solar absorbers in thin film solar cells and the investigation of a ternary phase diagram. It is therefore necessary to determine the crystal structure of the films that were prepared. X-ray diffraction (XRD) is one of the most common ways to characterize the structure of crystalline materials.

a) *Basics of X-ray diffraction: phase identification, crystallite size and texture*

In crystalline materials, atoms are arranged in a regularly repeated pattern, or lattice, forming sets of parallel and identical planes of atoms. As it hits the sample, the incident x-ray beam is scattered by the atoms' electrons, which density also follows a regular pattern. If the atomic planes of the sample are situated such that the Bragg condition (equation 2.1) is satisfied, then constructive interference of the scattered x-rays occurs. This is shown in Figure 2.14, where the path difference between the two rays is BC + CD, it is equal to $2d \sin\theta$. To obtain constructive interference between the two rays diffracted from two successive atomic planes, the path difference should equal one wavelength (λ). Thus, the Bragg condition is satisfied when

$$\lambda = 2d \, \sin\theta \qquad\qquad (2.1)$$

where λ is the wavelength of the incident X-ray, d (or d_{hkl}) is the distance between equivalent atomic planes spacing in the crystal, and θ is the incidence angle of the x-ray, also called the Bragg angle. When the Bragg condition is met, a diffraction peak occurs.
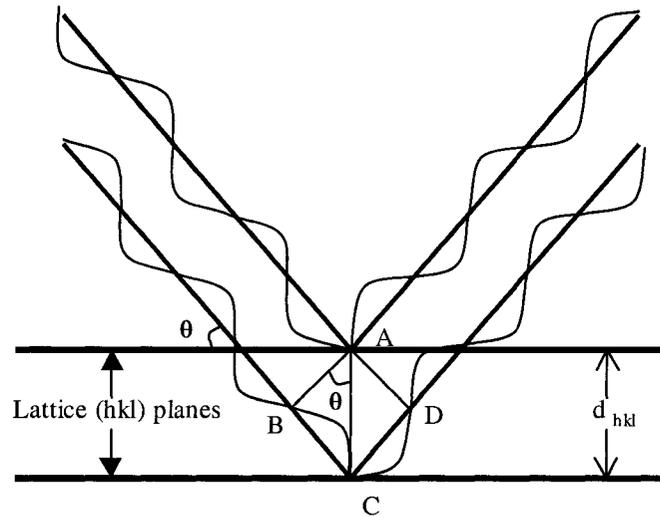
Figure 2.14. Origin of constructive interference (adapted from reference [8]). The path difference between the two rays is BC+CD, which equals one wavelength herein.

The orientation of the atomic planes is determined by the Miller indices (hkl). If the plane intersects the axes at $m_1 a$, $m_2 b$ and $m_3 c$ (with $m_i \leq 1$ or $m_i = \infty$ if the plane is parallel to the axis), then the Miller indices are the set of integers reduced to the smallest common denominator that are the reciprocals of the intercepts such that:

$$(h, k, l) = (\frac{1}{m_1}, \frac{1}{m_2}, \frac{1}{m_3})$$

(2.2)

The set (hkl) is referred to as the Miller indices of the plane, the set [hkl] corresponds to the direction perpendicular to the (hkl) plane.

92

In a simple approach, the intensity of the diffracted x-ray beam from a set of (hkl) planes obeys equation (2.3) [9]:

$$I_{hkl} = \left| F_{hkl} \right|^{-2M} V \qquad\qquad (2.3)$$

Here F_{hkl} is the structure factor for the (hkl) diffraction peak; it is related to the arrangement in the crystal and the scattering factor of the (hkl) plane atoms. The exponent, $-2M$, is the Debye-Waller factor, also known as the temperature factor; it describes the decrease in intensity of the scattered beam due to the thermal motion of the atoms or due to crystal disorder. Lastly, V is the diffracting volume; it depends on the beam size, penetration depth (*i.e.* x-ray absorption coefficient of the material) and in the case of thin-films (< 500 Å) it also depends on the film thickness. More details about these concepts may be found in [10] or [11].
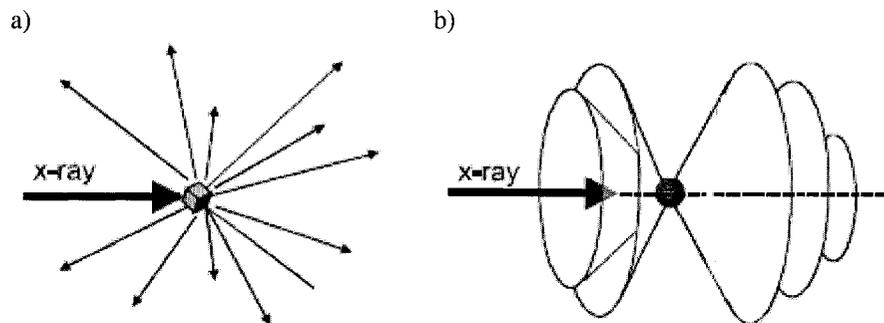
Figure 2.15. The patterns of diffracted X-rays: a) from a single crystal and b) from a polycrystalline sample (from reference [12]).

Figure 2.15 shows diffraction from a single crystal and from a polycrystalline sample. The diffracted beams from a single crystal point to discrete directions in space, each corresponding to a set of diffraction planes. Each set of (hkl) planes is precisely oriented in space, in other words, each [hkl] direction points in a unique direction in

93

space, and therefore the Bragg condition can only be met accordingly to that direction, yielding a discrete diffraction direction, also called pole. On the other hand, the diffraction pattern from a polycrystalline sample (powder, non-textured film) forms a series of diffraction cones. Polycrystalline samples are made of a large number of small crystallites oriented randomly in space. Thus, an X-ray beam striking a polycrystalline sample will be diffracted in all possible directions, as governed by the Bragg equation. Each set of (hkl) plane will give rise to a cone of diffraction; each cone actually consisting of a string of closely spaced dots, each one of which represents a diffraction from a single crystallite (*i.e.* orientation) within the powder sample. An intermediate situation between single crystal and perfectly polycrystalline samples include textured polycrystalline samples, such as textured thin-films. These samples are also made of a large number of crystallites; however, despite some random orientation, a significant number of crystallites are oriented in a preferred direction. Thus, from what has been said previously, the x-ray beams will preferably be diffracted in the directions that correspond, in terms of Bragg conditions, to the preferred orientation. Therefore, texture or preferred crystallite orientation yields discontinuous diffraction cones, as shown in Figure 2.16. Texture mostly affects the values of the relative intensities. In the case of thin-films, the preferred orientation of the crystallites is usually due to a substrate-related preferred growth direction – a film may be seen as a 2D object, the direction perpendicular to the substrate being unique.

94
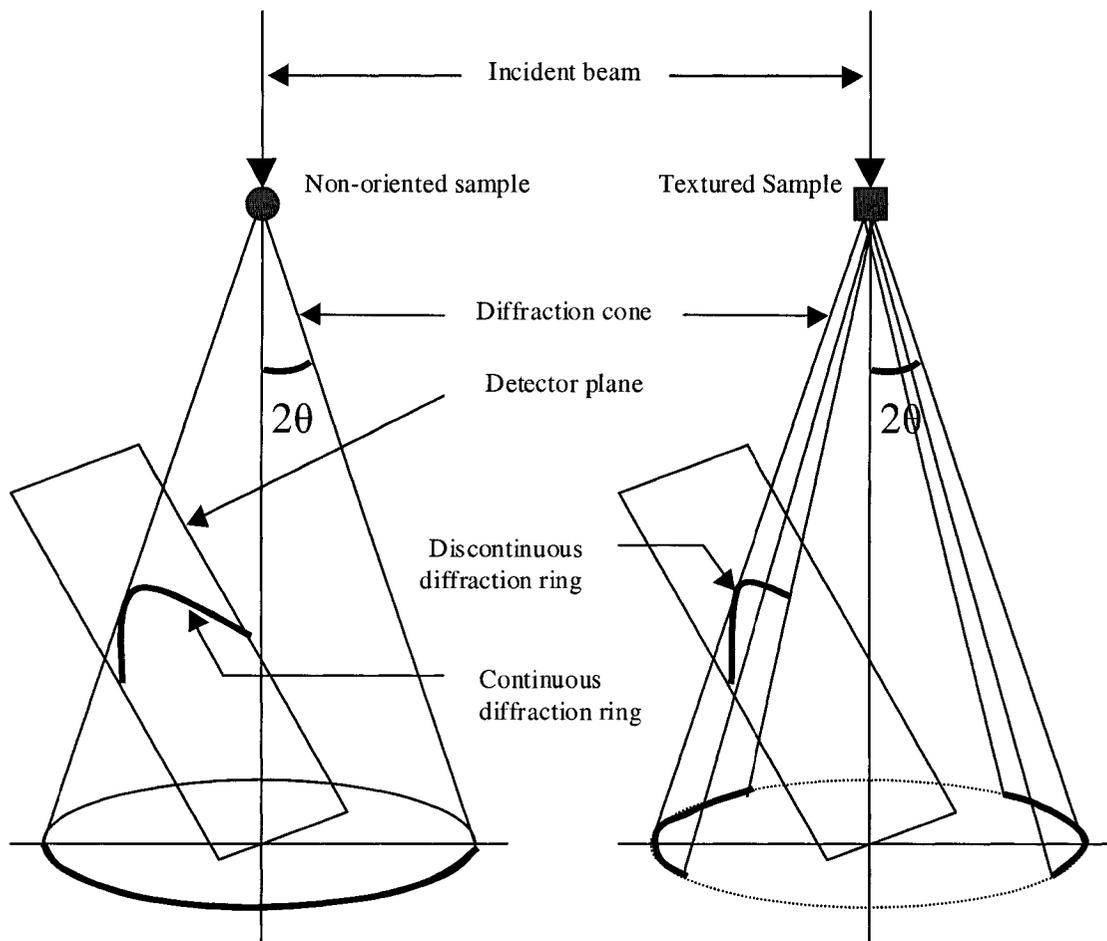
Figure 2.16. A diffraction cone and the conic section with a 2D detector plane, a) for a non-oriented sample and b) for a textured sample (from reference [12]).

The size of crystalline grains also has an impact on the diffraction pattern that is obtained. In order to observe sharp diffraction maxima in the powder x-ray diffraction pattern, the crystallites needs to be of sufficient size to ensure that at angles slightly different from the Bragg angle, complete destructive interference occurs. Indeed, for a large number of planes, the summation of the slightly out of phase waves (*i.e.* with θ values close to the Bragg angle) yields destructive interference, *i.e.* no diffracted intensity. For materials with very small crystallites, with few planes, the diffracted x-ray intensities slightly out of phase do not completely destructively interfere, leading to

broader and less intense diffraction peaks. The Scherrer formula relates the thickness of the crystallites to the peak broadening [8,10]:

$$t = \frac{0.9\,\lambda}{\sqrt{B_M^2 - B_S^2}\,\cos\theta}$$
(2.4)

where t is the crystallite thickness in Å, λ the x-ray wavelength (1.5418 Å for Cu K_α), θ the Bragg angle (half the measured diffraction angle), B_M is the width in radians of one of the sample diffraction peaks at half height and B_S is the width in radians of one of the standard diffraction peaks at half height. The standard peak width B_S should be obtained from a highly crystalline sample with a diffraction peak at a similar diffraction angle to that of the sample. This value represents the instrumental broadening.

Because it has its own crystal structure, in terms of atom types and positions, a crystalline material yields a unique diffraction pattern, also called the powder pattern when the sample is polycrystalline. These powder patterns are unique sets of diffraction peaks, each defined by an angle, 2θ, and a relative intensity, I (I in percent of the most intense diffraction peak). Crystal structure (lattice type, d-spacing and atom positions) may be determined from powder patterns; however, for complex crystal structures, this is not a trivial task and, therefore, is still the aim of many traditional mineralogy and solid state chemistry studies. Regarding the work presented herein, crystal structures of films made of known materials were determined by matching the film powder patterns to reference powder patterns contained in the Joint Committee on Powder Diffraction Standards (JCPDS) database.

b)   *Instrumentation used: D8 Discover from Bruker AXS, Inc.*

XRD data were collected using a D8 DISCOVER diffractometer from Bruker AXS, Inc. This diffractometer is specially designed for combinatorial thin film R&D experiments with its fast and small area x-ray data collection capabilities. Schematics and picture of the instrument are reproduced in Figure 2.17. The diffractometer is equipped with a Cu sealed tube, in which X-rays are generated by bombarding a Cu target (anode) with electrons emitted from a filament (cathode). The filament current was set to 40 mA and the accelerating voltage to 40 kV. The x-ray spectrum generated from the sealed tube (white radiation and characteristic lines) should be monochromatized. This is achieved using a single crystal monochromator: the wavelength of the X-rays diffracted by the crystal is given by the Bragg condition. Thus, the crystal was set to a diffraction condition such that only the Cu K_α ($K_{\alpha 1}$ and $K_{\alpha 2}$) radiation satisfies the Bragg law; the wavelength of Cu K_α equals 1.5418 Å. This radiation is then collimated with a 0.5 mm pinhole collimator. As it allows sampling of small areas, this feature is particularly advantageous for combinatorial thin film experiments, where films are obtained on rather small areas (as small as ~4 mm^2). The X-ray take-off angle from the sealed tube target, monochromator crystal and collimator should be carefully and very precisely aligned to yield an intense monochromatic, convergent beam aligned with the center of the goniometer.

a)

c)

b)
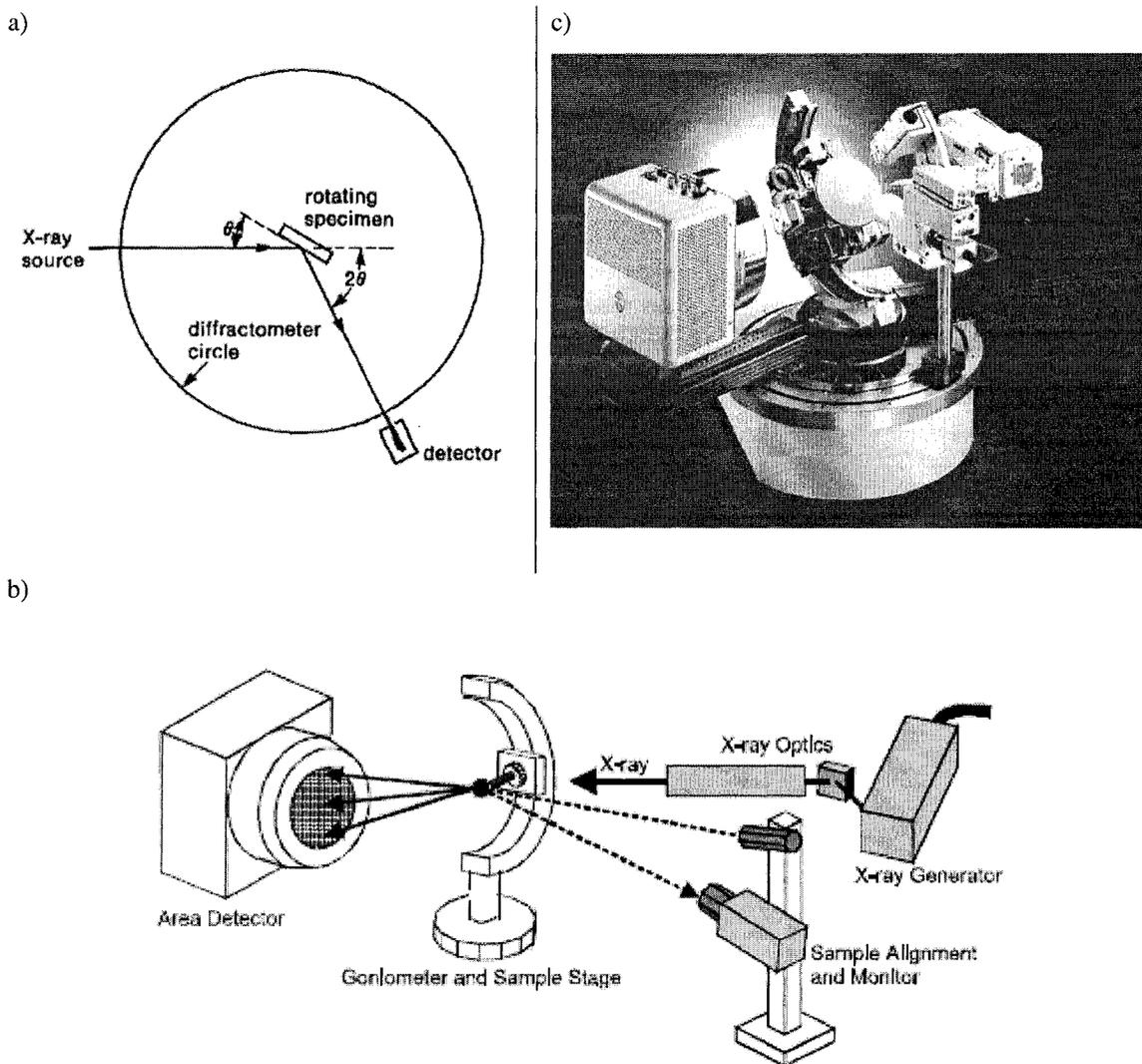
Figure 2.17. a) Schematic of the θ-2θ geometry: the x-ray source is fixed, the sample is rotated by an angle of θ while the detector is rotated by an angle of 2θ (adapted from reference [9]). b) Schematic of the system we used (from reference [12]); x-ray optics are composed of a monochromator (grating) and a collimator. c) Picture of the D8 discover instrument with XYZ suction stage.

Several sample stages were available, including an XYZ suction stage that was particularly useful for mounting thin films. Any area of the film may be selected for diffraction, thanks to the X and Y drives (motion parallel to the stage plane); these drives also allow for X and Y motions during data collection, in order to sample larger areas. In addition, each selected area should be aligned with the center of the

98

goniometer. As shown in Figure 2.17.b, the instrument contains an optical alignment system composed of a laser beam and a video camera: when the laser beam is reflected at the center of the goniometer, it is centered on the crosshair of the video image (pre-set during an alignment procedure). Thus, to align the sample with the center of the goniometer, the sample stage is moved back and forth (Z drive) until the laser beam reflected from the substrate falls at the center of the crosshair of the video image.

Once the sample has been aligned, data collection may start. The diffractometer is equipped with an area detector, commonly called a GADDS detector for General Area Detector Diffraction System. The detector is made of three, two-dimensional arrays of thin wires in a Xe/methane gas environment. When an X-ray photon enters the detector chamber, it interacts with a Xe atom, ionizing the gas and generating an electron, this electron is then accelerated and collected with the three two-dimensional arrays of thin wires. To account for slight spatial non-uniformity of the x-ray photon detection (some areas might be slightly more sensitive than others) and to account for the flat nature of the wire arrays (distortion of the cones), correction procedures are periodically performed using a glassy iron foil that evenly scatters the Cu K_α radiation by fluorescence. In addition, the system needs to be calibrated: assuming that the goniometer is well aligned, the powder pattern of a corundum standard (obtained from NIST) is collected, the shape and position of the cone sections are matched to the standard, determining therefrom the center of the detector and its distance from the center of the goniometer. The system can then be reliably used. Advantages of the area detector include shorter collection times and the ability to measure oriented samples,

because of the extended 2θ (number of cones) and χ (cone section width) range that are measured simultaneously. For instance, when the detector is located at $\sim$15 cm from the center of the goniometer, the 2θ range covers $\sim$30° with a resolution of $\pm$ 0.04°.
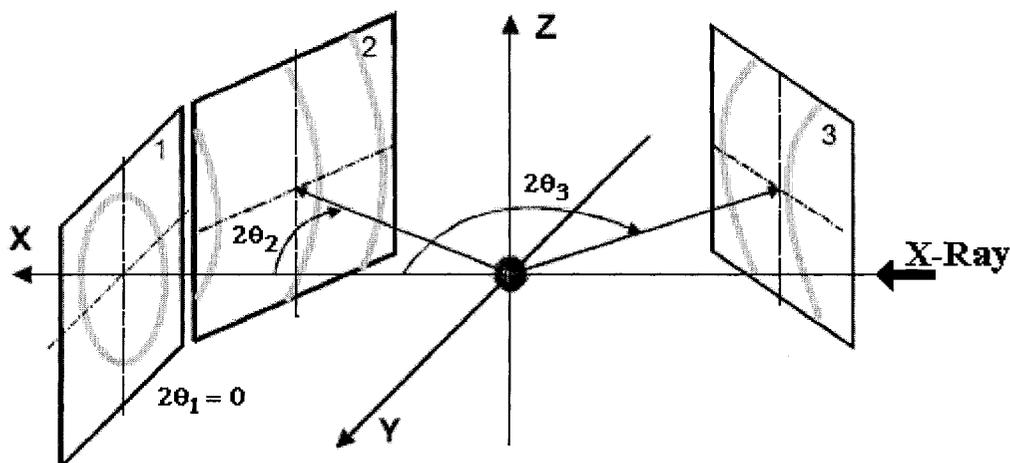
Figure 2.18. The entire powder pattern of a sample may be obtained from several different positions of the area detector, or "snap shots" (adapted from reference [12]).

The diffracted signal was collected from 2θ = 3° to 2θ = 85°. This may be achieved in three steps or snap shots (frames), as illustrated in Figure 2.18. The detector, located at $\sim$15 cm from the goniometer center, is positioned successively at 2θ = 20°, 45° and 70°, while the sample is rotated by an angle θ from 3° to 17°, from 15.5° to 29.5°, and from 28° to 42°, respectively, as the system obeys a θ-2θ geometry. If the incident beam hits the sample with an angle, θ, then the diffracted beam leaves the sample with an angle 2θ with respect to the fixed incident x-ray beam, as shown in Figure 2.17.a. Although not necessary for truly polycrystalline sample, the θ-rotation of the sample is preferred for textured sample, as poles may be missed if the Bragg condition (*i.e.* specific θ values) is not met. Each detector position was held for 60 to

100

240 seconds (*i.e.* 60 to 240 seconds per frame). In addition, as mentioned previously, the stage was usually oscillated in the X and Y (0.5 to 1 mm) directions to sample larger areas of the samples. Finally, once collected, the frames are integrated in χ, this means that at fixed 2θ values, the intensity values obtained are summed and normalized along a cone section. This leads to the conventional I vs. 2θ diffraction powder patterns, that are then studied and matched to the reference patterns in the database, using EVA software from Bruker AXS Inc.

As detailed in Chapters 4, 5 and 6 and in Appendix 2, thin films were sometimes obtained combinatorially, indeed several distinct films could be obtained on a single substrate or small (1 cm^2) substrate pieces from one deposition or annealing run. Small substrate pieces were taped onto a glass slide large enough to be mounted on the diffractometer suction stage. In this context, it is interesting to be able to efficiently collect x-ray data for these several samples. Thus, thanks to the XYZ suction stage, several points (*i.e.* samples) can be chosen, aligned and pre-set. A routine that I wrote can then operate the instrument automatically, the routine controls the various drives (X, Y, Z, θ and 2θ), collects the data, and then stores and names the data. The routine is show in Appendix 3. A frame integration routine has also been written; however, this step is less critical as it can be easily and efficiently (very quickly) done manually for up to 20 data points.

Basics and experimental details about small angle x-ray diffraction and x-ray reflectometry will be given in Chapter 3.

2.2.2 Scanning electron microscopy (SEM)

SEM is the method of choice to evaluate the morphology of the films that were prepared. In a scanning electron microscope, electrons are usually thermionically emitted from a tungsten cathode, or for higher resolution instruments, electrons are emitted via field effect at a sharp metal tip, electrons are then accelerated towards an anode. Condenser lenses then focus the electrons into a beam with a very fine focal spot on the order of a few nanometers across. Pairs of scanning coils in the objective lens deflect the beam in a raster fashion over a rectangular area of the sample surface. When the primary electrons strike the surface, they are scattered by atoms in the sample and interact with a volume known as the interaction volume. Interactions in that region lead to emission of secondary electrons, backscattered electrons and even x-ray photons, as the depth of the volume increases, *i.e.* the primary beam energy increases. Due to their low energy (~10 eV), secondary electrons originate only from within a few nanometers off the surface, are detected by a scintillator-photomultiplier device, and the resulting signal rendered into a two-dimensional intensity distribution map. This process relies on the synchronous scans of the electron beam and the scintillator. The brightness of the signal depends on the number of secondary electrons reaching the detector: steep surfaces and edges tend to be brighter than flat surfaces, which results in images with a 3D appearance. Moreover, electrons elastically scattered (*i.e.* without or with a small loss of kinetic energy), known as backscattered electrons, have higher energies (> 50 eV). As the probability of backscattering is higher for larger atomic numbers [13], the collection of backscattered electrons ensure the detection of areas with different chemical compositions, since the contrast between areas with low and high average

102

atomic number is enhanced. Compositional information cannot always be extracted from the backscattered electron signal, since the film topography will also affect this signal; therefore, in the case of a rough film, backscattered electron images are usually not very informative. The spatial resolution of the SEM depends on the size of the electron spot and is limited by the size of the interaction volume, in other words, by the extent of the material that interacts with the electron beam. Both the spot size and the interaction volume are large compared to the distances between atoms, and the highest resolution of SEM instruments ranges from 10 to 100 Å. The advantages of SEM include the ability to image large areas of the sample, the ability to image the bulk of materials from cross-section views, the ability to image the film topography from tilt view; advantages also include the ease of sample preparation: almost any sample size and shape can be accommodated, and only a thin conductive coating (*e.g.* Cr was used for the thin films presented herein) is required to ensure appropriate charge dissipation. Lastly, at high energy, X-ray photons may be generated and detected with an Energy Dispersive X-ray (EDX) detector, for qualitative and even quantitative (careful calibrations are required) elemental analysis.

Morphology and, sometimes, composition of as-deposited and annealed films were evaluated with a field emission scanning electron microscope (JEOL – 6301 F) equipped with a backscattered electron detector and an Energy Dispersive X-ray (EDX) detector. Morphology was usually evaluated from Scanning Electron Microscopy (SEM) images obtained using an accelerating voltage of 5 kV, to limit the penetration depth of the beam (*i.e.* the extent of material sampled) and therefore increasing the sharpness

103

(resolution) of the image. Top surface, cross-section and tilt views were usually collected with magnifications up to 70,000 times, but more commonly 20,000 times to 40,000 times. The elemental composition of the films was, when possible, also determined from EDX data, using a 20 kV accelerating voltage. This determination was possible for films containing only antimony and sulfur, as the characteristic x-ray energies (peaks) of these two elements are well separated; nonetheless, this determination was not possible for films containing both lead and sulfur, as the characteristic x-ray energies (peaks) of these two elements are overlapping (K_α for S at 2472 eV and M_α for lead at 2484 eV), preventing reliable peak area integration, which is necessary for quantitative analysis. Samples were usually glued onto Al stubs with silver paint and were coated with Cr (~1.5 nm thick) or occasionally coated with carbon when the same sample piece was also used for WDX.

2.2.3 Electron microprobe (EPMA – WDX)

For more accurate compositional analysis, especially for Pb-Sb-S ternary films, Wavelength Dispersive X-ray analysis is required. This analysis was performed with an electron microprobe (JEOL – 8900) equipped with five wavelength dispersive spectrometers, which cover different wavelength ranges. A brief description of the electron microprobe technique will be given here, a more detailed descriptions can be found in reference [14].

Similarly to SEM, in an electron microprobe instrument, a primary beam of energetic electrons (~15 keV) is generated. These energetic electrons are able to eject

104

inner shell electrons from the atoms in the sample. Thus, when an outer-shell electron fills the vacant inner-shell (relaxation), a characteristic X-ray photon is generated with a well-defined wavelength or energy. The energy of the emitted photon is equal to the difference in binding energies of an electron in the outer shell and in the inner shell that is being filled in the transition. The transition names follow a precise nomenclature. First, the transitions are identified as K (n=1), L (n=2), M (n=3), etc...; these letters correspond to the vacant inner shells that will be occupied by outer-shell electrons. Second, the outer shell that gives up the electron to the vacant inner shell is labeled with a Greek letter: for instance, α or β, if the outer shell has a principal quantum number equal to n+1 or n+2, respectively; n is the principal quantum number of the inner shell. Lastly, a number terminates the name of a transition, since the transitions can occur from different electronic configurations (different angular momentum), which differ slightly in energy. For instance, $K_{\alpha 1}$ means the transition of an electron from the first orbital of the L shell to the K shell. Since the electronic structures and, therefore, the electron energies vary from element to element and are specific to a given element, the emitted X-rays can be used to identify which elements are present in the sample.

The X-rays emitted by the analyzed object are collected by the spectrometers. In the spectrometer, X-rays are collimated towards and diffracted by a known crystal. Using the Bragg conditions ($n\lambda = 2d \sin\theta$, *c.f.* Section 2.2.1), it is possible to position (θ) the crystal in order to direct (*i.e.* select) the X-ray wavelength (λ) of interest towards a detector, connected to a photomultiplier. Intensities of the x-rays produced from the sample to those produced from known standards should be compared. To do so, matrix

105

corrections must be made to account for effects related to the atomic number (Z), absorption (A) and fluorescence (F) of the elements in the sample; this is commonly know as the ZAF correction method. Atoms with high atomic number have more electrons and therefore are more likely to interact with the incident electron beam. Indeed, elements with high atomic numbers are more likely to elastically scatter (*i.e.* backscatter) the electrons, preventing them from ejecting electrons from the inner shells of the atoms. In addition, elements with high atomic numbers will stop incident electrons faster, yielding smaller penetration depths, *i.e.* smaller interaction volumes. Thus, the atomic number correction factor accounts for the relative backscattering and stopping power of the elements; this is especially important when the atomic numbers of the elements in the sample vary widely. Moreover, since x-rays are generated in the interaction volume, beneath the surface of the sample, some of the x-rays may be absorbed travelling through the sample to reach the detectors. The amount of absorption depends on the elements in the sample. This is the origin of the absorption correction factor. Lastly, if one element in the sample has a characteristic x-ray energy that is slightly higher than a characteristic x-ray energy of another element, the x-ray generated from the first element may be absorbed by the second element that then emits its own x-ray. This phenomenon is called secondary fluorescence and causes to over count the second element at the expense of the first one. The fluorescence correction factor accounts for this phenomenon.

106

Table 2.2. Transition, crystal and standard used for each element

Element	Crystal	λ range (Å)	Transition	λ (Å)	Standard
Si	TAP[1]	5.6 – 23.8	Kα	7.1254	Quartz
O	LDE1/H[2]	13.5 – 53.7	Kα	23.6200	Quartz
S	PET[3]	1.9 – 8.1	Kα	5.3721	Sphalerite ZnS
Sb	PET[3]	1.9 – 8.1	Lα	3.4394	Sb metal
Pb	PET/H[4]	1.9 – 8.1	Mα	5.2860	Pb metal
Si	TAP[1]	5.6 – 23.8	Kα	7.1254	Quartz
O	LDE1/H[2]	13.5 – 53.7	Kα	23.6200	Quartz
Zr	PET[3]	1.9 – 8.1	Lα	6.0705	Zr metal
Hf	TAP[1]	5.6 – 23.8	Mα	7.5390	Hf metal
Sb	PET/H[4]	1.9 – 8.1	Lα	3.4394	Sb metal

Notes: (1) TAP = Thallium Acid Phthalate

(2) LDE1/H = multiLayered Dispertion Element

(3) PET = Pentaerythritol

(4) PET/H = Pentaerythritol / high resolution

Each spectrometer was calibrated before each measurement series for the appropriate electronic transitions. The optimum usage of the five spectrometers (*i.e.* crystals) was determined according to the elements that were quantified and the transitions that can be observed for each. These conditions, as well as the standards used for calibration, are summarized in Table 2.2. An XYZ-stage allows for point selection and alignment. For each sample several points (10 to 15) were selected, for each point, the sample is optically aligned with the spectrometers. It is interesting to mention that the electron microprobe stage can accommodate four 2.5 cm × 4.4 cm samples, meaning that up to 12 to 15 of my thin film samples could be run at once. This was particularly appreciated, given our limited access to microprobe time. Once the points are preset, the

107

beam is set to 15 kV and 15 nA, with a spot size of 10 μm, in order to sample a large area of the sample. Count times were typically about 60 seconds. The system's software performs the ZAF corrections and provides the mass and atomic percentage of elements in the sample for each preset point. For each sample, compositions of the several preset points are statistically averaged, yielding the thin film sample composition. According to the standard deviation that were observed, the atomic percents reported have typically an error of ~1 - 2 at. % [14].

2.2.4   UV-VIS optical measurements

One of the main goals of this work is to identify candidate materials to be used as solar absorbers in thin film solar cells; therefore, it is important to determine the optical band gap of the thin films prepared. In semiconductors, the absorption of sunlight creates electron-hole pairs: a phenomenon essential to solar cell operation. The excitation of an electron from the valence band to the conduction band (fundamental absorption) may occur through four different types of transitions, as reviewed in Section 1.3.1. For each type of transition, a relationship between the absorption coefficient and the band gap energy may be derived [15]: (hvα) is proportional to (hv - E_g ± E_p)$^{1/n}$ where E_g is the band gap energy, E_p is the energy of the emitted (-) or absorbed (+) phonon (E_p=0 for direct transitions) energy and n = 2, $\frac{2}{3}$, $\frac{1}{2}$ or $\frac{1}{3}$ for direct allowed, direct forbidden, indirect allowed or indirect forbidden optical transitions, respectively [16]. Therefore, it is critical to know the absorption coefficient of the film as a function of the incident photon energy to extrapolate the value and nature of the bandgap. α, the

108

absorption coefficient of the films can be calculated from optical transmittance (T) and reflectance (R), using relation (2.5) that accounts for multiple internal reflections [15].

$$T = \frac{(1-R)^2 e^{-\alpha d}}{1 - R^2 e^{-2\alpha d}}$$ (2.5)

or, assuming that αd is large (which is practically the case for direct band gap semiconductors), the approximated relation:

$$T \approx (1-R)^2 e^{-\alpha d}$$ (2.6)

Equations (2.5) and (2.6) yield the exact and approximated equations for the absorption coefficient, α, respectively (demonstration shown in Appendix 4):

$$\alpha = \frac{1}{d} \ln \left[\frac{(1-R)^2 + \sqrt{(2RT)^2 + (1-R)^4}}{2T} \right]$$ (2.7)

$$\alpha \approx \frac{1}{d} \ln \left[\frac{(1-R)^2}{T} \right] = \frac{1}{d} \ln \left[\frac{1}{T_c} \right]$$ (2.8)

where T_c is the corrected transmittance that account for reflection losses at the air-film interface, it is calculated using the following equation:

$$T_c = T/(1-R)^2$$ (2.9)

To measure the wavelength (i.e. energy) dependence of the transmittance and the reflectance in the UV-Vis range a UV-Vis spectrophotometer is used. A spectrophotometer contains a light source, a sample holder, a diffraction grating or monochromator to separate the different wavelengths of light, and a detector. It can be either single beam or double beam. In a single beam instrument, all the light passes through the sample cell, whereas in a double-beam instrument, the light is split into two

109

beams before it reaches the sample: one beam is used as the reference or blank; the other beam passes through the sample: sample and reference beams are measured at the same time. Unless specified, the optical transmittance and near-normal reflectance spectra presented in this thesis were obtained using a PerkinElmer Lambda 35 UV-VIS spectrophotometer. This spectrophotometer is a double-beam spectrophotometer, it has a deuterium (UV) and a tungsten (VIS) source with automatic switch at λ = 326 nm. The monochromator is made of a holographic concave grating with 1053 lines per mm, allowing for wavelength resolution of $\pm$ 0.1 nm. Spectra were recorded between 190 nm and 1100 nm with 1 nm resolution at a scan speed of 240 nm/min. The beam width was set to 2 mm. For both transmittance and reflectance spectra, blanks were collected: for transmittance a clean film-free substrate was used, whereas for reflectance a 100 % reflective aluminum mirror was used. Percent transmittance and percent reflectance are then automatically recorded by the spectrometer according to the 100 % transmitive and 100 % reflective blanks. Near-normal reflectance spectra were collected using a variable-angle, relative specular reflectance accessory (PerkinElmer B0137314). Optical path for specular reflectance is shown in Figure 2.19.a. The angle closest to normal that could be set was 15° from normal and yielded satisfactory spectra in agreement with expectation for semiconductor thin-films. Specular reflectance was appropriate for most of the film presented in this thesis, since they featured smooth mirror-like surfaces.

Nevertheless, for rougher films that were obtained first, a near-normal (~5°) diffuse reflectance stage was used, this stage focuses the beam on the surface (rough) and collects the scattered beam with hemispherical mirror that focalizes the scattered

110

beam towards the detector. This stage was adapted to a Varian Cary 500 spectrometer (instrument retired in summer 2005). Optical path for diffuse reflectance is shown in Figure 2.19.b. Optical data (transmittance and reflectance) are then processed according to the equations (2.8) and usually (2.9), in order to obtain the wavelength dependence of the absorption coefficient, α. Then, curve $(h\nu\alpha)^n$ is graphed as a function of the energy $(h\nu)$ with $n = 2$, $\frac{2}{3}$, $\frac{1}{2}$ or $\frac{1}{3}$, the curve yielding the best straight line fit is then considered and allows for determination of the band gap type and energy (intercept with the x-axis [17]).

a)   **Specular reflectance**

b)   **Diffuse reflectance**

▨ Mirror
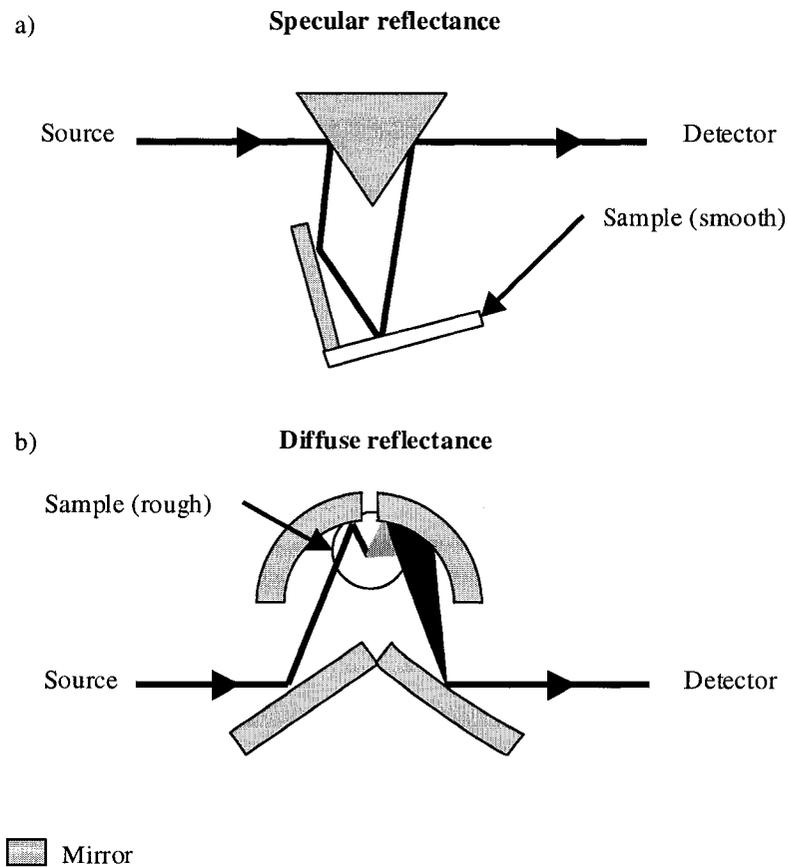
Figure 2.19. Optical paths for a) specular and b) diffuse reflectance.

2.3   References

[1]   M. Ohring, The Materials Science of Thin Films, Academic Press, San Diego, CA, 1992.

[2]   D.M. Mattox, Handbook of Physical Vapor Deposition (PVD) Processing: Film Formation, Adhesion, Surface Preparation and Contamination Control, Noyes Publications, Westwood, NJ, 1998.

[3]   S. Rossnagel, Handbook of Thin-Film Deposition Processes and Techniques - Principles, Methods, Equipment and Applications, Noyes Publications / William Andrew Publishing, Norwich, NY, 2002.

[4]   K. Wasa, M. Kitabatake, H. Adachi, Thin Film Materials Technology - Sputtering of Compound Materials, William Andrew Inc., Norwich, NY, 2004.

[5]   J.E. Mahan, A. Vantomme, Phys. Rev. B 61 (2000) 8516.

[6]   M. Ohring, The Materials Science of Thin Films - Deposition and Structure, Academic Press, San Diego, CA, 2002.

[7]   J.E. Mahan, Physical Vapor Deposition of Thin Films, Wiley, New York, NY, 2000.

[8]   M.T. Weller, Inorganic Materials Chemistry, Oxford University Press, Oxford, UK, 1994.

[9]   M.F. Toney, in: R.C. Brundle, C.A.Jr. Evans, S. Wilson, L.E. Fitzpatrick (Eds.), Encyclopedia of Materials Characterization, Butterworth-Heinemann, Stoneham, MA, 1992.

[10]   B.D. Cullity, S.R. Stock, Elements of X-Ray Diffraction, Prentice-Hall Inc., Upper Saddle River, NJ, 2001.

[11]   G.H. Stout, L. Jensen, H., X-Ray Structure Determination - A Practical Guide, John Wiley and Sons, Toronto, 1989.

[12]   Bruker AXS, General Area Detector Diffraction System (GADDS) - Version 4.0: User's Manual, Bruker AXS Inc., Madison, WI, 1999.

[13]   J.B. Bindell, in: R.C. Brundle, C.A.Jr. Evans, S. Wilson, L.E. Fitzpatrick (Eds.), Encyclopedia of Materials Characterization, Butterworth-Heinemann, Stoneham, MA, 1992.

[14]   D.E. Newbury, in: R.C. Brundle, C.A.Jr. Evans, S. Wilson, L.E. Fitzpatrick (Eds.), Encyclopedia of Materials Characterization, Butterworth-Heinemann, Stoneham, MA, 1992.

[15]   J.I. Pankove, Optical Processes in Semiconductors, Prentice-Hall Inc., Englewood Cliffs, NJ, 1971.

[16]   R.A. Smith, Semiconductors - 2nd Edition, Cambridge University Press, Cambridge, NY, 1978.

[17]   R.H. Bube, Electrons in Solids - An Introductory Survey, Academic Press Inc., San Diego, CA, 1981.

Chapter 3:   Film Deposition Rate Determination and Calibration

3.1   Introduction

To prepare compound thin films, it is important to know the amount of material (thickness, mass and/or moles) that is deposited according to the different deposition parameters. To calibrate the deposition rate (sputtering) or to determine the film thickness monitor tooling factor (evaporation), two techniques have been employed:

- mass measurement of the as-deposited film,

- and small angle X-ray diffraction.

A third technique, namely the determination of the Sb:Pb stoichiometric ratio by WDX, has been used in the case of co-sputtered films.

In this Chapter, one will first find a description of the basics of small angle X-ray diffraction and experimental details on the instrumentation that is required. Then, results regarding the calibration of the film thickness monitor for the evaporation of zirconium and hafnium will be given. The deposition rate calibration of sputtered antimony and lead will then be detailed. The determination of co-sputtered films Sb:Pb stoichiometric ratio by WDX is then explained. Lastly, the deposition rate calibration of sputtered Sb_2S_3 will be described. The results presented in this Chapter were used to determine the deposition parameters of the films presented in Chapters 4, 5 and 6 and in Appendices 1 and 2.

114

3.2 Small Angle X-ray diffraction

a) Basics of small angle x-ray diffraction: reflectometry

Small angle X-ray diffraction experiments are particularly useful to determine the overall thickness of a thin film or even the repeat thickness in films made of regularly stacked layers of different materials (multilayered structures) [1]. Thus, this thickness characterization method is useful for calibration of the deposition rate (sputtering) and for determination of the film thickness monitor tooling factor (evaporation). Small angle x-ray diffraction experiments are also called x-ray reflectometry or reflectivity, with the θ-2θ geometry. Low angle X-ray diffraction can non-destructively provide determination of the film thickness. The density and smoothness of the film may also be determined using simulation software to obtain the best match between calculated theoretical diffraction patterns and the experimental data. In the case of multilayered structures, interfacial roughness and interdiffusion may also be determined via simulation [2]. θ is usually varied from $0°$ to $1.5°$ or $4°$, depending on the intensity of the x-ray source and how rapidly the signal decays. Depending on the instrument resolution and the intensity of the X-ray source, thicknesses on the order of 1 nm to 1 μm may be measured.

Considering the simpler case of a single layered film deposited on a semi-infinite substrate (*e.g.* thick (> 5 μm) glass), an example of small angle diffraction pattern obtained for an ~70 nm thick antimony film on glass is shown in Figure 3.1.

115

m	2θ (°)	m	2θ (°)
3	0.74	15	2.03
4	0.81	16	2.16
5	0.90	17	2.28
6	1.00	18	2.40
7	1.09	19	2.53
8	1.21	20	2.65
9	1.32	21	2.77
10	1.44	22	2.90
11	1.55	23	3.02
12	1.67	24	3.14
13	1.79	25	3.27
14	1.91	26	3.40
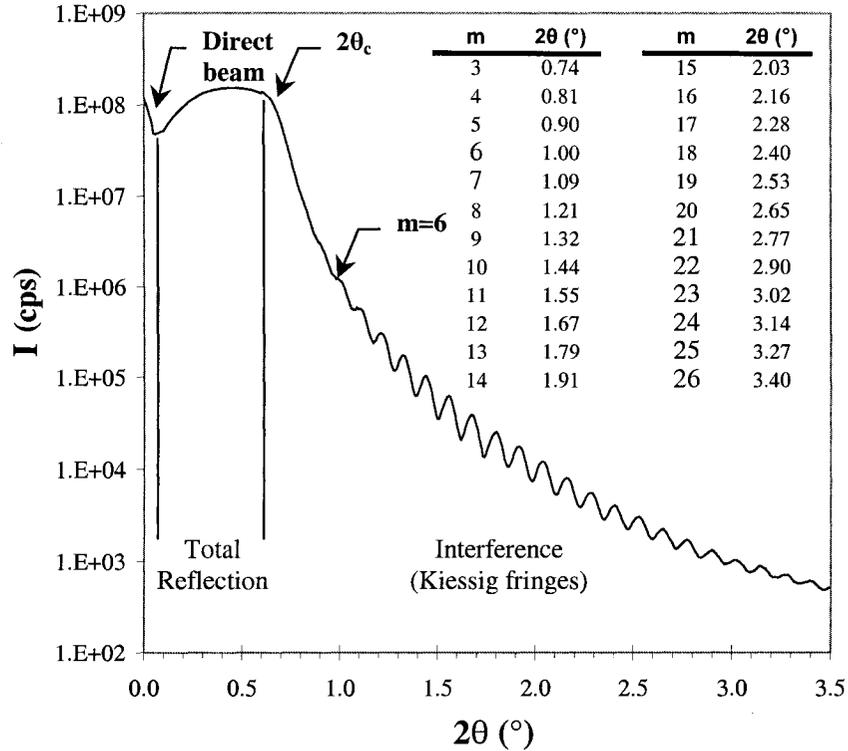
Figure 3.1. X-ray reflectometry pattern for a 690 Å thick antimony film; peak orders (m) and positions are also shown (inset). θ_c is the critical angle, after which the incident beam start to penetrate into the film.

The pattern shown in Figure 3.1 has a certain number of features that will be explained below. From 0° to 0.05°, the intensity of the signal is quite high, as the direct beam travels over the top of the sample and directly into the detector (protected by a Cu-foil absorber, see Section 3.2.b). As θ increases, the intensity drops rapidly, because the direct beam no longer impinges upon the detector. In addition, all the x-rays are reflected off the film surface because no x-rays penetrate the film below the critical angle. The intensity of the reflected beam increases as sin θ, as more of the incident beam impinges upon the sample as θ increases. Therefore, below the critical angle at 2θ~0.65°, these two competing phenomena (direct beam and reflection of the incident beam) create a minimum at 2θ~0.05°. At 2θ~0.65°, the intensity starts to drop. Indeed, at

116

this critical angle the incident beam starts to penetrate into the sample. The pattern then clearly shows that interference fringes are superimposed on the exponential intensity decay. The interference fringes, also named Kiessig fringes after H. Kiessig who first described them in a 1931 film thickness determination using x-ray reflectivity, originate from constructive interference between the reflected waves at the air-film and film-substrate interfaces, a situation similar to what was described earlier with the atomic planes in Bragg conditions.

The differences are essentially the distance scale (*i.e.* the angles involved) and more importantly the refraction phenomena occurring when the x-ray waves enter and leave the film. Thus, a corrected Bragg's law takes the refraction into account [2]:

$$m\lambda = 2d \sin\theta \left(1 - \frac{\delta}{\sin^2\theta}\right) \tag{3.1}$$

Here λ, d and θ are the wavelength of the x-ray beam, the film thickness and the angle between the incident beam and the film surface, respectively. Moreover, m is the order of the fringe peak, *i.e.* the integral number of wavelengths contained in the optical path difference. δ is related to the refraction index, n, of the film by:

$$n = 1 - \delta \tag{3.2}$$

δ is also related, in a first approximation, to the electronic density ρ_e of the film by [2]:

$$\delta \approx \frac{\lambda^2 e^2}{2\pi m_e c^2} \rho_e \tag{3.3}$$

where e and m_e are the charge and mass of the electron, and c is the speed of light. Thus, once collected, data may be analyzed using the above formulas or using simulation software that fit a theoretical pattern with the actual data, yielding thickness, density,

117

and even roughness of the film. This will be described below. A final remark about the influence of surface waviness and roughness on the diffracted pattern is needed. Surface waviness causes broadening of the fringes, since the irradiated surface may be represented as several domains with slightly different thicknesses, yielding slightly different interference pattern. Therefore, it is essential to use as flat a substrate as possible and to limit the irradiated area to a few microns, large enough to obtain an intense enough signal, but small enough to minimize the influence of the waviness. Surface roughness (on the micron scale) causes a decrease in both the amplitude of the interference oscillations and the overall reflectivity (faster decay). This is due to an increase of diffuse reflection (scattering) at the expense of specular reflection (interference) of the x-ray beam and to the introduction of variations in the phase of reflected wavefronts. Therefore, to be useful, x-ray reflectometry requires films of very good morphology, with limited waviness and roughness.

Now considering the case of regular, multilayered films deposited on a semi-infinite substrate. Examples of small angle diffraction patterns obtained for two different superlattices are shown in Figure 3.2. The patterns shown in Figure 3.2 were obtained from films made of ten identical layers, each containing 37 Å of Zr and 15 Å of Hf (Figures 3.2.a and 3.2.c) or 25Å of Zr and 15 Å of Hf (Figures 3.2.b and 3.2.d). The small angle x-ray diffraction patterns feature two different types of peaks. Similar to what has been observed with single-layered films, the closely-spaced peaks are interference fringes arising from constructive interference between the reflected waves at the air-film and film-substrate interfaces.

118

a)

I (cps)

1.E+06
1.E+05
1.E+04
1.E+03
1.E+02
1.E+01
1.E+00

0.5 1.0 1.5 2.0 2.5 3.0 3.5 4.0 4.5
2θ (°)

b)

I (cps)

1.E+06
1.E+05
1.E+04
1.E+03
1.E+02
1.E+01
1.E+00

0.5 1.0 1.5 2.0 2.5 3.0 3.5 4.0 4.5
2θ (°)

c)

Leptos Chart

Intensity

Fit ⎯⎯ ⎯⎯ Data

.8   1.2   1.6   2
axis

N	R	Material	Thickness	Roughness	DeltaT	DeltaR	Lateral	Hurst	Density T	Density B	Density N	Density Profile	Strain Profile
1	10	Hf	1.5468	0.04695	0.0000	0.0000	0.0000	0.0000	13.22420	13.22420	13.22420	No Gradient	No Gradient
2	10	Zr	3.6952	0.04695	0.0000	0.0000	0.0000	0.0000	6.23950	6.23950	6.50547	No Gradient	No Gradient
SUB	1	SiO2	0.0000	0.30100	0.0000	0.0000	0.0000	0.0000	2.65000	2.65000	2.65000	No Gradient	No Gradient

d)

Leptos Chart

Intensity

Fit ⎯⎯ ⎯⎯ Data

.8   1.2   1.6   2   2.4
axis

N	R	Material	Thickness	Roughness	DeltaT	DeltaR	Lateral	Hurst	Density T	Density B	Density N	Density Profile	Strain Profile
1	10	Hf	1.4814	0.27300	0.0000	0.0000	0.0000	0.0000	13.05560	13.05560	13.22420	No Gradient	No Gradient
2	10	Zr	2.5072	0.27300	0.0000	0.0000	0.0000	0.0000	6.46820	6.46820	6.50547	No Gradient	No Gradient
SUB	1	SiO2	0.0000	0.30100	0.0000	0.0000	0.0000	0.0000	2.65000	2.65000	2.65000	No Gradient	No Gradient

Figure 3.2. X-ray reflectometry patterns for multilayered films. X-ray pattern for 10 bilayers of a) 37 Å of Zr and 15 Å of Hf and b) of 25 Å of Zr and 15 Å of Hf. c) and d) show the actual data and the fit obtained with the simulation software LEPTOS for the x-ray patterns a) and b), respectively.

119

In addition, two and one Bragg diffraction peaks are observed in Figure 3.2.a and 3.2.b, respectively. These Bragg diffraction peaks, broader and more intense, result from the electron density modulation in the sample, in other words, from the repeat distance. Modeling and analysis of the diffraction intensities from superlattices to yield structural information have been the subject of numerous papers, a quite comprehensive approach maybe found in reference [3]. Because of the complexity of the diffracted patterns and the limited number of Bragg peaks arising from the modulated structure of the superlattice, collected data should be analyzed using simulation software that fit a theoretical pattern with the actual data. This will be briefly described below.

b)   Modifications of the instrument: K-knife and point detector.

In order to perform small angle x-ray diffraction experiment, a few modifications to the instrument should be made, as illustrated in Figure 3.3. A Knife Edge Collimator (KEC) may be adapted on the suction stage and the area detector should be replaced by a fixed slit assembly and a point detector (scintillation counter). These operations can be performed without disturbing the goniometer alignment, due to the versatility of the D8 goniometer. One should note that the knife edge collimator was not used for the results presented in Sections 3.3 and 3.4.1, the beam was only focussed with the 0.5 mm pinhole collimator. Several stages can be reliably mounted on the goniometer platform, the knife edge collimator can be easily screwed onto the suction stage, its main roles are to cut off the direct beam, and reduced the area probed by the X-ray. Area and point detectors may be interchanged by sliding them in and out of the movable goniometer arm. A locating pin and a locking system ("push-plug") ensure reproducible positioning,

so that only a quick automated optical repositioning of the arm and goniometer, as well as a corundum calibration (~3 minutes) are required when switching from the point detector configuration to the area detector configuration.
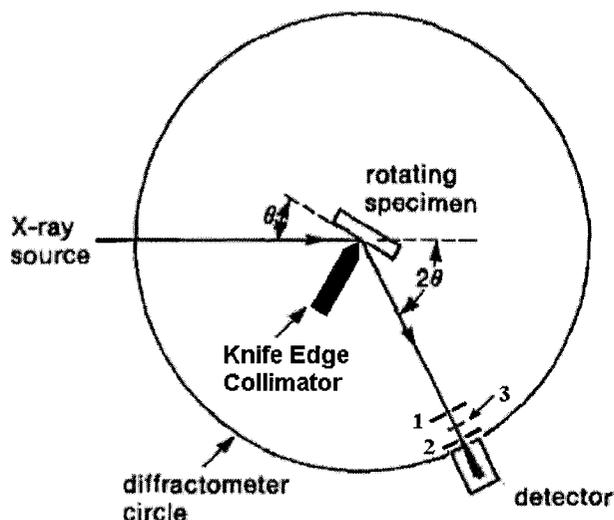
Figure 3.3. Schematic of the instrument configuration for x-ray reflectometry (adapted from reference [4]). *Note:* 1, 2 and 3 indicate the anti-scatter slit, the detector slit and the absorber, respectively; these elements constitute the fixed slit assembly.

Small angle X-ray diffraction is very sensitive to sample alignment; thus, critical alignment procedures must be carefully followed. When starting with the point detector/fixed slit assembly configuration, the detector should be aligned with the direct beam and the stage, zeroing the θ and 2θ scales and centering the anti-scatter slit with the direct primary beam. The procedure is well described in the user manual [5] and easily performed. The last step is to align the sample mounted on the reflectometry stage and set the knife edge collimator. Once again, this procedure is well described in the manual [6]. The principle is to have the film X-Y plane parallel to the incoming beam (Z-alignment, zeroing of θ scale, and χ tilting) and to set the knife edge collimator just above the film surface (~ 20 μm) to block some of the primary beam and therefore

121

reduce the diffraction volume. If no knife edge collimator is used, the incident x-ray beam illuminates a very large area of the sample at these very small angles, yielding poorer resolution of the diffracted beam and more destructive interference, due to sample irregularities (waviness, roughness) over large areas. Data collection may be started: a θ-2θ scan is performed according to the following parameters:

- from 0° to 0.6°: the θ increment equals 0.05°/step at a scan speed of 1 s/step,

- from 0.6° to 3°: the θ increment equals 0.008°/step at a scan speed of 6 s/step.

Limit angles, increment and scan speed values may have been slightly varied around the values stated above. Moreover, a Cu foil is usually placed before the detector for the lowest angles (< 1.6°) to absorb some of the diffracted signal and avoid detrimental saturation of the detector. Intensities for the lowest angles are then multiplied to compensate for the absorption.

For single layered films, small angle X-ray diffraction data could be treated either with Excel or with LEPTOS, a Bruker AXS, Inc. software package that simulates and fits theoretical X-ray reflectometry patterns to the actual data. As precise and more easily implemented, the method using Excel was preferred. The method is detailed below. The amplitudes of the reflected and transmitted waves can be calculated from the amplitude of the incident wave by the reflection and the transmission tensors, which takes into account the refraction phenomena [7]. These rather complex calculations and the small angle (θ < 2°) approximation of sin $\theta \sim \theta$ (in rad), yield the following equation for the interference maxima:

$$m\lambda \cong 2d \sqrt{\theta^2 - 2\delta} \tag{3.4}$$

122

Here λ, d, θ and m are the wavelength of the x-ray beam, the film thickness, the angle between the incident beam and the film surface and the order of the interference fringe, respectively. A simple rearrangement of equation (2.8) yields:

$$\theta^2 \cong \frac{\lambda^2}{4d^2}m^2 + 2\delta \tag{3.5}$$

Thus, a plot of the diffraction angle of the maxima (in rad) squared as a function of peak order squared yield a straight line; the slope and intercept with the y-axis of which allow calculation of the film thickness and δ, that is to say the film refractive index (see equation 3.2). The critical angle (in rad) that was described earlier may be calculated from the intercept with the y-axis (*i.e.* 2δ) [7] since:

$$\theta_c \cong \sqrt{2\delta} \tag{3.6}$$

Then, from equation (3.3) an estimate of the actual electron density of the film can be obtained. The electron density (ρ_e) may be related to the material mass density (ρ_m) for an elemental film:

$$\rho_m = \frac{\rho_e \, M}{N \, n_e} \tag{3.7}$$

where N, M and n_e are the Avogadro's number, the elemental molar mass and the number of electrons per atom, respectively. This estimation of the film density may then be compared to the theoretical material density. Deposition rate ($\mathring{A}.s^{-1}$) was determined from the thickness and the known deposition time at a given power. In addition, for convenience, a molar deposition rate ($mol.s^{-1}.cm^{-2}$) may also be calculated using the calculated density, the molar mass of the compound and an arbitrary area unit. Herein, 1 cm^2 was chosen as it relates well to the overall deposition area available (4.4 $\times$ 4.4 =

123

19.36 cm^2). The molar deposition rate (in mol.s^{-1}.cm^{-2}) may be calculated according to the equation (3.8).

$$R_{mol/sec/cm^2} = R_{\mathring{A}/sec} \frac{\rho_m}{M} \times 10^{-8} \tag{3.8}$$

where R's are the deposition rates in mol.s^{-1}.cm^{-2} and $\mathring{A}$.s^{-1}, ρ_m and M are the materials density (g.cm^{-3}) and molar mass (g.mol^{-1}), respectively. 10^{-8} is the conversion factor between $\mathring{A}$ and cm.

For the multilayered films, it is necessary to treat the small angle X-ray diffraction data with LEPTOS. Detailed scientific background and software operation for LEPTOS may be found in [7]. Collected data may be analyzed using this simulation software. A global optimization method based on Monte Carlo calculations, namely simulated annealing, is used to fit theoretical patterns to actual data, by randomly varying the following parameters: layer thickness, roughness, and density. Starting values and variation spans should be implemented for each parameter. These values are determined after a quick inspection of the diffracted pattern assuming Bragg's law without refraction. Basic fitting conditions have been used as described pages 1.1 to 1.7 of reference [7]. The fitting was also limited to the θ range where diffraction patterns were of good quality. Once the software reached a fit that matches the actual data with a certain tolerance, the fitting procedure is stopped and values for the thickness, roughness and density of the layers are obtained.

124

3.3   Deposition rate calibrations of hafnium and zirconium evaporation

In order to prepare the films presented in Appendix 2 with composition gradients of hafnium, zirconium and antimony, it was necessary to know quite precisely the deposition rates of these elements. As will be described in Appendix 2, hafnium and zirconium were deposited via e-beam evaporation. As mentioned in Chapter 2, because of variations in the deposition flux, the e-beam evaporation rates are monitored in real-time using a Film Thickness Monitor (FTM). The FTM measures the amount of material (mass and thickness) that is deposited; to equate the measured thickness on the FTM and the actual film thickness on the substrate a tooling factor has to be determined.

Zirconium and hafnium films were deposited on thin glass slides. To determine the tooling factor of the Film Thickness Monitor for these elements, two sets of films presenting ten repeat bi-layers of zirconium and hafnium were prepared. For one of the sets, the zirconium thickness was varied while the hafnium thickness was kept constant. For the other set, the hafnium thickness was varied while the zirconium thickness was kept constant. Small angle X-ray diffraction was used to measure the repeat thickness. A graph of the intended repeat thickness, *i.e.* the ones entered in the FTM using a tooling factor of 100 %, as a function of the actual repeat thickness measured by small angle X-ray diffraction will give the FTM tooling factor according to the following equation:

$$T_F (\%) = T_{Fi} \times \frac{d_{actual}}{d_{intended}} \tag{3.9}$$

125

Here T_F and T_{Fi} are the actual and the initial tooling factors in percent, respectively (with

T_{Fi} set to 100 %); where d_{actual} and $d_{intended}$ are the measured and the pre-set thicknesses,

respectively.
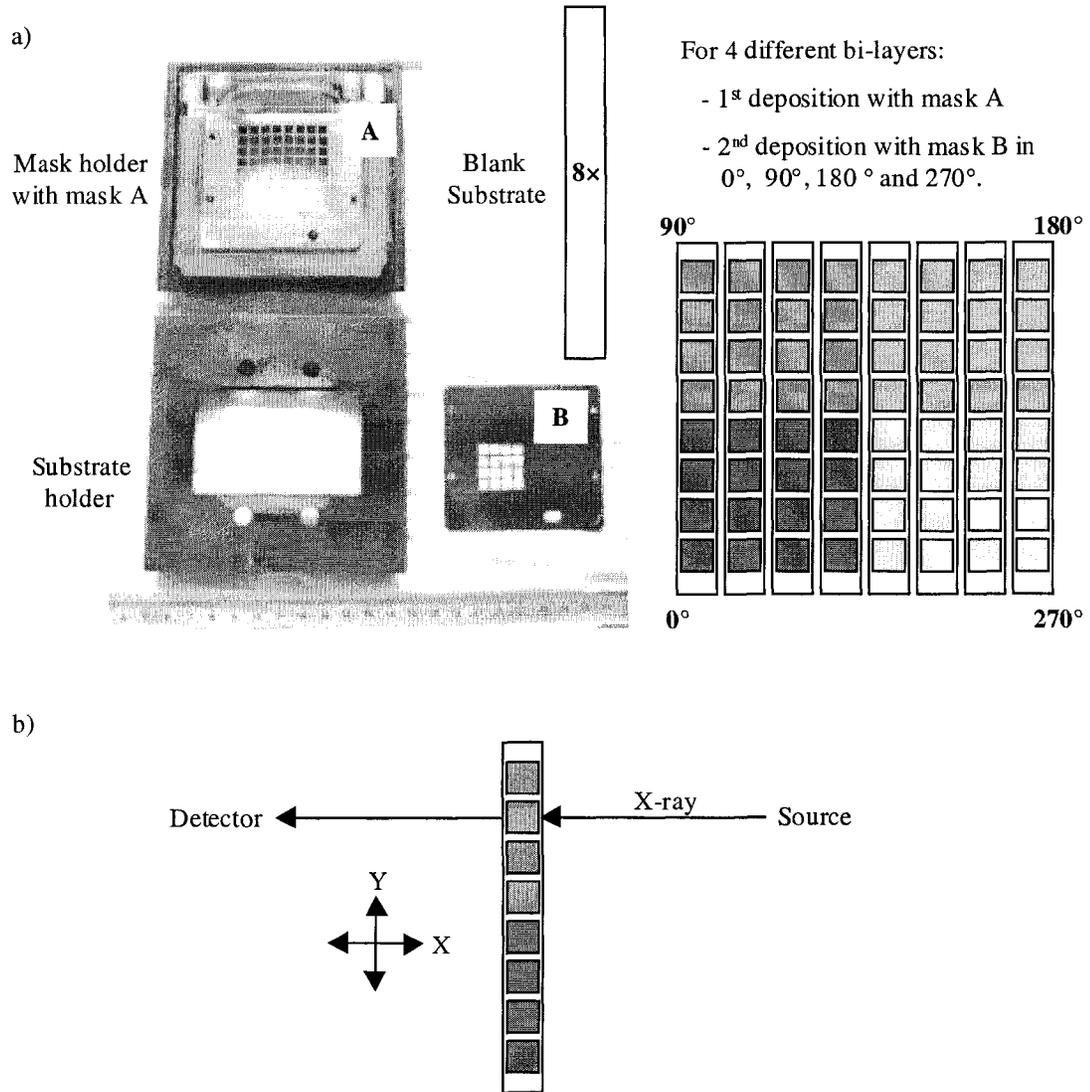
Figure 3.4. Schematic of the deposition strategy implemented for the calibration of the deposition of zirconium and hafnium: a) mask system used for deposition and b) schematic of the small angle X-ray data collection.

126

Films were prepared using the masking strategy described in Figure 3.4. The sequences to create the repeat units are described below.

- For the four films with a constant zirconium layer thickness, mask [A] was first used in the 0° position to deposit 20 Å of zirconium, mask [B] was then used in the 0°, 90°, 180° and 270° positions to deposit 10, 25, 40 and 55 Å of hafnium, respectively.

- For the four films with a constant hafnium layer thickness, mask [B] was first used in the 0°, 90°, 180° and 270° positions to deposit 55, 40, 25 and 10 Å of zirconium, respectively, mask [A] was then used in the 0° position to deposit 20 Å of hafnium.

These sequences were repeated ten times to yield two sets of four distinctive films, made of ten repeat layers (or bi-layers). The evaporation parameters during deposition of zirconium and hafnium are given in the Table 3.1.

Table 3.1. Parameters recorded during the evaporations of zirconium and hafnium

Element	Current (Amps)	Pressure (Torr)	FTM deposition rate (Å/s)
Zirconium	$0.185 - 0.270$	low 10^{-9} – low 10^{-8}	$0.4 \leftrightarrow 0.6$
Hafnium	$0.105 - 0.120$	low 10^{-9} – mid 10^{-9}	$0.4 \leftrightarrow 0.6$

Once deposited, small angle X-ray diffraction data were collected as shown in the schematic in Figure 3.4.b. Experimental patterns are fitted to simulated patterns with the software LEPTOS, as described earlier and in Figure 3.2. The film thicknesses there determined are presented in Tables 3.2 and 3.3. The actual repeat thickness is plotted as a function of the intended thickness, the slope of this straight line × 100 yields the tooling factor for the element whose thickness was varied. The linear regression and

127

tooling factor for hafnium and zirconium are given in Tables 3.2 and 3.3, respectively.

The FTM tooling factors are 96 % and 82 % for hafnium and zirconium, respectively.

Table 3.2. Results of the FTM calibration for the hafnium evaporation

d_{set} for Zr (Å)	d_{set} for Hf (Å)	intended d_{repeat} (Å)	actual d_{repeat} (Å)
20	10	30	30
20	25	45	44
20	40	60	57
20	55	75	74

Linear regression:

a =	0.96		**Tooling factor = 96 %**
b =	1.174	Å	
r^2 =	0.996		

Table 3.3. Results of the FTM calibration for the zirconium evaporation

d_{set} for Zr (Å)	d_{set} for Hf (Å)	intended d_{repeat} (Å)	actual d_{repeat} (Å)
55	20	75	65
45	20	60	52
60	20	45	40
75	20	30	28

Linear regression:

a =	0.82		**Tooling factor = 82 %**
b =	3.25	Å	
r^2 =	0.99996		

128

3.4   Deposition rate calibration of antimony DC-sputtering

3.4.1   Deposition rate calibration of Sb sputtered at 25 W and 1.33 Pa

Herein, results obtained for antimony films sputtered at 25 W and 1.33 ($\pm$0.03) Pa ($\sim$10 mTorr) are given. These conditions were used for the deposition of the Hf-Zr-Sb films presented in Appendix 2. Four different thicknesses of an antimony film were deposited on a glass substrate (microscope slide) using the quaternary mask [A]. The sputtering ran for 8, 6, 4 and 2 minutes with mask [A] at, respectively, 0°, 90°, 180° and 270° with respect to the substrate, as shown in Figure 3.5.a. While sputtering, the mask/sample assembly was rotated at 10 s/rev. Experimental low X-ray diffraction patterns were collected as shown in Figure 3.5.b, and were then fitted to simulated patterns using the LEPTOS software as described earlier (see Figure 3.2). Results and the equation of the calibration curve are given in the Table 3.4. The molar deposition rate (in mol/s/cm^2) is calculated assuming the bulk density of antimony (*i.e.* 6.69 g/cm^3) using equation (3.8).

Table 3.4. Results for small angle X-ray diffraction calibration of sputtered antimony

Power (W)	Time (s)	Thickness (Å)	Rate (Å/s)	Rate (mol/s/cm^2)
25	480	341	0.71	3.9E-10
25	360	262	0.73	4.0E-10
25	240	158	0.66	3.6E-10
25	120	84	0.70	3.9E-10

Linear regressions:

a (dep. Rate) =	0.70	Å/s		a =	3.8E-10	mol/s/cm^2
b =	0			b =	0	mol/cm^2
r^2 =	0.995			r^2 =	0.995	

129
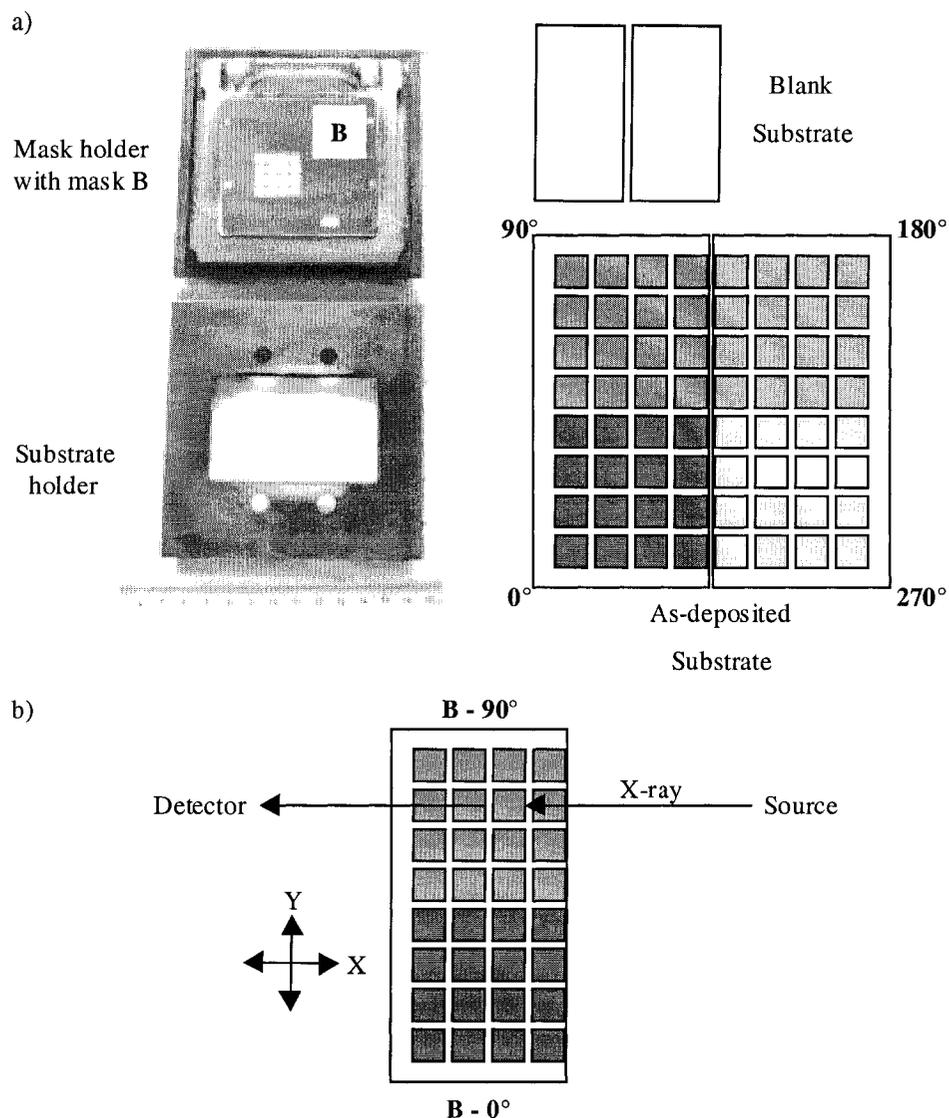
Figure 3.5. Schematic of the deposition strategy implemented for the calibration of the sputter deposition rate of antimony: a) mask system used for deposition and b) schematic of the small angle X-ray data collection.

3.4.2 Deposition rate calibration of Sb sputtered at 0.667 Pa

Herein, results obtained for antimony film sputtered with a plasma pressure of 0.667 (±0.03) Pa (~5 mTorr) are given. These conditions were used for the deposition of the antimony metal precursor films presented in Chapter 4 and for the lead/antimony precursor films presented in Chapter 5. Mass measurement and the X-ray reflectometry

130

using the knife edge collimator were used to determine the deposition rate of DC sputtered antimony.

a)   *Mass calibration*

Films were deposited via DC sputtering of an antimony target. Films need to be sufficiently thick to have a mass able to be weighed accurately; moreover, in order to increase the significance of the mass variation between of the substrate before and after the deposition, thin cover glass slides were used as substrates. The substrate was weighed before and after deposition with a balance accurate to $\pm$ 1 $\times$ 10^{-2} mg. A calibration curve was obtained using three depositions of thick antimony films. Experimental parameters are given in Table 3.5.

Table 3.5. Experimental parameter for mass calibration of the antimony deposition

Dep.[1]	Power (W)	Time (s)	Film mass (mg)	Thickness[2] (Å)	Rate (Å/s)
#1	15	6000	5.68	4385	0.7
#2	30	3000	5.93	4579	1.5
#3	45	1980	6.00	4633	2.3

Note: (1) Dep. = Deposition.
          (2) Calculated thickness

The thickness of the film was calculated assuming the bulk density of antimony for the as-deposited film, *i.e.* 6.69 g.cm^{-3}, and a surface area of 4.4 $\times$ 4.4 cm^2, corresponding to the dimensions of the mask that was used for these depositions. The calibration curve is shown in Figure 3.6. As one notices, the deposition rate (Å/s) varies linearly with power over the 10 – 50 W range. This calibration was essentially

131

performed for comparison with the more elaborate X-ray reflectometry calibration method, presented hereafter.
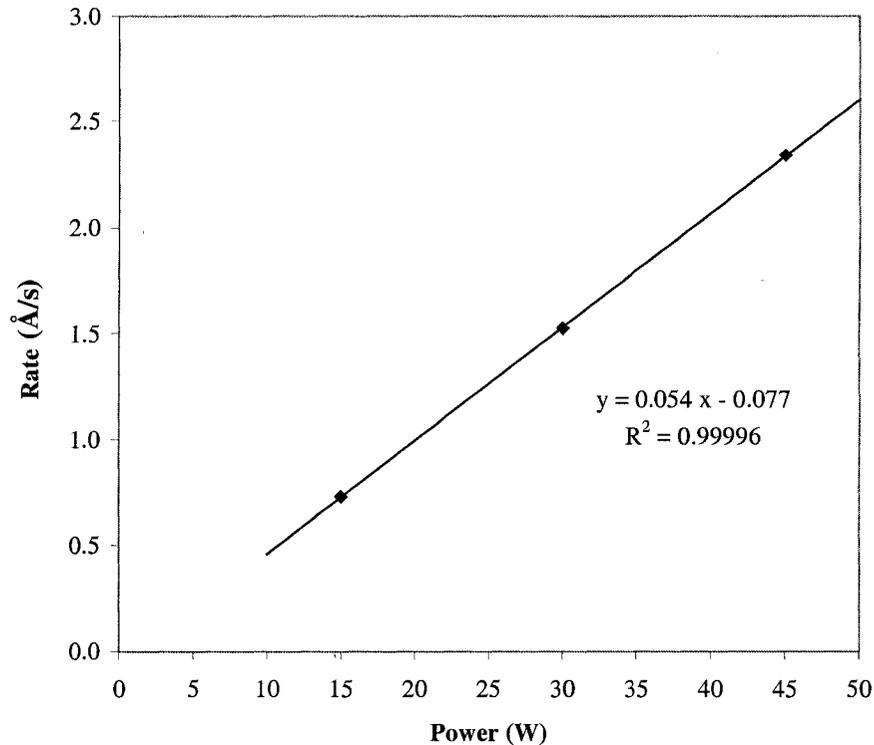
Figure 3.6. Calibration curve for DC sputtering of antimony obtained from the mass of the deposited films.

b)   *X-ray reflectometry calibration*

The calibration via X-ray reflectometry of the DC sputtering of antimony has been the occasion to further implement this technique and reach better resolution using the knife edge collimator, as mentioned in Section 2.1. Calibration series that yielded the highest quality patterns and, therefore, the most reliable film thickness determinations are presented hereafter. Despite requiring a long development period with our equipment and a quite strict requirement for film smoothness, X-ray reflectometry may be an efficient and accurate calibration method, as:

- it only requires $2 \times 2 \ cm^2$ films of ~500Å thick, that may be rapidly and combinatorially deposited (~10 minutes each),

- once in place, the x-ray reflectometry set-up is easily and rapidly implemented on the D8 diffractometer,

- it is a direct determination of the film thickness (no density assumption),

- it may give an estimate of the actual film density,

- and lastly, it is an accurate method (approximately ±5 Å with our set-up).
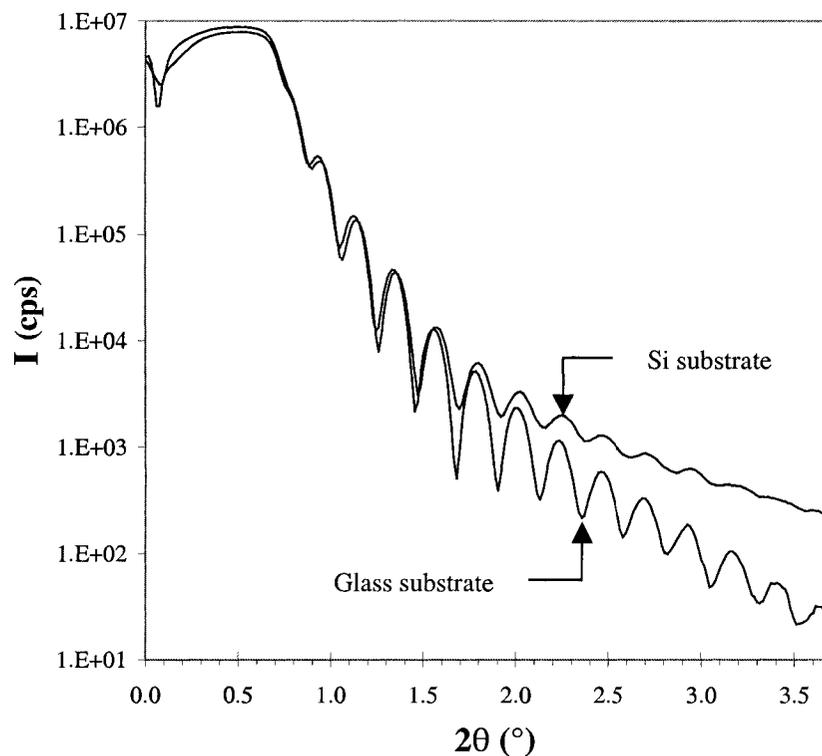
Figure 3.7. X-ray reflectometry patterns for a ~370 Å thick evaporated antimony film on a glass substrate and on Si wafer substrate.

First, the influence of the substrate was determined using both Si wafers and glass slides as substrates. Figure 3.7 shows the x-ray reflectometry patterns for an

133

evaporated 370 Å thick antimony film. As one notices, despite a slightly faster decay, glass substrates yielded x-ray interference peaks with higher resolution compared to the Si wafer substrates. This result may be explained by a slightly greater roughness (sub-micron scale) of the film deposited on glass and by a slightly more important waviness (> 5 μm range) of the Si wafer, as detailed in Section 3.2. Considering these results, glass substrates were judged appropriate for film thickness determination via x-ray reflectometry of ~ 500 Å thick antimony films, as it yielded enough interference peaks to accurately determine the film thickness using Excel calculations, detailed in Section 3.2. A plot of θ^2 as a function of m^2, where m and θ are the peak order and the angle of the maxima (in radians), allows for determination of the film thickness, the film critical angle, the film electron density and the film density according to equations (3.5), (3.6), (3.3) and (3.7). As it is convenient, a molar deposition rate ($mol.s^{-1}.cm^{-2}$) was also calculated using the deposition rate (Å/s), the calculated density, the molar mass of antimony (121.76 $g.mol^{-1}$), according to equation (3.8).

Several sets of DC-sputtered antimony films were characterized via X-ray reflectometry. Each set was composed of different films deposited on glass substrates (microscopy slides) at constant energy (*i.e.* power times deposition time), to ensure that all of the films in a set had roughly the same thickness. For the first set the DC source power was varied from 25 W to 200 W in increments of 25 W, the deposition time was varied from 750 to 94 seconds in order to maintain an energy of ~19 kJ and film thicknesses of ~1000 Å. This set could be deposited quite efficiently using a quadrant mask in four different positions (0°, 90°, 180° and 270°) with respect to the substrate,

134

with each film having an area of 2×2 cm^2. This strategy is illustrated in Figure 3.8. Thus, the eight different films of the set were deposited on two substrates, requiring that the system be loaded and pumped down only once. Similar information obtained from mass calibration would have required eight substrates (loading the system twice) and thicker films, in other words longer depositions.
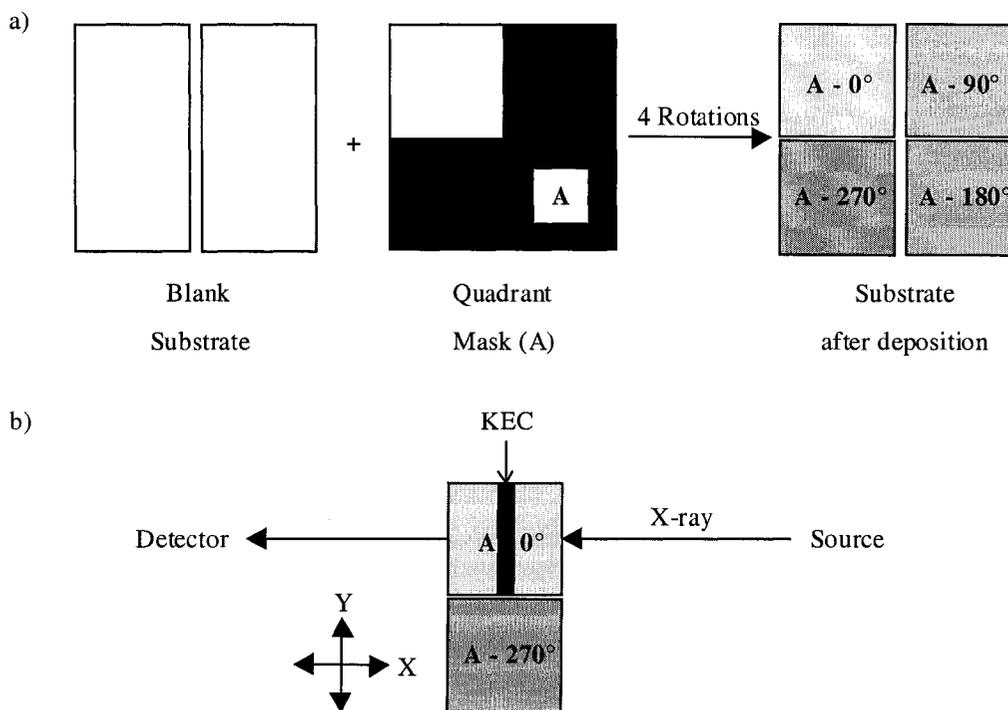
Figure 3.8. Illustration of the "quadrant" combinatorial strategy. a) Four successive mask rotations and depositions yield four different films. The 5×5 cm^2 substrate has been split into two parts prior to deposition; this is necessary because of the very small angles required for X-ray reflectometry so that the "wide" beam only impinges on the desired quadrant, moreover there is no X-axis translation possible between the stage and the KEC (Knife Edge Collimator). b) Schematics of the X-ray reflectometry set-up: each piece of the substrate is mounted successively, an X-ray pattern is collected from the first quadrant, then the stage is moved with the Y-drive and an X-ray pattern is collected from the second quadrant.

Results are presented in Figure 3.9 and in Table 3.6. The calibration curve is shown in Figure 3.12. As shown in Figure 3.9, this set yielded interference fringes that are quite close together; and it is quite difficult to determine accurately the first few

135

interference peak positions, given our experimental set-up accuracy. This issue may be address by decreasing the film thickness and, therefore, spreading out the interference fringes.

a)

b)
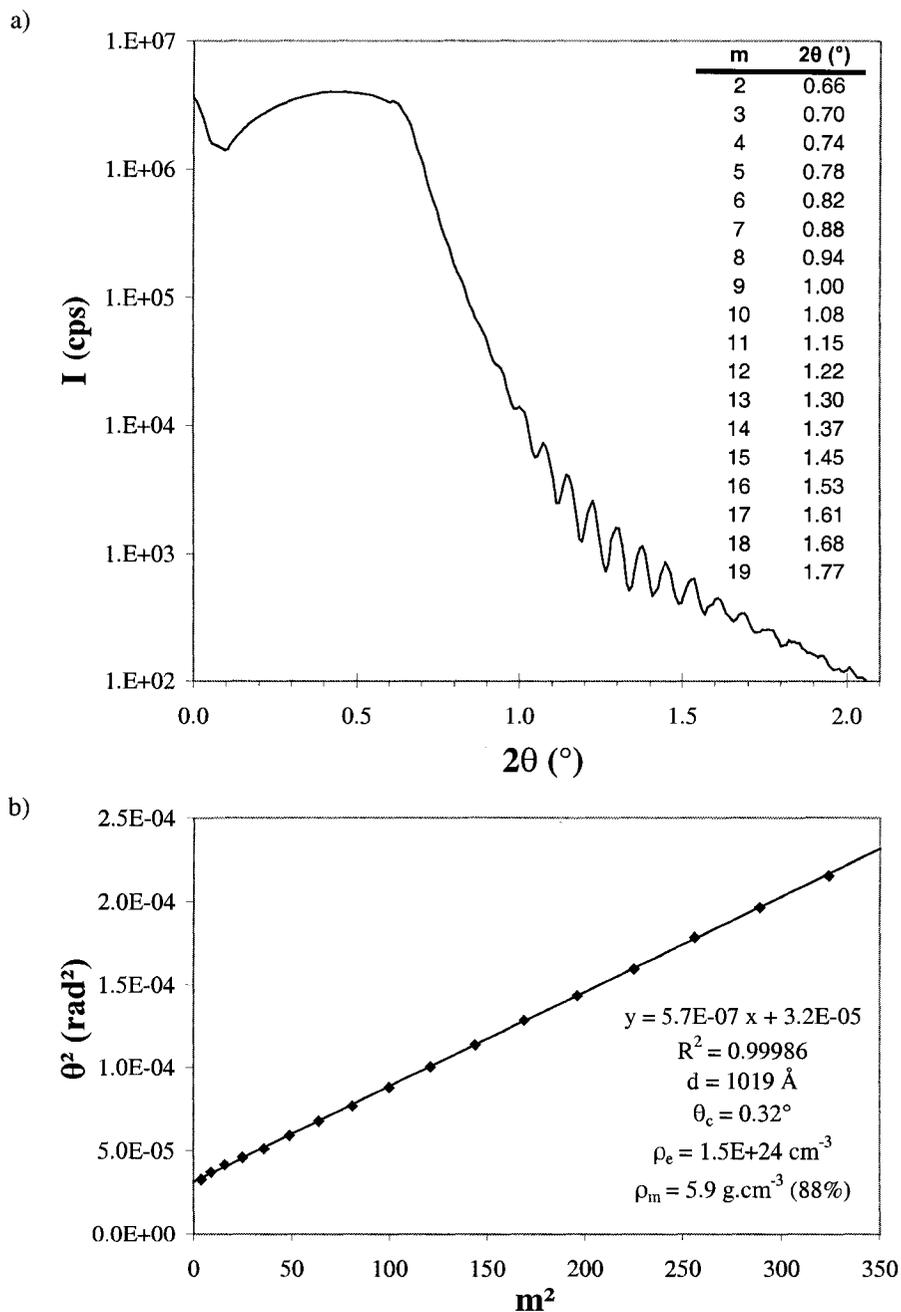
Figure 3.9. X-ray reflectometry of a 1019 Å thick Sb film: a) X-ray pattern and peak orders (m) and positions, b) data analysis from θ^2 vs. m^2, thickness (d), critical angle (θ_c), electronic density (ρ_e), film density (ρ_m) determination. The film density is also indicated as a percentage of the bulk density of Sb.

136

Table 3.6. Results of x-ray reflectometry calibration of the antimony deposition (set #1)

Power (W)	Time (s)	Thickness (Å)	Rate (Å/s)	Density (g/cm³)	Rate (mol/s/cm²)
25	750	1019	1.4	5.87	6.5E-10
50	375	1037	2.8	5.90	1.3E-09
75	250	1029	4.1	5.92	2.0E-09
100	188	1036	5.5	6.13	2.8E-09
125	150	1043	7.0	5.94	3.4E-09
150	125	1071	8.6	6.45	4.5E-09
175	107	1057	9.9	6.12	5.0E-09
200	94	1071	11.4	6.38	6.0E-09

Linear regressions:

a =	0.0574	Å/s/W	a =	3.03E-11	mol/s/W/cm²
b =	-0.1434	Å/s	b =	-2.01E-10	mol/s/cm²
r^2 =	0.9996		r^2 =	0.9949	

Another set of films with smaller thickness was deposited to spread out the interference fringes and ease their position determination. For this set, the DC source power was set to 60, 90 110 and 140 W, while the deposition time was set to 183, 122, 100 and 78 seconds, in order to maintain an energy of ~11 kJ and film thicknesses of ~600 Å. The quadrant mask deposition strategy was also used for this set. Results are presented in Figure 3.10 and in Table 3.7. The calibration curve is shown in Figure 3.12. As shown in Figure 3.10, this set yielded interference fringes that are more spread apart and it is therefore easier to determine the position of the first few order fringes; fewer fringes are accessible in the useable 2θ range, however, their is a sufficient number to plot θ^2 vs. m^2 and obtain a satisfactory linear regression.

137

a)

m	2θ (°)
2	0.69
3	0.78
4	0.89
5	1.00
6	1.11
7	1.24
8	1.37
9	1.50
10	1.63
11	1.77
12	1.91
13	2.04
14	2.19
15	2.32
16	2.47
17	2.63

b)

$y = 1.7E\text{-}06\ x + 3.4E\text{-}05$

$R^2 = 0.99990$

$d = 594\ \text{Å}$

$\theta_c = 0.33°$

$\rho_e = 1.6E\text{+}24\ \text{cm}^{-3}$

$\rho_m = 6.3\ \text{g.cm}^{-3}\ (94\%)$
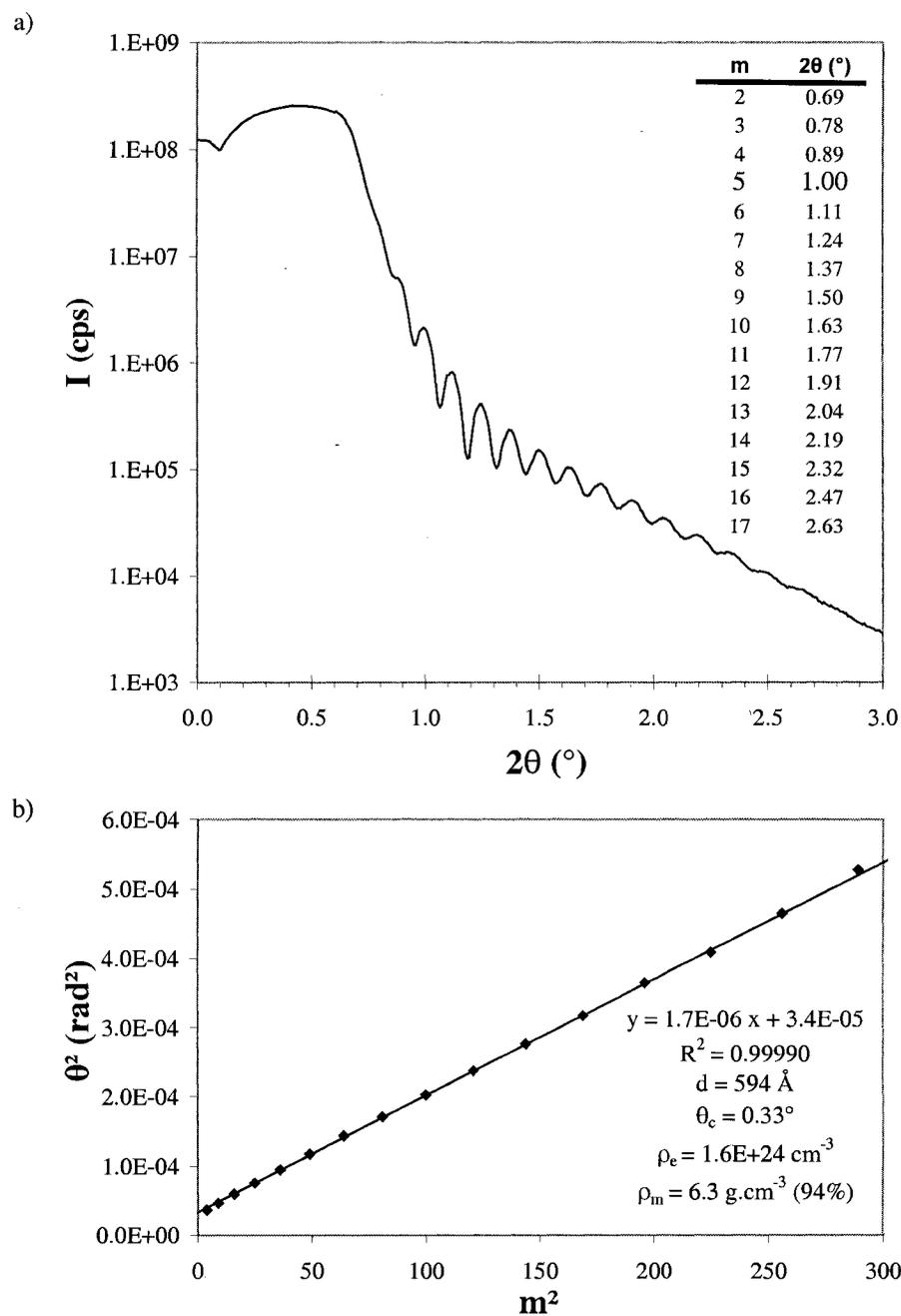
Figure 3.10. X-ray reflectometry of a 594 Å thick Sb film: a) X-ray pattern and peak orders (m) and positions, b) data analysis from θ^2 vs. m^2, thickness (d), critical angle (θ_c), electronic density (ρ_e), film density (ρ_m) determination. The film density is also indicated as a percentage of the bulk density of Sb.

138

Table 3.7. Results of x-ray reflectometry calibration of the antimony deposition (set #2)

Power (W)	Time (s)	Thickness (Å)	Rate (Å/s)	Density (g/cm^3)	Rate (mol/s/cm^2)
60	183	586	3.2	5.67	1.5E-09
90	122	594	4.9	6.31	2.5E-09
110	100	600	6.0	5.90	2.9E-09
140	78	585	7.5	6.24	3.8E-09

Linear regressions:

a =	0.0539	Å/s/W	a =	2.88E-11	mol/s/W
b =	0.0054	Å/s	b =	-1.92E-10	mol/s
r^2 =	0.9990		r^2 =	0.9923	

Lastly, a set of films has been deposited to show how the film quality influences the quality of the x-ray reflectometry data. For this set, the DC source power was set to 60, 90, 110 and 140 W, while the deposition time was set to 250, 167, 136 and 107 seconds, in order to maintain an energy of ~15 kJ and film thicknesses of ~700 Å. The quadrant mask deposition strategy was also used for this set. More importantly, the substrate deposition temperature was set at 125 °C for this set. The warm substrate temperature improved the film crystallinity and more importantly the film morphology, in particular the film roughness was decreased. Results are presented in Figure 3.11 and in Table 3.8. The calibration curves is shown in Figure 3.12. As shown in Figure 3.11, this set yielded interference fringes that are exploitable on the full 2θ range, as their resolution is greatly improved. Also, it should be noticed that the film thickness has been slightly increased compared to the set just previously presented in order to increase the number of interference fringes, while still less than the number in the first set presented.

This allowed for adequate spread of the fringes at the lowest angles and more accurate data processing.

a)

m	2θ (°)		m	2θ (°)
3	0.74		15	2.03
4	0.81		16	2.16
5	0.90		17	2.28
6	1.00		18	2.40
7	1.09		19	2.53
8	1.21		20	2.65
9	1.32		21	2.77
10	1.44		22	2.90
11	1.55		23	3.02
12	1.67		24	3.14
13	1.79		25	3.27
14	1.91		26	3.40

b)

$y = 1.3E\text{-}06\ x + 3.2E\text{-}05$
$R^2 = 0.99998$
$d = 688\ \text{Å}$
$\theta_c = 0.32°$
$\rho_e = 1.5E\text{+}24\ \text{cm}^{-3}$
$\rho_m = 5.9\ \text{g.cm}^{-3}\ (88\%)$
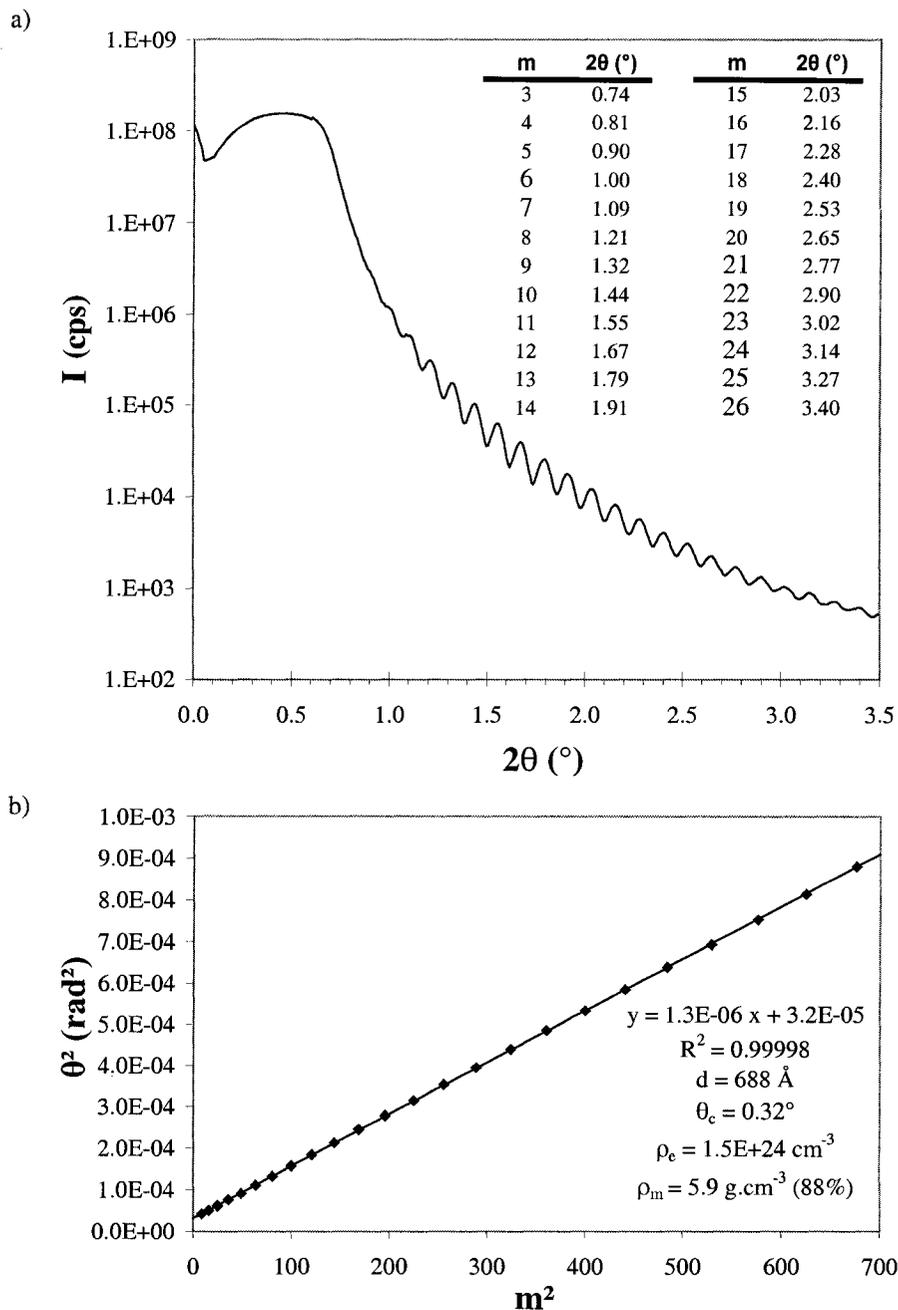
Figure 3.11. X-ray reflectometry of a 688 Å thick Sb film: a) X-ray pattern and peak orders (m) and positions, b) data analysis from θ^2 vs. m^2, thickness (d), critical angle (θ_c), electronic density (ρ_e), film density (ρ_m) determination. The film density is also indicated in a percentage of the bulk density of Sb.

140

Table 3.8. Results of x-ray reflectometry calibration of the antimony deposition (set #3)

Power (W)	Time (s)	Thickness (Å)	Rate (Å/s)	Density (g/cm³)	Rate (mol/s/cm²)
60	250	688	2.8	5.87	1.3E-09
90	167	709	4.2	5.97	2.1E-09
110	136	720	5.3	6.06	2.6E-09
140	107	720	6.7	6.11	3.4E-09

Linear regressions:

a =	0.0499	Å/s/W	a =	2.57E-11	mol/s/W
b =	-0.2340	Å/s	b =	-2.19E-10	mol/s
r^2 =	0.9997		r^2 =	0.9996	

c)   *Discussions*

As shown in Figure 3.12, mass calibration and x-ray reflectometry calibration experimental set #1 and #2 yielded similar results, especially at low power values (<120 W) for both the deposition rate (Å/s) and the molar rate (mol.s^{-1}.cm^{-2}). One may notice, that in the case of the molar rate, mass calibration yielded a slightly higher rate, this is due to the fact that the bulk density was used to calculate the molar rate; the density of the as-deposited film being always less than the bulk density. This is shown by the density values estimated from the X-ray reflectometry data: densities vary from 5.67 g.cm^{-3} to 6.45 g.cm^{-3}, which correspond to 85 % and 96 % dense films compared to the bulk density of 6.69 g.cm^{-3}. Lastly, both for the deposition rate in Å/s and the molar rate, the x-ray reflectometry calibration for set #3 (warm substrate) yielded slower depositions rates. Some re-evaporation of the film may occur after deposition, due to the higher substrate temperature. This necessarily decreases the net deposition rates.

141

a)

b)
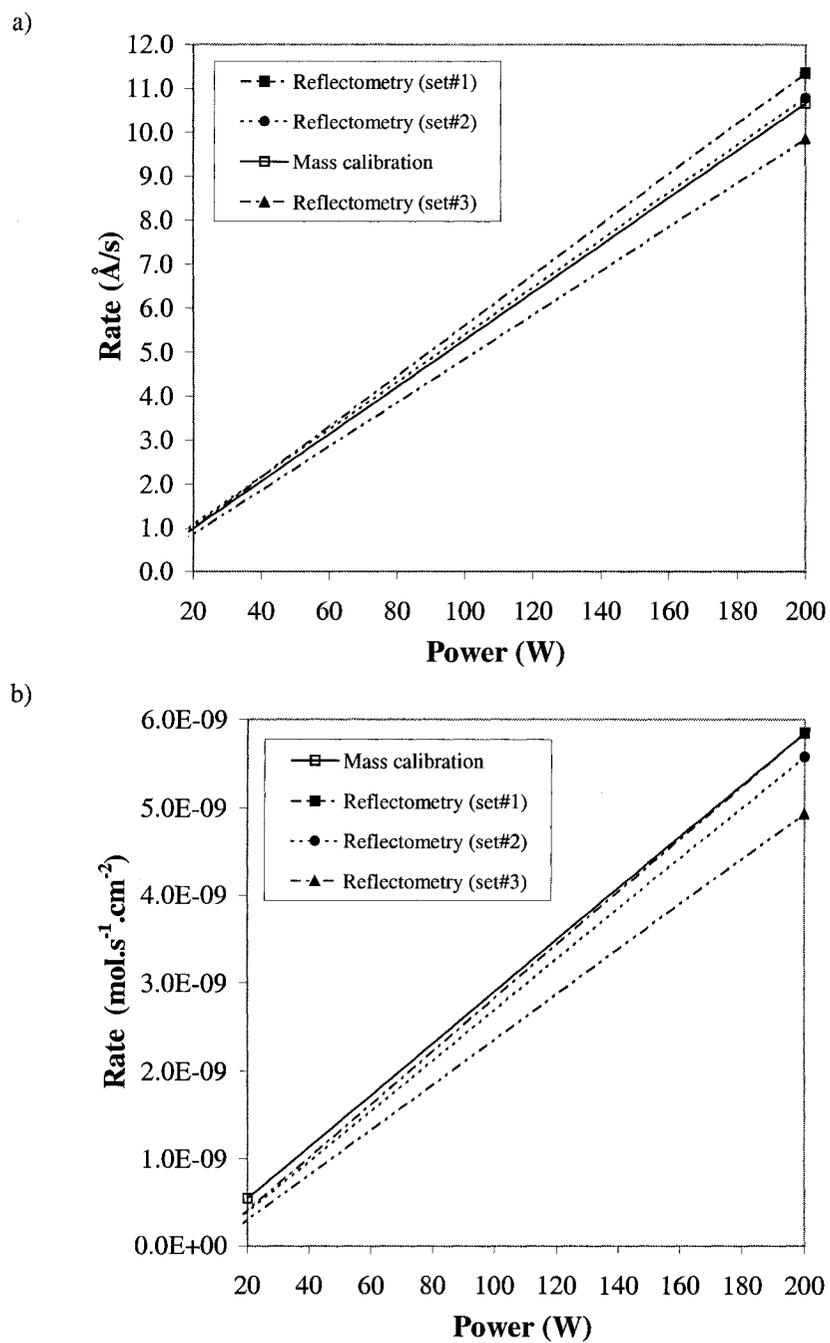
Figure 3.12. Calibration curves for the various mass and x-ray reflectometry calibration sets, a) in Å/s and b) in $mol.s^{-1}.cm^{-2}$.

142

3.5   Deposition rate calibration of lead DC-sputtering by mass
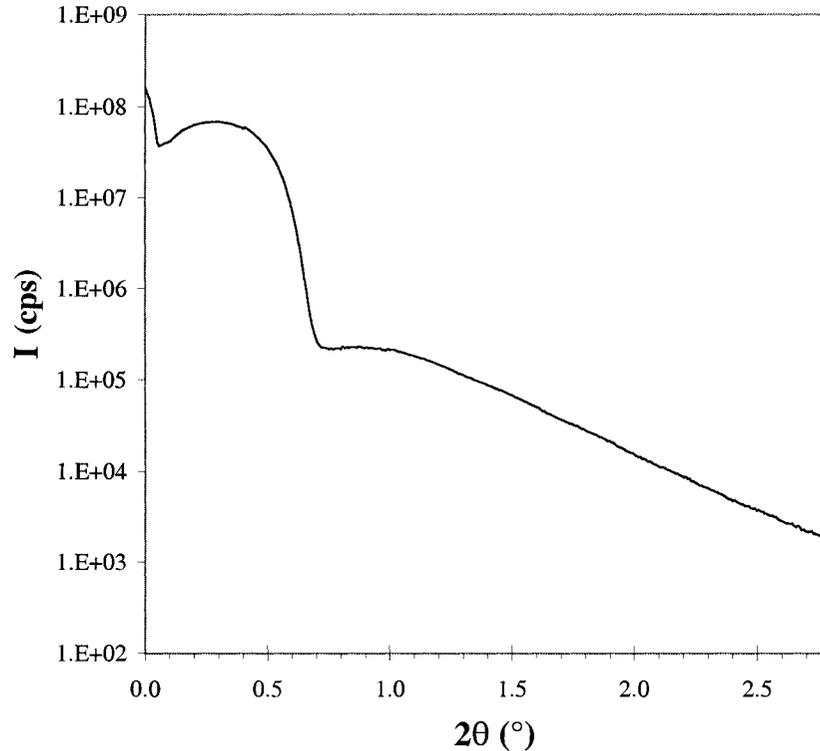
Figure 3.13. X-ray reflectometry pattern a 450 Å thick lead film.

Similar to antimony deposition, lead deposition was calibrated from measurements of the mass of the deposited film. Probably due to the overly pronounced roughness of as-deposited sputtered lead films, no X-ray reflectometry data could be obtained for these films. Indeed, as shown in Figure 3.13, the reflectometry x-ray pattern does not feature any interference fringes and the signal decay is very fast after the critical angle, as mentioned in the introduction. Thus, it was necessary to use another calibration method. A calibration curve was obtained from four depositions of thick lead films (deposition #1, #2, #3 and #4 in Table 3.9). Films were deposited via DC sputtering. Films need to be sufficiently thick to have a mass able to be weighed accurately; moreover, in order to increase the significance of the mass variation between

143

of the substrate before and after the deposition, thin cover glass slides were used as substrates. The substrate was weighed before and after deposition with a balance accurate to $\pm 1 \times 10^{-2}$ mg. Experimental parameters are given in Table 3.9.

Table 3.9. Experimental parameter for mass calibration of lead deposition

Dep.[1]	Power (W)	Time (s)	Substrate mass (mg)	S.+F.[2] mass (mg)	Film mass (mg)	Thck.[3] (Å)	Rate (Å/s)	Rate (mol/s /cm^2)
#1	50	1800	962.40	977.06	14.66	6678	3.7	2.03E-09
#2	75	1500	958.97	978.21	19.24	8764	5.8	3.20E-09
#3	100	1200	966.15	986.69	20.54	9356	7.8	4.27E-09
#4	100	900	971.95	987.81	15.86	7224	8.0	4.39E-09
#5	10	5400	955.64	962.64	7.00	3185	0.6	3.23E-10

Notes: (1) Dep. = Deposition.

(2) S.+F. Mass = Mass of the substrate and film after deposition.

(3) Thck. = Calculated thickness.

The thickness of the film was calculated assuming the bulk density of lead for the as-deposited film, i.e. 11.34 g.cm^{-3}, and a surface area of 4.4×4.4 cm^2, corresponding to the dimensions of the mask that was used for these depositions. For convenience, a molar deposition rate (mol.s^{-1}.cm^{-2}) was also calculated using the mass of the film, the deposition area (19.36 cm^2) and the molar mass of lead (207.2 g.mol^{-1}), according to the following equation:

$$R_{mol/sec/cm^2} = \frac{m}{M} \times \frac{1}{A\,t} \qquad (3.10)$$

Here, m, M, t and A are the mass of the film (g), the molar mass of lead (g.mol^{-1}), the deposition time (s) and the deposition area (cm^2). The calibration curves are shown in Figure 3.14.

144
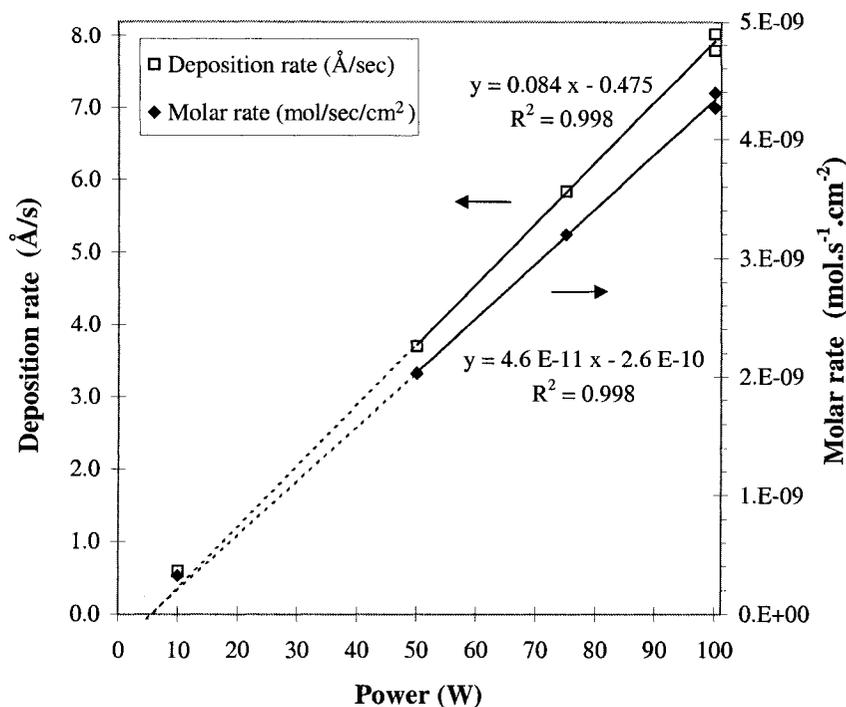
Figure 3.14. Calibration curve for DC sputtering of lead obtained from the mass of the deposited films.

As 10 W turned out to be the power of choice for the sequential sputtering of Sb_2S_3 and Pb (see Chapter 6), a complementary calibration has been performed at 10 W, shown in Figure 3.14. As one notices, the deposition rate (Å/s) varies quite linearly with the power over the 10 – 100 W range; given the high sputtering yield of lead, this is a convenient working range, as it yields deposition rates smaller than 10 Å/s.

3.6   Determination of co-sputtered films Sb:Pb stoichiometric ratio by WDX

Another method of calibrating deposition rates involved elemental composition analysis (WDX) of a set of co-sputtered films. Co-sputtering means that both the lead and antimony targets are powered at the same time. The powers applied to each target are different and set at the appropriate levels so that the target Sb:Pb stoichiometric ratio

145

is achieved. This target ratio was calculated from the molar rate calibrations that were

obtained from the mass measurement and x-ray reflectometry experiments, described in

Sections 3.4.2 and 3.5 for antimony and lead, respectively. Table 3.10 gathers the

experimental parameters for several co-sputtered films; the power applied to the lead

target has been kept at 40 W while the one applied to the antimony target has been

varied in order to have the Sb:Pb stoichiometric ratio vary from ~1 to 2.6. Lead molar

deposition rates were determined according to the molar rate calibration curve shown in

Figure 3.12, while antimony molar deposition rates were determined according to the X-

ray reflectometry experiment shown in Table 3.7 and the calibration curve shown in

Figure 3.10 (set#2).

Table 3.10. Results for WDX calibration of co-sputtered films (set #1)

Power - Pb (W)	Power - Sb (W)	Time (min)	Pb mol. Rate (mol/s/cm^2)	Sb mol. Rate (mol/s/cm^2)	Expected Sb:Pb	WDX Sb:Pb
40	60	30	1.58E-09	1.54E-09	0.98	0.76
40	90	13	1.58E-09	2.40E-09	1.52	1.27
40	104	20	1.58E-09	2.81E-09	1.78	1.70
40	110	13	1.58E-09	2.98E-09	1.89	1.62
40	130	11	1.58E-09	3.56E-09	2.26	2.16
40	150	11	1.58E-09	4.13E-09	2.62	2.45
40	151	15	1.58E-09	4.16E-09	2.64	2.98

A plot of the expected Sb:Pb stoichiometric ratio from calibration of individual

deposition rates to the actual Sb:Pb stoichiometric ratio obtained for Pb-Sb co-sputtered

films is shown in Figure 3.15.a.

146

a)

b)
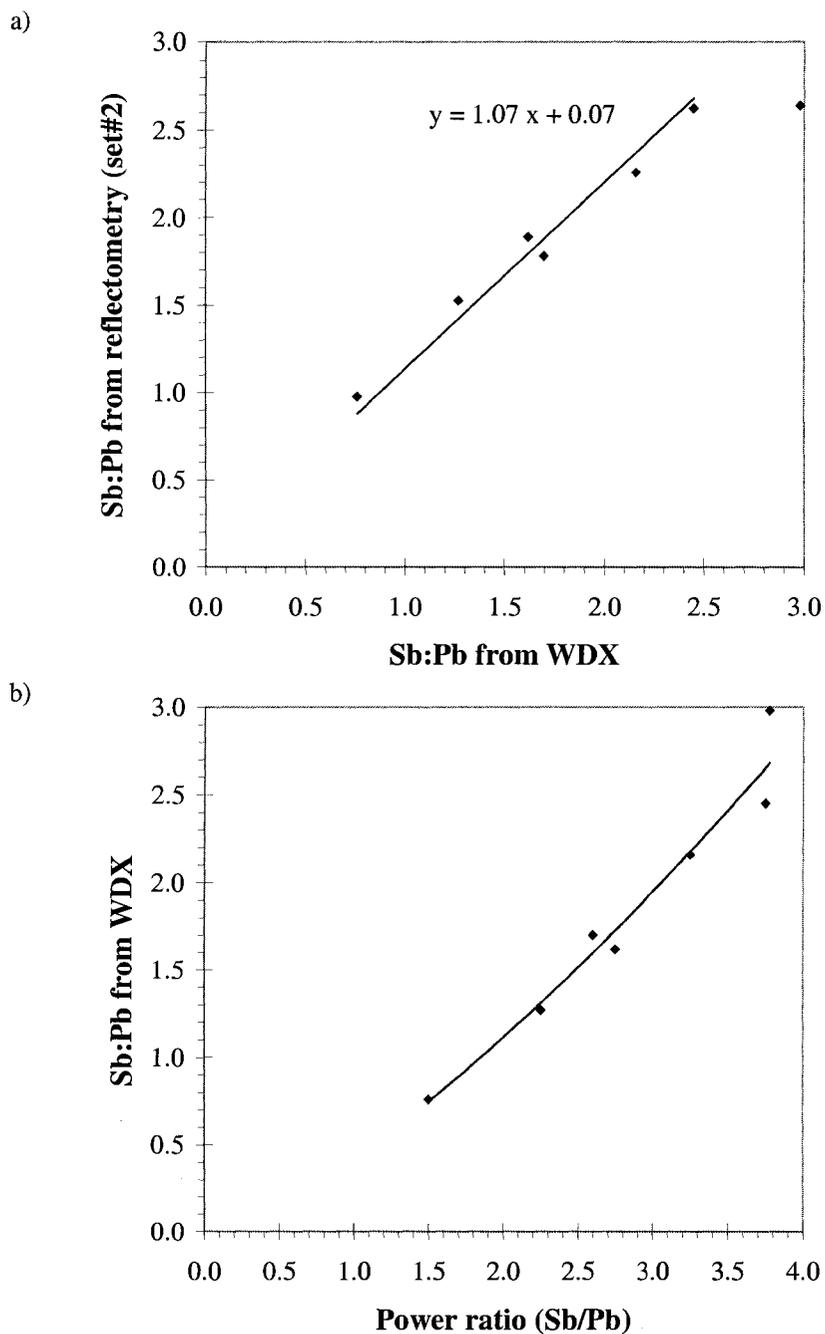
Figure 3.15. a) Plot of the expected Sb:Pb stoichiometric ratio from individual calibrations as a function of the actual Sb:Pb stoichiometric ratio obtained for Pb-Sb co-sputtered films. b) Plot of the actual Sb:Pb stoichiometric ratio obtained for Pb-Sb co-sputtered films as a function of the ratio between the powers applied to the antimony and lead targets. The power applied to the lead target was set to 40W.

As one can notice in all cases but one (for an applied power on the antimony target larger than 150 W), the composition of the film is antimony poor compared to

147

what was expected from the individual calibrations obtained for lead and antimony. This antimony deficiency may result from scattering due to the heavier lead atoms in the plasma or preferred re-evaporation of the antimony atoms after deposition (during deposition the substrate warms up). Lastly, Figure 3.15.b shows a plot of the Sb:Pb stoichiometric ratio of the co-sputtered film as a function of the ratio between the powers applied to the antimony and the lead targets; the power applied to the lead target being set to 40 W. As one sees, the uncertainty is too large to precisely define a calibration curve, however a trend-line may serve as a guide for the eye when planning future depositions, the power applied on the lead target being kept at 40 W.

Table 3.11. Results for WDX calibration of co-sputtered films (set #2)

Power - Pb (W)	Power - Sb (W)	Time (min)	Pb mol. Rate (mol/s/cm^2)	Sb mol. Rate (mol/s/cm^2)	Expected Sb:Pb	WDX Sb:Pb
10	16	118	3.23E-10	2.70E-10	0.83	0.65
10	19	110	3.23E-10	3.56E-10	1.10	0.87
10	29	80	3.23E-10	6.45E-10	2.00	1.62
10	36	67	3.23E-10	8.46E-10	2.62	2.20
10	56	45	3.23E-10	1.42E-09	4.41	4.04
10	150	20	3.23E-10	4.13E-09	12.80	11.02

Another set of co-sputtered films has been deposited with the power applied on the lead target maintained at 10 W, while the power applied to the antimony target was varied in order to have the Sb:Pb stoichiometric ratio varying from ~1 to 2.6. Results are gathered in Table 3.11. The molar deposition rate of lead at 10 W was determined according to Table 3.9. Antimony molar deposition rates were determined according to the X-ray reflectometry experiment shown in Table 3.7 and the calibration curve shown in Figure 3.12 (set#2).

148

a)

$y = 1.15 x + 0.054$
$R^2 = 0.9989$

b)
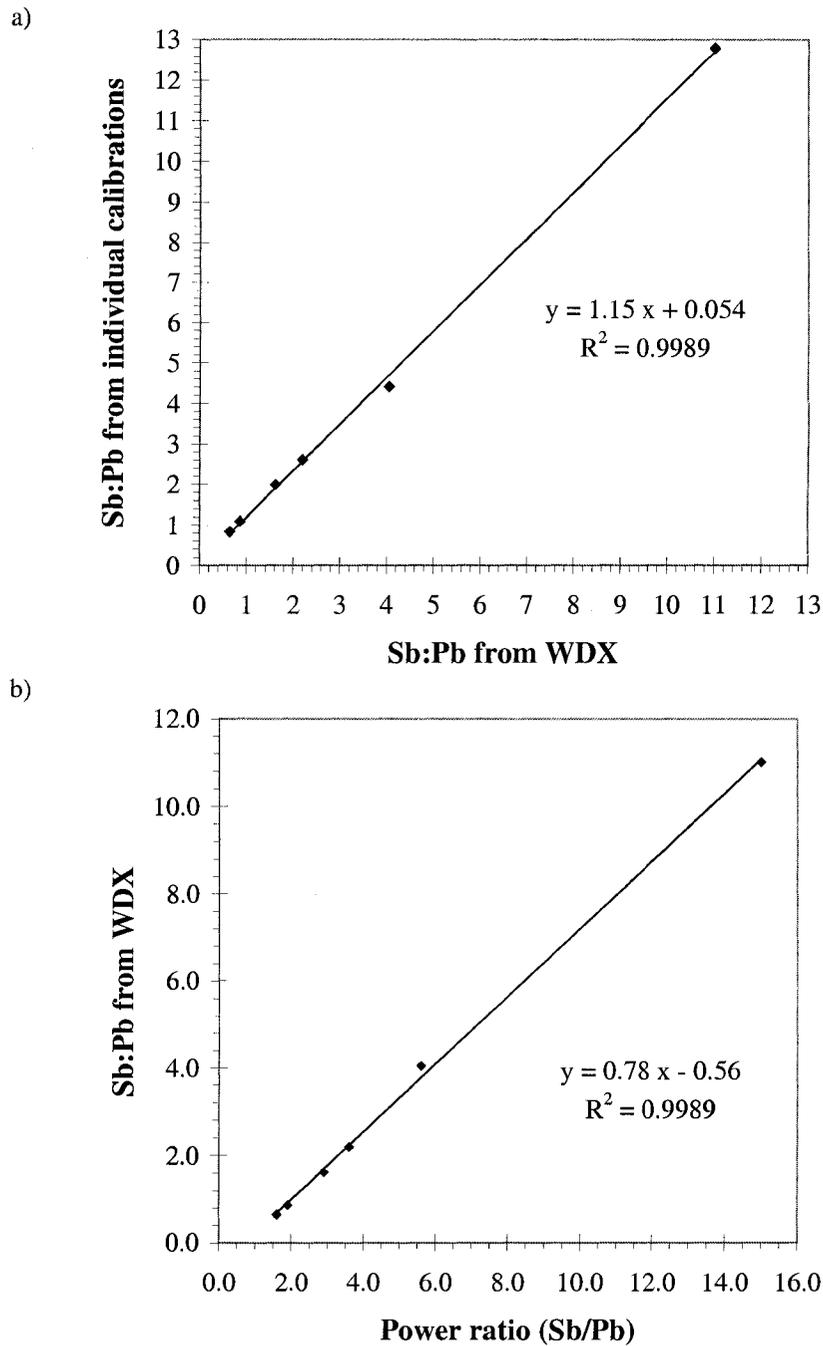
Figure 3.16. a) Plot of the expected Sb:Pb stoichiometric ratio from individual calibrations as a function of the actual Sb:Pb stoichiometric ratio obtained for Pb-Sb co-sputtered films. b) Plot of the actual Sb:Pb stoichiometric ratio obtained for Pb-Sb co-sputtered films as a function of the ratio between the powers applied to the antimony and lead targets. The power applied to the lead target was set to 10W.

A plot of the expected Sb:Pb stoichiometric ratio from individual deposition rate calibration *vs.* the actual Sb:Pb stoichiometric ratio obtained for Pb-Sb co-sputtered

149

films is shown in Figure 3.16.a. this plot confirmed what has been previously noted, *i.e.* the composition of the film is antimony poor compared to what was expected from the individual calibrations obtained for lead and antimony. Lastly and more interestingly, Figure 3.16.b shows a plot of the Sb:Pb stoichiometric ratio of the co-sputtered film as a function of the ratio between the powers applied to the antimony and the lead targets; the power applied on the lead target being set and maintained to 10 W. Contrary to the previous case with a power value of 40 W applied on the lead target, a calibration curve may be defined: thus, for a target Sb:Pb stoichiometric ratio, a corresponding power ratio (ratio between the powers applied to the antimony and the lead targets) may be calculated, the power applied to the lead target being set to 10 W, the power applied to the antimony target is easily calculated.

All the results obtained throughout the Sections 3.4.2, 3.5 and 3.6 are consistent, regardless of the technique employed. The determination of the various deposition rates was achieved with sufficient accuracy to prepare the layered and co-sputtered metallic Pb-Sb precursor films that will be presented in Chapter 5, especially as the stoichiometry is significantly affected upon annealing.

3.7 Deposition rate calibration of a-Sb$_2$S$_3$ RF-sputtering

The calibration via X-ray reflectometry of the RF sputtering of the Sb$_2$S$_3$ target is presented herein. Several films were sputtered on glass substrates (microscopy slides) at RF powers of 40 W, 55 W and 70W, the deposition time ranges from ~6 to 20 minutes,

150

for film thicknesses ranging from 185 to 860 Å. Results are presented in Table 3.12 and in Figures 3.17 and 3.18. The calibration curve is shown in Figure 3.19.

m	2θ (°)	m	2θ (°)
2	0.67	10	2.16
3	0.79	11	2.36
4	0.96	12	2.57
5	1.15	13	2.79
6	1.34	14	3.00
7	1.54	15	3.21
8	1.74	16	3.43
9	1.95	17	3.65
		18	3.85

$y = 3.4\ E\text{-}06x + 1.3\ E\text{-}05$
$R^2 = 0.9999$
$d = 415\ Å$
$\theta_c = 0.20°$
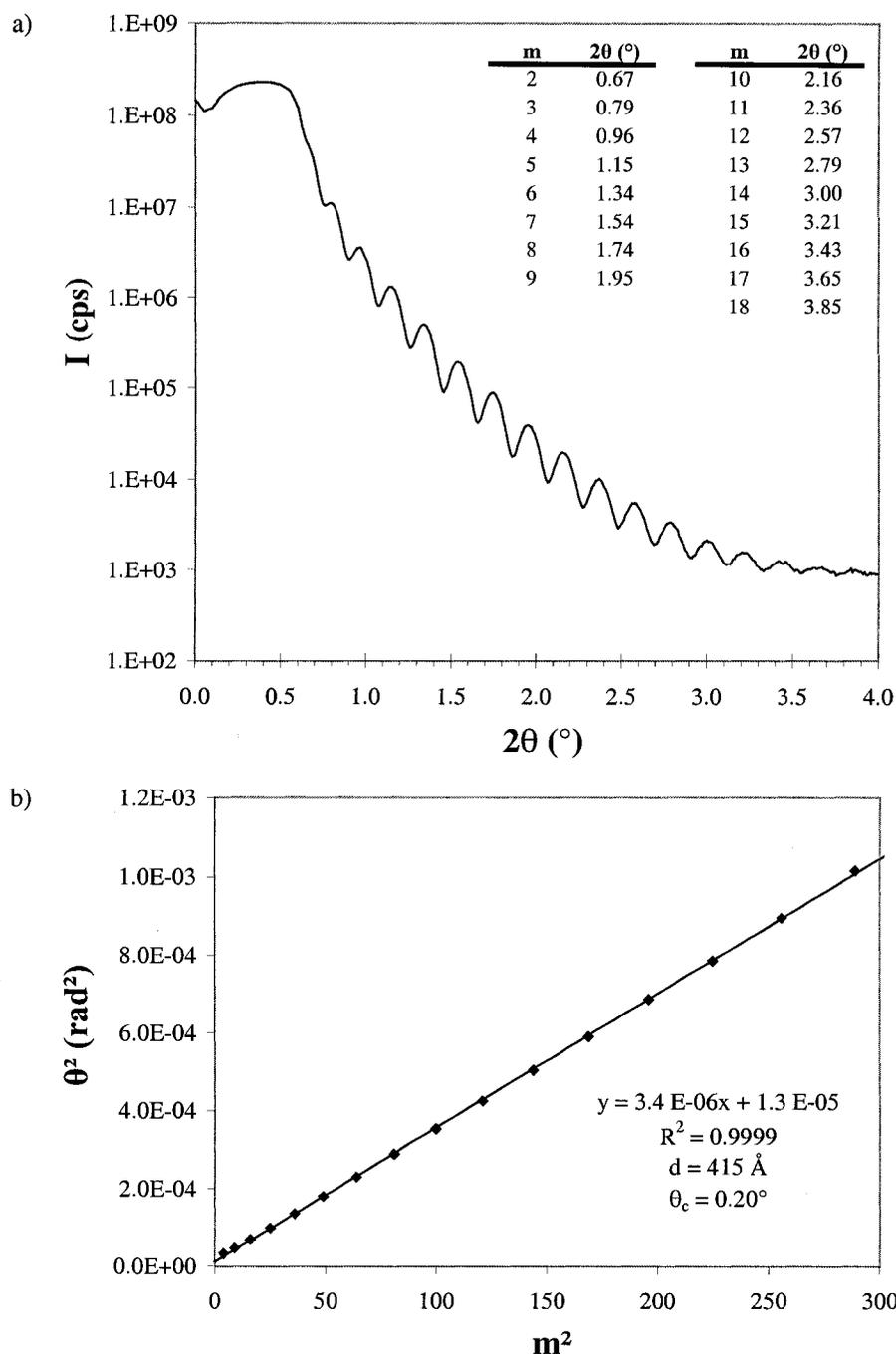
Figure 3.17. X-ray reflectometry of a 415 Å thick a-Sb$_2$S$_3$ film: a) x-ray pattern and peak orders, m, and their positions; and b) data analysis from θ^2 vs. m^2 and thickness, d, and critical angle, θ_c, determination.

151

a)

m	2θ (°)		m	2θ (°)
4	0.66		13	1.42
5	0.73		14	1.52
6	0.80		15	1.62
7	0.88		16	1.72
8	0.96		17	1.82
9	1.05		18	1.92
10	1.14		19	2.02
11	1.24		20	2.12
12	1.33		21	2.22
			22	2.32
			23	2.42
			24	2.52
			25	2.62
			26	2.73
			27	2.83
			28	2.94

b)

$y = 8.1\text{E-}07\ x + 1.8\ \text{E-}05$
$R^2 = 0.99995$
$d = 855\ \text{Å}$
$\theta_c = 0.24°$
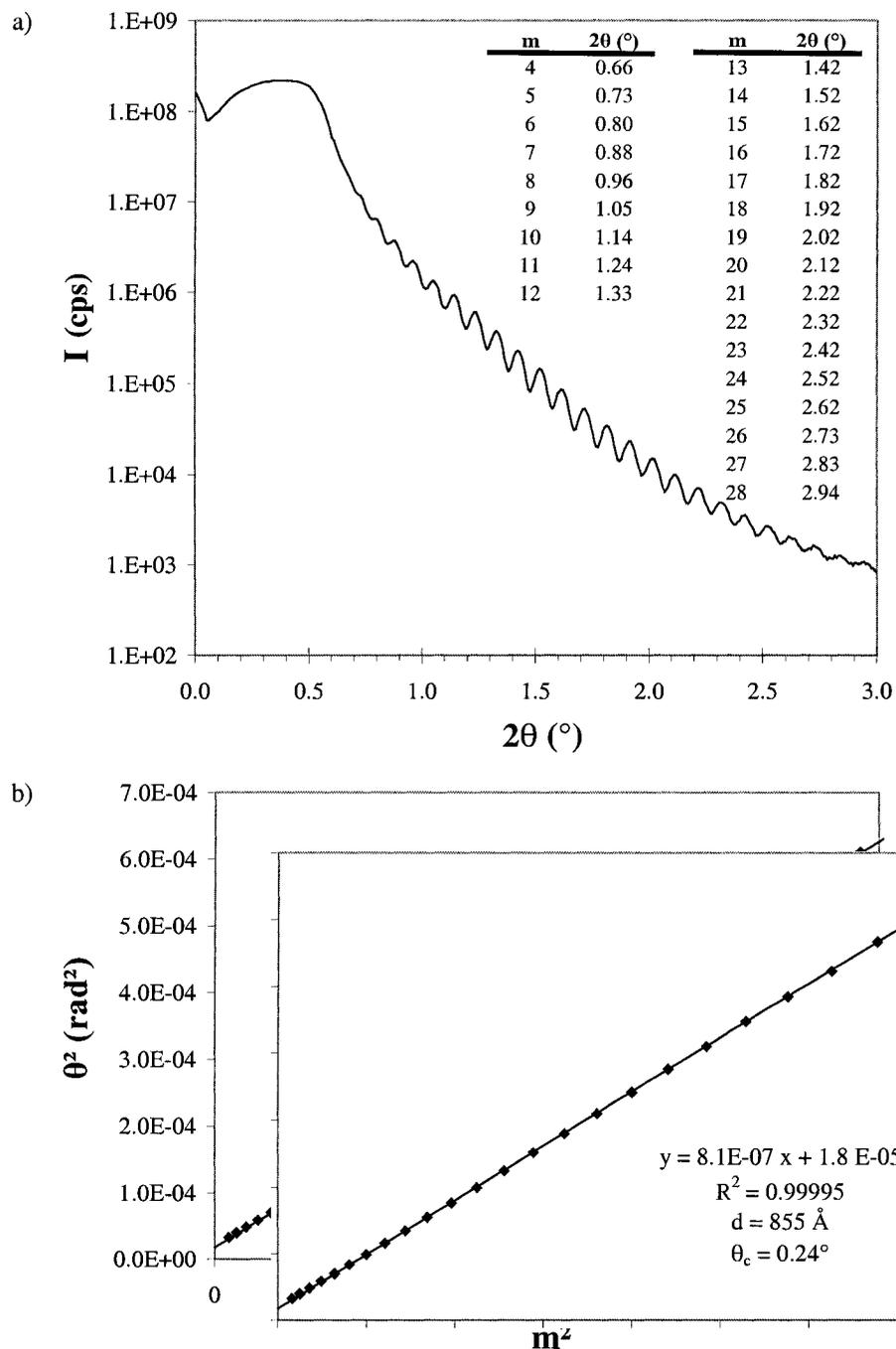
Figure 3.18. X-ray reflectometry of a 855 Å thick a-Sb_2S_3 film: a) x-ray pattern and peak orders (m) and positions, b) data analysis from θ^2 vs. m^2, thickness (d) and critical angle (θ_c) determination.

As shown in Figures 3.17 and 3.18, this set yielded interference fringes that were adequate to determine the film thicknesses. Plots of θ^2 as a function of m^2, where m and

152

θ are the peak order and the angle of the maxima (in radians), were obtained with high correlation coefficients.

Table 3.12. Results of x-ray reflectometry calibration of the Sb_2S_3 target RF sputtering

Power (W)	Time (s)	Thickness (Å)	Rate (Å/s)
40	1200	415	0.35
55	436	240	0.55
70	343	301	0.88
70	900	855	0.95

Trend line:

	a=	0.019	Å/s/W
	b=	-0.458	Å/s
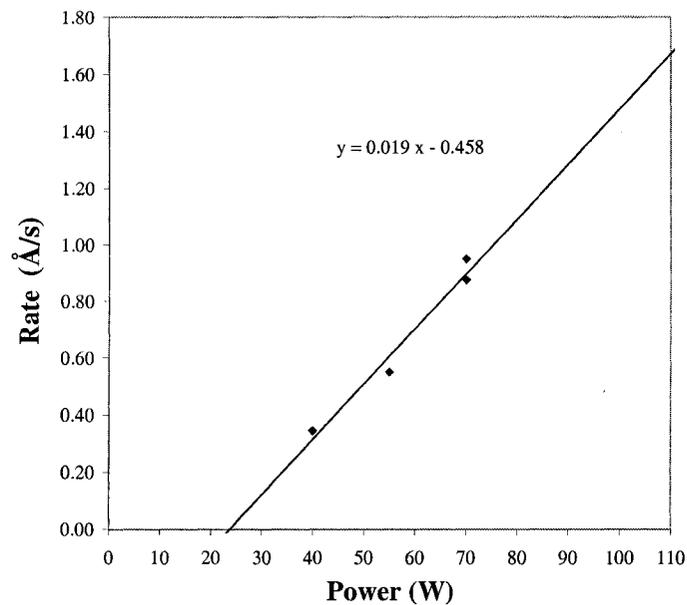
Figure 3.19. Deposition rate (Å/s) as a function of RF power applied on the Sb_2S_3 target; the straight line is given as guide for the eye.

153

A plot of the deposition rate (Å/s) as a function of the RF power applied to the Sb_2S_3 target is shown if Figure 3.19. At 100 W, a 1.4 Å/s deposition rate may be anticipated. One may notice that the rate varies around a mean straight line, which will serve as a guide to plan future deposition, especially the ones described in Chapters 4 and 6.

3.8   Conclusions

A lot of effort has been devoted to determination of deposition rates. Mass and X-ray reflectometry calibrations have been compared. Both have advantages and disadvantages. The mass calibration technique may be used with any element, as it does not have stringent film morphology (roughness) quality. However, mass calibration may be less accurate, especially for the determination of deposition rate in Å/s determination as it assumes the bulk density for the film material. The X-ray reflectometry technique requires some X-ray diffraction skills; however, once set-up, this method may be performed quite easily with easy to handle glass substrates (no need for very thin cover-slit substrates). This method not only yields accurate film thickness determination, but also may give estimates of the film electron and mass densities. Furthermore, it requires only 50 to 100 nm thick films (*i.e.* short deposition time); with our experimental set-up an optimum thickness around 75 nm was found.

Thus, the results described in this Chapter were used for the deposition of the film presented in the Chapter 4 (results of Sections 3.4.2 and 3.7), Chapter 5 (results of Sections 3.4.2, 3.5 and 3.6) and Appendix 2 (results of Sections 3.3 and 3.4.1).

154

3.9   References

[1]   U. Pietsch, V. Holy, T. Baumbach, High-Resolution X-Ray Scattering: From Thin Films to Lateral Nanotructure - 2nd Edition, Springer-Verlag, Berlin, 2004.

[2]   T. Novet, S. Kevan, D.C. Johnson, Mater. Sci. Eng., A A195 (1995) 21.

[3]   L. Fister, T. Novet, C. Grant, A., D.C. Johnson, in: T.E. Mallouk (Ed.) Advances in the Synthesis and Reactivity of Solids, JAI Press Inc., Greenwich, CT, 1994.

[4]   M.F. Toney, in: R.C. Brundle, C.A.Jr. Evans, S. Wilson, L.E. Fitzpatrick (Eds.), Encyclopedia of Materials Characterization, Butterworth-Heinemann, Stoneham, MA, 1992.

[5]   Bruker AXS, D8 Discover D8 Advance X-ray Diffraction: User's Manual, vol. 1, Bruker AXS GmbH, Karlsruhe, 2002.

[6]   Bruker AXS, D8 Discover D8 Advance X-ray Diffraction: User's Manual, vol. 3, Bruker AXS GmbH, Karlsruhe, 2001.

[7]   Bruker AXS, Diffrac^{plus} LEPTOS v1.04 - Analytical software for XRD and XRR - User's manual, Bruker AXS GmbH, Karlsruhe, 2002.

Chapter 4: Structural and Optical Properties of Amorphous and Crystalline Antimony Sulfide Thin-films

4.1 Introduction

Among the metal sulfides, antimony trisulfide (Sb_2S_3) has attracted attention for its application as a target material for television cameras [1,2], and in microwave devices [3], switching devices [4] and various optoelectronic devices [5-7]. Amorphous and crystalline thin films of antimony sulfide have been prepared using a wide variety of thin film deposition techniques: chemical bath deposition [8-13], electrodeposition [14], spray pyrolysis [15,16], vacuum thermal evaporation [2,6,17-21] or a tarnishing reaction [22,23]. To our knowledge, this is the first report of Radio Frequency (RF) sputtering of antimony sulfide.

A survey of the literature indicates that most of the antimony sulfide thin films deposited at low or room temperature are amorphous, regardless of the deposition process. Heat treatment of the as-deposited films are often done at temperatures around 250 °C and 300 °C in an inert gas to yield crystalline thin films, since the amorphous – crystalline (stibnite) phase transition happens at around 225 °C. Indeed, the glass transition (T_g) and crystallization (T_c) temperatures were respectively measured to be at 215 °C and 250 °C from Differential Thermal Analysis measurements [21].

Amorphous thin films of antimony sulfide have been widely used as a photoconductive target for the vidicon type of television camera tube [1,2]. More

156

recently, electron beam induced structural modification of amorphous antimony sulfide films has been demonstrated [20], showing potential for application in direct production of micron, sub-micron and nanometer structures and in various optoelectronic devices such as gratings. Lastly, Vedeshwar and coworkers have demonstrated the possibility of using amorphous antimony sulfide thin films for write once read many times type data storage [18,19]; moreover thin amorphous films of Ge-Sb-S alloys are potential candidates for phase-change optical recording technology.

Recently, thin films of nanocrystalline and polycrystalline antimony sulfide (stibnite phase, Sb_2S_3) have been investigated as potential materials for solar cells [10]. Indeed, faced with the adverse impact of global warming and increasing energy demand, renewable sources of energy, such as solar energy, have attracted considerable interest. Photoelectrochemical cells and thin film solar cells based on direct mid band gap semiconductors are foreseen as alternatives to the expensive dominant technology based on single crystalline silicon cells. Several materials currently used in thin film solar cells (e.g. CdTe, $Cu(In,Ga)Se_2$) may raise availability (In, Te) [24] and toxicity (Cd) issues if widely used. Thus, in an effort to develop new solar absorbers containing only cost effective, abundant, and relatively less toxic materials, several naturally occurring sulfides, among them stibnite, are promising materials for photovoltaic applications because of suitable energy gaps and photoconductivity properties [22,25-27].

Nanocrystalline [28,29] and polycrystalline [9] thin films of antimony sulfide have been used in photoelectrochemical cells of configuration: $n\text{-}Sb_2S_3 \| KI, I_2 \| C$; solar

157

to electrical conversion efficiencies up to 3.9 % [9] have been reported. Moreover, chemically deposited films have been used in Schottky barrier solar cells of Pt-Sb_2S_3 with a conversion efficiency of 5.5 % [30], and in heterojunction solar cells, n-Sb_2S_3/p-Ge, with a conversion efficiency of 7.3 % [31]. Finally, chemically deposited Sb_2S_3 has been used in the following p-i-n structure: SnO_2:F/p-CdS:In/i-Sb_2S_3/n-$CuSbS_2$/Ag [32].

Reported values and types of optical band gaps (E_g) of amorphous and crystalline (stibnite phase) antimony sulfide (Sb_2S_3) vary. The amorphous phase has been reported to be indirect with E_g values ranging from 1.5 to 1.85 eV [2,9,15,19,33] and also direct with E_g values ranging from 1.7 to 2.7 eV [8,10,17,34]. In the most recent reports, the crystalline phase, stibnite, is widely reported as a direct band gap semiconductor with E_g values between 1.7 and 1.8 eV [8,10,11,17]. Several studies on the variation in band gap with crystallite size [16,29,35] or stoichiometry [17,19] have been reported.

Crystalline Sb_2S_3 thin-films were prepared via reactive annealing of two different types of precursors: DC-sputtered Sb-metal precursor films and RF-sputtered amorphous Sb_2S_3 precursor films. This chapter includes a brief description of the preparation and characterization methods of the various crystalline and amorphous Sb_2S_3 thin films. Structural properties and annealing conditions of both Sb-metal and amorphous Sb_2S_3 precursors are discussed and compared. Finally, structural and optical properties of amorphous and crystalline antimony sulfide thin films, obtained from RF-sputtering of Sb_2S_3 and subsequent annealing in sulfur vapor, are described.

158

4.2 Thin-film preparation and characterization

The Sb-metal and amorphous Sb_2S_3 precursor films were deposited on quartz substrates in our ultra high vacuum thin film deposition system with a base pressure of $10^{-6} - 10^{-7}$ Pa. Substrates were cleaned using Piranha etch (H_2SO_4 (75 vol. %) / H_2O_2 (25 vol. %)), rinsed with water and blown dry with compressed air before deposition. Substrates were usually pumped down for at least 12 hours.

Sb-metal precursor films were deposited at a rate of ~3.5 Å/s, from 65 W DC – magnetron sputtering of an antimony metal target (Kurt J. Lesker, 99.99 %) with an argon plasma pressure of 667 (±3) mPa. The as-deposited film thickness was approximately 900 nm. More detailed on the antimony deposition rate calibration may be found in Section 3.4.2. Amorphous Sb_2S_3 precursor films were deposited at a rate of ~1.4 Å/s, from 100 W RF - magnetron sputtering of a stibnite (Sb_2S_3) target (Sophisticated Alloy Inc.) with an argon plasma pressure of 667 (±3) mPa. The stibnite target is 3 in. in diameter and 0.125 in. thick, target was manufactured by hot pressing of a 99.99 % of a stibnite (Sb_2S_3) powder. Upon arrival in our laboratory, targets are tested: the stibnite target is pure by X-ray diffraction. Further details regarding the calibration of the Sb_2S_3 target deposition rates will be included herein, in Section 3.7. The target bias voltage was constant at -148 (±1) V. Deposited film thicknesses were typically from 275 nm to 525 nm. As will be described later, RF-sputtering of Sb_2S_3 yielded amorphous films; thus, to obtain crystalline thin films of stibnite (Sb_2S_3) without a sulfur deficiency, it was necessary to anneal deposited films under sulfur vapor.

159

Therefore, to anneal Sb-metal and amorphous Sb_2S_3 precursor films, a two-zone tube furnace was used: films were centered in an evacuated tube and were heated: temperature and duration were varied to determine the optimal annealing conditions. The elemental sulfur was maintained to ~185 °C at one end of the tube, while the other end of the tube remained at room temperature, creating a sulfur flux through the tube.

Morphology and composition of as-deposited and annealed films were systematically evaluated with a field emission scanning electron microscope (JEOL – 6301 F) equipped with an Energy Dispersive X-ray (EDX) detector. Morphology was evaluated from Scanning Electron Microscopy (SEM) images obtained using an accelerating voltage of 5 kV. The elemental composition of the obtained films was determined from EDX data, using a 20 kV accelerating voltage or from microprobe measurement, as described in Chapter 2.

Crystal structures of the films before and after annealing were investigated by standard x-ray diffraction (XRD). Powder patterns were collected with a Bruker-AXS D8 diffractometer equipped with a Cu K_α source (λ = 1.5418 Å) collimated with a 0.5 mm pinhole collimator and a GADDS area detector. Films were appropriately Z-aligned with the center of the goniometer, during data collection films were oscillated in X and Y (±1 mm) in order to sample larger areas. The diffracted signal was collected from 2θ = 3° to 2θ = 85°.

Optical properties of stibnite (crystalline) films obtained from Sb-metal precursors were evaluated using diffuse reflectance spectroscopy measurements, a technique well-suited for rough thin-films. For both amorphous and crystalline Sb_2S_3 thin films obtained from Sb_2S_3 target RF-sputtering, the optical transmittance and near-normal reflectance (specular) spectra were recorded between 190 nm and 1100 nm using a PerkinElmer Lambda 35 UV-VIS spectrometer with 1 nm resolution at a scan speed of 240 nm/min.

4.3   Crystalline Sb_2S_3 films obtained by annealing Sb-metal precursors

4.3.1   Structural properties of as-deposited Sb-metal thin films

SEM images (top surface and tilt views) of the as-deposited antimony metal precursor film are shown in Figure 4.2. The film is approximately 900 nm thick. As-deposited films of antimony metal are dense and smooth, with mirror-like surfaces. X-ray diffraction patterns of these films, shown in Figure 4.1 indicate that they are polycrystalline and textured. Indeed, in Figure 4.1, significant differences in relative intensities can be observed between the powder pattern from the film and the reference powder pattern. The texture can also be observed with the as-collected diffracted x-ray beam on the area detector. Discontinued diffraction rings are observed, indicating that the x-ray beam is diffracted preferentially in certain directions; the diffraction cone in a given 2θ direction is not continuous, indicating that the sample is not a non-oriented polycrystalline sample. Such a sample yields continuous diffraction rings, which result from the intersection of complete diffraction cones in diffracting 2θ directions with the detector plane, as shown in Section 2.2.1. Comparing the diffracted intensities of the

161

actual as-deposited film and of the reference powder pattern, significant decreases in intensity are observed for the (012), (110), (024), (116) and (122). More interestingly, intensity increases can be observed for the (003), (006), (009) and (202) planes, suggesting two preferred growth directions (normal to the substrate) for the antimony crystallites along the [001] and [101] directions. This may explain the "spiky" texture of the as-deposited film top-surface shown in Figure 4.2.
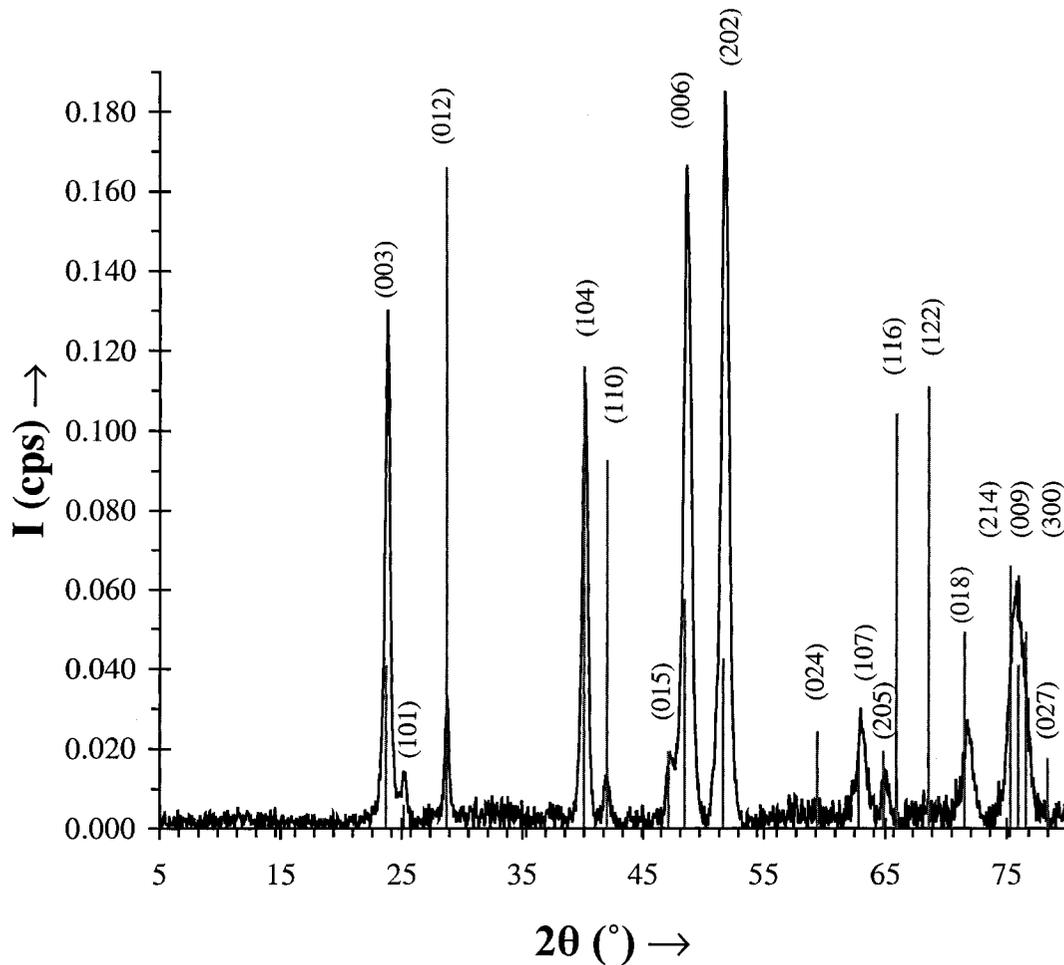
Figure 4.1. XRD data of an ~900 nm thick antimony metal precursor film with reference powder pattern [36,37] and peak miller indices.

162
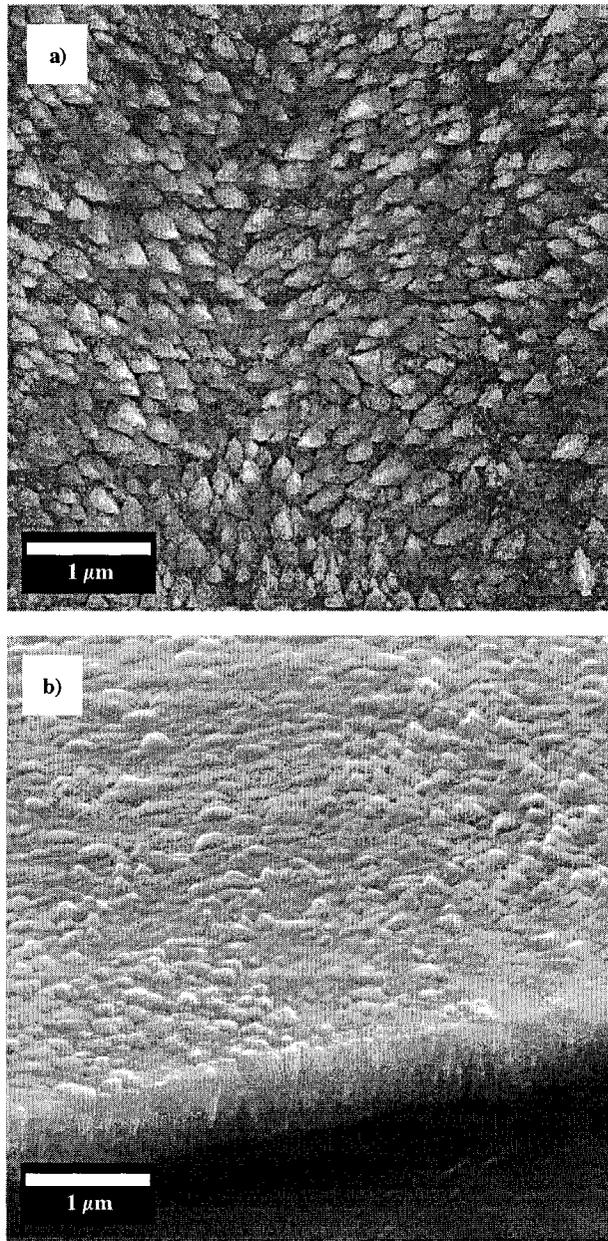
Figure 4.2. SEM images a) top surface and b) tilt view of the cross-section of an ~900 nm thick antimony metal precursor film.

4.3.2 Structural properties of annealed Sb-metal films as a function of the annealing conditions

In an effort to obtain stibnite Sb_2S_3 films of the appropriate quality, several annealing conditions have been tested. A few of the significant results obtained are

163

shown in Figure 4.3 (film morphologies) and in Figure 4.4 (film XRD data). It is important to mention that films shown in Figures 4.3.a, 4.3.b, 4.3.c and 4.3.d correspond to the XRD data shown in Figures 4.4.a, 4.4.b, 4.4.c and 4.4.d, respectively. Also, Figure 4.5 is an expanded part of the pattern shown in Figure 4.4.d.
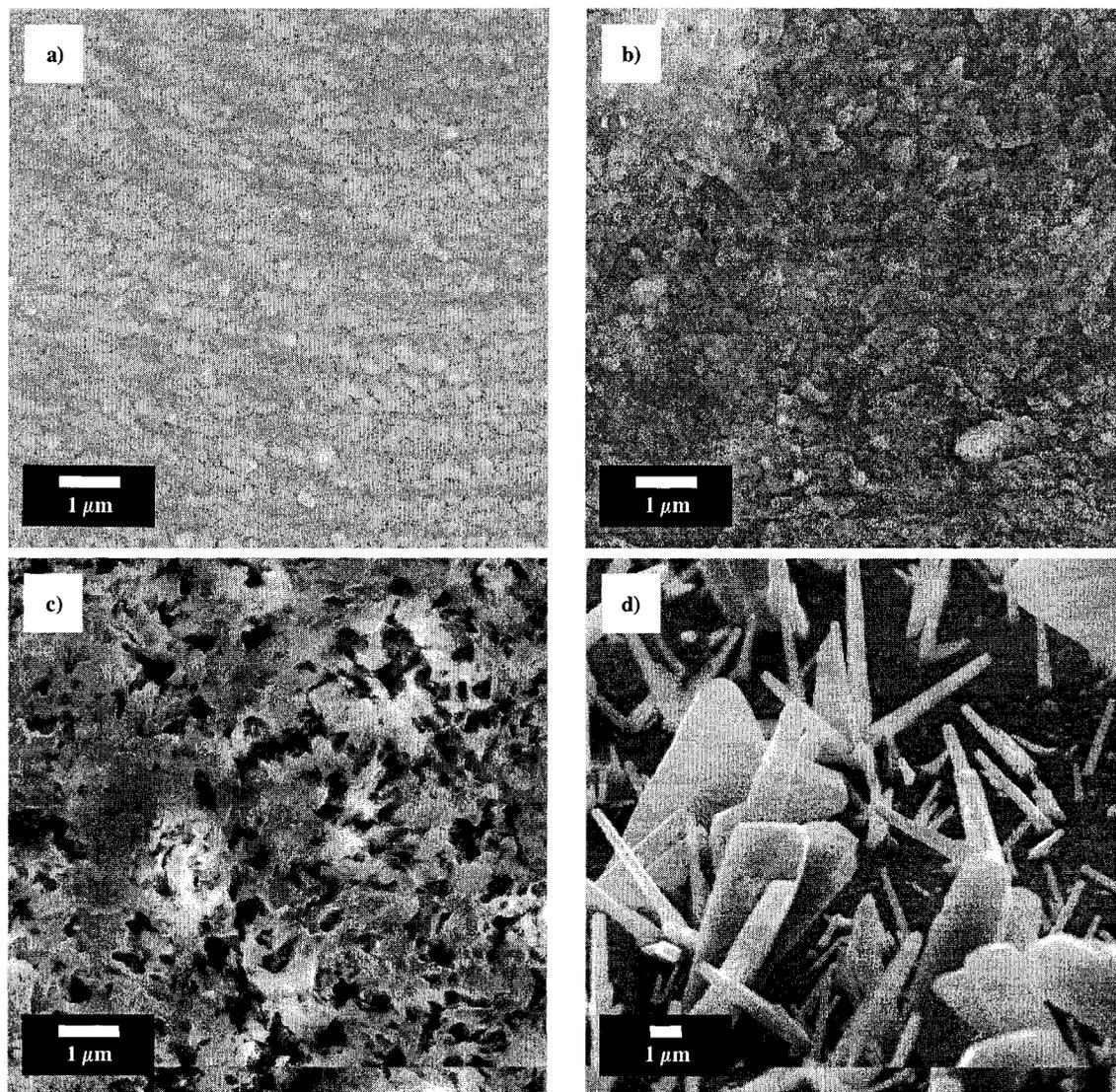
Figure 4.3. SEM images of antimony metal precursor films annealed in sulfur vapor: a) at 300 °C for 60 min. (top surface), b) at 300 °C for 45 min. and at 350 °C for 1 hour and 45 min. (top surface), c) at 300 °C for 30 min. and at 375 °C for 2 hours and 30 min. (top surface) and d) at 375 °C for 1 hour 30 min. and 200 °C for 6 hours (tilt view of the top surface).

164
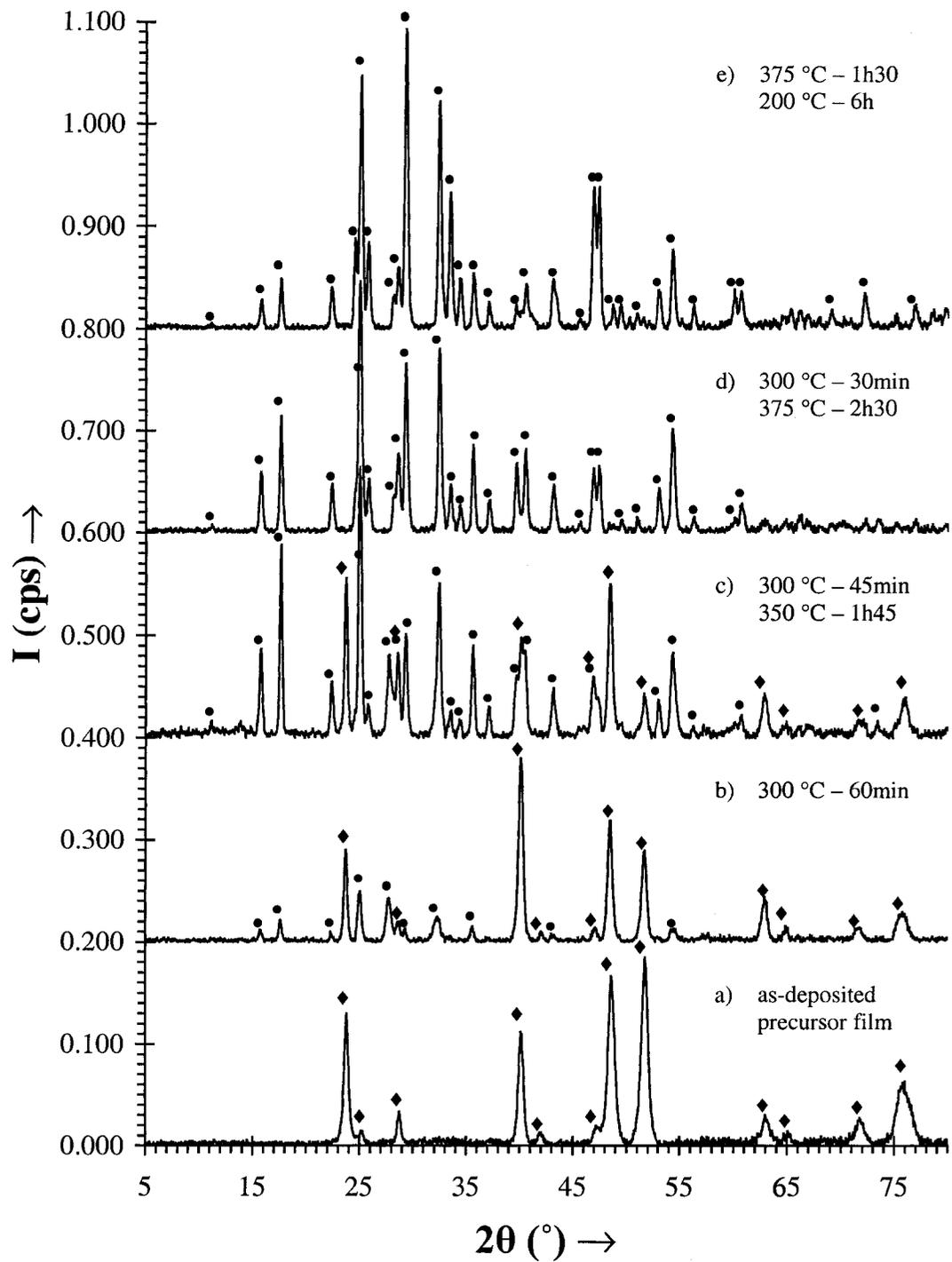
Figure 4.4. XRD data of a) an as-deposited antimony metal precursor films and b), c), d) and e) after different annealings in sulfur vapor (♦ for Sb peaks and ● for Sb_2S_3 peaks).

165
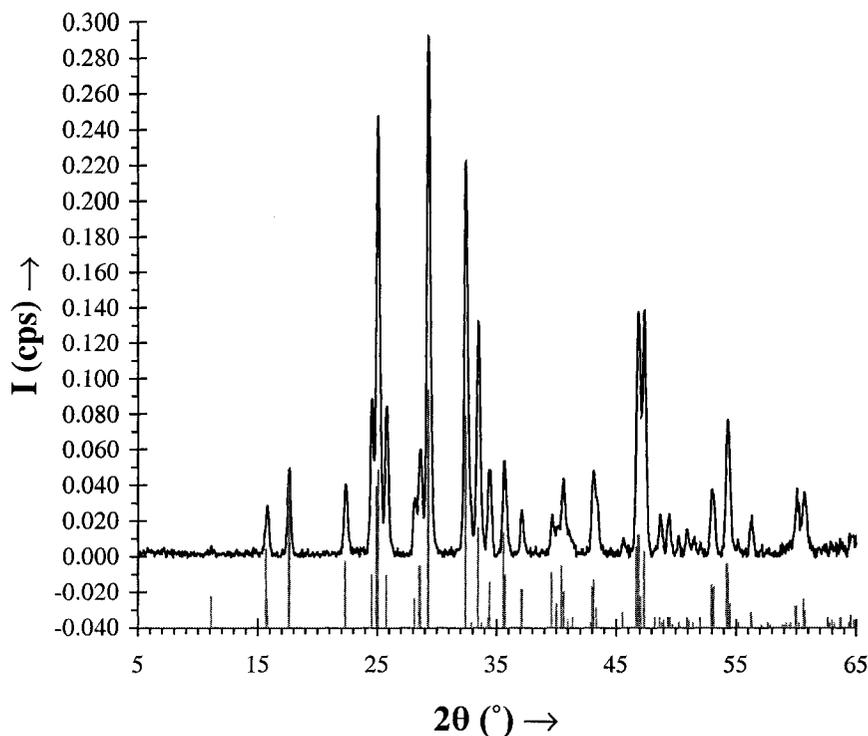
Figure 4.5. XRD data of antimony metal precursor films after annealing at 375 °C for 90 minutes and at 200 °C for 6 hours in sulfur vapor. XRD data match the Sb_2S_3 reference powder pattern [38,39].

The high temperature dwells for the annealing of Sb-metal precursor films were maintained at a temperature in the range of 160 °C to 375 °C, for one to three hours. The yellow sulfur source was maintained at 300 °C (Figures 4.3.a and 4.4.a), at 135 °C (Figures 4.3.b and 4.4.b), at 185 °C (Figures 4.3.c, 4.4.c, 4.3.d and 4.4.d). The conversion of antimony into stibnite (Sb_2S_3) requires a minimum annealing temperature. Indeed, films annealed below 300 °C for more than two hours showed no sign of Sb_2S_3 formation by XRD. After annealing at 300 °C for 60 minutes (Figures 4.3.a and 4.4.a), the film is approximately 5 % stibnite by WDX. To achieve more significant conversion, a minimum annealing temperature of 325 °C is required. Thus, films annealed at 350 °C for 105 minutes (Figures 4.3.b and 4.4.b) and films annealed at 375 °C (Figures 4.3.c,

166

4.4.c, 4.3.d, 4.4.d and 4.5) contained 64 % of stibnite and 100 % of stibnite by WDX, respectively. One can see the evolution of the conversion of antimony into stibnite as a function of the annealing temperature in Figure 4.4.

Many annealing experiments yielded films such as the one presented in Figures 4.3.d, 4.4.d and 4.5. These films feature some crystal growth on top of the film base, as needle- or delta-plane-like crystals grew on the film surface. These crystallites are well above a micron long or high and give a dull appearance to the film. This phenomenon has been observed using many annealing conditions and seems hard to prevent. Nevertheless, it was most pronounced after annealing for a long time (~2 to 6 hours) at a moderate temperature (200 °C to 350 °C) for final dwell. Indeed, one can compare two limiting cases: annealing at 375 °C for 150 minutes (Figure 4.3.c), during which no surface crystals grew, and the annealing at 375 °C for 90 minutes followed by a 6h dwell at 200 °C (Figure 4.3.d), during which surface crystal growth occurred. This result suggests that the surface growth of stibnite crystals occurs preferentially at lower temperatures, after the conversion of the antimony metal film into Sb_2S_3. Considering the shape of the crystals and the magnitude of their growth above the film surface (several microns), their growth must occur from the vapor phase by evaporation and recondensation of Sb_2S_3. Such a mechanism is very likely due to the volatility of this sulfide. The vapor pressure of stibnite is comparable to the one of antimony, which has been observed to be a volatile element in various occasions. Indeed, the vapor pressure of stibnite is 6×10^{-9} Pa at 200 °C and 1×10^{-3} Pa at 350 °C [40]. The formation of the projecting crystals by evaporation and recondensation of Sb_2S_3 is more likely than their

167

formation by evaporation of antimony and its reaction with sulfur in the vapor phase. Indeed, the film obtained at 375 °C for 150 minutes shown in Figure 4.3.c is also 100 % stibnite, but does not have these surface crystallites; nevertheless, this film looks depleted, which suggests that once formed the Sb_2S_3 sublimed, leaving voids behind. As the film temperature was hotter in that experiment, it did not recondense at the surface, and no needle- or delta-plane-like crystal growth was observed. The second scenario (*i.e.* evaporation of antimony and its reaction with sulfur in the vapor phase) does not seem to comply with the experimental data: indeed, the film annealed at 375 °C for 150 minutes (Figure 4.3.c) in that hypotheses should be a lot more depleted and thinner as no recondensation-reaction of antimony seemed to occur (no surface crystals growth), thereby depleting dramatically the film in antimony. Lastly, in an effort to quench the evaporation of stibnite once formed and avoid the formation of projecting crystals on the film surface, films were annealed in sulfur vapor at similar temperatures, but under N_2 (atmospheric pressure) rather than in evacuated tubes. Nevertheless, these conditions did not seem to impact the film morphology, crystallinity or conversion.

Also, films treated at high or moderate temperatures for long periods of time sometimes had somewhat bumpy film bases. This may indicate the early stage of de-wetting of the film. This could be due to the difference in lattice parameters between antimony and stibnite causing some expansion and causing some stress, when sulfur reacts with antimony metal. The formation of these bumps seemed to decrease when cooling rates are slower, conditions that are, unfortunately, also favorable to the formation of large stibnite crystallite on the film surface.

168

Lastly, in Figure 4.5, one can appreciate the polycrystalline and non-oriented nature of the films with large crystals on their surface. Due to these crystals, these films were rough with a dull aspect. Therefore, only diffuse reflectance spectroscopy could be performed. Figure 4.6 shows the diffuse reflectance spectrum of such a stibnite film. The band edge was determined at an energy of 1.72 eV. This value is well within the range of values that have been reported for the band gap of stibnite [8,10,11,17].
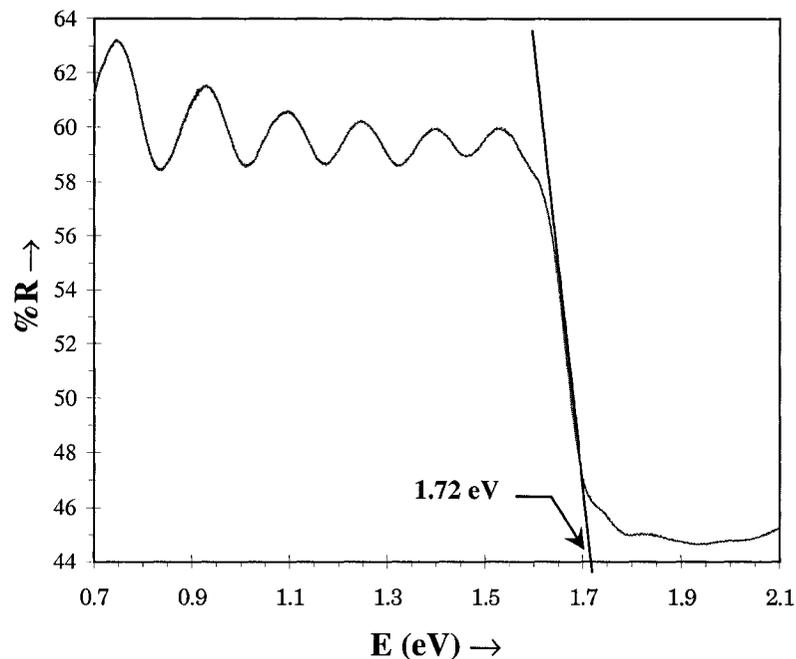
Figure 4.6. Diffuse reflectance spectrum of an Sb_2S_3 crystalline thin film obtained from annealing of an antimony metal precursor film at 375 °C for 1h30 and 200 °C for 6h in sulfur vapor. Band edge energy extrapolation (1.72 eV).

As a conclusion, full conversion in sulfur vapor of Sb films into Sb_2S_3 films with an acceptable morphology is a challenging problem, as once formed Sb_2S_3 tend to evaporate, yielding to depleted films or films with micron-sized crystals on the surface as Sb_2S_3 recondenses on the surface. As will be shown in the following paragraph, formation of Sb_2S_3 films with an acceptable morphology has been achieved more easily

169

through the deposition of amorphous Sb_2S_3 precursor films followed by annealing under sulfur vapor.

4.4   c- and a-Sb_2S_3 films obtained from RF-sputtering of Sb_2S_3

4.4.1   Structural properties of as-deposited amorphous thin films
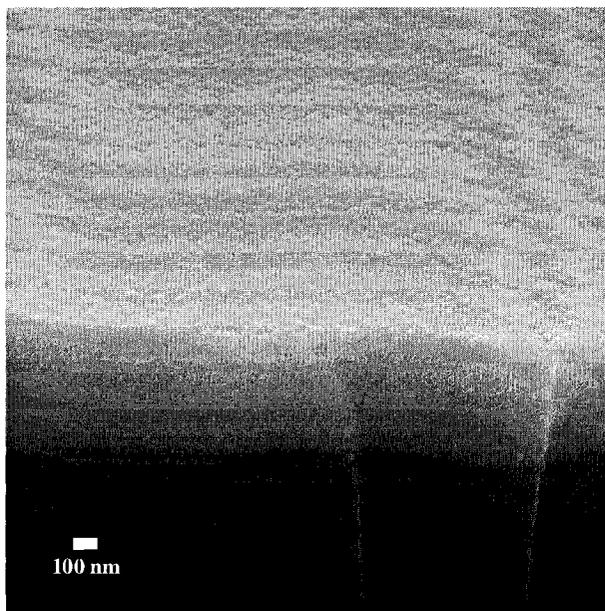
Figure 4.7. SEM image (tilt view) of an ~525 nm thick Sb_2S_3 amorphous thin film as-deposited on fused silica.

A SEM tilt view of an as-deposited antimony sulfide thin film is shown in Figure 4.7. The film shown is approximately 525 nm thick. As-deposited films of antimony sulfide are dense and smooth, with mirror-like surfaces. X-ray diffraction patterns of these films indicate that they are amorphous, featuring a typical broad peak centered at $2\theta \sim 23°$. Compositions of the as-deposited films determined by EDX measurements indicate that the films are sulfur deficient with a composition of Sb_2S_{3-x} (with $x = 0.28$),

170

which represents a 9.3 at. % sulfur deficiency of the film compared to the ideal Sb_2S_3 stoichiometry.

Because sputtering is an atomic process, there are atoms of antimony and sulfur in the plasma, which must recombine at the substrate. Moreover, sputtering is a high-energy process, and the substrate warms up during the deposition because of the heat of condensation of the atoms, the kinetic energy of the incident adatoms and the "plasma heating" (*i.e.* bombardment of neutrals and electrons). The temperature, measured by a thermocouple in contact with the deposition platen that supports the substrate holder, reaches 68°C during the deposition. Thus, the difference in vapor pressure between antimony and sulfur might explain the sulfur deficiency compared to the ideal stoichiometry. Indeed, because sulfur has a higher vapor pressure, it may recondense on the warm substrate at a slower rate than antimony, yielding a slightly sulfur deficient film composition. It is interesting to note that the as-deposited film remains amorphous, as there is not enough thermal energy to achieve crystallization. Also, because of their lower atomic number and mass, ejected sulfur atoms are more likely to be thermalized by collisions with the argon gas and consequently may not reach the substrate.

4.4.2 Structural properties of annealed crystalline thin films

As mentioned in Section 4.2, as-deposited films were annealed in sulfur vapor to obtain crystalline Sb_2S_3 thin films. The as-deposited 525 nm thick amorphous film shown in Figure 4.7 was annealed for 30 minutes at 400 °C, yielding the film shown in Figure 4.9. The cross-sectional image (Figure 4.9.a) and the tilt view (Figure 4.9.c)

171

indicate that the film is dense, crystalline and smooth, with a mirror-like surface. The top-surface view (Figure 4.9.b) shows that the film is primarily composed of two different grain sizes: large grains in the range of 400 to 600 nm and grains smaller than 150 nm. The polycrystalline nature of the film is confirmed by the XRD powder pattern (Figure 4.8) that shows an excellent match with the PDF reference card no. 65-2434 [38,39]; antimony sulfide crystallizes in the Pnma (62) space group, the parameters of the orthorhombic lattice are a = 11.30 Å, b = 3.83 Å and c = 11.22 Å. As mentioned earlier, this phase is commonly named stibnite. Lastly, EDX data yielded a composition of Sb_2S_{3-x} (with $x = 0.16$), corresponding to a 5 at. % sulfur deficiency.
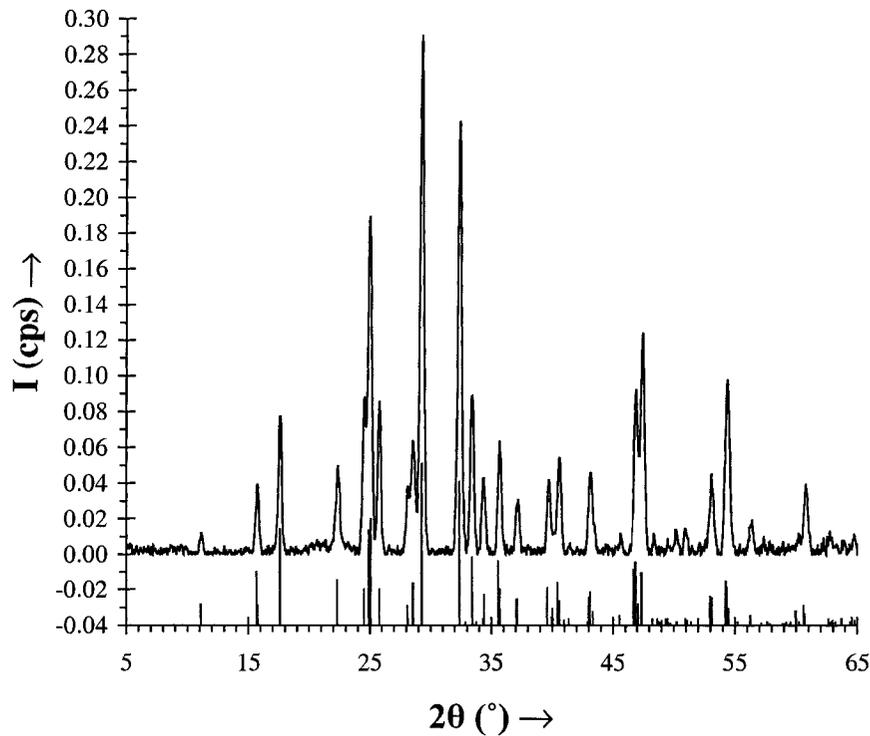
Figure 4.8. XRD data of an ~600 nm thick Sb_2S_3 crystalline thin film after annealing in sulfur vapor (400 °C – 30 minutes) with Sb_2S_3 reference powder pattern [38,39].

172
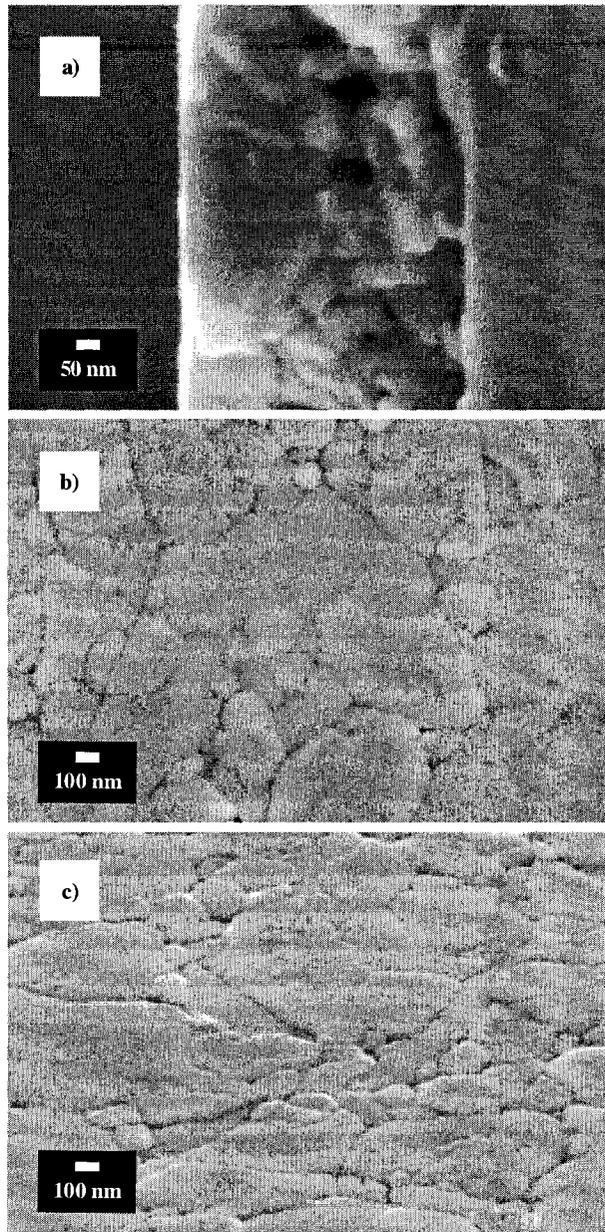
Figure 4.9. SEM images of an ~600 nm thick Sb_2S_3 crystalline thin film after annealing in sulfur vapor (400 °C – 30 minutes): a) cross-section, b) top surface and c) tilt view.

Given our deposition process and laboratory set-up for annealing, the conditions used for annealing (*i.e.* sulfur vapor, 400 °C for 30 minutes for an ~525 nm thick as-deposited film) appear to be close to optimal. Indeed, annealing performed under similar conditions at 350 °C for ~30 minutes or at 400 °C for 15 minutes yielded stibnite films

173

with smaller crystal grains, as shown in Figures 4.10.b and 4.10.c. Heat treatment without sulfur vapor but under N_2 at $\geq$ 300 °C, always yielded films with poor morphology (large pin-holes) as shown in Figure 4.10.a. Moreover, these films were composed of a mixture of antimony metal and stibnite. This indicates that the as-deposited film is significantly depleted in sulfur during annealing in nitrogen. These experimental results suggest, first, that the presence of sulfur vapor is necessary to avoid film depletion and maintain good film morphology, and, second, that enough thermal energy is required to achieve complete crystallization of the amorphous film. Thus, crystallization of our amorphous precursor films seems to require slightly harsher conditions (sulfur vapor and higher temperature) to obtain larger crystal grains than previously reported [8,10,17]. A possible explanation for this phenomenon could be the presence and amount of very short-range order within the amorphous matrix. That is to say, small nanocrystalline domains that may form, or not (depending on the deposition process), and then act as nuclei for crystal growth. Moreover, compiling the results of experiments shown in Figures 4.9.b. and 4.10.c, it appears that first the Sb_2S_3 crystallites nucleate from the amorphous as-deposited film and then form 10 to 50 nm grains that eventually coalesce into micron-sized grains. The grain boundaries of these micron-sized crystals seem to be predetermined by areas where the nucleation from the amorphous and the subsequent growth of stibnite crystallites occurred more rapidly (slightly larger grains are observed in these areas). Lastly, the formation of crystals on the film surface has rarely been observed and only moderately upon long duration annealing at 400 °C for 50 minutes. It was easier to control the film morphology through the sulfurization of the amorphous Sb_2S_3 film.

174
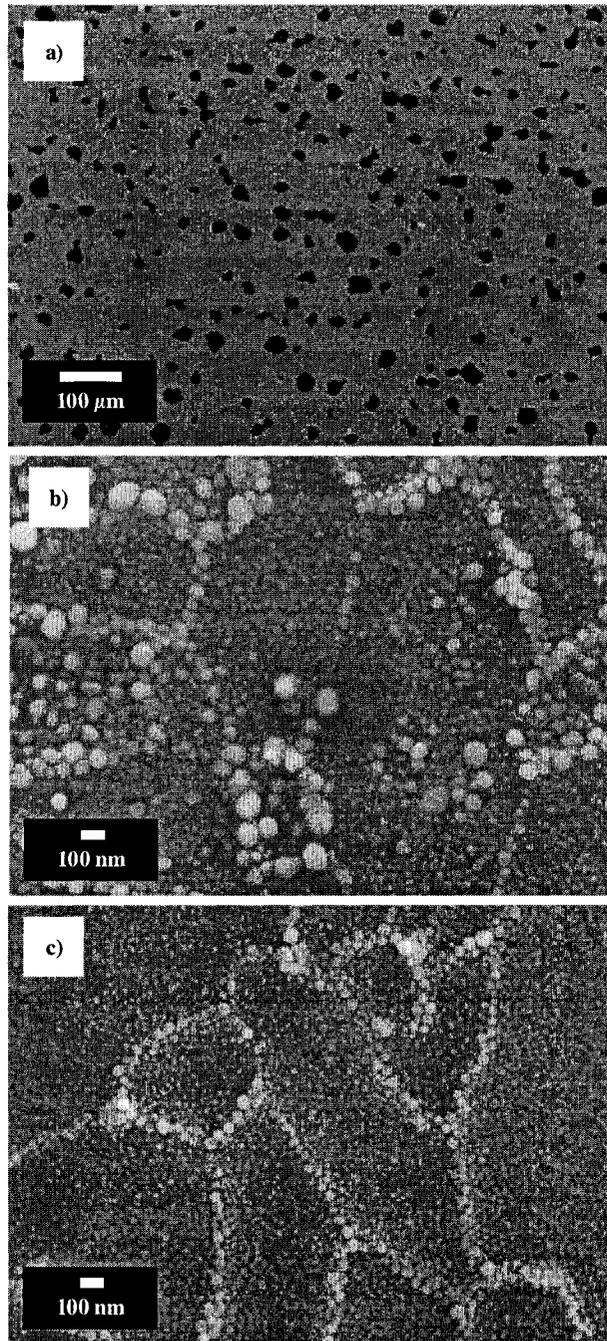
Figure 4.10. SEM images of amorphous Sb_2S_3 precursor films annealed: a) at 350 °C for 20 min. in a N_2 atmosphere without sulfur vapor (top surface), b) at 350 °C for ~30 min. in sulfur vapor (top surface), and c) at 400 °C for 15 min. in sulfur vapor (top surface).

175

4.4.3 Optical properties of amorphous and crystalline thin films

a)

b)
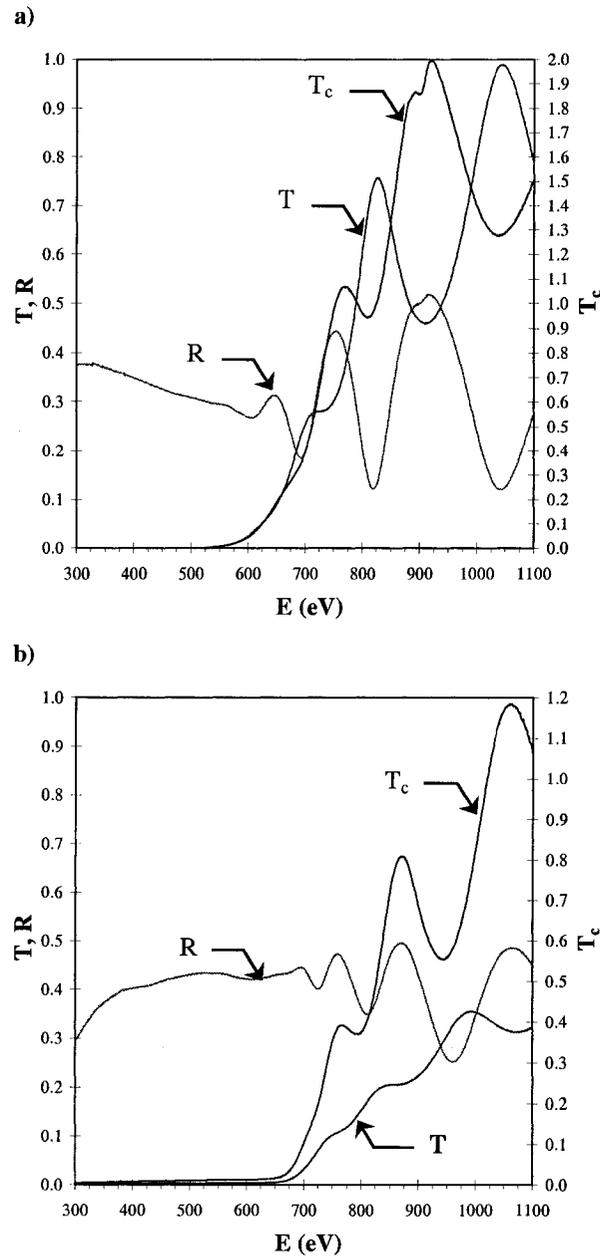
Figure 4.11. Optical transmittance (T) and reflectance (R) and corrected transmittance (T_c) for a) an ~525 nm thick Sb_2S_3 amorphous thin film and b) an ~600 nm thick Sb_2S_3 crystalline thin film.

Figure 4.11 shows the optical transmittance and near-normal reflectance spectra for a 525 nm thick amorphous (Figure 4.11.a) and a 600 nm thick crystalline (Figure

176

4.11.b) antimony sulfide thin film. Optical transmittance and reflectance are processed using the equation (2.6) (herein labeled (4.1)) for the transmittance [41], as the approximation of αd large is verified. One should note that both the approximate and exact formula have been used, yielding similar results.

$$T \approx (1 - R)^2 e^{-\alpha d} \tag{4.1}$$

The absorption coefficients, α, of the films have been calculated using the relation (2.8) (herein labeled (4.2)) [41]:

$$\alpha \approx \frac{1}{d} \ln\left[\frac{(1-R)^2}{T}\right] = \frac{1}{d} \ln\left[\frac{1}{T_c}\right] \tag{4.2}$$

where T and R are the transmittance and the reflectance values, respectively; and where d is the film thickness in cm, evaluated from high magnification cross-sectional SEM images. The corrected transmittance, T_c, for reflection losses at the air-film interface (also displayed in Figures 4.11.a and 4.11.b.) is calculated using the equation (2.9) (herein labeled (4.3)):

$$T_c = T / (1 - R)^2 \tag{4.3}$$

The energy dependence of the absorption coefficient for a 525 nm thick amorphous antimony sulfide film and a 600 nm thick crystalline antimony sulfide film are shown in Figure 4.12: both films are strongly absorbing at energies above their absorption edge. Indeed, the absorption coefficients for amorphous and crystalline films are respectively, 1.8×10^5 cm^{-1} and 7.5×10^4 cm^{-1}. For the amorphous film, the line displayed for energies larger than 2.4 eV is given as a guide for the eye, the spread in the value of the absorption coefficient can be attributed to the near zero transmittance value,

177

introducing a large spread for the value of $1/T_c$, its Neperien logarithm value and consequently for α.
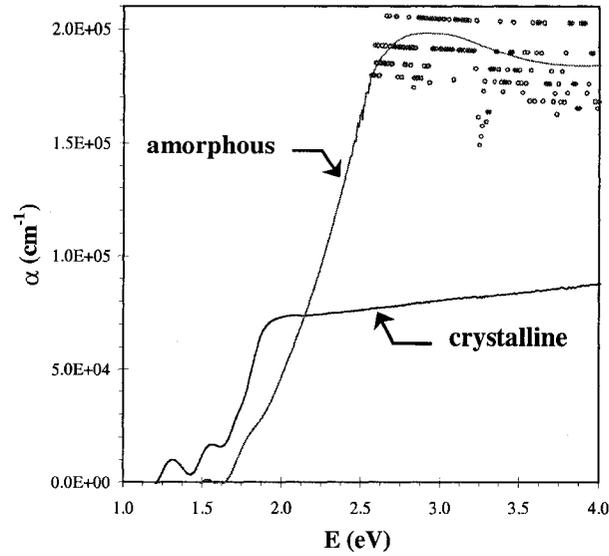
Figure 4.12. Absorption coefficient of an ~525 nm thick Sb_2S_3 amorphous thin film and an ~600 nm thick Sb_2S_3 crystalline thin film. Note: for high energy values, in the case of the amorphous film, the line is given as a guide for the eye, the spread in the value of the absorption coefficient is attributed to the near zero transmittance value.
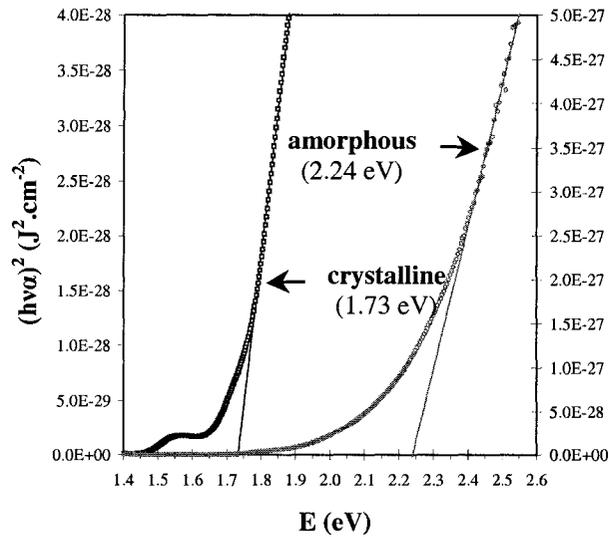
Figure 4.13. Direct optical band gaps of an ~525 nm thick Sb_2S_3 amorphous thin film (right y-axis) and an ~600 nm thick Sb_2S_3 crystalline thin film (left y-axis) extrapolated from $(h\nu\alpha)^2$ vs. E (eV).

178

In semiconductors, (hvα) is proportional to $(hv - E_g)^{1/n}$ where E_g is the band gap

energy and n = 2, ⅔, ½ or ⅓ for, respectively, direct allowed, direct forbidden, indirect

allowed or indirect forbidden optical transition [42]. Thus, a plot of $(hvα)^n$ vs. (hv) would

yield a straight line plot, where the band gap value can be determined from the intercept

on the photon energy axis. Concerning both amorphous and crystalline antimony sulfide

films, the best straight line fit has been found for values of n = 2, meaning a direct

allowed transition between the valence and the conduction band, which is in good

agreement with the high values of the absorption coefficients. Thus, Figure 4.13 shows

plots of $(hvα)^2$ vs. (hv) for a 525 nm thick amorphous film $((hvα)^2$ values displayed on

the right axis) and for a 600 nm thick crystalline film $((hvα)^2$ values displayed on the left

axis). Direct band gap values of amorphous and crystalline antimony sulfide films are

respectively 2.24 eV and 1.73 eV. These values are in good agreement with those

previously reported [8,10,17], as shown in Table 4.1.

Table 4.1. Optical band gap energies of amorphous and polycrystalline antimony sulfide thin films

Deposition Process	Conditions	Structure	E_g (eV) - direct	Reference
Thermal evaporation	As-deposited	Amorphous	1.70 – 2.07 increases with S at. %	[17]
	Annealed at 300 °C in N_2 for 3h	Polycrystalline	1.42 – 1.65 increases with S at. %	[17]
Chemical bath deposition	As-deposited	Amorphous	2.48	[8]
	Annealed at 170-200 °C	Polycrystalline	1.70	[8]
Chemical bath deposition	As-deposited	Amorphous	2.2	[10]
	Annealed at 300 °C in N_2 for 1h	Polycrystalline	1.78	[10]
RF-sputtering	As-deposited	Amorphous	2.24	This work
	Annealed at 400 °C in S vapor for ½h	Polycrystalline	1.73	This work

179

Focusing on the plot $(h\nu\alpha)^2$ *vs.* $(h\nu)$ in the case of the amorphous film (Figure 4.13), one notices an exponential-like tailing of the straight line. Indeed, for photon energies below the optical gap, the absorption drops off more slowly compared to the crystalline film. Indeed, contrary to crystalline semiconductors, there is a large number of localized energy states or trap states within the band gap of amorphous materials, yielding a band edge tail. This increased subband absorption is similar to the absorption in heavily doped crystalline semiconductors and can be described by the Urbach law [43]:

$$\alpha_U(h\nu) = C(h\nu)\exp\left[\frac{-(E_g - h\nu)}{E_0}\right] \tag{4.4}$$

where $C(h\nu)$ is a slowly varying function of the energy and E_0 is the Urbach energy which relates directly to the characteristic distribution width of the band tail states. Amorphous antimony sulfide can be considered as a degenerate direct band gap semiconductor: due to the high density of defects, such as dangling bonds, in amorphous materials, a large number of states exist within the energy gap between the conduction and the valence bands, yielding an increased subband absorption.

4.5 Conclusion

The conversion of antimony metal precursor films into crystalline Sb_2S_3 films with an acceptable morphology proved to be challenging, as micron-sized crystals on the surface. A more efficient and reliable synthesis method has been implemented, reporting the first preparation of amorphous and crystalline antimony sulfide (Sb_2S_3) thin films from RF-sputtering of an Sb_2S_3 target and subsequent annealing at 400 °C in sulfur vapor. Both as-deposited (amorphous) and annealed (crystalline) films showed good

180

morphological properties: both films are smooth and compact, and polycrystalline films are mostly made of ~500 nm grains. Both amorphous and crystalline antimony sulfide proved to have strong absorption coefficients, α, 1.8×10^5 and 7.5×10^4 cm^{-1} and direct band gaps with band energies of 2.24 eV and 1.73 eV, respectively. Both crystalline and amorphous antimony sulfide thin films should be considered as potential materials for the active layer in various solid state devices, such as thin film solar cell.

4.6   References

[1]   S.V. Forgue, R.R. Goodrich, A.D. Cope, RCA Review 12 (1951) 335.

[2]   C. Ghosh, B.P. Varma, Thin Solid Films 60 (1979) 61.

[3]   J. Grigas, J. Meshkauskas, A. Orliukas, Phys. Status Solidi A 37 (1976) K39.

[4]   M.S. Ablova, A.A. Andreev, T.T. Dedegkaev, B.T. Melekh, A.B. Pevtsov, N.S. Shendel, L.N. Shumilova, Soviet Physics Semiconductors - USSR 10 (1976) 629.

[5]   M.J. Chockalingam, N. Nagaraja Rao, K. Rangarajan, C.V. Suryanarayana, J. Phys. D: Appl. Phys. 3 (1970) 1641.

[6]   E. Montrimas, A. Pazera, Thin Solid Films 34 (1976) 65.

[7]   J. George, M.K. Radhakrishnan, Solid State Commun. 33 (1980) 987.

[8]   I. Grozdanov, Semicond. Sci. Technol. 9 (1994) 1234.

[9]   O. Savadogo, K.C. Mandal, J. Electrochem. Soc. 139 (1992) L16.

[10]   M.T.S. Nair, Y. Pena, J. Campos, V.M. Garcia, P.K. Nair, J. Electrochem. Soc. 145 (1998) 2113.

[11]   R.S. Mane, B.R. Sankapal, C.D. Lokhande, Thin Solid Films 353 (1999) 29.

[12] R.S. Mane, C.D. Lokhande, Mater. Chem. Phys. 65 (2000) 1.

[13] B.R. Sankapal, R.S. Mane, C.D. Lokhande, Journal of Materials Science Letters 18 (1999) 1453.

[14] N.S. Yesugade, C.D. Lokhande, C.H. Bhosale, Thin Solid Films 263 (1995) 145.

[15] C.H. Bhosale, M.D. Uplane, P.S. Patil, C.D. Lockhande, Thin Solid Films 248 (1994) 137.

[16] S.R. Gadakh, C.H. Bhosale, Mater. Chem. Phys. 78 (2002) 367.

[17] S. Mahanty, J.M. Merino, M. Leon, J. Vac. Sci. Technol., A 15 (1997) 3060.

[18] P. Arun, A.G. Vedeshwar, N.C. Mehra, J. Phys. D: Appl. Phys. 32 (1999) 183.

[19] P. Arun, A.G. Vedeshwar, J. Non-Cryst. Solids 220 (1997) 63.

[20] R.K. Debnath, A.G. Fitzgerald, Appl. Surf. Sci. 243 (2005) 148.

[21] M.S. Droichi, F. Vaillant, E. Bustarret, D. Jousse, , J. Non-Cryst. Solids 101 (1988) 151.

[22] J.S. Curran, R. Philippe, in: W.H. Bloss, G. Grassi (Eds), Fourth European Community Photovoltaic Solar Energy Conference, Stresa, Italy, May 10-14, 1982, p.853.

[23] J.S. Curran, R. Philippe, J. Joseph, A. Gagnaire, Chem. Phys. Lett. 89 (1982) 511.

[24] B.A. Andersson, Progress in Photovoltaics 8 (2000) 61.

[25] M.Y. Versavel, J.A. Haber, Chem. Commun. (2006) 3543.

[26] O. Savadogo, K.C. Mandal, Sol. Energy Mater. Sol. Cells 26 (1992) 117.

[27] H. Dittrich, D.J. Vaughan, R.A.D. Pattrick, S. Graeser, M. Lux-Steiner, R. Kunst, D. Lincot, in: W. Freiesleben (Ed.), Proceedings of the 13th European

Photovoltaic Solar Energy Conference, Nice, France, October 23-27, 1995, p.1299.

[28] K.Y. Rajpure, C.H. Bhosale, Mater. Chem. Phys. 63 (2000) 263.

[29] R.S. Mane, C.D. Lokhande, Mater. Chem. Phys. 78 (2002) 385.

[30] O. Savadogo, K.C. Mandal, J. Electrochem. Soc. 141 (1994) 2871.

[31] O. Savadogo, K.C. Mandal, J. Phys. D: Appl. Phys. 27 (1994) 1070.

[32] Y. Rodriguez-Lazcano, M.T.S. Nair, P.K. Nair, J. Electrochem. Soc. 152 (2005) G635.

[33] J.D. Desai, C.D. Lokhande, Thin Solid Films 237 (1994) 29.

[34] K.Y. Rajpure, C.D. Lokhande, C.H. Bhosale, Mater. Chem. Phys. 51 (1997) 252.

[35] R.S. Mane, C.D. Lokhande, Mater. Chem. Phys. 82 (2003) 347.

[36] Powder Diffraction File, International Center for Diffraction Data, Newton Square, PA, 2002, Card 35-732.

[37] H. Swanson, Fuyat, National Bureau for Standards, Circ. 539 vol. 3 (1954) 14.

[38] D.O. McKee, J.T. McMullan, Z. Kristallogr. 142 (1975) 447.

[39] Powder Diffraction File, International Center for Diffraction Data, Newton Square, PA, 2002, Card 65-2434.

[40] V. Piacente, P. Scardala, D. Ferro, J. Alloys Compd. 178 (1992) 101.

[41] J.I. Pankove, Optical Processes in Semiconductors, Prentice-Hall Inc., Englewood Cliffs, NJ, 1971.

[42] R.A. Smith, Semiconductors - 2nd edition, Cambridge University Press, Cambridge, NY, 1978.

[43] H.J. Möller, Semiconductors for Solar Cells, Artech House, Boston, MA, 1993.

Chapter 5: Pb-Sb-S Thin-films Obtained from Reactive Annealing of Sb-Pb Metal Precursor Films

5.1 Introduction

As established in Chapter 1, having band gaps around 1.4 eV and containing only cost effective, abundant and relatively less-toxic materials, Pb-Sb-S ternary phases are potential candidates for thin-film solar cells. The previous reports of thin films of Pb-Sb-S ternary phases are brief. Deposition methods that were employed are chemical bath deposition of $PbSb_2S_4$ (zinkenite) [1], and thermal evaporation of amorphous and multiphase Pb-Sb-S thin films [2]. Ternary films of Pb-Sb-S were prepared via vacuum thermal evaporation by co-evaporation of sulfur, metal or binary compounds [2]. The substrate temperature proved to be important for the growth and structure of the deposited films; from 30 °C to ~150 °C the films were amorphous, from 150 °C to ~250 °C the films were polycrystalline with a tendency to be oriented, and finally above 250 °C the films were polycrystalline with random orientation. Nevertheless, definitive determinations of the crystalline phases deposited were not reported, and we believe that films were multi-phased. Lastly, to our knowledge, no H_2S or S vapor sulfurization of lead-antimony metal precursor films has been reported.

Given our deposition system set-up, deposition methods were somewhat limited. For instance, it is impossible to deposit antimony via electron-beam evaporation, as it yields very large and fluctuating deposition rates (> 50 Å/s), even at the lowest currents possible. These kinds of deposition rates do not enable a good control over the deposited

184

Sb-Pb metal precursor film stoichiometry. Deposition rates for good stoichiometric control should be stable, reproducible and have an easy to work with value of 1 to 5 Å/s. Also, electron-beam evaporation of compounds is not trivial, as it often leads to decomposition of the compounds. Thus, electron-beam evaporation of PbS or Sb_2S_3 might dissociate these sulfides into lead, antimony and sulfur. Not only would this lead to poor control of the stoichiometry, but, more importantly, it also generates sulfur vapors that would condense on the deposition chamber walls and that ultimately would be trapped in the cryo-pump, contaminating and degrading its cold surfaces. Because of its high vapor pressure, sulfur is extremely detrimental to UHV systems, since until it has been completely eliminated, solid sulfur generates vapor, preventing high vacuum base pressures from being reached and contaminating vacuum pump fluids and/or surfaces. Moreover, electron-beam evaporation is not highly reproducible and requires manual adjustment of the applied current to maintain and control the deposition rates that must be continuously monitored using, for our system, a quartz crystal film thickness monitor. As described in Section 2.1.1, the film thickness monitor should be calibrated. At high deposition rates (> 50 Å/s), it appears difficult to precisely control the deposited amount of antimony, and therefore, the stoichiometry of the deposited precursor film from one deposition to another. Lastly, our system does not allow independent co-evaporation of several compounds, since only one electron-beam source is available; thus a manual position change of the four pocket crucible liner is required and only layered precursor films may be deposited.

185

In conclusion, electron-beam evaporation of metals or sulfide compounds did not appear like the method of choice for Pb-Sb-S ternary phase precursor films, due to:

- poor control of electron-beam deposition rate of antimony metal,

- risk of sulfur contamination of the system using PbS or Sb_2S_3 as evaporation sources,

- lower reproducibility of the electron-beam evaporation process, leading to difficulty controlling the stoichiometry of the as-deposited film,

- lack of independent co-evaporation capability.

Thus, bearing in mind the requirements on the film crystallinity and morphology (single-phased with preferably large crystallites ($>$ 1 μm), dense and smooth films) and also considering the technical and practical limitations arising from our particular experimental set-up, the first preparation approach was simple and consists of the reactive annealing in H_2S or sulfur vapor of metallic precursor films deposited via DC-sputtering of lead and antimony metal targets. DC sputtering of metals such as Pb and Sb is very reproducible for a set of deposition parameters, once deposition rates have been calibrated. Moreover, with two independent DC sources and three distinct magnetrons, our system enables both co- and sequential sputtering of the two different metals to respectively generate alloyed or layered metal precursor films. As mentioned earlier, DC sputtering is a scalable process used in the photovoltaics industry and has yielded very efficient CIGS thin-film solar cells.

186

In this chapter, the preparation of Pb-Sb-S ternary phase thin films from reactive annealing in H_2S or sulfur vapor of metal precursor films is reported. Experimental preparation and characterization will be briefly recalled from Chapter 2, enhancing relevant details to this chapter. Results on the preparation of Pb-Sb-S ternary phase thin films by reactive annealing of metal precursor films in both H_2S and sulfur vapor will then be presented and discussed.

5.2 Thin-film preparation and characterization

Precursor films were deposited on iso-propanol-cleaned glass slides via magnetron sputtering at an argon plasma pressure of 667 (±3) mPa (5 mTorr). The UHV thin film deposition system had a base pressure of $10^{-6} - 10^{-7}$ Pa. Antimony and lead were deposited via DC magnetron sputtering of Sb and Pb targets (Kurt J. Lesker, 99.999 % and 99.99 % pure, respectively). For antimony, deposition rate calibration was performed both by weighing deposited films and by X-ray reflectometry; while for lead, only the weighing method could be used, as no useful X-ray reflectometry data could be collected. Lastly, WDX analyses were performed on co-sputtered films. The determination of the various deposition rates was achieved with sufficient accuracy to prepare layered and co-sputtered metallic Pb-Sb precursor films. Indeed, as it will be shown later, a precise determination of the as-deposited Sb:Pb ratio is not required, as the stoichiometry is significantly altered during annealing. The deposition calibration works are detailed in Chapter 3. Once deposited, precursor films were annealed either in a H_2S environment in our deposition system annealing chamber, or under sulfur vapor in a two-zone tube furnace. Films were centered in an evacuated tube and heated to a high

temperature (300 °C – 400 °C), while the elemental sulfur was maintained at approximately 185 °C (± 5 °C) at one end of the tube, whereas the other end of the tube remained at room temperature, creating a sulfur flux through the tube.
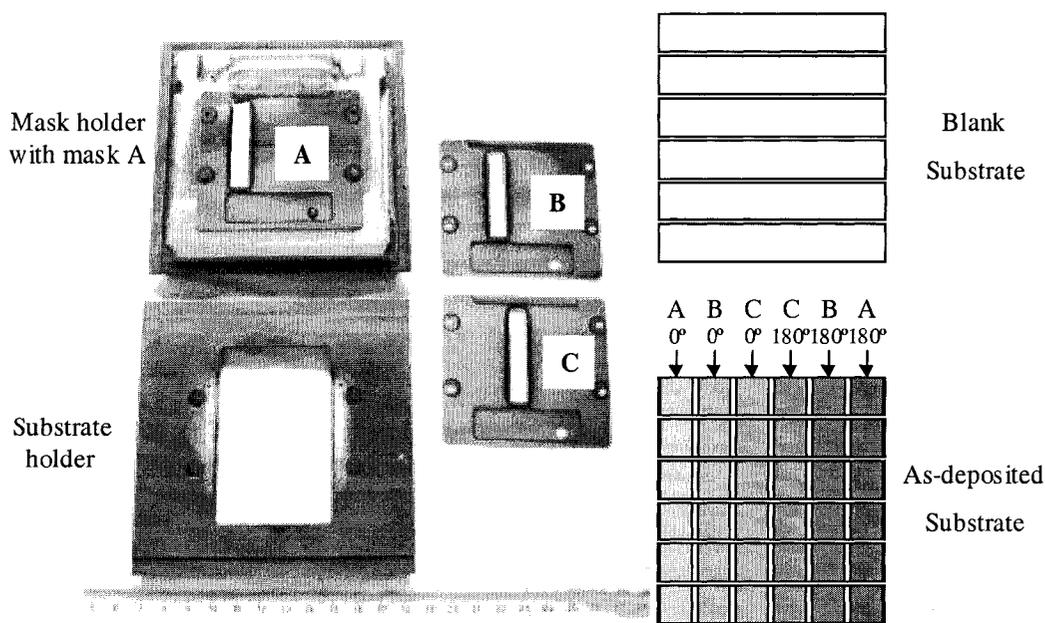
Figure 5.1. Schematic of a combinatorial deposition of six different films (different shades) on six identical pieces of substrate (glass strips). The substrate holder and one of the mask holders are shown, along with the three masks (A, B and C) that are necessary for this combinatorial strategy. The orientation of the blank substrate and the orientations of each mask are also indicated, in order to achieve this combinatorial deposition.

The experimental throughput for the preparation of thin films of plagionite group phases was increased by using a combinatorial approach for films annealed in elemental sulfur. First, the precursor films were deposited on 5×5 cm^2 area made of six 5 cm × 0.8 cm glass strips (1 mm thick). Second, a set of three masks, shown in Figure 5.1, was used. Each mask was positioned 0° and 180° with respect to the substrate, yielding the deposition of six different films on a single glass strip, with each glass strip being identical. As shown in Figure 5.1, if the glass strips are kept in the same orientation, the

188

combinatorial strategy requires six successive depositions using each of the three masks (A, B and C) in two different orientations: 0° and 180° rotations. This combinatorial strategy allows for the annealing of six different films at a time (on a single glass strip) with five different annealing runs; one glass strip was saved for characterization of the as-deposited film. For instance, the six different films deposited could be three different compositions using both layered and co-sputtered precursor films, or the six different films deposited could be co-sputtered (or layered) precursor films with six different compositions. The small film area ($\sim$0.7 $\times$ 0.7 cm^2) is of sufficient size for sequential XRD, SEM and WDX characterization. The relatively high number of identical precursor films was particularly advantageous to screen annealing conditions over exactly the same set of films.

Crystal structures of the films before and after annealing were investigated by standard x-ray diffraction (XRD). Powder patterns were collected with a diffractometer using a Cu Kα source (λ = 1.5418 Å) collimated with a 0.5 mm pinhole collimator and equipped with a GADDS area detector. The diffracted signal was collected from $2\theta = 3°$ to $2\theta = 85°$. Morphologies of as-deposited and annealed films were systematically evaluated with a field emission scanning electron microscope (SEM). Elemental compositions of as-deposited and annealed films were also systematically determined by wavelength dispersive x-ray analysis (WDX), performed on an electron microprobe (EPMA).

5.3   First attempt: H$_2$S annealing of metal precursor films

Once deposited, the sample is transferred from the deposition to the annealing chamber. The annealing chamber, with a base pressure in the mid 10^{-7} Torr, was filled to 50 Torr with H$_2$S$_{(g)}$.Annealing program lengths ranged from 4 to 24 hours. Once, the annealing was accomplished, the annealing chamber was purged with nitrogen overnight, then three cycles of pumping down to $\sim 10^{-3}$ Torr (roughing) and back-filling with N$_2$ were performed. Purges and back-filling were required to remove the hydrogen sulfide from the chamber before opening the gate valve to the distribution chamber. Purge and pump exhaust lines are connected to a scrubber (bleach – Na$^+$ClO$^-$) to neutralize the hazardous hydrogen sulfide. As this procedure is long and, when all included, it may take up to two working days for a single annealing run. In addition, considering the needs of other users for time, the H$_2$S annealing process soon became the bottleneck in thin film preparation. Because of unencouraging morphologies of the films grown using this method and, more importantly, the time-consuming nature of the procedure, only a few experiments could be performed. Results will therefore be presented succinctly.

As previously mentioned, precursor films were either co-sputtered or layered films of lead and antimony. However, most of the films were co-sputtered films, as it was noticed that the layered films have a greater tendency to crack and flake off, due to the presence of strain, with repeat distances of ~250 nm. Moreover, it was also observed that flaking was enhanced when a lead layer was deposited as a bottom layer. This suggests that the adhesion of lead on the substrate is less than that of antimony. One

190

should note that this phenomenon has also been observed for annealing of layered metal precursors in sulfur vapor. Films were deposited so that they had an overall thickness of ~1 to 1.3 μm and were deposited on quartz substrates. Since Sb and Pb co-sputtering was calibrated for a power applied to the lead target of 40 W, the power applied to the lead target was maintained at 40 W while the power applied to the antimony target was varied in order to achieve various Sb:Pb stoichiometric ratios, predicted according to the calibration results presented in Chapter 3. Films were then annealed at various temperatures.

First, some films were annealed at temperatures below 250 °C (4, 9 or 24 hours), yielding rough films with 1 to 5 μm wide voids/cavities. In addition, films were composed of two crystalline phases: galena (PbS) and antimony. This means that these temperatures were too low to activate the ternary phase formation, even with intimate mixing (co-sputtering of Pb and Sb) or thin layers (sequential sputtering of 40 nm of Pb and 55 nm of Sb), but high enough to degrade film morphology and composition (antimony depletion). Thus, to obtain ternary phases, temperatures larger than 300 °C and quite long reaction times were necessary. Annealings at 300 °C to 325 °C with an initial low temperature dwell intended to convert Pb into PbS have therefore been performed. Results are presented in Table 5.1 and Figure 5.2.

As shown in Table 5.1 and Figure 5.2, the morphology of the films was generally poor. Indeed, it seems that under these annealing conditions Pb does not wet the quartz substrate appropriately, thus forming lead-rich lumps and creating "huge" voids. This

was especially observed with Pb rich films (#3, 4, 7 and 8). Also, all films featured needle-like grains: wider than 500 nm and 1 to 10 μm long, consistent with the synthesis of Pb-Sb-S acicular phases present in the PbS-Sb$_2$S$_3$ phase diagram. Films annealed under the longer and hotter conditions (*i.e.* 225 °C for 24h and 325 °C for 12h) showed superior morphologies: no de-wetting, few voids (< 1 μm) and long needle-like grains.
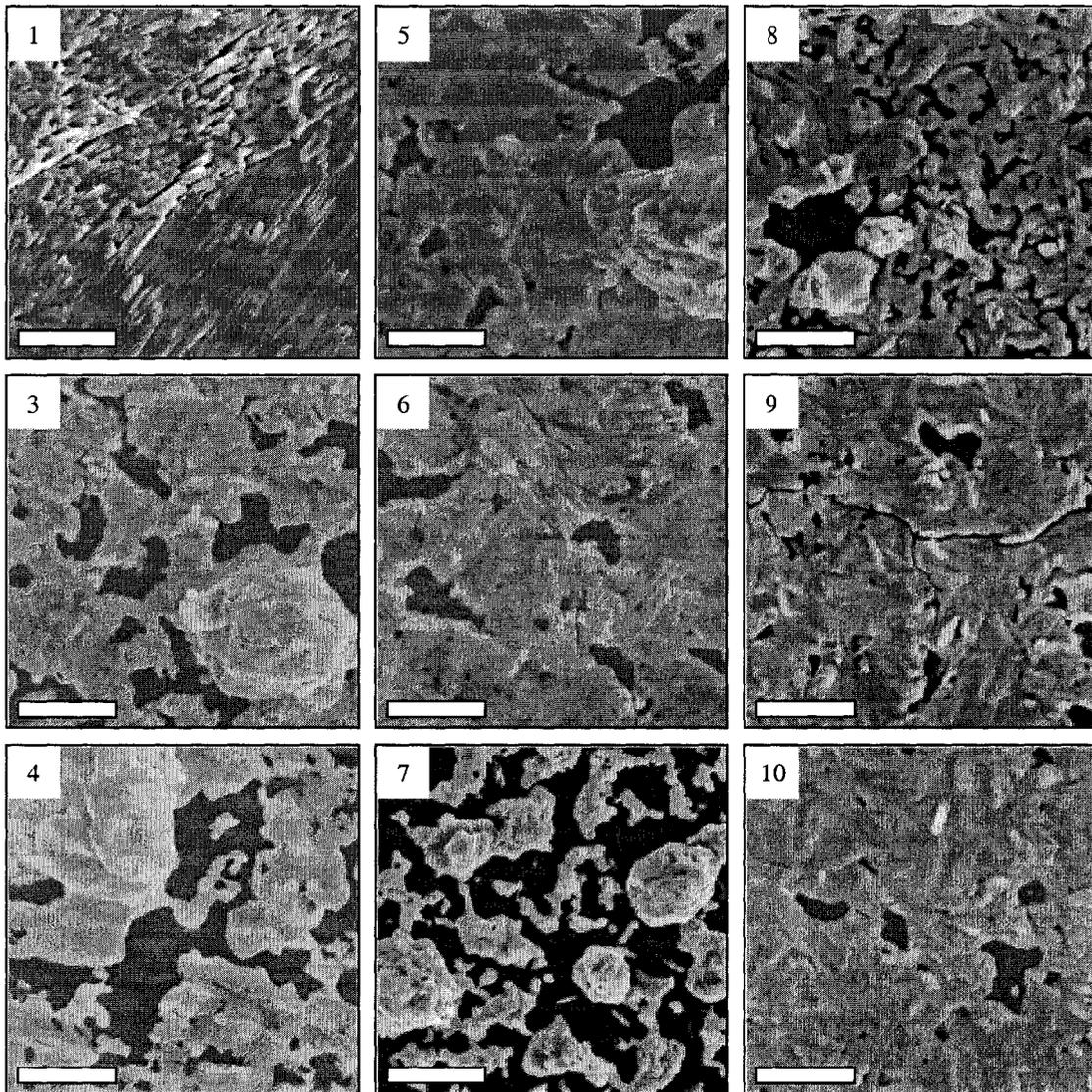
Figure 5.2. SEM images of Pb-Sb-S films obtained from Pb-Sb co-sputtered precursor films annealed in H$_2$S. Image numbers correspond to the film numbers presented in Table 5.1. The scale bars all represent 10 μm. Film #2 (not shown) has a morphology identical to film #1.

192

Table 5.1. Experimental parameters for metallic precursor films annealed in H_2S

Film	Technique	As-deposited Sb:Pb	Annealing Program	Final Sb:Pb[1]	Comments on results
#1	Co-sputtering	2.16	225 °C (24h) + 325 °C (12h)	N/A	1. Flaking 2. Sub-micron voids between grains 3. Needle-like grains (1 to 10 μm)
#2	Layered 5× { Pb : 72nm, Sb : 168nm }	2.16	225 °C (24h) + 325 °C (12h)	N/A	1. Flaking, cracks, de-wetting 2. Sub-micron voids between grains 3. Needle-like grains (1 to 10 μm)
#3	Co-sputtering	1.27	225 °C (10h) + 325 °C (6h)	1.02	1. Rough, de-wetting (10 μm beads) 2. > 5 μm voids 3. Needle-like grains (1 to 5 μm)
#4	Co-sputtering	1.62	225 °C (10h) + 325 °C (6h)	1.42	1. Rough, de-wetting (10 μm beads) 2. > 10 μm voids 3. Needle-like grains (1 to 5 μm)
#5	Co-sputtering	2.16	225 °C (10h) + 325 °C (6h)	1.48	1. Rough, de-wetting (10 μm beads) 2. > 1 μm voids 3. Needle-like grains (1 to 2 μm)
#6	Co-sputtering	2.45	225 °C (10h) + 325 °C (6h)	0.88	1. Rough, de-wetting (10 μm beads) 2. > 1 μm voids (less voids) 3. Needle-like grains (1 to 5 μm)
#7	Co-sputtering	< 0.5	225 °C (15h) + 300 °C (7h)	0.37 (beads) 0.79 (base)	1. Rough, de-wetting (> 10 μm beads) 2. Large voids (> 50 μm) 3. Needle-like grains
#8	Co-sputtering	1.70	225 °C (15h) + 300 °C (7h)	1.53 (beads) 1.69 (base)	1. Rough, de-wetting (10 μm beads) 2. ~5 μm voids 3. Needle-like grains (1 to 2 μm)
#9	Co-sputtering	~3.0	225 °C (15h) + 300 °C (7h)	1.54 (beads) 1.63 (base)	1. Rough, de-wetting (10 μm beads), cracks 2. 2 to 10 μm voids 3. Needle-like grains (1 to 2 μm)
#10	Co-sputtering	> 3.0	225 °C (15h) + 300 °C (7h)	1.57 (beads) 1.57 (base)	1. Rough, de-wetting (5 μm beads), cracks 2. 2 to 5 μm voids (less voids) 3. Needle-like grains (1 to 5 μm)

Note: (1) Films (#7,8,9 and 10) featured beads on top of a film base.

193

It was not possible to positively identify the crystal structure of these films, as a technical issue with the sample stage caused a slight misalignment of the sample during XRD data collection, yielding both positive and negative shifts of the diffraction peak positions. This phenomenon was observed for the PbS (galena) phase, which crystallizes in a cubic (simpler) lattice. Indeed, film #7 is very likely to contain mostly PbS. For the other films, it was not possible to identify the different phases, since they produce many peaks with quite similar patterns: therefore assigning the most intense diffraction peaks, which is crucial for XRD pattern interpretation and subsequent phase identification, could not be achieved. The needle-like shape of the crystals may indicate the formation of acicular phases, such as boulangerite, robinsonite and zinkenite. The problem with the stage required machine shop time and was definitely fixed after this series of experiment was performed. At the time of the experiments, the XRD phase determination was not seen as a major problem as the morphology and composition of the films was not well controlled.

As shown in Table 5.1 with the Sb:Pb stoichiometric ratios of the as-deposited and annealed films obtained from elemental WDX analysis, films always suffered major antimony depletion: from 20 at. % of antimony, for lead-rich films, to 65 at. % of antimony, for antimony-rich films, are lost during annealing. This antimony depletion may be explained by a low reactivity of antimony with hydrogen sulfide, especially at low temperatures, and by the volatility of antimony. Antimony then preferentially evaporates before reacting. Thus, the first annealing stage at 225 °C, intended to convert lead into galena (PbS) below the melting point of lead (~325 °C), may have had a non-

194

negligible contribution on the antimony depletion. A similar explanation involves the reactivity of Sb or Sb_2S_3 (if formed) with PbS *vs.* their re-evaporation. In addition, results on both H_2S and elemental sulfur vapor annealings of pure lead and pure antimony thin films showed that the reactivity of both lead and antimony is greater with elemental sulfur. The H_2S-annealing then requires longer processing times and, therefore, increases the likelihood of film morphology and composition degradation.

In summary, it is difficult to conclude if it is possible to use these types of precursor films (deposited on quartz and annealed in $H_2S_{(g)}$), to obtain "pure" Pb-Sb-S phases thin films with appropriate stoichiometry, crystallinity, and morphology. However, what must be said is that, due to poor initial results (composition and morphology), a large number of samples would have been required for optimization of the film synthesis. Thus, the very low throughput of this annealing procedure made that method inefficient for the development of the Pb-Sb-S ternary phase thin-film synthesis. Consequently, metal precursor films were annealed under elemental sulfur vapor.

5.4 Second attempt: annealing of metal precursor films under sulfur vapor

In an effort to prepare Pb-Sb-S thin films from elemental sulfur vapor annealing of metallic precursor films, both layered and co-sputtered films of lead and antimony have been prepared. The films that yielded the best and most significant results are presented in Table 5.2. Films were deposited on isopropanol-cleaned glass microscopy slides. Film deposition powers and times were determined according to the calibration curves detailed in Chapter 3, in order to obtain films with the desired Sb:Pb

195

Table 5.2. Experimental parameters for metallic precursor films annealed in elemental sulfur vapor

Film	Deposition technique and parameters		As-deposited Sb:Pb
#1	Co-sputtering	30' $\begin{cases} Pb:40W \\ Sb:60W \end{cases}$	0.76
#2	Layered	10× $\begin{cases} Pb:54nm\ (50W) \\ Sb:46nm\ (65W) \end{cases}$	0.69
#3	Co-sputtering	20' $\begin{cases} Pb:40W \\ Sb:104W \end{cases}$	1.70
#4	Layered	10× $\begin{cases} Pb:31nm\ (40W) \\ Sb:61nm\ (65W) \end{cases}$	1.44
#5	Co-sputtering	15' $\begin{cases} Pb:40W \\ Sb:151W \end{cases}$	2.98
#6	Layered	10× $\begin{cases} Pb:22nm\ (40W) \\ Sb:71nm\ (65W) \end{cases}$	2.45
#7	Co-sputtering	20' $\begin{cases} Pb:10W \\ Sb:150W \end{cases}$	11.02
#8	Co-sputtering	45' $\begin{cases} Pb:10W \\ Sb:56W \end{cases}$	4.04
#9	Co-sputtering	67' $\begin{cases} Pb:10W \\ Sb:36W \end{cases}$	2.20
#10	Co-sputtering	80' $\begin{cases} Pb:10W \\ Sb:29W \end{cases}$	1.62
#11	Co-sputtering	110' $\begin{cases} Pb:10W \\ Sb:19W \end{cases}$	0.87
#12	Co-sputtering	118' $\begin{cases} Pb:10W \\ Sb:11W \end{cases}$	0.65

stoichiometric ratios and an overall thickness of about 1 μm. As previously mention in Section 5.2, for this preparation route, the experimental throughput was increased by a combinatorial approach, allowing the annealing of six different films at a time (on a single glass strip) and under five different annealing conditions from a single deposition. Many annealing conditions were tested. Films annealed at temperatures below 350 °C (105 minutes) did not yield any significant conversion of the precursor film into ternary phases, but rather lead to mixtures of PbS (galena) and antimony. It was observed that

196

375 °C was the minimum annealing temperature required to obtain the presence of a ternary phase upon annealing in sulfur vapor. Figure 5.3 shows annealing programs that yielded the most significant results. Most of the annealing programs followed the sequence described below:

film: 25°C $\xrightarrow{\sim30°C/min}$ 300°C (30 min.) $\xrightarrow{\sim20°C/min}$ 375°C to 400°C $\xrightarrow{varied}$

sulfur: 25°C $\xrightarrow{\sim17°C/min}$ 185°C (until the end of film high temperature dwell) ↑ S furnace stopped N_2 flow started
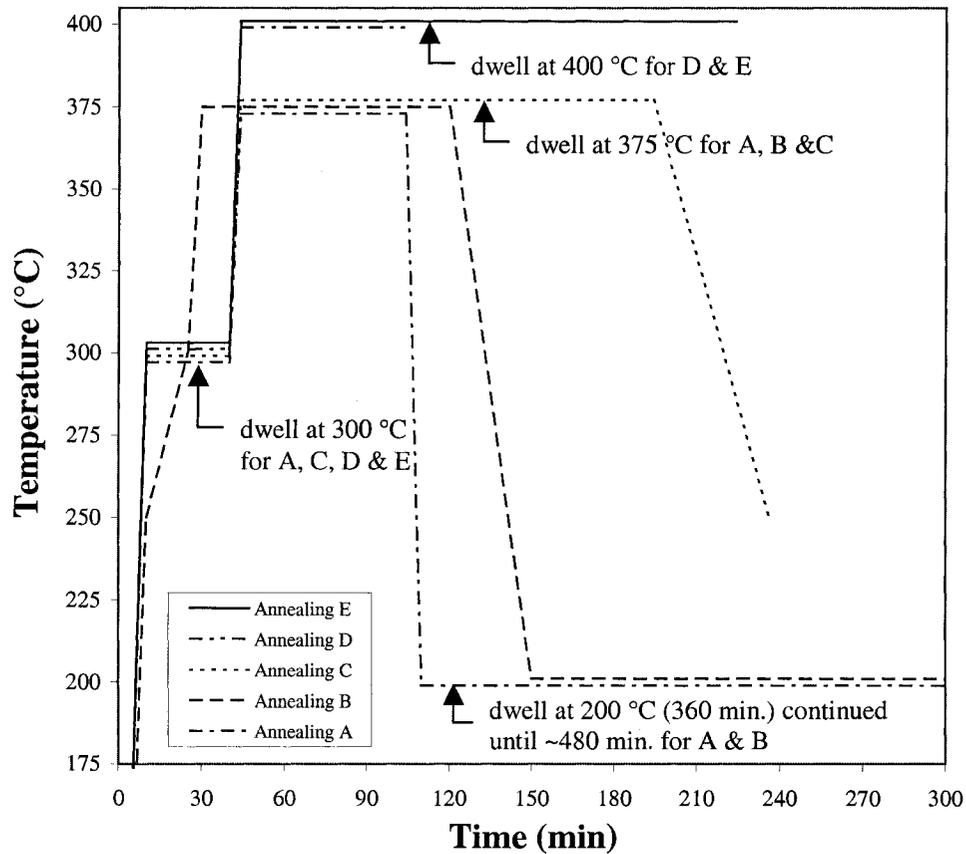
Figure 5.3. Most significant annealing programs: plot of the film temperature as function of time.

The low temperature (300 °C) was intended for the conversion of lead into lead sulfide (galena) at a temperature below the melting point of lead (~325 °C). This low temperature stage was set to be as short as possible (~30 min) since, as shown in the case of H_2S annealing, this stage may favor antimony depletion, as antimony sublimes easily and requires higher temperatures (> 375 °C) to react significantly with sulfur. As

197

one notices for annealing B, this stage was replaced by a slower ramp up to 300 °C. In addition, temperature and length of the high temperature dwell has been varied. Thus, annealings A, B and C featured dwells at 375 °C for 60, 90 and 150 minutes, respectively; while annealing D and E featured dwells at 400 °C for 60 and 180 minutes, respectively. As previously mentioned, at the end of the high temperature dwell, heating of the sulfur source was systematically stopped and a N_2 flow was also systematically set up via a Schlenk line. However, the speed of cooling has been varied. Thus, for annealings D and E, the cooling was very fast as furnace was opened and the tube removed. For annealings of type C, a 3 °C/min cooling rate was maintained until 250 °C, while for annealings A and B, a low temperature dwell was maintained at 200 °C for 6h.

a) *Layered and co-sputtered precursor films*

As was noted before for precursor films annealed in H_2S, the observable differences between co-sputtered and layered precursor films after reaction, in terms of morphology and crystal structure, are small. However, SEM images show that the layered precursor films have a greater tendency to generate cavities and to yield cracked Pb-Sb-S films, which would consequently flake off the substrate. These phenomena are illustrated in Figure 5.4. Both layered and co-sputtered films display > 1 μm aggregates of particles with grain sizes of ~ 0.1 μm, layered films tend to be more porous, as they feature deeper cavities. As shown in Figures 5.4 and 5.5, the different mixtures of PbS and semseyite-like phase were obtained for films #1 to #6 upon the program C:

$$
\begin{cases}
\underline{\text{film}}: & 25°C \xrightarrow{\sim 30°C/min} 300°C\,(30\,\text{min.}) \xrightarrow{\sim 20°C/min} 375°C\,(150\,\text{min.}) \xrightarrow{\text{varied}} \\
\underline{\text{sulfur}}: & 25°C \xrightarrow{\sim 6°C/min} \qquad\qquad\qquad 185°C\,(185\,\text{min.}) \qquad\qquad \uparrow\,\text{S furnace stopped} \\
& \qquad\qquad\qquad\qquad\qquad\qquad\qquad\qquad\qquad\qquad\qquad\qquad\qquad N_2\,\text{flow started}
\end{cases}
$$

198
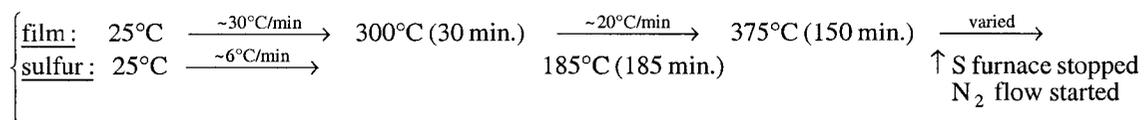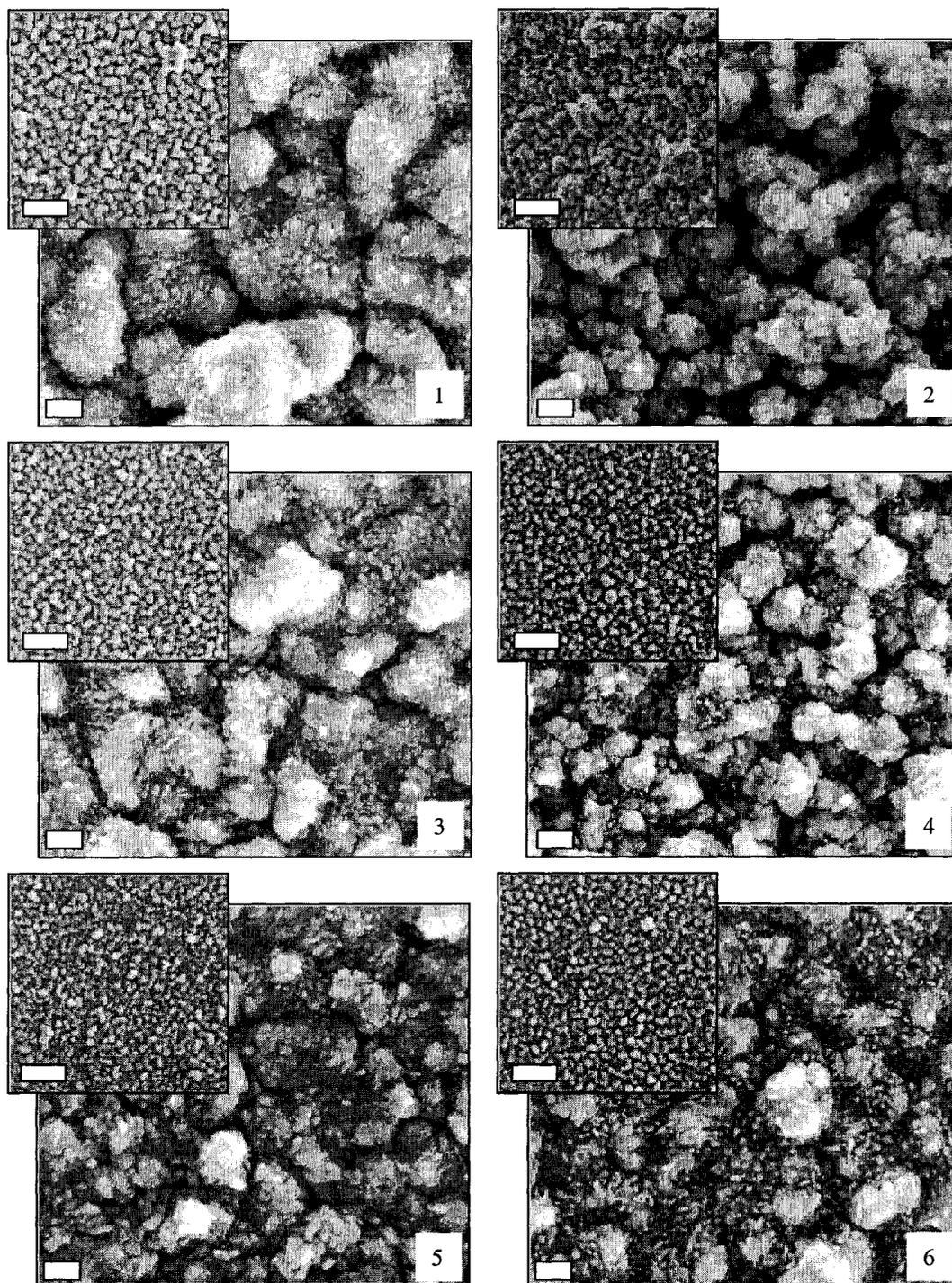
Figure 5.4. SEM images of Pb-Sb-S films obtained from Pb-Sb co-sputtered and layered precursor films annealed in sulfur vapor at 300 °C (30 min.) and 375 °C (150 min.) (annealing C). Image numbers correspond to the film numbers presented in Table 5.2. The scale bars represent 10 μm for the low magnification images (smaller images) and 1 μm for the high magnification images (larger images).

199

(1)

(2)

(3)

(4)

(5)

(6)
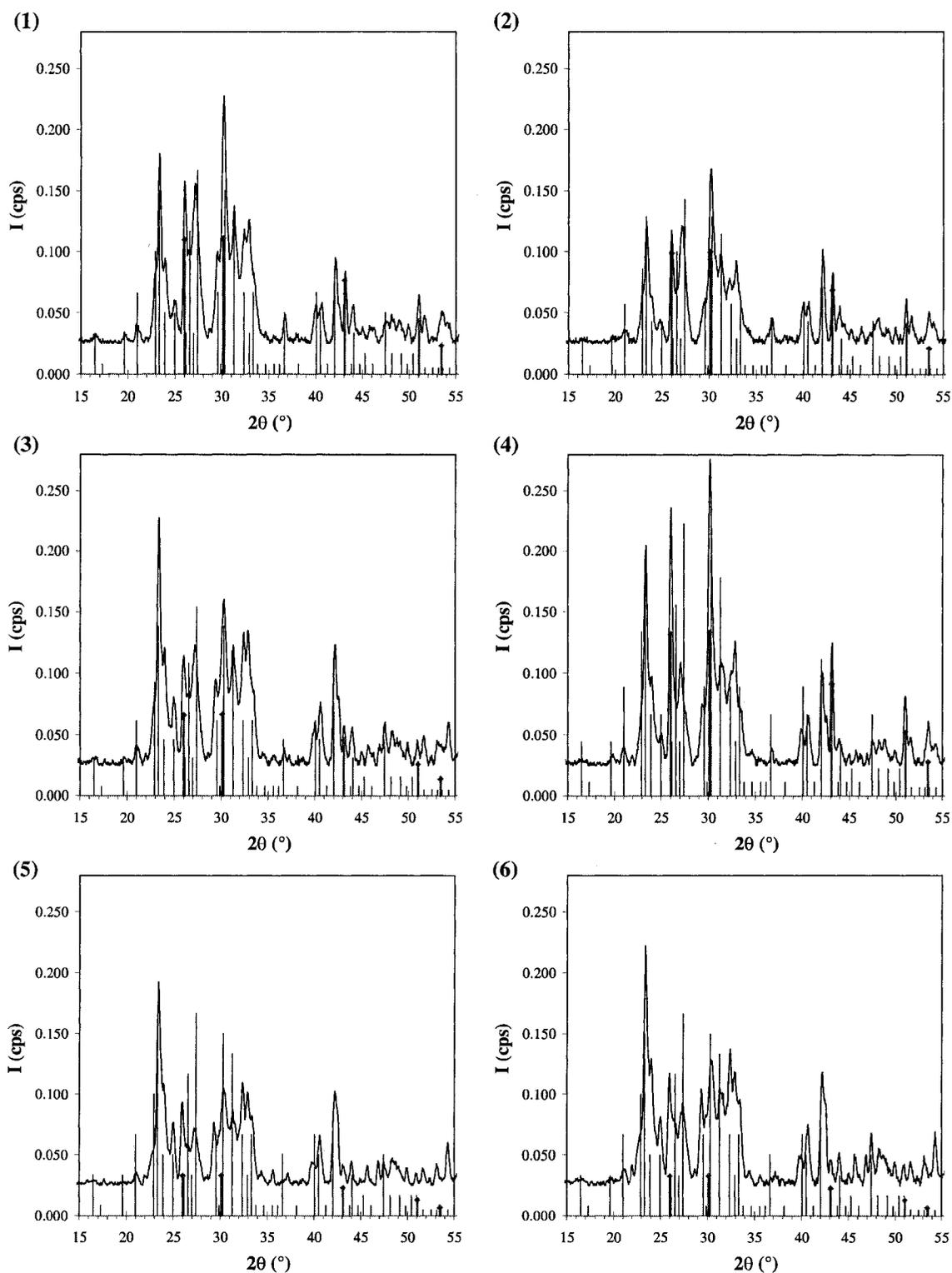
Figure 5.5. XRD data of Pb-Sb-S films obtained from annealing C in sulfur vapor of Pb-Sb co-sputtered and layered precursor films. Pattern numbers correspond to the film numbers presented in Table 5.2. The reference patterns are semseyite (lines) [3,4] and galena (diamonds) [5,6].

200

For comparable Sb:Pb ratios, that is to say comparing film #1 with film #2, #3 with #4, #5 with #6, and for identical annealing conditions, the same phases with both layered and co-sputtered films were obtained. However, by XRD (Figure 5.5), it seems that layered films (#2 and #4) were generally richer in galena (PbS), as the relative peak intensities for the PbS reflection were larger. This phenomenon may be partially, but not completely, attributed to the slightly richer Pb starting composition of the layered precursor films compared to the corresponding co-sputtered films. This difference may also be explained by a lower reactivity of the constituents in the multilayered films compared to co-sputtered films, where constituents are intimately mixed. Indeed, the initially formed PbS then has to react with antimony to form a ternary phase. Two competitive phenomena may occur: diffusion and subsequent reaction of antimony with PbS or evaporation of antimony. Thus, the lower reactivity of the layered precursors may favor antimony depletion upon annealing, leading to PbS richer films.

From now on, one should consider the results presented in Tables 5.4 to 5.9, which gather results for films #7 to #12, respectively, for the annealing types A to E.

b)   *General comments regarding film morphologies and crystallinity*

Considering the morphology of the films obtained using the sulfur vapor annealing method, for most of the precursor films, except for the most antimony-rich (film #7 in Table 5.2), films featured 10 to 100 μm "bumps" on their surfaces, one of the most dramatic cases is shown in Figures 5.7 and 5.9. This is most likely due to expansion of the precursor films upon reaction with sulfur: this creates mechanical stress

and causes de-wetting of the films. The stress may be large, as these "bumps" may collapse, some examples may be observed in Figure 5.7. These morphological defects of the films are detrimental to the preparation of solid state devices, such as thin film solar cells, as they lead to rough and discontinuous films.

For the Pb-rich films (#10, #11 and #12 in Table 5.2), morphologies similar to those of the ones of the PbS films (see Appendix 1) were observed. In other words, films were rough, featuring ~1 micron aggregates of 0.1 μm grains and large cavities in between. Cavities appeared to be larger as the length of the high temperature dwell was increased, *i.e.* for annealings C and E. Now considering the Sb-rich films (#7 and #8 in Table 5.2), these films usually yielded smoother films with a quite flat film base with somewhat larger grains (up to 0.5 μm). Usually, pores were observed, rather than cavities, this is especially true for films #7 and films annealed at 400 °C, *i.e.* annealings D and E.

Finally, a post reaction dwell time at lower temperature (200 °C for 6 hours) were attempted to enhance the film crystallinity, by enabling the ternary phase crystallites nucleated at high temperature to grow into larger crystals. As the temperature was kept low and the tube quenched with N_2 at atmospheric pressure, one should expect no or minor changes in composition at this stage. Thus, films annealed with final long and cooler dwells (*i.e.* annealings A and especially B) present somewhat better submicron morphologies as fewer voids and/or cavities and cracks were observed, and the crystal grains were a bit larger (up to 0.4 μm). However, no positive effect has been

202

observed in the release of film stress, and films annealed under conditions A and B usually featured 10 to 100 μm "bumps" as well.

Except in a few cases, single ternary phase films were not obtained. Indeed, ternary phases were mostly obtained mixed with the binary phases – PbS and/or Sb_2S_3 – upon annealing at 375 °C (*i.e.* annealings A, B and C); while mixtures of two ternary phases were usually obtained upon annealing at 400 °C (*i.e.* annealings D and E). Both tabular (plagionite group) and acicular phase were obtained. Semseyite ($Pb_9Sb_8S_{21}$) and fülöppite ($Pb_3Sb_8S_{15}$), which are plagionite group phases, were obtained. Boulangerite ($Pb_5Sb_4S_{11}$), robinsonite ($Pb_4Sb_6S_{13}$) and zinkenite ($Pb_9Sb_{22}S_{42}$), which are the three low temperature phases present in the $PbS-Sb_2S_3$ phase diagram (Figure 1.14), were also observed. Except for zinckenite, acicular phases have only been observed for annealings at 400 °C, while semseyite and fülöppite were mostly observed for annealings at 375 °C. Overall, semseyite was the phase that was the most easily nucleated and, therefore, was observed over a broad range of starting Sb:Pb compositions.

These observations concerning film morphologies and crystallinity may be explained by careful analyses of the various films and annealing conditions presented in Tables 5.4 to 5.9. Indeed, from these results, and especially the phase that are observed, different reaction pathways may be extrapolated as presented in Table 5.3.

203

Table 5.3. Schematic view of the possible reaction pathways

Initial Sb:Pb ratio of the precursor film	~11.0	~4.0	~2.2 or smaller
Initial ramp up	Formation of PbS	Formation of PbS	Formation of PbS *a dwell increases its extent with detrimental consequences* *Sb does not react with S and Pb at T < 375 °C, therefore Sb re-evaporation may occur due to the volatility of antimony*
375 °C dwell dwell progresses	Nucleation of fülöppite	Nucleation of zinkenite ↓ *Sb depletion* Formation of $Pb_4S_4S_{11}$	Nucleation of semseyite ↓ *Sb depletion* PbS amount increases
400 °C dwell dwell progresses	Nucleation of fülöppite ↓ Sb depletion semseyite	Nucleation of zinkenite ↓ *Sb depletion* robinsonite	Nucleation of semseyite ↓ *Pb depletion* robinsonite ↓ *Sb depletion* boulangerite

Table 5.4. Results for films #7 annealed under conditions A to E

Ann.	SEM image	Phase Identification	Morphology
A		- mostly fülöppite - and textured Sb_2S_3 SIMILAR PATTERN	- no surface crystallite - a few $50\mu m$ pin-holes - $0.1~\mu m$ pores
B		- mostly fülöppite - and textured Sb_2S_3 SIMILAR PATTERN	- delta-plane like crystallite on surface - no pin-holes - a few $0.1~\mu m$ pores - WDX: Sb:Pb=5.1
C		- mostly fülöppite - and textured Sb_2S_3 SIMILAR PATTERN	- no surface crystallites - a few $50~\mu m$ pin-holes - $0.1~\mu m$ pores
D		- mostly fülöppite	- no surface crystallites - more and larger pores: 0.2 to $0.3~\mu m$ pores - 100 nm cube-like grains - EDX: Sb/Pb = 1.3
E		- mostly semseyite	- no surface crystallites - start to flake off - porous with 0.4 to $0.7~\mu m$ pores - crystallites are not as well defined
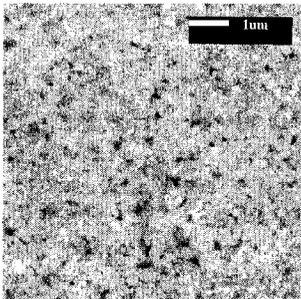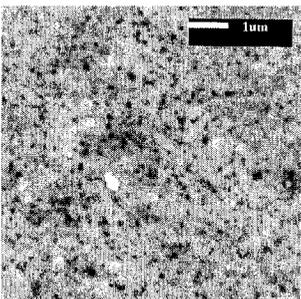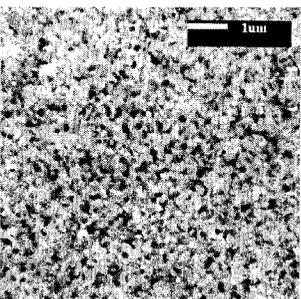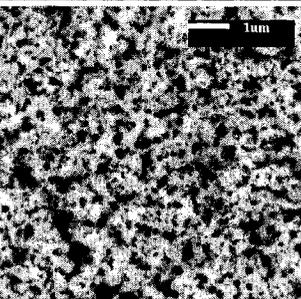
205

Table 5.5. Results for films #8 annealed under conditions A to E

Ann.	SEM image	Phase Identification	Morphology
A		- some zinkenite - a bit of Sb_2S_3 - and probably $Pb_4Sb_4S_{11}$	- few 2 to 5 μm bumps, - quite smooth background - crystal grains: 0.2 – 0.3 μm
B		- zinkenite - a bit of Sb_2S_3 - and a bit of fülöppite	- 10 μm bumps - a few cracks - smooth background - crystal grains: 0.2 – 0.3 μm - WDX: Sb:Pb=1.9
C		- mostly zinkenite - a bit of Sb_2S_3 - and probably $Pb_4Sb_4S_{11}$	- very few 5 μm bumps - a few cracks - crystal grains: 0.1 – 0.2 μm
D		- zinkenite - robinsonite	- 5 to 10 μm bumps - cracks - 0.2 μm voids btw. grains - crystal grains: ~0.5μm long
E		- robinsonite - zinkenite ($\downarrow$)	- 5 to 10 μm bumps - cracks: start to flake off - porous with voids up to 1 μm - 1 to 2 μm needle like grains
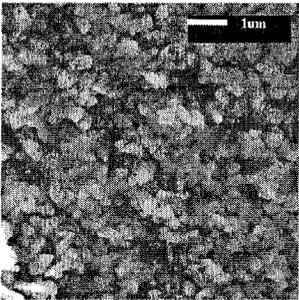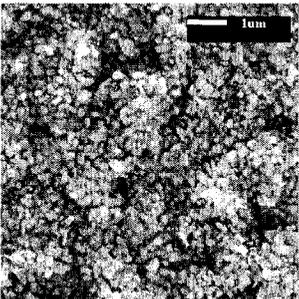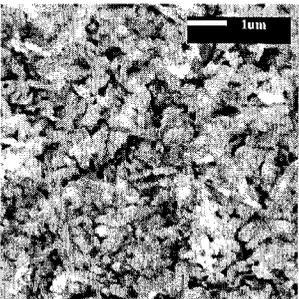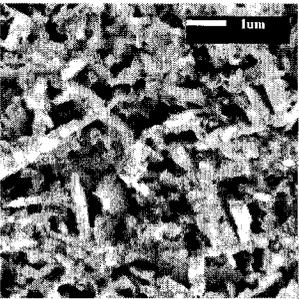
206

Table 5.6. Results for films #9 annealed under conditions A to E

Ann.	SEM image	Phase Identification	Morphology
A		- semseyite - PbS	- 0.5 μm cavities - ~0.2 μm grains aggregated into 1 μm lumps - and also small grains (< 0.1 μm) blended over 2 to 3 μm areas
B		- semseyite - a little bit of PbS	- a few10 μm bumps - 0.3 μm grains blended into 1 μm "plate" - WDX: Sb:Pb=1.1
C		- Semseyite - some PbS (↑)	- 1 μm cavities - ~0.2 μm grains aggregated into 1 μm lumps - and also small grains (< 0.1 μm) blended over 2 to 3 μm areas
D		- semseyite - robinsonite	- 3 μm bumps - cracks: start to flake off near the edge - some 1 μm aggregates - 0.3 – 0.4 μm grains
E		- robinsonite - boulangerite	- very few 5 μm bumps - cracks: flake off - some ~1 μm aggregates - 0.2 – 0.3 μm grains
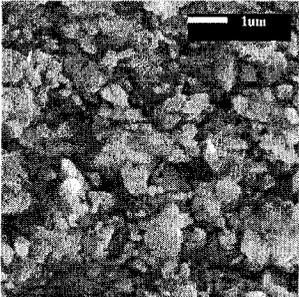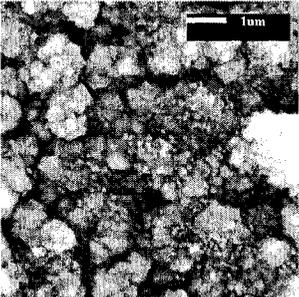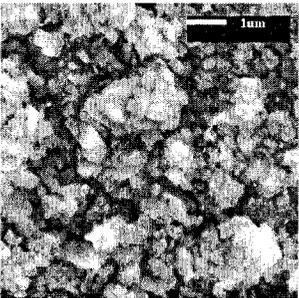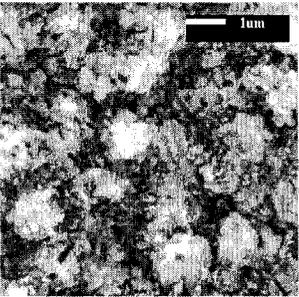
207

Table 5.7. Results for films #10 annealed under conditions A to E

Ann.	SEM image	Phase Identification	Morphology
A		- PbS - semseyite	- ~0.25 μm wide cavities - rough - 100 μm bumps - ~1 μm aggregates - ~0.1 μm grains
B		- semseyite	- pin-holes (on the edge) - 100 μm burst bubbles - 1 μm aggregates - 0.4 μm grains - WDX: Sb:Pb=0.9
C		- PbS - semseyite	- 0.5 μm wide cavities - rough - ~2 μm aggregates - ~0.1 μm grains
D		- robinsonite - a little of semseyite	- cracks: start to flake off - 1 μm aggregates - ~0.3 μm grains
E		- mostly robinsonite	- cracks: flake off - rough - ~1 μm aggregates - ~0.1 μm grains
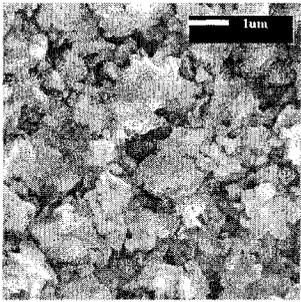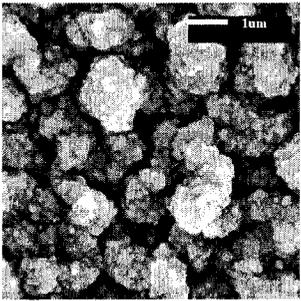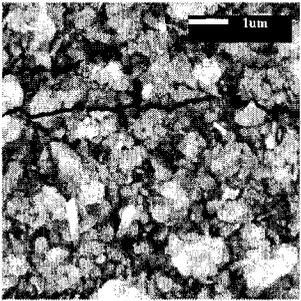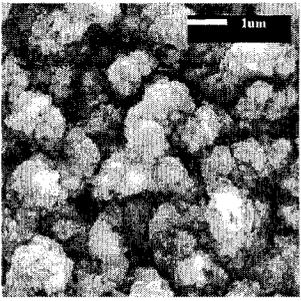
208

Table 5.8. Results for films #11annealed under conditions A to E

Ann.	SEM image	Phase Identification	Morphology
A		- mostly PbS - a little of semseyite	- rough - ~1 μm aggregates - ~0.1 μm grains
B		- semseyite - and PbS	- pin-holes on the edge - up to 100 μm burst bubbles - 1 μm aggregates - 0.4 μm grains - WDX: Sb:Pb=0.8
C		- mostly PbS - a little of semseyite	- rough - ~1 μm aggregates - ~0.1 μm grains
D		- mostly robinsonite - a little of semseyite	- very few 5 μm bumps - cracks - 1 μm aggregates - ~0.3 μm grains (some looked elongated)
E		- mostly robinsonite	- few 5 to 10 μm bumps - rough - ~1 μm aggregates - ~0.1 μm grains
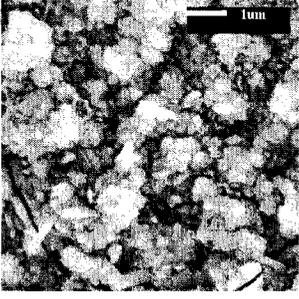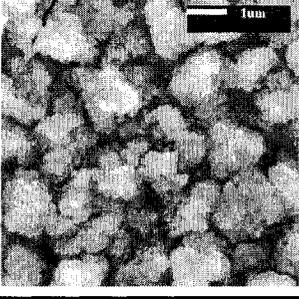
209

Table 5.9. Results for films #12 annealed under conditions A to E

Ann.	SEM image	Phase Identification	Morphology
A		- mostly PbS - a little of semseyite	- rough - a few 50 μm bumps - cavities - < 1 μm aggregates - ~0.1 μm grains
B		- semseyite - and PbS	- pin-holes (on the edge) - up to 100 μm burst bubbles - 1 μm aggregates - 0.5 μm grains - WDX: Sb:Pb=0.5
C		- mostly PbS - a little of semseyite	- rough - cavities - ~1 μm aggregates - ~0.1 μm grains
D		- semseyite - robinsonite	- rough - 1 μm aggregates - ~0.2 μm grains
E		- semseyite - robinsonite	- rough - 100 μm bumps - cavities - < 1 μm aggregates - ~0.2 μm grains
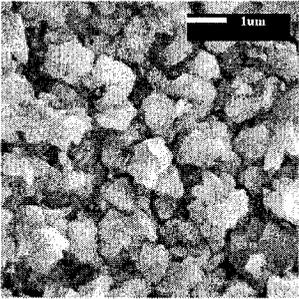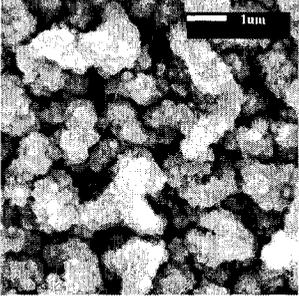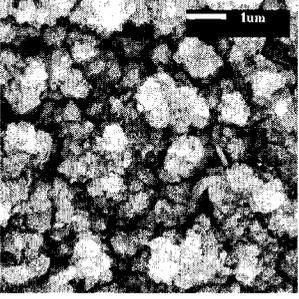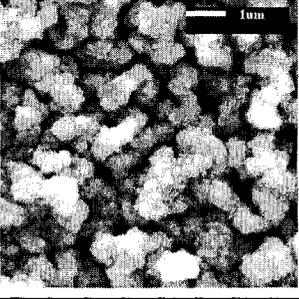
210

c)   *Observation concerning Pb-rich films*

Herein, we first consider the results obtained for the Pb-rich films (#10, #11 and #12 in Table 5.2) for annealings at 375 °C (*i.e.* annealings A, B and C); results are presented in Tables 5.7, 5.8 and 5.9. As previously mentioned, the Pb-rich precursor films annealed at 375 °C with a first dwell at 300 °C (*i.e.* annealings A and C) yielded films with morphologies similar to those of galena (PbS) films. Therefore, it is no surprise that the majority phase, according to the XRD relative intensities, is galena (PbS) formed along with semseyite ($Pb_9Sb_8S_{21}$). As the formation and growth of PbS crystal grains must be enhanced by the 30 minutes dwell at 300 °C, the conversion of the film into Pb-Sb-S phase appeared to be limited, yielding PbS-like films with cavities and aggregates of small 0.1 μm grains. This suggests that the reactivity of the PbS grains with antimony and sulfur is less favorable than antimony re-evaporation at 375 °C. However, with annealing conditions B, which differs from annealing conditions A mostly by the absence of the short (30 minutes) dwell a 300 °C, galena (PbS) is the minority phase, while semseyite ($Pb_9Sb_8S_{21}$) is the majority phase. As one notices, the time spent at temperatures lower than 300 °C was 25 minutes for annealing B instead of 40 minutes for annealings A and C; in addition, the time required to reach 375 °C is 30 minutes for annealing B, while it was 45 minutes for annealings A and C. Thus, the faster ramp to 375 °C in annealing B may limit the formation and growth of galena (PbS) crystal grains, thereby enhancing the proportion of Pb-Sb alloy left to react with the sulfur at 375 °C. So, at 375 °C, the reactivity of PbS with antimony and sulfur seems lower than the reactivity of Pb-Sb alloy with sulfur. In other words, the extent of the PbS inevitably formed in the first stage of the annealing, regardless of the Sb:Pb

211

stoichiometric ratio of the precursor film, may be detrimental to the formation of ternary phases at 375 °C. A consequence of this appears to be the greater antimony depletion in films annealed at 375 °C according to the annealing programs A or C. Indeed, Sb:Pb stoichiometry shifted and for instance, as shown by WDX analyses for annealing B, films #10, #11 and #12 went from Sb:Pb = 1.62, 0.87 and 0.65 to Sb:Pb = 0.9, 0.8 and 0.5, respectively; in other words, it appears that 46, 4 and 18 at. % of the antimony initially contained in the precursor films was lost. Lastly, regardless of the starting Sb:Pb stoichiometric ratio (from 1.62 to 0.65), semseyite was the ternary phase that nucleated. Semseyite is the most Pb-rich plagionite group phase, as shown later in Chapter 6, these phases are believed to be metastable; therefore, the activation energy to form them may be lower, leading to the preferred formation of semseyite from a Pb-rich precursor film. Interestingly, the precursor film that was the closest, in terms of Pb-Sb composition, to semseyite was the least depleted. Also, one should mention that the faster temperature ramp, although reducing the extent of the PbS grains formation, seemed nevertheless to promote the larger morphological defects (> 10 μm "bumps") that are especially noticeable from annealing B.

Annealing with a high temperature dwell at 400 °C yielded the phases semseyite ($Pb_9Sb_8S_{21}$) and robinsonite ($Pb_4Sb_6S_{13}$) for the Pb-rich films (#10, #11 and #12 in Table 5.2). The amount of robinsonite compared to the amount of semseyite seems to increase as the duration of the dwell at 400 °C increases from 1h (annealing D) to 3h (annealing E) and as the initial Sb:Pb ratio of the film increases (film #12 to film #10). After the formation of galena (PbS) during the 30-minute dwell at 300 °C, galena then react with

212

antimony and sulfur at 400 °C to form the semseyite, the most lead-rich plagionite phase, believed to be metastable and, therefore, preferentially nucleated from a Pb-rich precursor film. However, long duration heating of these phases is known to lead to their decomposition into acicular phases, which are stable in the PbS-Sb_2S_3 phase diagram [7,8]. Thus, as the high temperature dwell progresses, the initially formed semseyite either reacts with unreacted antimony or slowly transforms to robinsonite. The PbS-like morphology of the film may be explained by the initial formation of PbS and the growth of semseyite from this PbS, and the subsequent transformation into robinsonite. These phenomena seem all the more acute when the initial composition of the precursor film is lead rich. Lastly, films annealed at 400 °C and cooled down rapidly were more likely to feature cracks and, consequently, flake off the substrate. Regarding the Sb:Pb composition changes, as robinsonite (1.50) and semseyite (0.89) were formed upon annealings at 400 °C (*i.e.* annealings D and E), films #11 and #12 with starting Sb:Pb ratio of 0.87 and 0.65, respectively, appear to be lead deficient, while film #10 with a starting Sb:Pb ratio of 1.62 appears to be antimony deficient. Considering the films that appear to be lead deficient, antimony losses probably occurred first followed by lead losses during the transformation into robinsonite, explaining thereby the enhanced formation of cavities.

The case of film #9, presented in Table 5.6, may also be classified into this section, as semseyite is formed along with PbS at 375 °C (*i.e.* annealings A, B and C) and as semseyite and robinsonite are formed at 400 °C (*i.e.* annealings D and E). As previously observed, one may notice an increase in the amount of PbS formed with

213

annealings A and C. However, as the initial amount of lead in the film is much less, PbS is never formed as a majority phase. Finally, at 400 °C, semseyite is partially converted into robinsonite after one hour and is mostly converted into robinsonite and boulangerite after three hours, the formation of boulangerite, a more lead-rich phase suggests antimony depletion as the 400 °C dwell progresses. Thus, regarding the Sb:Pb composition change, the starting film had a Sb:Pb of 2.2 whereas both annealings at 375 °C and at 400 °C yielded fairly lead rich phases: robinsonite, semseyite and boulangerite with Sb:Pb ratios of 1.50, 0.89, and 0.80, respectively, suggesting overall antimony depletion. Lastly, as less galena (PbS) is initially formed, the morphology of the film is not completely similar to the ones of the films previously described.

d)   *Observation concerning Sb-rich films*

       The results obtained for the very antimony-rich film #7, presented in Table 5.4 should be considered first. Annealings A, B and C at 375 °C yielded films with the same powder patterns and very similar morphologies featuring 0.1 μm pores. Contrary to what was observed for the Pb-rich precursor films, no definite effect of the 30 minute 300 °C dwell could be observed. Indeed, as there are much fewer Pb atoms in the Pb-Sb alloy film, galena (PbS) grains that form during this first stage may be smaller and more scattered into the antimony atom matrix of the films. Once, the high temperature (375 °C or 400 °C) dwell is reached, it is possible to form Sb_2S_3, which then reacts with the PbS, and, similarly to what occurs in the case of Pb-rich films, fülöppite – the most Sb-rich plagionite phase – forms as its nucleation may be promoted by its metastability. In the case of the 375 °C dwell textured stibnite (Sb_2S_3) always seemed to remain, while short

214

(1h) annealing at 400 °C (*i.e.* annealing D) initially yielded mostly fülöppite. Yet, contrary to what occurs in the case of lead-rich films, as the length of the high temperature (400 °C) dwell increases, fülöppite was not converted into an acicular phase stable in the $PbS-Sb_2S_3$ phase diagram, but rather into semseyite, another plagionite phase. This result suggests that the crystal structure of the ternary phase evolved from the most Sb-rich plagionite phase to the most Pb-rich antimony phase as major depletion of antimony occurred upon heating of the initial fülöppite film at 400 °C. Comparing the annealings A and C, no effect of the final long low temperature dwell at 200 °C may be observed, except for slight increases in porosity and antimony depletion that can be observed for the film annealed upon annealing C at 375 °C for 2h30 without final dwell at 200 °C. Once again, the overall Sb:Pb composition shifted during annealing; in this case, it yields a film that is poorer in antimony than the very Sb-rich starting film. One of the consequences of such a drastic composition change is the increased porosity of the film as the high temperature dwell length and temperature are increased.

For an antimony rich film, film #8, similar to what has been observed for film #7, no strong effect of the 30 minute 300 °C dwell can be observed as the amount of lead in the as-deposited film is only 20 at. %, despite a smoother film base without a 30 minute 300 °C dwell. This is consistent with the lesser amount of the initial PbS formed. Also, comparing the annealings A, B and C, no effect of the final long low temperature dwell at 200 °C may be observed, except for an advantageous slight increase in the grain size. The major difference in this case concerns the ternary phase that is initially formed. Indeed, zinkenite – an acicular phase – is obtained and this even at 375 °C and despite

215

an initial antimony composition suitable for the formation of fülöppite. Zinkenite is formed along with some Sb_2S_3. Annealing at 400 °C caused, once again, significant antimony depletion as the initially formed zinkenite transformed into robinsonite as the high temperature dwell progresses, increasing the films porosity. Interestingly, annealings D and E at 400 °C produced needle-like crystals of 0.5 to 2 μm long, along with some detrimental large voids between these crystal grains unfortunately. Regarding the Sb:Pb composition changes, the starting film had an Sb:Pb ratio of 4 whereas both annealings at 375 °C and at 400 °C yielded more lead rich phases: zinckenite and robinsonite with Sb:Pb ratios of 2.44 and 1.50, respectively, suggesting an overall antimony depletion.

e)   Summary

Table 5.3 gathers the different observations that were made regarding the reaction pathway and the sequential formation of the various phases according to the annealing time and temperature. The extent of the initial formation of PbS for precursor films with Sb:Pb ratio smaller than 2.2, seem to govern the morphology of the film (PbS-like) and reduce the amount of ternary phase that can be formed. A faster ramp up to the high temperature dwell may limit the extent of the PbS nucleation, however, it has very detrimental on the 10 to 100 μm scale morphology of the film. For antimony rich films, as the amount PbS initially formed is less, this effect was not observed.

In addition, at low temperature (*i.e.* 375 °C), if the stoichiometry at that point is appropriate, the most lead rich or the most antimony rich plagionite phases, namely

216

semseyite and fülöppite, nucleate. Moreover, at higher temperature (*i.e.* 400 °C), the transformation of semseyite into robinsonite or boulangerite was observed as the length of the dwell increased.

Thus, the inevitable initial formation of lead sulfide, the difficulty controlling which ternary phase is nucleated first, their subsequent transformation into other possibly more stable phases and the resulting Sb:Pb composition shift during annealing limited the usefulness of the co-sputtered and layered Pb-Sb metallic precursor films for the preparation of device quality-like films. Indeed, phase-pure film syntheses were rarely, if ever, achieved; furthermore, both 10-100 micron and micron scale morphologies presented important defects, that are not suitable for the integration of this films as light absorbers into thin-film solar cells.

f)   Some notable films

Despite difficult controls of the film composition (crystal structure) and morphology, some films were almost phase-pure with encouraging morphology were, somewhat serendipitously, obtained. Thus, fülöppite, semseyite, zinkenite and robinsonite have been obtained nearly phase-pure by XRD and/or with interesting morphologies on the micron scale. Figure 5.6 shows a fülöppite film obtained from precursor film #1 annealed at 400 °C according to the annealing program D. The film is porous with very small grains, 100 nm or less. The XRD pattern matches appropriately with the reference PDF card # 65-2330 [9,10] for fülöppite. Figure 5.7 shows a semseyite film obtained from precursor film #4 annealed at 375 °C according to the

217

annealing program B. The film features large 100 μm bumps, however, its morphology

on the micron scale looks more promising, with 0.3 to 1 μm crystal grains. The XRD

pattern matches appropriately with the reference PDF card # 22-1130 [3,4] for

semseyite.
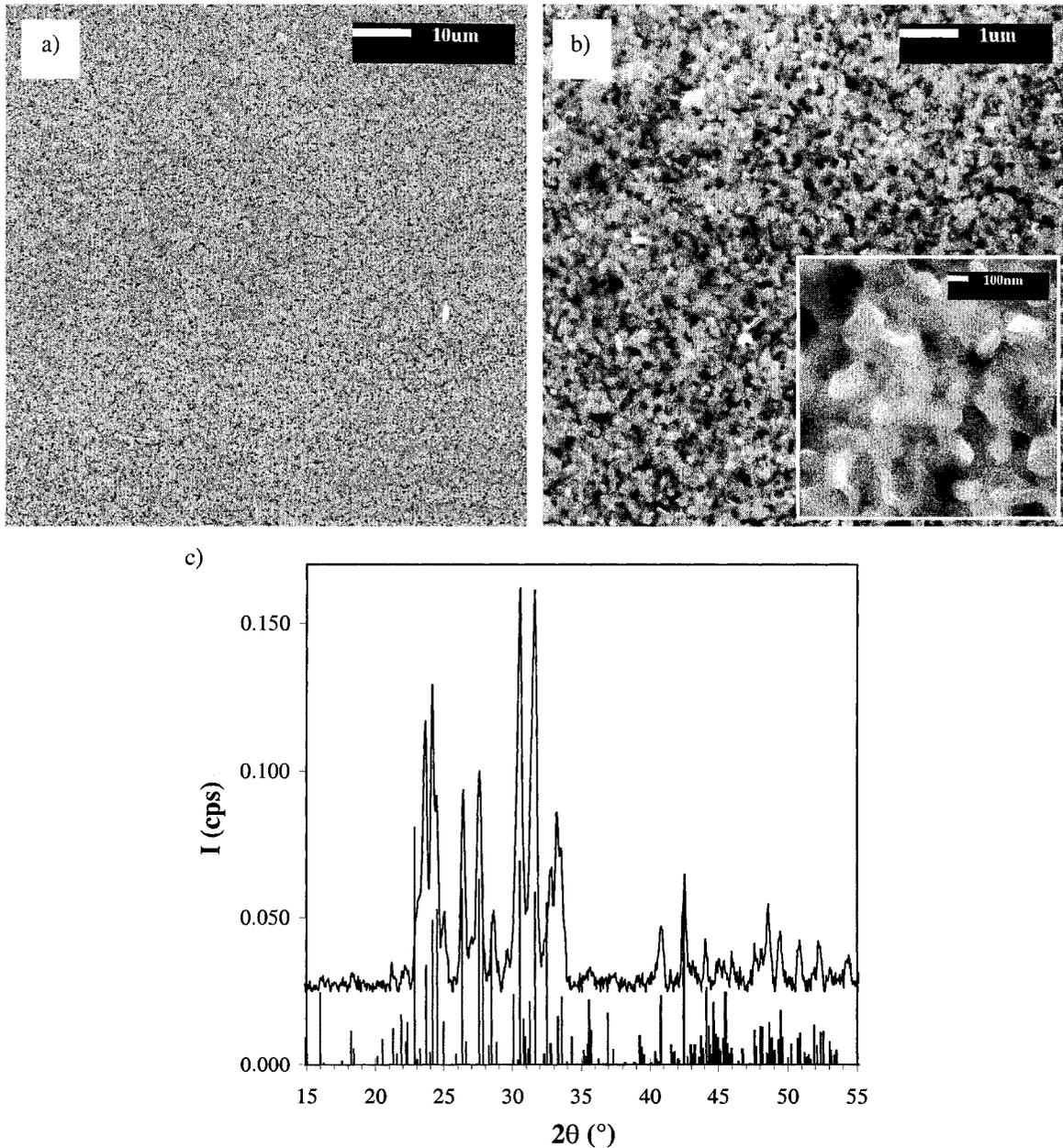
Figure 5.6. Fülöppite ($Pb_3Sb_8S_{15}$) film. a) and b) top surface SEM images. c) XRD pattern and reference for fülöppite (PDF card # 65-2330) [9,10].

218
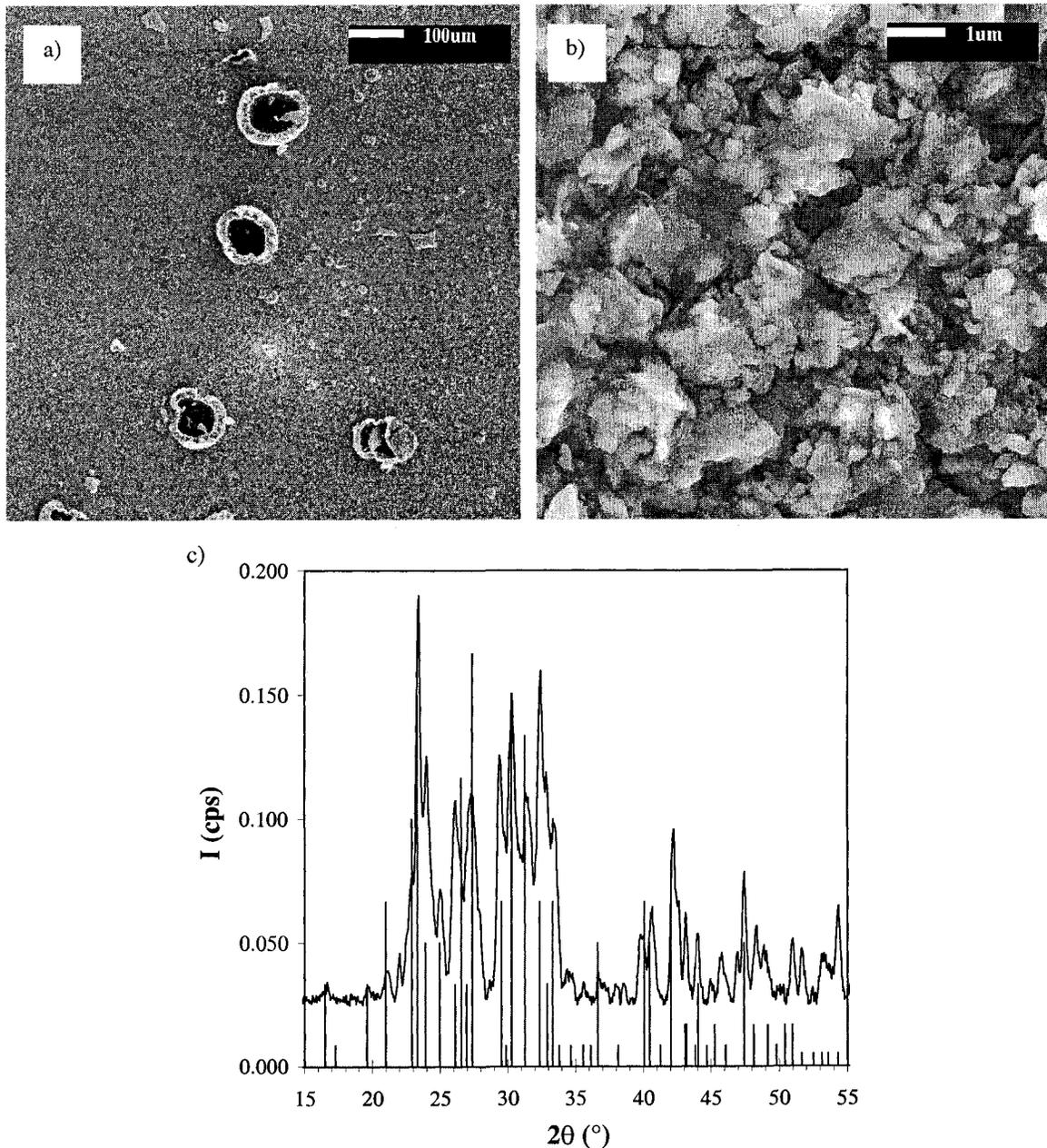
Figure 5.7. Semseyite ($Pb_9Sb_8S_{21}$) film. a) and b) top surface SEM images. c) XRD pattern and reference for semseyite (PDF card # 22-1130) [3,4].

Figure 5.8 shows a zinkenite film obtained from precursor film #2 annealed at 375 °C according to the annealing program B. The film features a smooth base with up to 10 μm bumps, the morphology on the micron scale showed 0.2 to 0.3 μm grains. The XRD pattern matches appropriately with the reference PDF card # 45-1424 [11,12] for

219

zinkenite; one should notice that some Sb_2S_3 is also present in the film, as shown by comparison to reference PDF card # 65-2434 [13,14].

c)
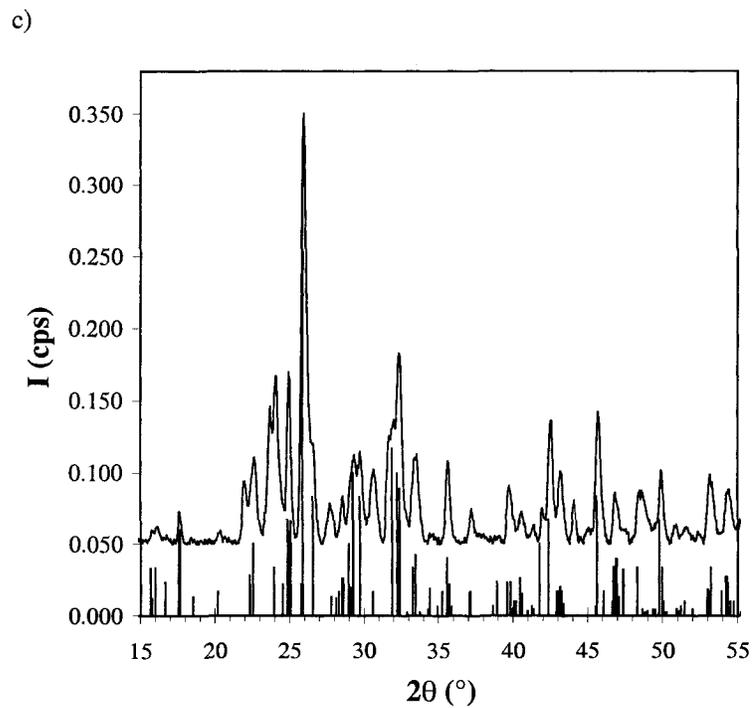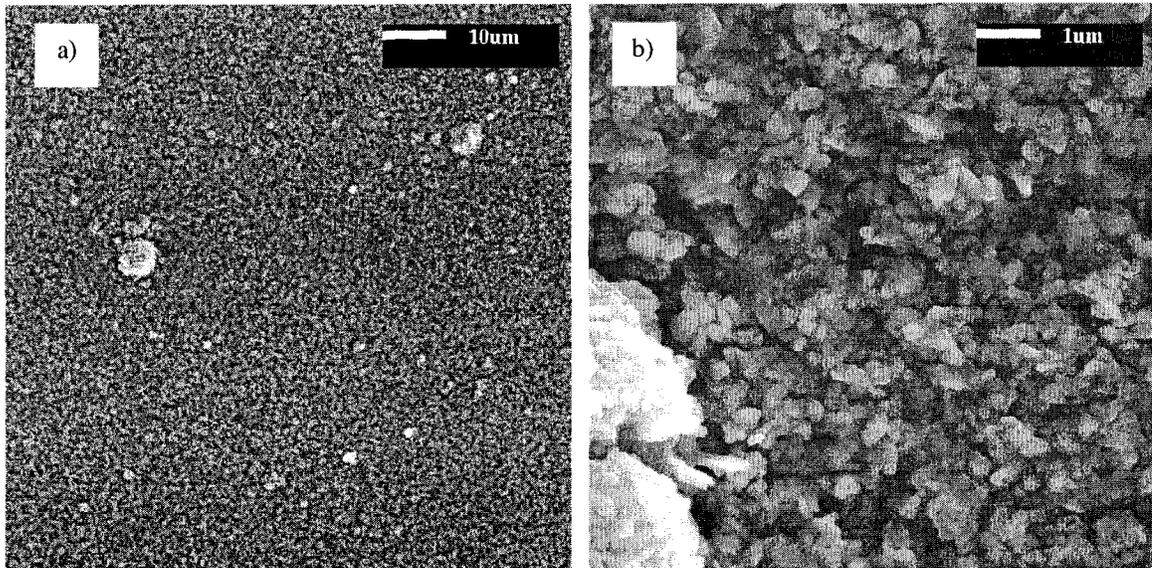
Figure 5.8. Zinkenite ($Pb_9Sb_{22}S_{42}$) film. a) and b) top surface SEM images. c) XRD pattern and reference for zinkenite (PDF card # 45-1424, lighter lines) [11,12] and stibnite (PDF card # 65-2434, darker lines) [13,14].
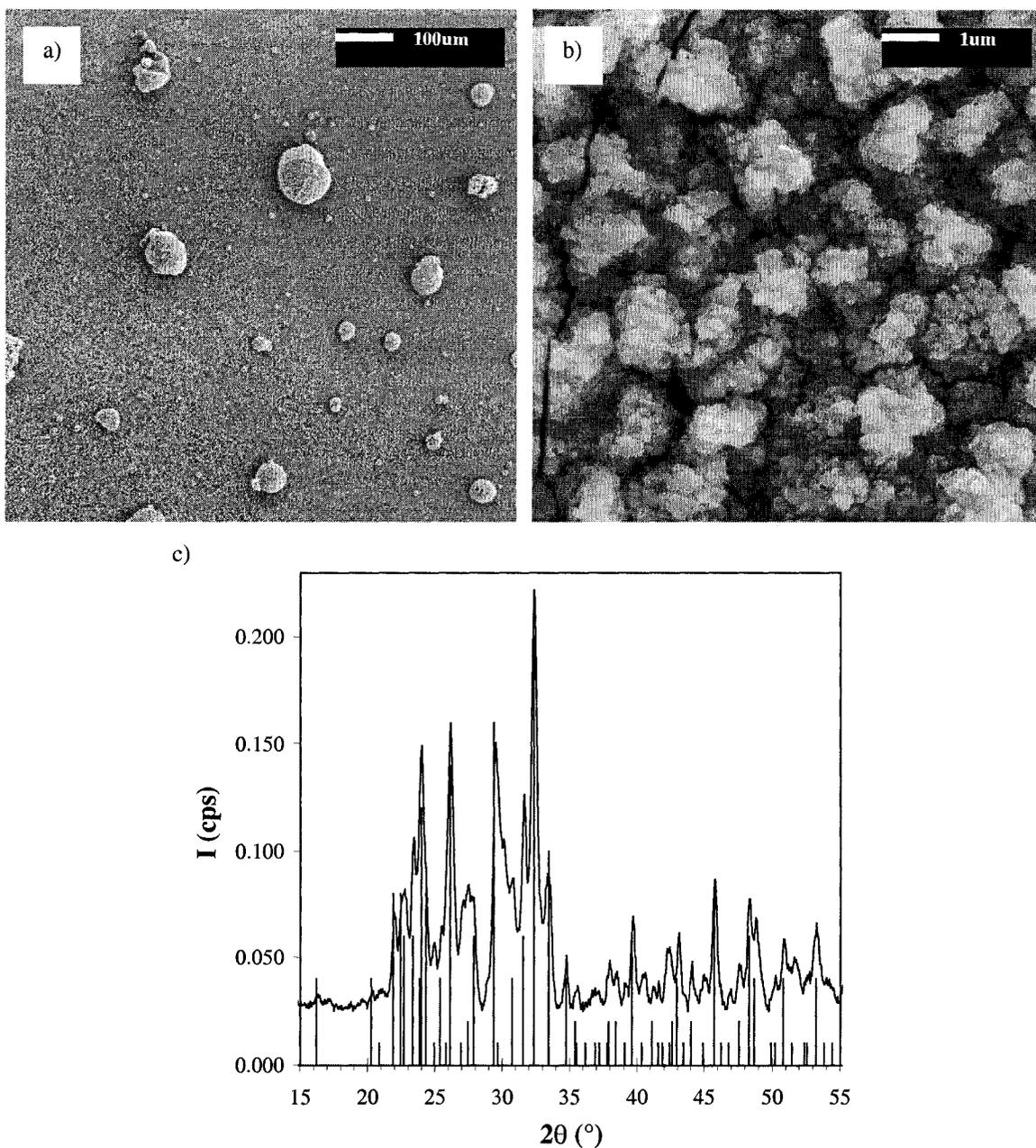
Figure 5.9. Robisonite ($Pb_4Sb_6S_{13}$) film. a) and b) top surface SEM images. c) XRD pattern and reference for robinsonite (JCPDS card # 21-0463) [15,16].

Figure 5.9 shows a robinsonite film obtained from precursor film #5 annealed at 400 °C according to annealing E. The film features large 100 μm bumps, the morphology on the micron-scale is made of 1 μm aggregates of 0.1 μm grains. This film had some cracks as

221

seen on Figure 4.9.b; however, no sign of flaking could be observed. The XRD pattern

matches appropriately with the reference PDF card # 21-0463 [15,16]

5.5   Conclusions

The H_2S annealing procedure appeared to be overly time consuming and poorly

suited to the development of the preparation of thin films of Pb-Sb-S ternary phases,

especially as very little is known about their thin film syntheses. In addition, despite

producing long needle-like grains, this method mostly yielded rough and discontinuous

films. The elemental sulfur vapor annealing procedure allowed for a faster development

of the Pb-Sb-S thin film preparation, from which we gained insight into the behavior and

the reactivity of the Sb-Pb metallic co-sputtered films in sulfur vapor. However, because

of the sequence of phase formation that involves Sb:Pb compositional changes during

annealing, it was not possible to obtain films with both the crystallinity (purity) and

morphology to meet the requirements for their potential integration into thin film solar

cells as light absorbers. Because of the large number of phases that may form with Pb,

Sb and S, more control over the reactivity and stoichiometry is required. Thus, a more

promising and successful approach is to use a sulfur-containing precursor film: the

subject of Chapter 6.

5.6   References

[1]   A. Nunez, P.K. Nair, M.T.S. Nair, Mod. Phys. Lett. B 15 (2001) 605.

[2]   H. Dittrich, K. Herz, in: R.D. Tomlinson, A.E. Hill, R.D. Pilkington (Eds.),
       Ternary and Multinary Compounds: Proceedings of the 11th International

Conference on Ternary and Multinary Compounds, Salford, UK, September 8-12, 1997 Inst. Phys. Conf. Ser. 152 (1997) 293.

[3]   J.L. Jambor, Mineral. Mag. 37 (1969) 443.

[4]   Powder Diffraction File, International Center for Diffraction Data, Newton Square, PA, 2002, Card 22-1130.

[5]   Y. Noda, K. Masumoto, S. Ohba, Y. Saito, K. Toriumi, Y. Iwata, I. Shibuy, Acta Crystallogr., Sect. C: Cryst. Struct. Commun. C43 (1987) 1443.

[6]   Powder Diffraction File, International Center for Diffraction Data, Newton Square, PA, 2002, Card 65-135.

[7]   S.C. Robinson, Econ. Geol. 43 (1948) 293.

[8]   P.L. Garvin, Neues Jahrb. Mine. Abh. 118 (1973) 235.

[9]   A. Edenharter, W. Nowacki, Zeitschrift fur Kristallographie, Kristallgeometrie, Kristallphysik, Kristallchemie 142 (1975) 196.

[10]   Powder Diffraction File, International Center for Diffraction Data, Newton Square, PA, 2002, Card 65-2330.

[11]   A. Kitakaze, A. Sugaki, Scientific Report Tohoku University, Tohoku University, Sendai, Japan, 1988.

[12]   Powder Diffraction File, International Center for Diffraction Data, Newton Square, PA, 2002, Card 45-1424.

[13]   D.O. McKee, J.T. McMullan, Z. Kristallogr.142 (1975) 447.

[14]   Powder Diffraction File, International Center for Diffraction Data, Newton Square, PA, 2002, Card 65-2434.

[15]   J.L. Jambor, G. Lachance, Can. Mineral. 9 (1968) 426.

[16]   Powder Diffraction File, International Center for Diffraction Data, Newton

Square, PA, 2002, Card 21-0463.

224

Chapter 6: Pb-Sb-S Plagionite Phase Thin-films by Reactive Annealing of Layered Amorphous (Sb,S) and Crystalline PbS Precursor Films

6.1   Introduction

As established in Chapter 1, production of electricity using renewable energy sources, and especially photovoltaic solar cells, will play an increasingly important role in the energy sector, encouraged by the rising awareness of global warming and the increasing cost of oil. Solar energy has now proven its feasibility and economic viability thanks to the continual improvement of photovoltaic devices, in particular devices based on crystalline and amorphous silicon technologies. Although the efficiencies of silicon cells are close to the theoretical maximum, their cost remains too high and their energy payback time too long to really compete on the open energy market [1]. Thus, cells based on direct band gap semiconductors that absorb light more strongly are a promising alternative. Because of stronger light absorption, not only is the amount of material required reduced, so are the requirements for film crystallinity and purity. For historical reasons, several of these thin film cells are based on semiconductor absorbers exhibiting a chalcopyrite structure such as $CuInS_2$ and $Cu(In,Ga)Se_2$ (CIGS) or a sphalerite structure such as CdTe. Although the efficiencies of the CIGS cells are excellent and up to 18.4 % for small laboratory cells [2], the availability of indium will ultimately limit their electricity generation capacity to ~1 % of current global electricity production [3]. Moreover, the toxicity of cadmium, for instance, will raise important environmental issues if widely used. Thus, our approach is to prepare thin films of novel semiconductor materials that contain only cost effective, abundant, and relatively less-toxic materials.

225

A systematic study of the potential of many mineralogical compounds for photovoltaic applications indicated that many ternary sulfides exhibit suitable optical band gaps for thin film photovoltaic applications [4]. Indeed, most of the lead antimony sulfides have band gaps (E_g) around 1.4 eV [5,6], close to the optimal theoretical solar-to-electrical-energy conversion efficiency for a single-junction solar cell [7]. Dittrich *et al.* showed that $Pb_5Sb_4S_{11}$ (boulangerite) and $Pb_9Sb_8S_{21}$ (semseyite) displayed "device quality" properties [4] and reported preliminary thermal evaporation and subsequent characterization of multiphase Pb-Sb-S thin films [8]. Among the lead antimony sulfides, four phases known as the plagionite group phases are of particular interest herein. Indeed, $Pb_3Sb_8S_{15}$ (fülöppite), $Pb_5Sb_8S_{17}$ (plagionite), $Pb_7Sb_8S_{19}$ (heteromorphite) and $Pb_9Sb_8S_{21}$ (semseyite) have band gaps of 1.63, 1.53, 1.41 and 1.50 eV, respectively [5,6]. These four phases share common crystallographic features [9-12]. In the laboratory, they had been exclusively synthesized under hydrothermal conditions at temperatures near 400 °C, until we reported the PVD preparation of thin-films of the plagionite phases [13]. Our thin-film growth precludes the presence of hydrogen, indicating that the presence of hydrogen is not necessary for their occurrence, contrary to what was hypothesized previously [14] and suggesting their metastability [13]. Herein, we report the preparation of thin films of plagionite group phases. Structural and optical properties of plagionite group phases thin films are described and discussed.

Lead antimony sulfides have attracted the interest of numerous mineralogists, because of their chemical and mineralogical complexity, as well as their common association with ore-forming sulfides. Among the numerous lead antimony sulfide

226

phases (at least 18 such phases have been identified), most belong to the so called acicular phases, which may be synthesized in the laboratory using conventional solid state methods. However, the four phases known as the plagionite group are distinct from the acicular phases, they adopt tabular crystal habits [14], and share common crystallographic features [9-12]. Moreover, they are relatively rare in nature, and in the laboratory have, until now, been exclusively synthesized under hydrothermal conditions at temperatures near 400 °C. The plagionite phases, both natural and synthetic in origin, decompose into phases stable in the "dry" system upon heating at temperatures above 425 °C [9-12,14,15]. Garvin hypothesized that formation of the plagionite group compounds depended upon an additional essential volatile component, probably hydrogen, that would be liberated upon heating [14]. Thus, for over 30 years, the plagionite compounds have been regarded as not existing on the pure Pb-Sb-S phase diagram.

6.2   Thin-film preparation and characterization

Precursor films were deposited on Piranha etch-cleaned glass slides via magnetron sputtering at an argon plasma pressure of 667 (±3) mPa (~5 mTorr). The UHV thin film deposition system has a base pressure of $10^{-6} - 10^{-7}$ Pa. The layered precursor films were obtained from continuous 100 W RF-sputtering of an Sb_2S_3 target (Sophisticated Alloys Inc.) and cycled 10 W DC-sputtering of Pb with different ON and OFF times to achieve target Sb:Pb ratios. Precursor films with 15, 4 and 5 repeat units were prepared. Once deposited, precursor films were annealed under sulfur vapor in a two-zone tube furnace. Films were centered in an evacuated tube and were usually

227

heated to temperatures of 400 °C for 50 minutes, while the elemental sulfur was maintained at approximately 185 °C (± 5 °C) at one end of the tube, whereas the other end of the tube remained at room temperature, creating a sulfur flux through the tube.

The experimental throughput for the preparation of thin films of plagionite group phases was increased by a combinatorial approach. Indeed, the precursor films were deposited on 2 in. × 2 in. area made of four 2 in. × ½ in. to eight 2 in. × ¼ in. glass strips, that were split in two parts after the deposition, yielding eight (1 in. × ½ in.) to sixteen (1 in. × ¼ in.) identical precursor films per deposition. These smaller films are nevertheless of sufficient size for SEM, XRD and WDX characterization; the largest ones (1 in. × ½ in.) being large enough for optical characterization. This relatively large number of identical precursor films was particularly advantageous to fully characterize the as-deposited precursor film and, more significantly, to optimize the annealing parameters, as very reproducible conditions for the deposition of the precursor films could not be established (see Section 6.3.4). Moreover, because of the reduced size of these precursor films, several films could be placed in the central area of the annealing tube, where the furnace temperature is well controlled. Therefore, the same annealing conditions could be tested for different precursor film compositions and thicknesses.

The morphology of as-deposited and annealed films were systematically evaluated with a field emission scanning electron microscope (JEOL – 6301 F). Crystal structures of the films before and after annealing were investigated by standard x-ray diffraction (XRD). Powder patterns were collected with a Bruker-AXS D8

228

diffractometer using a Cu Kα source (λ = 1.5418 Å) collimated with a 0.5 mm pinhole collimator and equipped with a GADDS area detector. The diffracted signal was collected from $2\theta = 3°$ to $2\theta = 85°$. Elemental compositions of as-deposited and annealed films were systematically determined by wavelength dispersive x-ray analysis, performed on an electron microprobe (JEOL – 8900). The optical transmittance and near-normal reflectance spectra were recorded between 190 nm and 1100 nm using a PerkinElmer Lambda 35 UV-VIS spectrometer with 1 nm resolution at a scan speed of 240 nm/min.

6.3   Layered amorphous (Sb,S) and crystalline PbS precursor films

6.3.1   Layered precursor film structure and PbS formation

Before reviewing the deposition parameters, it is important to know what the layered precursor films are made of. Therefore, a typical layered precursor film is shown in Figure 6.1. SEM images of the layered precursor film are shown in Figure 6.1.a and 6.1.b. The XRD pattern (Figure 6.1.c) indicates that PbS is the only crystalline phase in these films, and qualitative depth profiling analysis (Figure 6.1.d), using TOF-SIMS during Ar^+ sputtering of the film, shows that both the sulfur and antimony content vary together. Therefore, the precursor films are stacks of crystalline PbS layers and amorphous layers containing Sb and S. This layered structure of the precursor films is clearly shown in the back-scattered electron SEM image of the film cross-section (Figure 6.1.b): the brighter layers are made of crystalline PbS, while the darker ones are made of the amorphous phase containing antimony and sulfur.

229
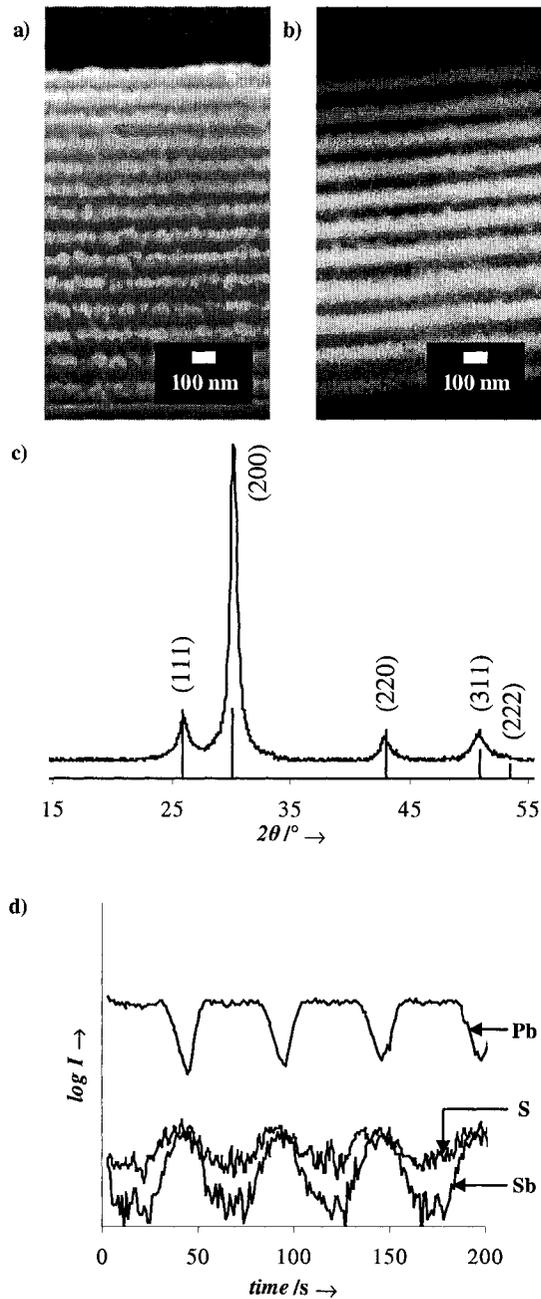
Figure 6.1. As-deposited layered precursor films. a) SEM image, b) backscattered electron image, c) XRD pattern, diffraction plane Miller indices and PbS reference pattern [16,17] and d) TOF-SIMS depth profiling analysis.

As previously mentioned, the layered precursor films were obtained from continuous 100 W RF-sputtering of an Sb_2S_3 target (Sophisticated Alloys Inc.) and cycled 10 W DC-sputtering of Pb with different ON and OFF times to achieve target

230

Sb:Pb ratios, which were determined from WDX data. Moreover, it has also been noted (by WDX) that when sputtering the two targets (Sb_2S_3 and Pb) simultaneously, no Sb or S are deposited on the substrate. Thus, over a deposition cycle, antimony and sulfur are deposited first and then only lead is deposited during the second half of the cycle. Considering the geometry of our deposition system, with off-normal sputtering guns, it is believed that the heavier and more energetic Pb atoms scatter away the lighter and less energetic Sb and S atoms, during the co-sputtering phase of a deposition cycle. This means that, when performing continuous sputtering of Sb_2S_3 and cycled sputtering of Pb, the formation of PbS does not occur during co-sputtering, but rather by interfacial reaction of lead with the sulfur contained in the layer of amorphous Sb and S. This yields stacks of amorphous layers containing Sb and S and crystalline PbS layers.

6.3.2 Layered precursor film deposition parameters

The power applied to the targets (100 W for Sb_2S_3 and 10 W for Pb) and the plasma pressure (667 (±3) mPa) have been kept constant; this should ensure that the amount of material deposited is proportional to the deposition time. Indeed, this is one of the well-known advantages of sputtering, especially for the DC-sputtering of metal such as lead. Nevertheless, some variability of the deposition rates has been observed and will be discussed later.

Table 6.1 gathers the deposition parameters for 14 films from 5 different representative batches (#24, #27, #28, #30 and #32):

- the Sb_2S_3 target number (two different targets were used, because of aging),

231

- the number of repeat units, *i.e.* the number of cycles (15, 4 or 5),

- the Sb_2S_3 deposition time – t_{Sb2S3} – in seconds (Pb target OFF),

- the Pb deposition time – t_{Pb} – in seconds (Pb target ON),

- the sum: $t_{Sb2S3} + t_{Pb}$ in seconds (~400 s),

- the deposition time ratio: t_{Sb2S3} / t_{Pb}.

Moreover, Table 6.1 gathers the following precursor film characteristics:

- the Sb:Pb stoichiometric ratio calculated from WDX data,

- the sulfur content of the precursor films in atomic percent measured by WDX,

- the total thickness of the precursor films in nanometers estimated from SEM images,

- the repeat unit thickness in nanometers (total thickness / number of repeat units),

- the PbS layer thickness in nanometers estimated from backscattered electron SEM images,

- the PbS grain size in nanometers calculated from XRD peak broadening.

232

Table 6.1. Deposition parameters and precursor film characteristics for several experimental batches

Films[1]	Sb_2S_3 target #	# of repeat units	t_{Sb2S3} (s)	t_{Pb} (s)	$t_{Sb2S3} + t_{Pb}$ (s)	t_{Sb2S3} / t_{Pb}	Sb:Pb	% S	total thick.[2] (nm)	repeat unit thick.[2] (nm)	PbS layer thick.[2] (nm)	PbS grain size (nm)
24_a	1	15	122	296	418	0.41	0.74	39	1010	67	60	13
24_b	1	15	142	269	411	0.53	0.86	43	1045	70	55	13
24_c	1	15	213	173	386	1.23	1.54	46	990	66	45	9
27_a	2	15	144	256	400	0.56	1.32	39	1185	79	65	9
27_b	2	15	151	249	400	0.61	1.17	37	1090	73	55	11
28_a	2	15	144	256	400	0.56	0.73	36	755	50	40	9
28_b	2	15	180	220	400	0.82	0.81	36	720	47	33	7
28_c	2	15	226	174	400	1.30	0.99	38	630	41	28	6
28_d	2	15	282	118	400	2.39	1.48	41	560	38	22	5
30	2	4	282	118	400	2.39	1.38	-	195	49	22	8
32_a	2	5	210	190	400	1.11	1.42	40	260	52	33	-
32_b	2	5	258	142	400	1.82	1.98	43	240	48	28	-
32_c	2	5	302	98	400	3.08	3.06	46	250	50	20	-
32_d	2	5	344	56	400	6.14	5.50	48	230	46	14	-

Notes: (1) 14 films from 5 different representative batches (#24, #27, #28, #30 and #32) are presented in this Table.

(2) thick. = thickness.

a) *Number of deposition cycles and overall thickness*

As shown in Table 6.1, precursor films were deposited using 15, 4 or 5 cycles, yielding precursor films with 15, 4 or 5 repeat units (also called bi-layers), respectively. Precursor films made of 15 repeat units (batches #24, #27 and #28) were 0.6 to 1.2 μm thick, while the ones made of 5 repeat units (batch #32) were ~0.25 μm thick. In an effort to reduce the overall deposition time from ~150 minutes per film to ~60 minutes per film, and thereby increase the experimental throughput, thinner precursor films were employed, since preliminary tests proved that it was possible to form and identify the plagionite phases using thinner precursor films. Semseyite, heteromorphite and plagionite thin films presented in this Chapter were obtained from precursor films with 15 repeat units, whereas the fülöppite thin films were obtained from precursor films with 5 repeat units.

b) *Deposition times and repeat thickness*

The bi-layers of amorphous (Sb,S) and crystalline PbS must be interdiffused during a post-deposition annealing process in sulfur vapor to yield Pb-Sb-S ternary phase thin films. In order to obtain films with satisfactory morphologies, annealing time and temperature should be reasonable: according to the experience gained from metallic Pb-Sb (S-free) precursor films and to some preliminary tests, 400 °C and one hour seemed to be the maximum appropriate temperature and duration for the annealing. In this context, preliminary tests showed that bi-layers with thicknesses smaller than 100 nm are adequate for our Pb-Sb-S thin film growth process.

234

As shown in Chapter 3, deposition rate (Å/s) calibrations have been performed for both the Sb_2S_3 (RF-sputtering) and the Pb (DC-sputtering) targets with an Ar plasma pressure of 667 (±3) mPa (5 mTorr). The deposition rate of Sb_2S_3 was measured to be 1.4 Å/s at 100 W (RF, magnetron #3) by film thickness measurements from X-ray reflectometry data and from SEM images of the film cross-sections. Because Pb films are too rough, it was not possible to carry out X-ray reflectometry experiments. Therefore, the deposition rate of Pb was estimated to 0.6 Å/s at 10 W (DC, magnetron #1) by the measurement of the mass of the deposited film over a known area, assuming the bulk density of Pb. This rate was confirmed by film thickness measurements from SEM images of film cross-sections. Assuming no sulfur losses and bulk densities for as-deposited amorphous Sb_2S_3 and for lead, estimates of the required deposition time for given Sb:Pb ratios were made. As will be explained later, the as-deposited Sb:Pb ratio must, in any case, be precisely measured by WDX after deposition, as some deposition rate variability has been observed (see Section 6.3.4).

Thus, the total deposition time for a repeat unit (Sb_2S_3 deposition duration – t_{Sb2S3} (Pb target OFF) plus Pb deposition time – t_{Pb} (Pb target ON)), has been kept constant at 400 s, with repeat units ranging from 40 nm to 80 nm thick, as the Sb:Pb stoichiometric ratio was varied from 5.50 to 0.70 by WDX. This repeat layer thickness range enabled complete interdiffusion of as-deposited sulfur into the lead layer and of the repeat layers during annealing. Indeed, XRD (see Figures 6.1.c and 6.2) of the as-deposited precursor films revealed no sign of crystalline lead and, as will be demonstrated later, they exclusively yielded plagionite group phases under sulfur vapor at 400 °C. The complete

235

interdiffusion and reaction of sulfur with the Pb layer to yield PbS is probably driven by substrate warming during the deposition process. Indeed, sputtering is a high-energy process, and the substrate warms during the deposition as a result of the heat of condensation of atoms, the kinetic energy of incident adatoms and "plasma heating" (*i.e.* bombardment of neutrals and electrons). The temperature, measured by a thermocouple in contact with the deposition platen that supports the substrate holder, usually reaches 40 °C and goes up to a maximum of ~60 °C during the deposition process.

6.3.3 Layered precursor film characteristics

a) *Deposition times, sulfur content, Sb:Pb ratio, PbS content and PbS layer thickness*

As obviously expected, and shown in Table 6.1, the overall sulfur content and the Sb:Pb stoichiometric ratio of the as-deposited precursor film increases with the (fractional) deposition time of Sb_2S_3 within a given batch, while the PbS content (see Figure 6.2) and the PbS layer thickness decreases. Thus, as easily seen in Figure 6.2, which shows XRD data of representative layered precursor films, one can easily notice that as the lead deposition time increases and the Sb:Pb ratio decreases, the PbS signal strongly increases, meaning that more lead sulfide was formed. Moreover, there is no sign of crystalline lead metal (when sputtered separately, as-deposited films of lead are crystalline, as shown in Figure 6.3), meaning that the interdiffusion of sulfur and its reaction with lead is complete by XRD.

236

a)

b)

c)

d)
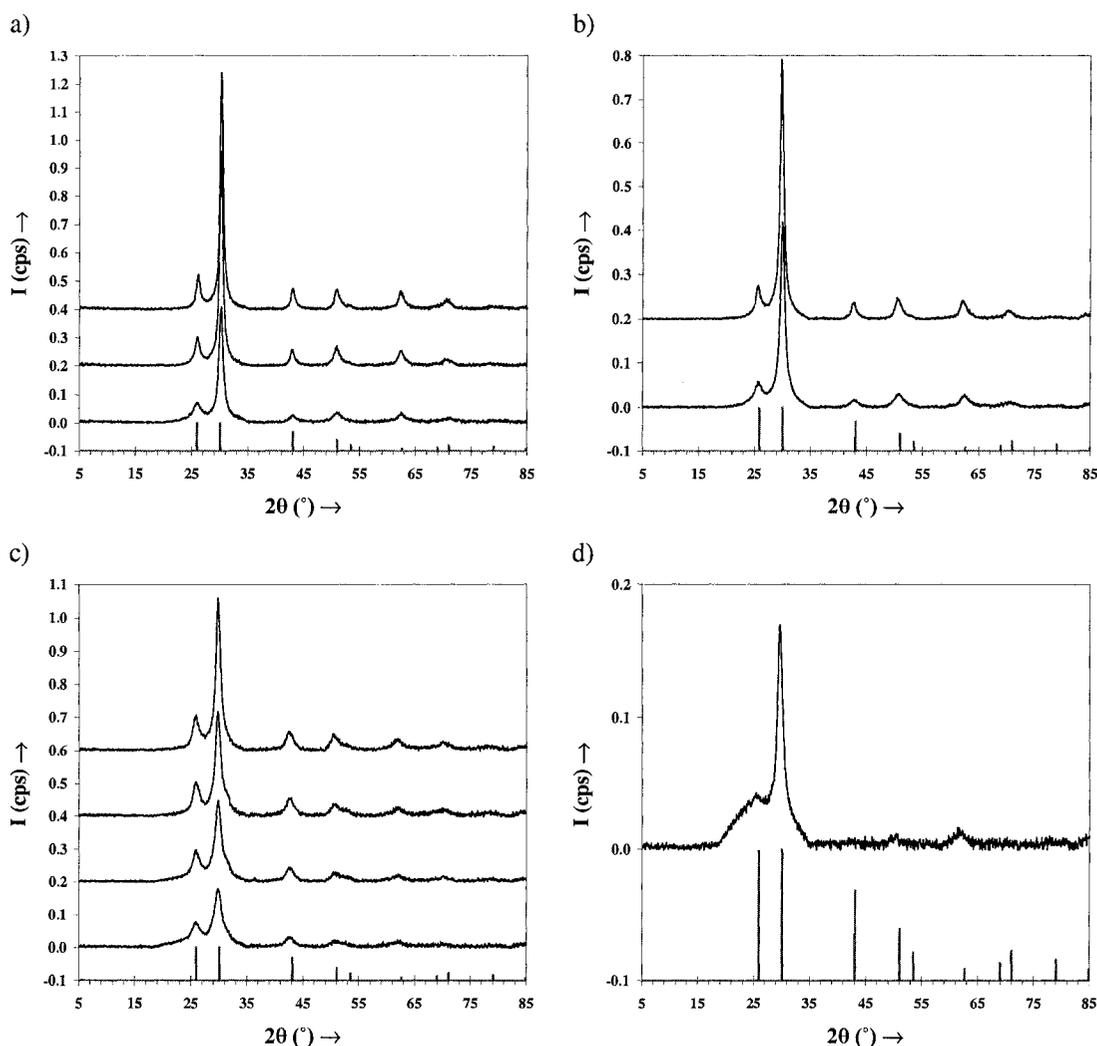
Figure 6.2. XRD patterns of as-deposited precursor films for a), b), c) and d) batches #24, #27, #28 and #30, respectively. On each graph, the lead content of the precursor film increases from bottom to top and the PbS reference pattern [16,17] is given.

Moreover, due to the variability of the deposition process, it is difficult to establish a quantitative relationship between the deposition times of Sb_2S_3 and Pb, the overall sulfur atomic content, the Sb:Pb stoichiometric ratio, or the PbS layer thickness of the as-deposited precursor film. Nevertheless, one notices that the sulfur content of the as-deposited film is generally 41 (±4) at. %, which is less than the target sulfur composition of the plagionite phases (~56 at. %); therefore, annealing in sulfur vapor is

237

required to compensate for the sulfur deficiency. Variability observed in the deposition calibration (Sb:Pb stoichiometric ratio vs. deposition time ratio) will be described and assessed in Section 6.3.4.

b)   PbS crystal growth orientation and PbS crystallite size
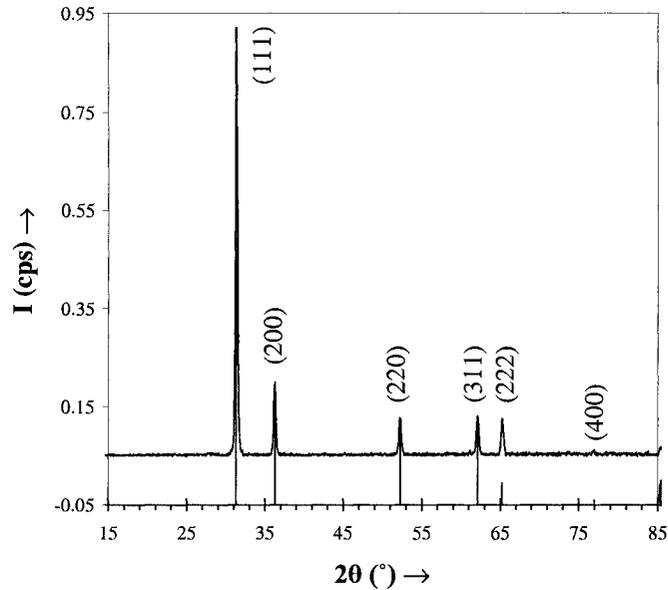
Figure 6.3. XRD pattern of an as-deposited lead film and Pb reference pattern [18,19].

As shown in Figure 6.3, films of lead deposited on glass substrates are polycrystalline and textured, as relative peak intensities show significant differences from the standard pattern. Indeed, they preferentially grew in the [111] direction (*i.e.* the (111) planes are preferentially parallel to the substrate). Moreover, Figures 6.1.b, 6.2.a, 6.2.b, 6.2.c and 6.2.d clearly show that there is also a preferred orientation of the PbS crystallites along the [200] direction (*i.e.* the (200) planes are preferentially parallel to the substrate) in the layered precursor films. Therefore, assuming that the lead deposited on the amorphous (Sb,S) layer is also oriented preferentially in the [111] direction (as is

238

the lead deposited on glass), then the film texture is retained during the interdiffusion and reaction of sulfur with the lead layer. One can hypothesize that the rearrangement of the Pb (111), (222) and (444) crystallographic planes lead to the PbS (200), (400) and (600) crystallographic planes.

Moreover, the PbS crystallite size has been determined from the x-ray line width using the following Scherrer formula:

$$t = \frac{0.9\,\lambda}{\sqrt{B_M^2 - B_S^2}\,\cos\theta_B} \tag{6.1}$$

where t is the crystallite thickness in Å, λ the x-ray wavelength (1.5418 Å for Cu Kα), θ_B the Bragg angle (half the measured diffraction angle), B_M is the width in radians of one of the sample diffraction peaks at half height and B_S is the width in radians of one of the standard diffraction peaks at half height.

The standard peak width B_S should be obtained from a highly crystalline sample with a diffraction peak at a similar diffraction angle to that of the sample. This value represents the instrumental broadening. The standard used was a highly crystalline thin film of lead with crystallites larger than 1 micron by SEM, an XRD pattern of this sample is shown in Figure 6.3. The lead (111) reflection at $2\theta_B \sim 31.3°$ was considered and the instrumental broadening was determined to be $B_S = 0.005$ rad.

The PbS crystallite size has been calculated for several precursor films, particularly for the precursor films that yielded the plagionite phase films presented in this Chapter. The lead sulfide (200) reflection at $2\theta_B \sim 30.1°$ was considered to

239

determined B_M and the crystallite size using the Scherrer formula (6.1) previously written. Results are given in Table 6.1. The calculated PbS grain sizes vary from approximately 13 to 5 nm. Comparison of batches #24 and #28 and film #27_b indicates that the PbS grain size decreases with the thickness of the PbS layer, but remains 4 to 5 times smaller than this thickness of the PbS layer. As one can see, for all the precursor films, the PbS crystallite size is smaller than both the repeat bi-layer thickness and the PbS layer thickness.

6.3.4 Variability in the deposition of layered precursor films
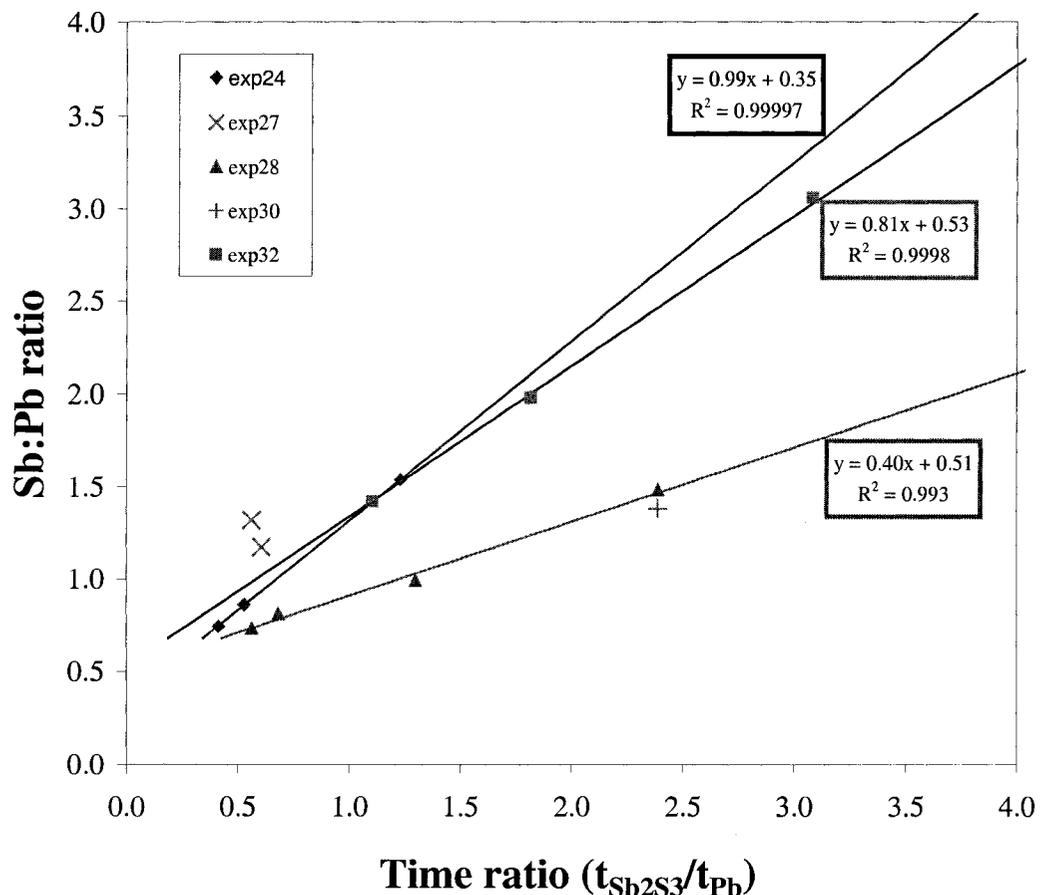
Figure 6.4. Calibration curves of the batches presented in Table 6.1. The Sb:Pb ratio is determined from WDX measurements.

240

Despite careful control of the deposition parameters, some variability in the stoichiometry of the as-deposited precursor films has been observed from one Sb_2S_3 target to another and even from one experimental batch to another. As shown in Section 6.3.1, no Sb_2S_3 is deposited during the Pb sputtering phase, despite the continuous sputtering of Sb_2S_3. The Sb:Pb stoichiometric ratio can therefore be related to the ratio of Pb OFF to Pb ON times. In other words the ratio of Sb_2S_3 deposition to Pb deposition times. Provided that the deposition rates remain constant with constant applied power and plasma pressure, the Sb:Pb stoichiometric ratio should be proportional to the ratio of Sb_2S_3 to Pb deposition times, with a fixed coefficient of proportionality; nevertheless, as shown in Figure 6.4, this coefficient of proportionality varies from 0.40 to 0.99 from one batch to another.

Films of the experimental batch #24 were obtained from one Sb_2S_3 target (target #1), while the other experimental batches were obtained from a different target (target #2). It was necessary to replace the first Sb_2S_3 target, as this target deteriorated during usage. Indeed, large pits and cracks appeared on the surface of the target, ultimately producing important charging of the target (inadequate dissipation of charges generated by the high energy plasma bombardment) and perturbation of the plasma. Indeed, charging occurred at a crack/pit on the electron racetrack of target #1, as indicated in Figure 6.5. It then propagated along the racetrack, causing local melting of the target (brighter part of the electron racetrack), causing vaporization of Sb_2S_3, changing the color of the plasma from purple (Ar^+) to bright green and sharply increasing the pressure in the deposition chamber. A large amount of black soot (Sb_2S_3) was deposited on the

241

target, outside of the electron racetrack as shown in Figure 6.5. Therefore, severely damaged target #1 was retired and target #2 was used. Despite a larger number of deposition cycles and a long overall usage time, no pits and many fewer and much smaller cracks appeared on target #2, as careful power ramp-ups and ramp-downs were implemented, before and after the active deposition phase of the target. Indeed, the power was ramped up from 15 W to 50 W at a rate of 5 W every 30 seconds, and from 50 W to 100 W at a rate of 2 W every 30 seconds; the same rates were used upon ramp down. These careful and slow power ramp-ups and ramp-downs allowed maintained more uniform temperatures across the target, preventing detrimental stress, while its temperature necessarily increased as more power was applied to it.

Some variability from one experimental batch to another has also been observed, despite the fact that deposition parameters have been kept constant, except for the Pb ON and OFF times. First, it is interesting to compare the films from experiments #24_b, #27_a and #28_a, which were all made using very similar conditions. Thus, comparing #24_b with #27_a in Table 6.1, one easily notices that despite similar time ratios, there was a significant difference in the Sb:Pb ratio, ~1.5 times more Sb was deposited with target #2 compared to target #1. It is also interesting to compare experiment #27_a with experiment #28_a, both films were deposited using exactly the same parameters; nevertheless, as one can notice from Table 6.1, there is a large difference in the as-deposited Sb:Pb ratio. 50 % less antimony was deposited in experiment #28_a compared to experiment #27_a. These results demonstrate the large variability of the as-deposited stoichiometry, despite rigorous control of the deposition parameters. It is also interesting

to compare the films from experiments #28_d and #30, which are two films deposited successively with the same target (different days and system loads though). The same deposition parameters were used, but different numbers of repeat layers were deposited. Comparable Sb:Pb ratios were obtained: 1.48 and 1.38.
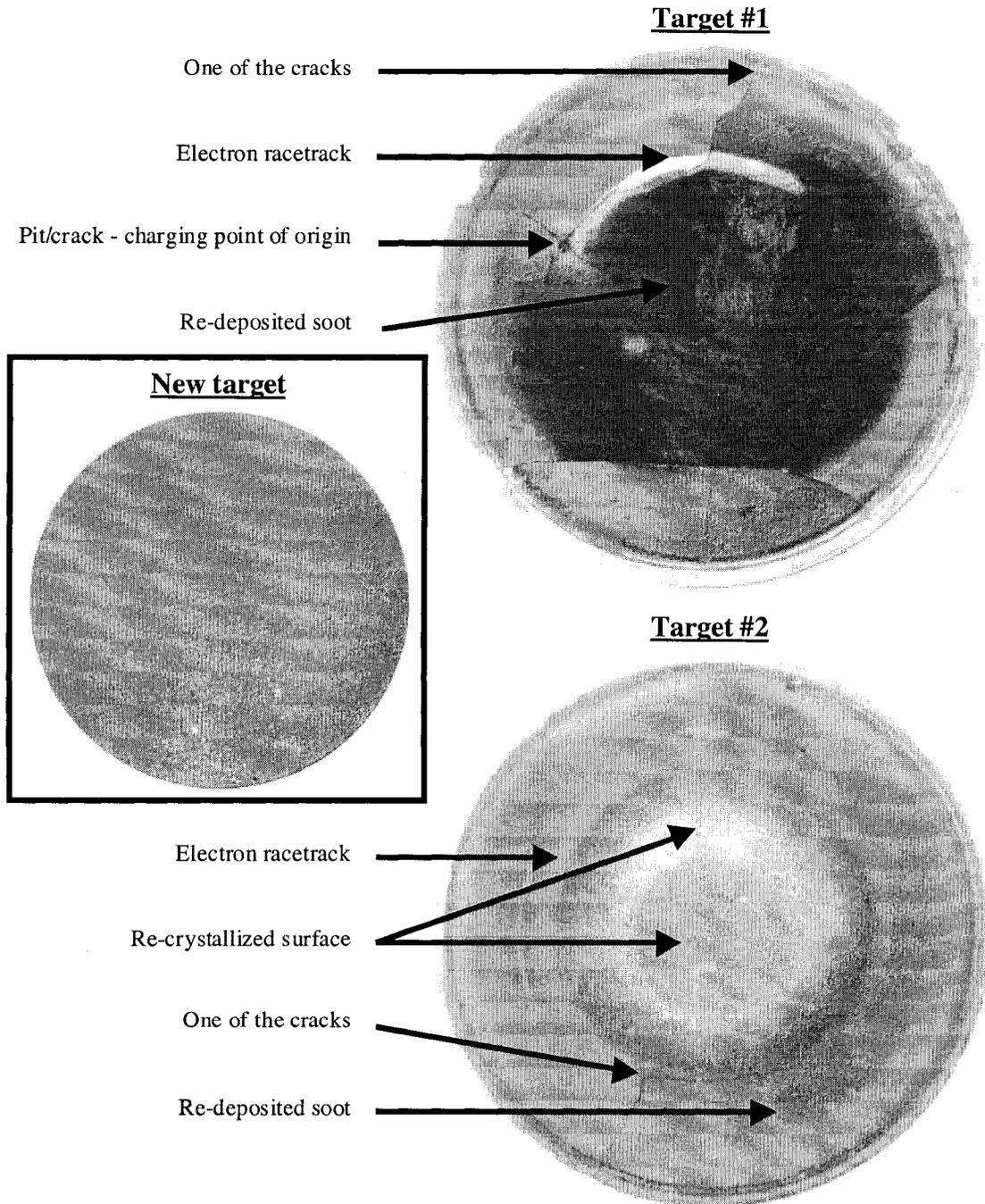
Figure 6.5. Pictures of target #1 after retirement, of target #2 during its lifetime and of a new target.

As shown in Figure 6.4, the linearity of the calibration curves within a given experimental batch is quite good; nevertheless, important variation in the slope of the calibration curves are observed from one experimental batch to another. Indeed, the deposition rate of target #2 decreased from experiment #27, to experiments #28 and #30, and increased with experiment #32; in other words, the slope for the calibration curve obtained for experiment #28 was smaller than the one for the calibration curve obtained for experiment #32. One might say that after a certain number of cycles, target #2 reached a calibration curve that could be compared to the calibration curve obtained for experiment #24 and target #1 just before retirement. One might hypothesize that the deposition rate of the antimony sulfide target evolved with deposition cycle towards some steady state.

In an effort to explain the variability observed in terms of Sb_2S_3 deposition rates, other deposition parameters – Pb and Sb_2S_3 target voltage and current – have been monitored and compared to the Sb:Pb ratio. These two parameters varied slightly with time ($\pm$ 5 V, $\pm$ 5 mA), but a careful treatment of these parameters can not be related to the variations reported above, and therefore does not explain them. Moreover, the value {Sb:Pb stoichiometric ratio / Sb_2S_3:Pb deposition time ratio} is proportional to the deposition rate in $mol.s^{-1}.cm^{-2}$ of antimony and inversely proportional to the deposition rate in $mol.s^{-1}.cm^{-2}$ of lead. The number of moles of Pb (deposited per cm^2) is given by the deposition time of Pb time the molar deposition rate of Pb, which is given in $mol.s^{-1}.cm^{-2}$:

$$n_{Pb} = t_{Pb} \times r_{Pb} \qquad (6.2)$$

244

The number of moles of Sb (deposited per cm^2) is given by the Sb:Pb molar ratio times the number of moles of Pb:

$$n_{Sb} = [Sb:Pb] \times n_{Pb} \qquad (6.3)$$

The molar deposition rate of Sb is then given by the number of moles of Sb divided by the deposition time of Sb$_2$S$_3$:

$$r_{Sb} = {n_{Pb}} \Big/ {t_{Sb2S3}} \qquad (6.4)$$

or

$$r_{Sb} = [Sb:Pb] \times r_{Pb} \times {t_{Pb}} \Big/ {t_{Sb2S3}} \qquad (6.5)$$

therefore,

$$\frac{[Sb:Pb]}{{t_{Sb2S3}} \Big/ {t_{Pb}}} = \frac{r_{Sb}}{r_{Pb}} \qquad (6.6)$$
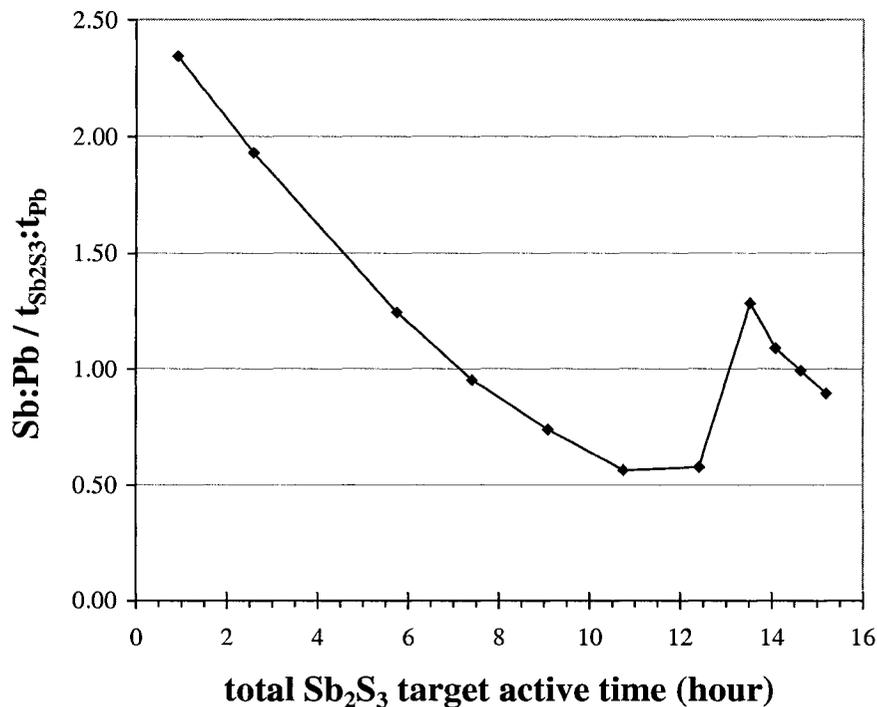
Figure 6.6. Value of the {[Sb:Pb] / [t$_{Sb2S3}$ / t$_{Pb}$]} ratio as a function of the target (target #2) lifetime.

245

A plot of $\{[Sb:Pb] / [t_{Sb2S3} / t_{Pb}]\}$ versus the approximate age of the Sb_2S_3 target (target #2) is shown in Figure 6.6. As own can see, overall, $\{[Sb:Pb] / [t_{Sb2S3} / t_{Pb}]\}$ decreases over the target lifetime, suggesting that the molar deposition rates of Sb and Pb decreased and increased, respectively during the target lifetime. Nevertheless the spike observed after ~12 hours of active use of the target (between experiments #30 and #32) can not be explained. Despite variability in the deposited PbS layer thickness roughly estimated from backscattered electron SEM image, the deposition rate of the lead target should remain constant over the target lifetime. Indeed, keeping the power applied to the target and the plasma pressure constant should ensure that the amount of material deposited is proportional to the deposition time, this is one of the well-known advantages of metal DC-sputtering. Therefore, the variability of the as-deposited Sb:Pb stoichiometric ratio observed, despite the careful and reproducible control of the deposition parameters, is most likely due to the Sb_2S_3 target.

Sb_2S_3 targets were manufactured by Sophisticated Alloy, Inc. (Butler, PA, USA) and produced by sintering of 99.99 % pure Sb_2S_3 (stibnite phase) powder in a hot isostatic press. Sb_2S_3 targets (shown in Figure 6.5) are 3 in. in diameter and 0.125 in. thick. As-delivered target crystallinity was verified in order to detect possible decomposition of the Sb_2S_3 powder during hot pressing. By XRD, the targets were Sb_2S_3 (stibnite) phase pure: no signs of sulfur, antimony metal, or oxides could be detected. Targets were then bonded with silver epoxy to a copper backing plate to allow more efficient cooling and electrical contact of the target with the magnetron gun. Sintering sometimes produces a surface layer, or skin, that is denser than the core of the target

[20]. Nevertheless, that skin should not be more than a few micrometers thick and would have been removed during the first conditioning of the target; indeed, using the deposition rate of Sb_2S_3 at 100 W (1.4 Å/s), the thickness removed from the target during the 60 minutes of conditioning can be estimated at 5 μm. If present, the skin of the target is mostly removed and therefore can not be responsible for the variability observed over the lifetime of the target. Moreover, before every active use of the target, a pre-sputtering was performed (previously mentioned as the power ramp-up) to remove oxides or contaminants prior to the deposition. Thus, the changes to the target surface that occur with use are more likely to significantly affect the deposition rate as the target ages. Indeed, despite the normal appearance of an electron-racetrack due to magnetron sputtering, other surface changes were observed, such as soot or "smut" deposition and surface roughening. Soot deposition observed outside of the racetrack is mostly due to vapor phase nucleation and re-deposition of the material sputtered from the target [20]. The fine particles deposited on the target may have a different sputtering rate than the actual target and, therefore, the time evolution of the amount of soot deposited on the target may affect the overall deposition rate. Another phenomenon that has been observed within the racetrack is some roughening, which may be due to differences in sputtering rates of different crystallographic planes in a polycrystalline target [20]. Also, it seems that some surface recrystallization occurred [20], especially at the center of the target, as the target looks shinier in that area (as shown in Figure 6.5 of target #2). Thus, all of these evolutionary changes may affect the deposition rate of the target over time and, therefore, may explain the variability observed. Obtaining a definitive answer regarding the influence of these phenomena would require a complex study that includes

247

target processing. Such a study is beyond the scope of this thesis, but would be of interest for scientists and engineers focussing on the development of manufacturing processes based on Sb_2S_3 sputtering. Despite the variation observed in the deposition of layered precursors that prevented precise control over the as-deposited Sb:Pb stoichiometric ratio, the deposition of the four plagionite phases was achieved, since many films were deposited, offering a broad range of initial Sb:Pb compositions to work with.

6.4   Structural properties of thin films of plagionite group phases

Table 6.2. Best results for thin films of plagionite group phases

Phase	Precursor film	Annealing conditions	Precursor film Sb:Pb	Annealed film Sb:Pb	$Pb_xSb_yS_z$	Figures
Semseyite $Pb_9Sb_8S_{21}$	28_c	400 °C 50 min.	0.99	0.88	$Pb_{8.6}Sb_{7.6}S_{21.7}$	6.8, 6.9, 6.17
Heteromorphite $Pb_7Sb_8S_{19}$	27_a	400 °C 50 min.	1.32	1.19	$Pb_{6.9}Sb_{8.2}S_{18.9}$	6.10, 6.11, 6.16
Plagionite $Pb_5Sb_8S_{17}$	28_d	400 °C 50 min.	1.48	1.40	$Pb_{5.2}Sb_{7.3}S_{17.4}$	6.12, 6.13, 6.18
Fülöppite $Pb_3Sb_8S_{15}$	32_c	350 °C 120 min.	3.06	2.66	$Pb_{2.9}Sb_{7.7}S_{15.4}$	6.14, 6.15, 6.19

Films of semseyite ($Pb_9Sb_8S_{21}$), heteromorphite ($Pb_7Sb_8S_{19}$), plagionite ($Pb_5Sb_8S_{17}$) and fülöppite ($Pb_3Sb_8S_{15}$) were successfully prepared from precursor films with different ratios of Sb:Pb. Figures 6.8, 6.10, 6.12 and 6.14 are SEM images of these thin films of plagionite group phases, and Figures 6.9, 6.11, 6.13 and 6.15 display the XRD data for these films. Table 6.2 presents the films that, in terms of XRD and WDX, were closest to the pure plagionite group phases. Table 6.2 indicates the precursor film (see Table 6.1) and the annealing conditions that yielded each of the films presented in

248

this Section (Figures 6.8 to 6.15), Section 6.6 (Figures 6.16 to 6.19). In addition, Table 6.2 summarizes the WDX data obtained for these films.

6.4.1   Films phase identifications from XRD and WDX data
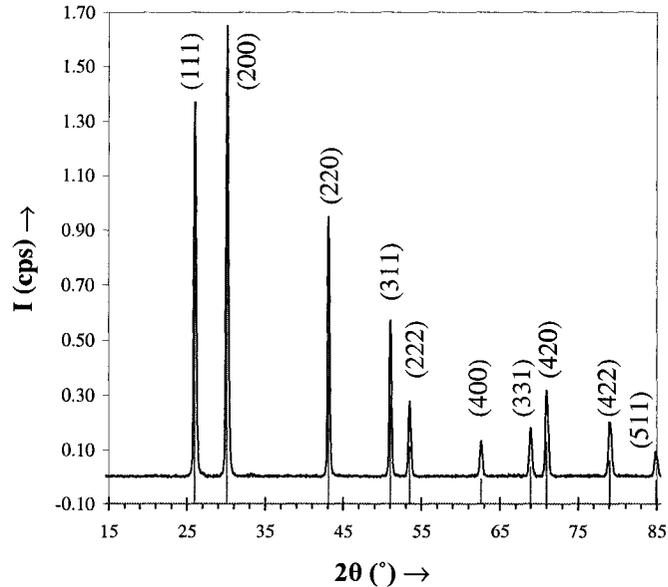
Figure 6.7. XRD patterns of a PbS film obtained by annealing in sulfur vapor of a lead precursor (Figure 6.3) and PbS reference pattern [16,17].

Generally speaking, the thin-film powder patterns match the reference powder patterns satisfactorily and indicate the absence of detectable PbS impurities. In order to assess this absence of PbS (galena) in the plagionite and semseyite films, it is informative to first look at the powder pattern obtained from an ~1 μm PbS film (Figure 6.7), that was prepared by sulfurization of a Pb film (Figure 6.3). Pb films were deposited on glass microscope slides via 10 W DC sputtering of Pb at an argon plasma pressure of 667 ($\pm$3) mPa (5 mTorr). Once deposited, Pb precursor films were centered in an evacuated tube and annealed under sulfur vapor in a two-zone tube furnace. They were heated at 170 °C for 2 hours and then at 300 °C for 5 hours. A sulfur flux was

249

generated across the tube as the elemental sulfur was maintained at ~185 °C at one end of the tube, while the other end of the tube remained at room temperature. PbS (galena) crystallizes in the face centered cubic Fm-3m space group (225). As shown in Figure 6.7, no significant peak position shift can be observed between the experimental film pattern and the reference pattern. Table 6.3 gives the reference peak positions and relative intensities [16,17] as well as the peak positions and relative intensities obtained from the thin film. It is important to note that PbS produces strong diffraction with a maximum count rate around 1.65 counts per second (cps).

Table 6.3. Reference and experimental peak positions and relative intensities [16,17]

$2\theta_{ref}$ (°)	I_{ref} (%)	$2\theta_{exp}$ (°)	I_{exp} (%)	(h,k,l)
25.997	99	26.05	83	(1,1,1)
30.108	100	30.15	100	(2,0,0)
43.099	69	43.15	57	(2,2,0)
51.025	39	51.05	35	(3,1,1)
53.469	21	53.50	17	(2,2,2)
62.591	9	62.60	8	(4,0,0)
68.952	13	69.00	10	(3,3,1)
71.008	23	71.00	19	(4,2,0)
79.017	16	79.05	12	(4,2,2)
84.875	9	84.85	6	(5,1,1)

a)   Semseyite films

The semseyite film shown in Figure 6.8 and which XRD pattern is shown in Figure 6.9 has been obtained by annealing the precursor film (#28_c) with an Sb:Pb ratio of 0.99 at 400 °C for 50 minutes in sulfur vapor. A satisfactory match was obtained with PDF card #22-1130 [9,21]. $Pb_9Sb_8S_{21}$ (semseyite) crystallizes in the monoclinic C2/c space group (#15).

250
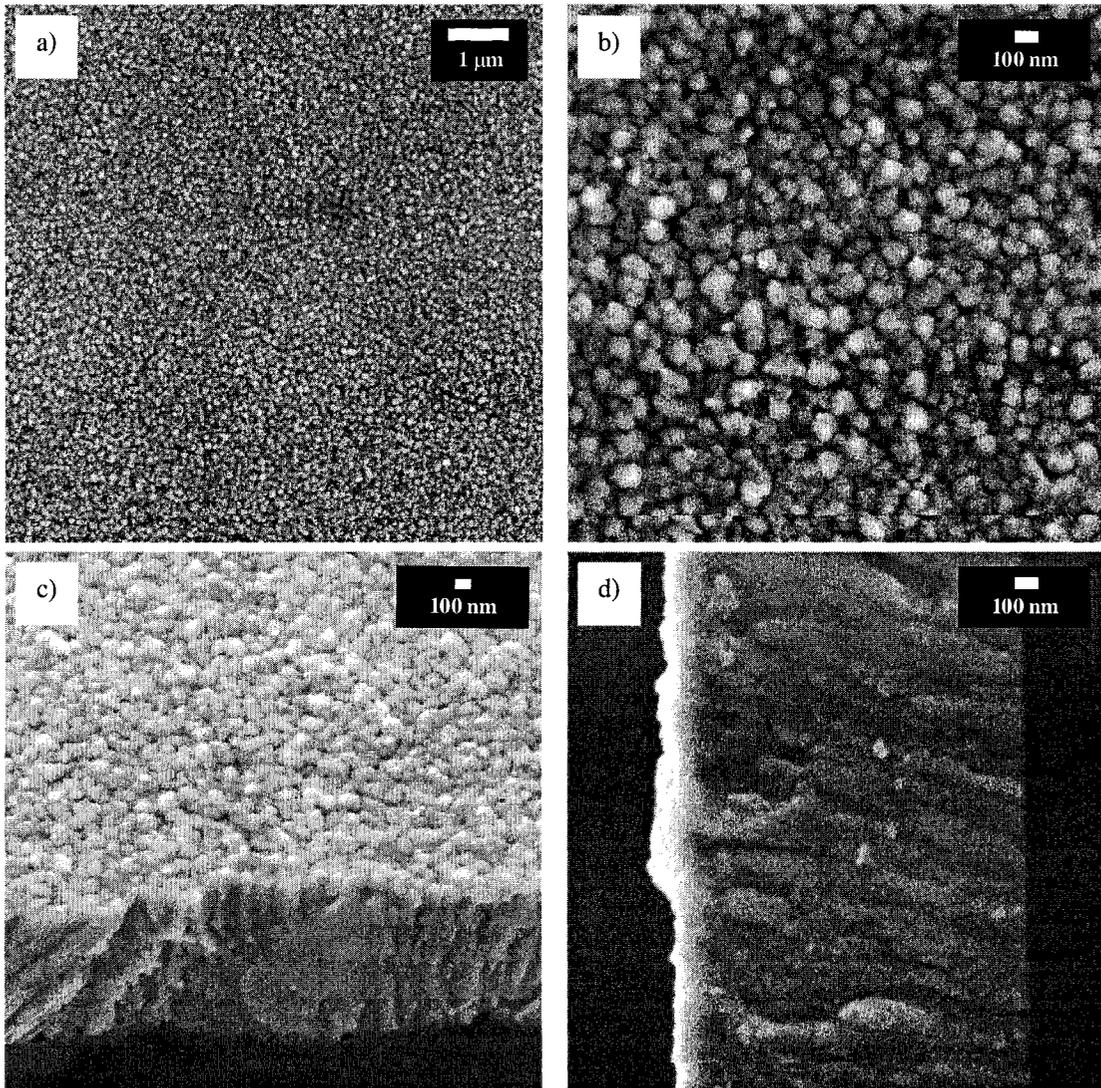
Figure 6.8. SEM images of a semseyite ($Pb_9Sb_8S_{21}$) film: a) and b) top surface images, c) tilt view of the cross-section and d) cross-sectional view.

In the powder pattern shown in Figure 6.9, the analysis of the XRD data is a little difficult, as all of the PbS reflections are positioned very close to semseyite reflections. Nevertheless, one notices that at $2\theta \sim 26°$, the film XRD pattern features a weak peak at 26.2° with a count rate of 0.022 cps. That peak position is more compatible with the semseyite reference pattern. Moreover, considering that it would correspond to the strong (111) PbS reflection, its weak intensity (0.022 cps) argues against attributing the

251

peaks at $2\theta \sim 43°$, $51°$ and $53.5°$ (with respective intensities of 0.013 cps, 0.009 cps and

0.015 cps) only to PbS; since these peak intensities would then respectively be 0.015

cps, 0.009 cps and 0.005 cps, according to the relative intensities observed for the PbS

film presented Figure 6.7. The higher angle peaks ($2\theta > 55°$, not shown) also do not

provide clear evidence of the presence of PbS. Lastly, microprobe data yield a

composition of $Pb_{8.6}Sb_{7.6}S_{21.7}$ for this semseyite film, compared to the theoretical

composition of $Pb_9Sb_8S_{21}$. Thus, microprobe data indicates that the film is sulfur rich,

but is also extremely close to the expected Sb:Pb ratio for semseyite: $Sb:Pb_{experimental} =$

0.88 while $Sb:Pb_{theroetical} = 8:9 = 0.89$. Therefore, by XRD and WDX analysis, phase-

pure films of semseyite without significant PbS have been prepared.
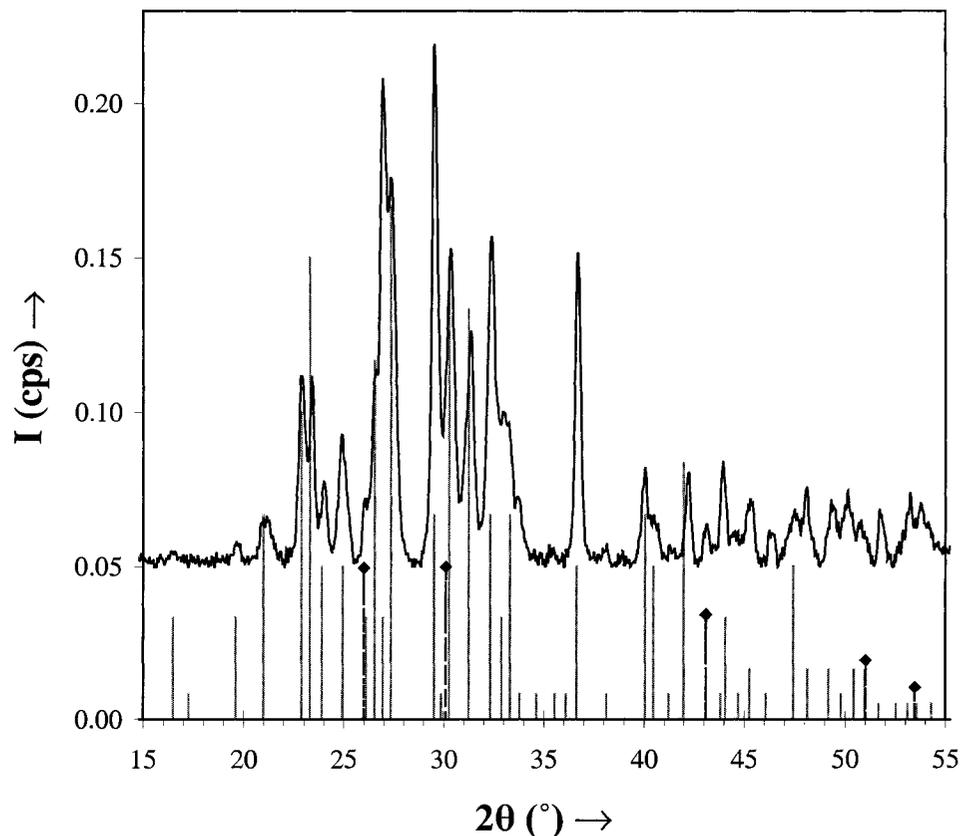
Figure 6.9. XRD pattern of a semseyite ($Pb_9Sb_8S_{21}$) film with semseyite [9,21] and PbS (diamond) [16,17] reference patterns.

252

b)   Heteromorphite films
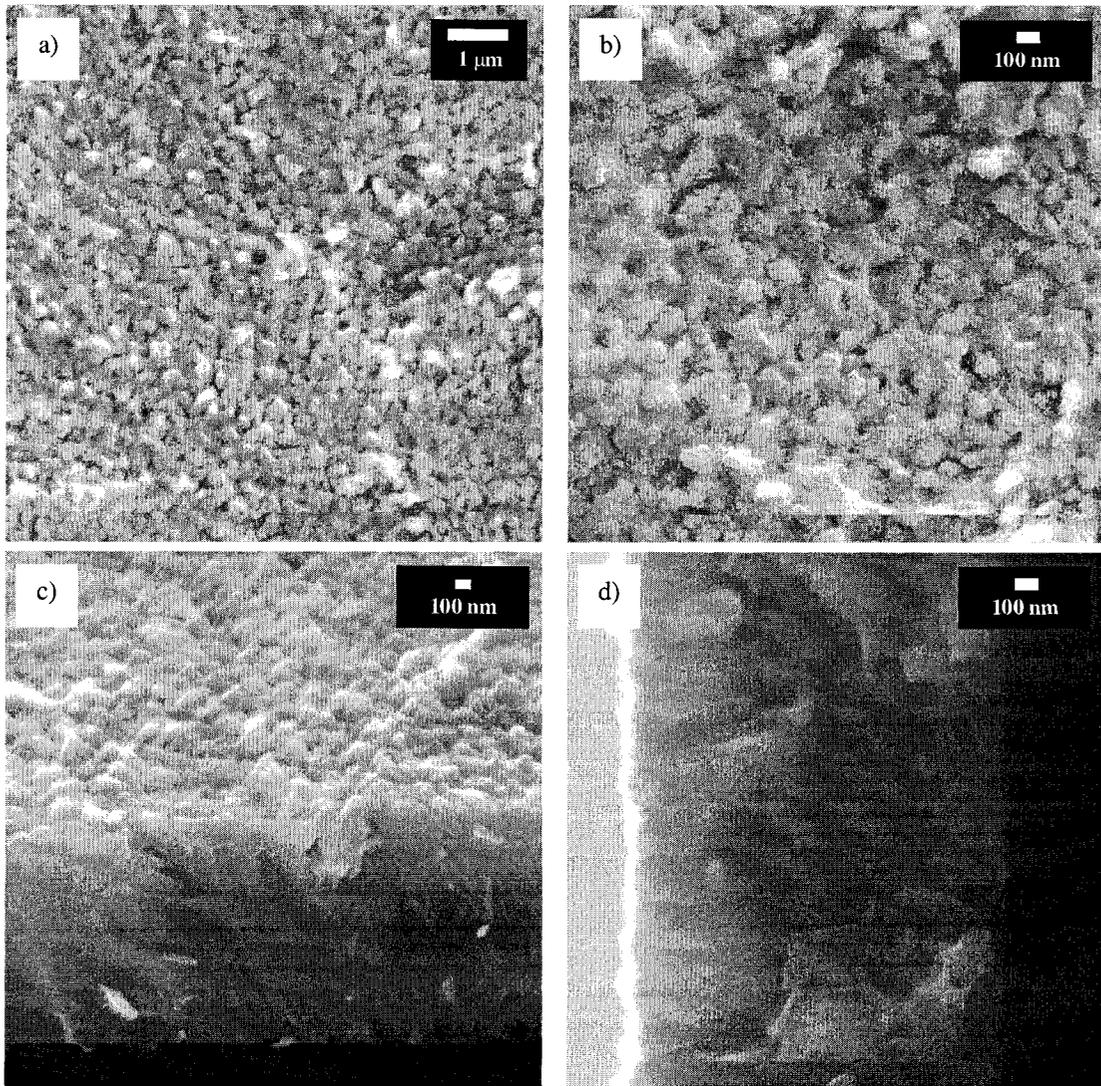
Figure 6.10. SEM images of a heteromorphite ($Pb_7Sb_8S_{19}$) film: a) and b) top surface images, c) tilt view of the cross-section and d) cross-sectional view.

The heteromorphite film shown in Figure 6.10 and which XRD pattern is shown in Figure 6.11 has been obtained by annealing the precursor film (#27_a) with an Sb:Pb stoichiometric ratio of 1.32 at 400 °C for 50 minutes in sulfur vapor. A satisfactory match was obtained with PDF card #83-1428 [22,23]. $Pb_7Sb_8S_{19}$ (heteromorphite) crystallizes in the monoclinic C2/c space group (#15).

253
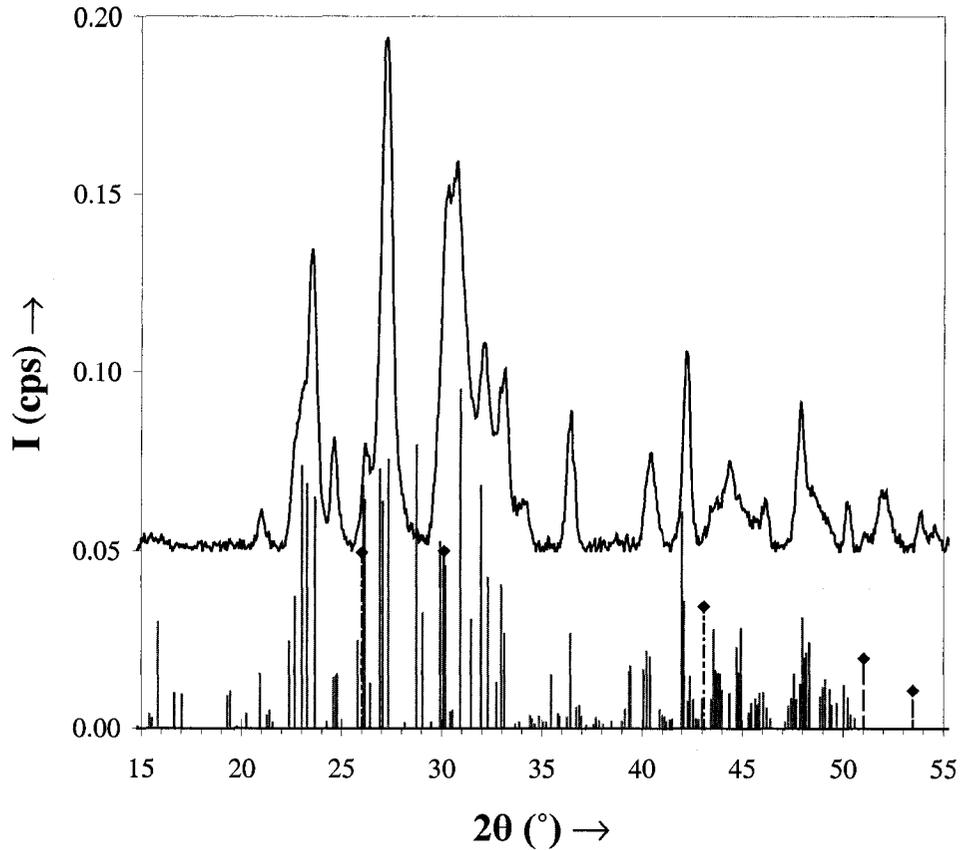
Figure 6.11. XRD pattern of a heteromorphite ($Pb_7Sb_8S_{19}$) film with heteromorphite [22,23] and PbS (diamond) [16,17] reference patterns.

The PbS reflections are positioned very close to some of the heteromorphite reflections, especially the ones at 2θ ~26° and 30°. Therefore, it is difficult to conclude anything from these reflections. More significantly, the absence of a reflection at $2\theta =$ 43.1° suggests the absence of a significant amount of PbS, as this is a strong reflection; indeed for a pure PbS thin-film this (220) reflection has an intensity of 0.95 cps. Lastly, microprobe data produced a composition of $Pb_{6.9}Sb_{8.2}S_{18.9}$ for this heteromorphite film, compared to the ideal composition of $Pb_7Sb_8S_{19}$. Thus, microprobe data indicates that while the film is very slightly antimony rich, but it is also very close to the expected Sb:Pb ratio for heteromorphite: $Sb:Pb_{experimental} = 1.19$ while $Sb:Pb_{theoretical} = 8:7 = 1.14$.

254

Therefore, by XRD and WDX analysis, phase-pure films of heteromorphite without significant PbS have been prepared.

c)   *Plagionite films*
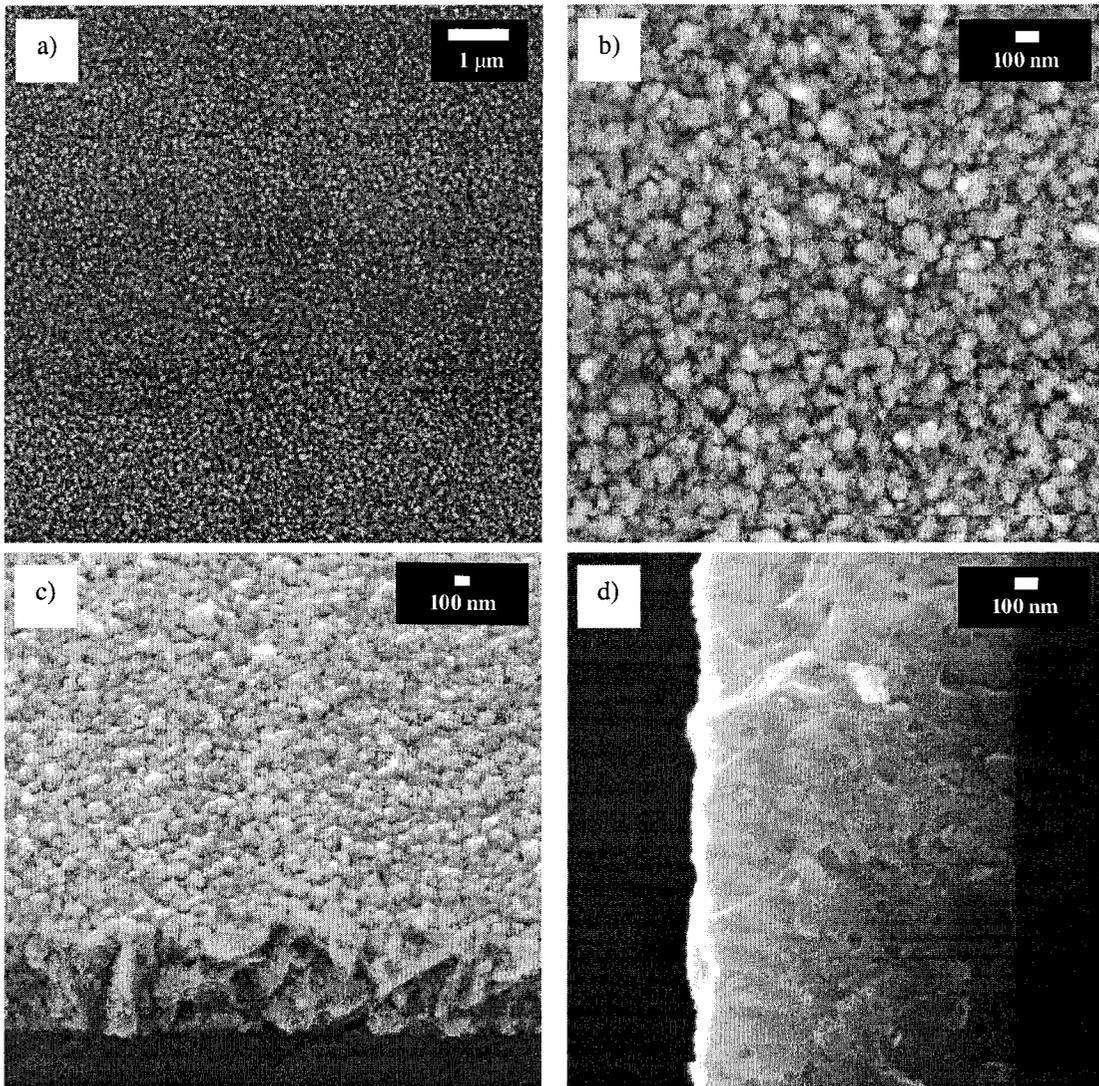
Figure 6.12. SEM images of a plagionite ($Pb_5Sb_8S_{17}$) film: a) and b) top surface images, c) tilt view of the cross-section and d) cross-sectional view.

The plagionite film shown in Figure 6.12 and which XRD pattern is shown in Figure 6.13 has been obtained by annealing the precursor film (#28_d) with an Sb:Pb stoichiometric ratio of 1.48 at 400 °C for 50 minutes in sulfur vapor. A satisfactory

255

match was obtained with PDF card #73-1112 [10,24]. $Pb_5Sb_8S_{17}$ (plagionite) crystallizes in the monoclinic C2/c space group (#15).
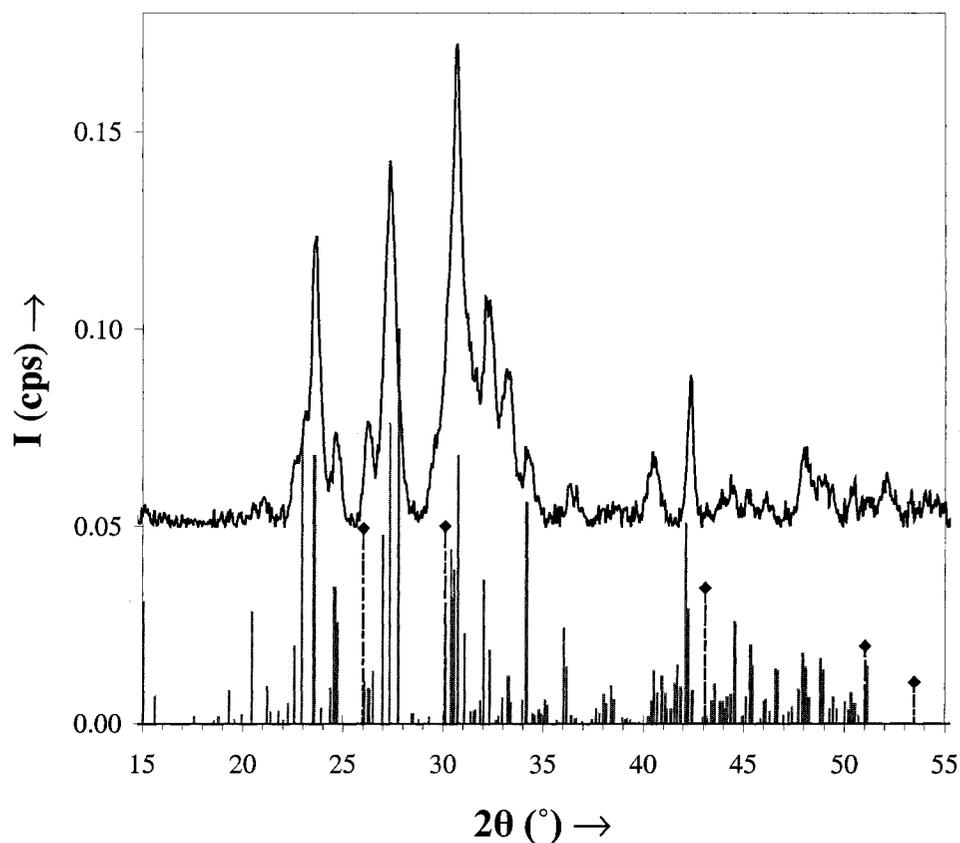
Figure 6.13. XRD pattern of a plagionite ($Pb_5Sb_8S_{17}$) film with plagionite [10,24] and PbS (diamond) [16,17] reference patterns.

The analysis of the XRD data shown in Figure 6.13 is similar to that described for the heteromorphite film. In the plagionite film powder pattern shown in Figure 6.13, peaks at 2θ values of 26°, 30° and 51° can all be attributed to plagionite phase reflections, since no strong diffraction peak can be observed at $2\theta = 43.1°$, which would correspond to the PbS (220) reflections. Lastly, microprobe data produced a composition of $Pb_{5.2}Sb_{7.3}S_{17.4}$ for this plagionite film, compared to the theoretical composition of $Pb_5Sb_8S_{17}$. Thus, microprobe data indicates that the film is antimony poor (~12 at. %)

256

and sulfur rich, but is also close to the expected Sb:Pb ratio for plagionite: Sb:Pb$_{experimental}$ = 1.40 while Sb:Pb$_{theroetical}$ = 8:5 = 1.60. Therefore, by XRD and WDX analysis, phase-pure films of plagionite without significant PbS have been prepared.

d)   Fülöppite films
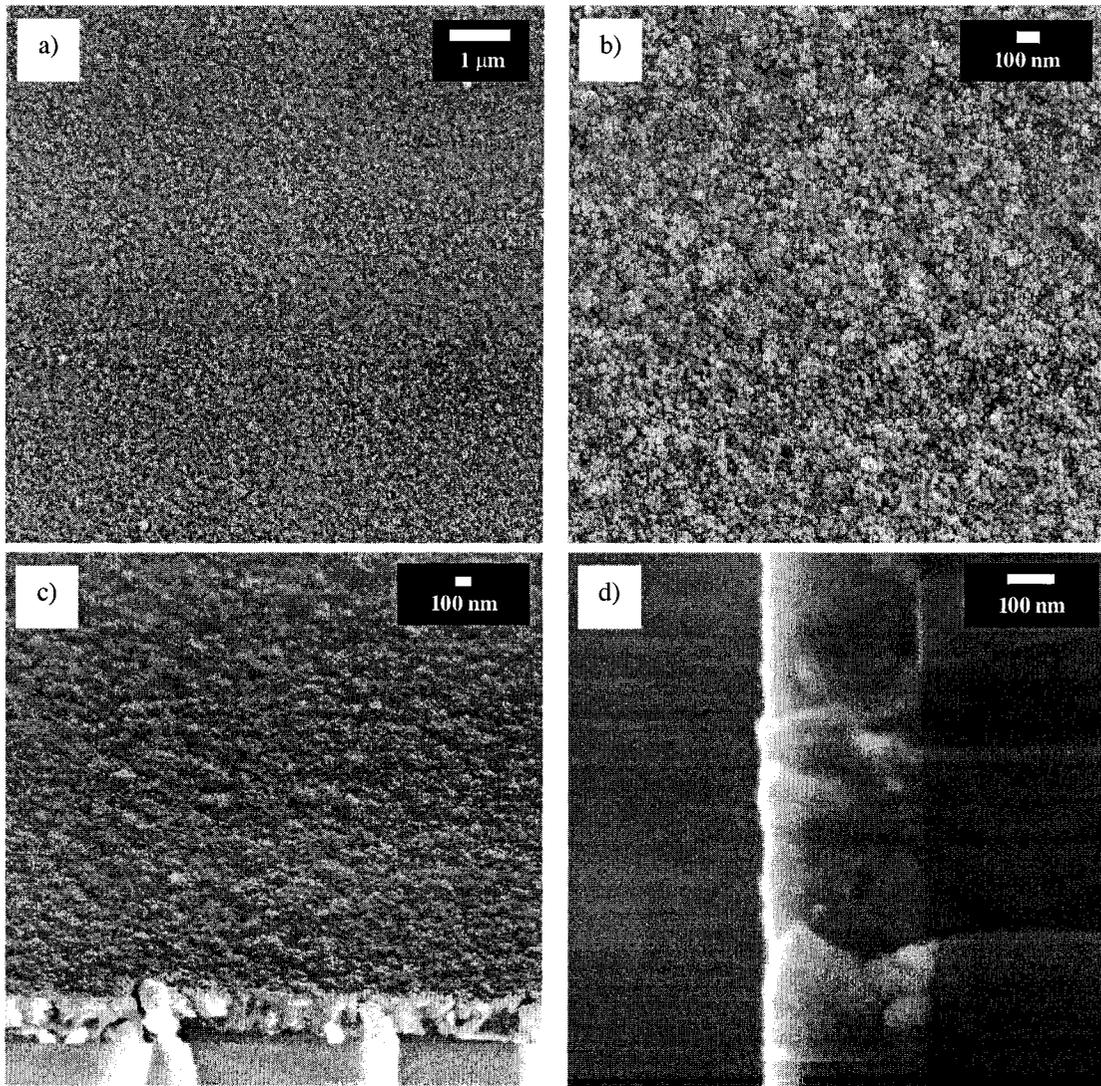
Figure 6.14. SEM images of a fülöppite ($Pb_3Sb_8S_{15}$) film: a) and b) top surface images, c) tilt view of the cross-section and d) cross-sectional view.
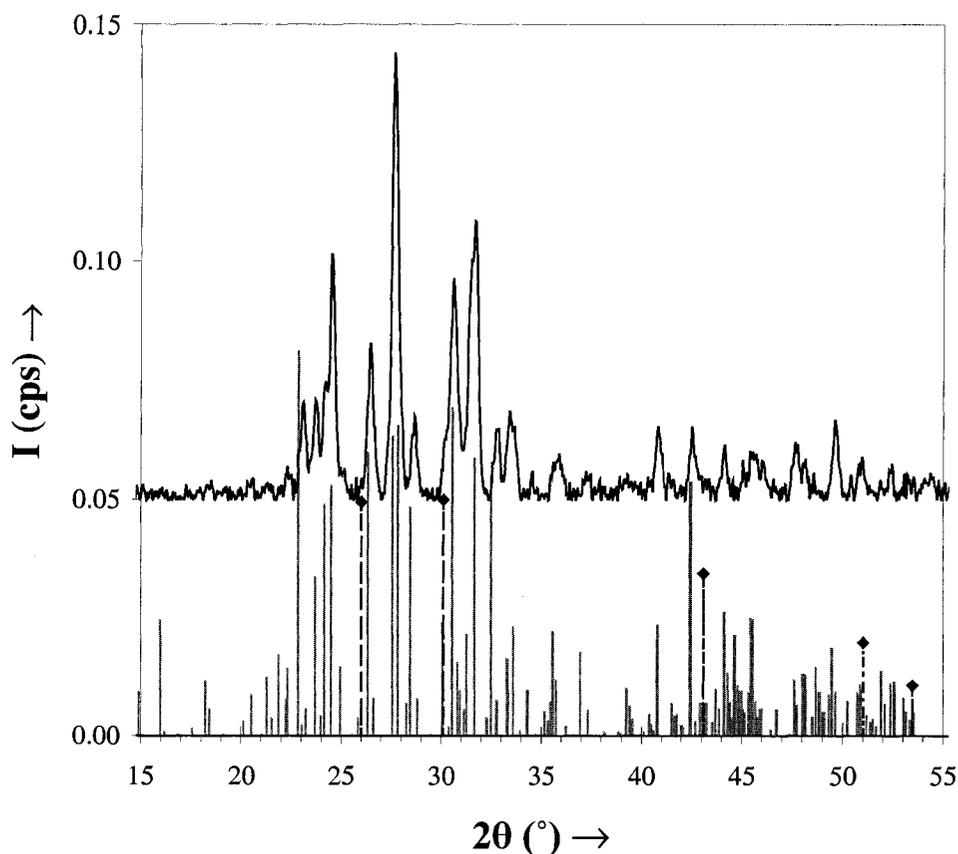
Figure 6.15. XRD pattern of a fülöppite (Pb$_3$Sb$_8$S$_{15}$) film with fülöppite [25,26] and PbS (diamond) [16,17] reference patterns.

The fülöppite film shown in Figure 6.14 and which XRD pattern is shown in Figure 6.15 has been obtained by annealing the precursor film (#32_c) with an Sb:Pb stoichiometric ratio of 3.06 at 350 °C for 120 minutes in sulfur vapor. A satisfactory match was obtained with PDF card #65-2330 [25,26]. Pb$_3$Sb$_8$S$_{15}$ (fülöppite) crystallizes in the monoclinic C2/c space group (#15). In the fülöppite film powder pattern shown in Figure 6.13, peaks at 2θ values of 30° and 51° can be attributed to fülöppite or PbS. Nevertheless, the absence of strong diffraction peaks at 2θ ~ 26° and 43°, which would correspond to the PbS (111) and (220) reflections, suggests the absence of any significant amount of PbS. Lastly, microprobe data produced a composition of

258

$Pb_{2.9}Sb_{7.7}S_{15.4}$ for this fülöppite film, compared to the theoretical composition of $Pb_3Sb_8S_{15}$. Thus, microprobe data indicates that the film is sulfur rich, but is also extremely close to the expected Sb:Pb ratio for fülöppite: $Sb:Pb_{experimental} = 2.66$ while $Sb:Pb_{theroetical} = 8:9 = 2.67$. Therefore, by XRD and WDX analysis, phase-pure films of fülöppite without significant PbS have been prepared.

e)   *Discussion*

For all the plagionite group phases, differences between the intensities of our films and the standard patterns collected from geological samples can be observed. These differences can be attributed to film texture and to slight displacements of the atoms from their lattice site that can affect the scattering factor and the peak intensity. On the plagionite film XRD pattern especially (Figure 6.13), one may notice that a few peaks are shifted ($< \pm0.2°$). This can be attributed to slight expansion or contraction of the lattice dimensions, compared to the geological sample used for the reference pattern. Also, considering the plagionite phase, one should remember that this phase has been obtained antimony poor, this should affect the crystal structure. Moreover, one should not forget that the plagionite phase unit cells contains between 38 (for semseyite) and 26 (for fülöppite) atoms. This large number of atoms per unit cell increases the probability of having defects, especially slight atom displacements, substitutions, interstitial occupancies or vacancies, these affect the scattering factor and the relative diffracted intensities. Regarding the complexity of the plagionite phases (large number of atoms per unit cell, monoclinic system) and the XRD data obtained from the thin films presented herein, it is not possible to further refine the crystal structure of the plagionite

259

thin films. The differences observed between our film XRD patterns and the geological sample XRD patterns used as references are minor and should not prevent the positive identification of these plagionite phases.

Lastly, for most of the layered precursor films, some antimony depletion occurred during annealing. Nevertheless, this depletion was limited: between 5 and 15 % antimony depletion was observed for layered precursor films with Sb:Pb ratio smaller than 2.0. The overall antimony depletion can be calculated from:

$$\text{Antimony depletion} = \frac{[Sb:Pb]_{initial} - [Sb:Pb]_{final}}{[Sb:Pb]_{initial}} \times 100 \qquad (6.7)$$

Thus, the overall antimony depletion is about 11 at. %, 10 at. % and 5 at. % for the precursor films #28_c (Sb:Pb = 0.99), #27_a (Sb:Pb = 1.32) and #28_d (Sb:Pb = 1.48), respectively, whereas it is about 26 at. % for the antimony-rich layered precursor #32_c (Sb:Pb = 3.06). Higher overall antimony depletion has been observed for most of the antimony-rich layered precursor films (Sb:Pb > 2). In the case of Sb:Pb < 2, it is important to note that 5 to 15 at. % overall antimony depletion can be considered as less, compared to the antimony depletion that occurred when annealing metallic Sb-Pb precursor films under sulfur vapor (see Chapter 5). Despite, some overall antimony depletion of the layered sulfur-containing precursor films, it is possible to prepare plagionite group phases thin film with good morphology and optical properties, as described below. One should note that antimony depletion, even limited, may prevent the formation of stoichiometric compounds. Deviation from the stoichiometry in a semiconductor can very adversely affect its electronic properties.

6.4.2 Morphology of thin films of plagionite group phases

All the films of plagionite group phases were continuous and smooth, with mirror-like surfaces, as shown with the tilt view SEM images (Figures 6.8.c, 6.10.c, 6.12.c and 6.14.c). The surface SEM images (Figures 6.8.a, 6.8.b, 6.10.a, 6.10.b, 6.12.a, 6.12.b, 6.14.a and 6.14.b) show dense films composed of small crystal grains (0.1 μm or less). Cross-sectional images (Figures 6.8.d, 6.10.d, 6.12.d and 6.14.d) show homogeneous films throughout their thickness, with no evidence of the layered precursor structure remaining. According to the film surface SEM images, it appears that the largest grains for the semseyite and heteromorphite films are 0.1 μm, for the plagionite film are 0.05 μm and for the fülöppite film are 0.025 μm. In the case of the fülöppite thin film, no XRD peak broadening is observed, therefore the very small features are believed to be localized to the surface and may result from solid film-sulfur vapor interface effect. Indeed, the cross-section SEM images from all the plagionite group films show the polycrystalline nature of the films, with 100 nm wide crystal grains. The thickness of the film is increased during annealing under sulfur vapor, since additional sulfur is incorporated into the film. The as-deposited layered precursor film thickness increases by ~30 % during reaction.

6.5 Discussion on the low-temperature film growth of plagionite group phases

6.5.1 Effects of the annealing conditions

a) Black and yellow sulfur, temperature of the sulfur source

Yellow sulfur (Alfa Aesar, sublimed, ~100 mesh, 99.5 %) was used as a source for elemental sulfur and placed in ~3 × 1 cm^2 quartz boat placed at the sealed end of the

261

annealing tube. Sulfur has a large number of allotropes. The most stable allotrope of sulfur at room temperature is the α-S_8 allotrope: this is an arrangement of 8-member rings of sulfur in an orthorhombic cell [27]. This allotrope species is commonly known as yellow sulfur.

Heating sulfur changes its viscosity. At approximately 110 °C [28], sulfur (α-S_8) melts to a yellow liquid, whose viscosity decreases until approximately 155 °C because of greater thermal motion. Further heating causes the viscosity to increase, dramatically so above 159 °C. Above 200 °C, the viscosity decreases again and the liquid becomes reddish [29]. These changes in viscosity are explained by the opening of S_8 rings into S_8 chains and by the subsequent polymerization of the S_8 chains forming S_{16} chains, S_{24} chains, and so on.

$$S_8 \text{ (ring)} \longrightarrow S_8 \text{ (chain)} \longrightarrow S_{16} \cdots$$
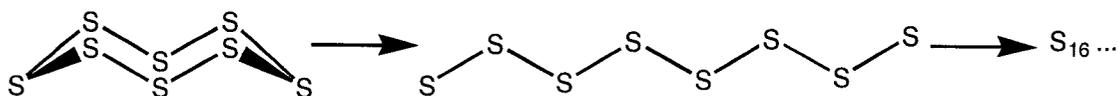
With the experimental set-up described in Section 2.1.5 (resistively heated brass extension over the end of the annealing tube), the sulfur source temperature was set and maintain at 185 ± 5 °C. According to what has been stated above, at 185 °C the sulfur ring should mostly be opened and the polymerization should be limited, thereby generating a large number of S_x (with $x = 2$ to 8) species and especially S_2, S_6, S_7 and S_8, according to reference [28].

The first annealing experiments were performed using black sulfur heated to ~185 °C. Black sulfur was obtained from the rapid cooling of the liquid sulfur heated at ~185 °C; thus, after one annealing cycle sulfur went from a yellow solid containing S_8

262

rings to a brown-black sulfur containing S_n chains. Black sulfur was used for the practical reasons of not needing to handle the yellow sulfur powder stored in the glove-box or to clean the boat. It was observed that after eight annealing cycles, the annealed films featured large pinholes, despite keeping the various annealing parameters the same. These film morphologies were similar to those obtained after annealings performed without any sulfur. Therefore, the partial pressure of sulfur generated was not sufficient to react sulfur with the precursor film and prevent depletion of the film and degradation of the film. As the solid sulfur undergoes repeated heating cycles at 185 °C, the S_n chains lengthen, making the liquid sulfur more and more viscous. More significantly, the other consequence of the S_n chains lengthening is likely a decrease of the vapor pressure of the liquid sulfur and, therefore, a decrease in the amount of sulfur species in the gas phase, as n increases. Therefore, recycling the solid black sulfur from one annealing run to another is unreliable and does not allow reproducible generation of sulfur vapor. In order to mitigate this issue, fresh solid yellow sulfur heated at ~185 °C was used for each of the reactive annealings presented in this Chapter. This yields satisfactory film morphologies and compositions (no harmful depletion), since enough reactive "short" sulfur vapor species S_x (with x = 2 to 8) were reproducibly generated and reacted with the precursor films.

b)   Temperature ramp-ups and ramp-downs rates

Annealing experiments have been performed with the same precursor films to determine appropriate temperature ramp-up and ramp-down rates. The optimal rates were found to be 10 °C/min for the ramp-up to the high temperature dwell and 3 °C/min

263

for the ramp-down to 100 °C (at which temperature the annealing tube was removed from the tube furnace to allow a rapid (~20 minutes) cooling to room temperature). Faster rates negatively impacted the film morphology, as films were more likely to display wrinkles, cracks and 10 μm surface bumps. To obtain thin films with appropriate morphology, the temperature ramp-up and ramp-down rates have been kept constant at 10 °C/min and 3 °C/min, respectively. These rates are apparently appropriate to avoid excessive thermal stress and, therefore, maintain good morphological properties.

c)   *Temperature and duration of the high temperature dwell*

In an effort to optimize the thin film properties, the temperature and duration of the high temperature dwell was varied. All annealings described hereafter follow the temperature program:

$$\begin{cases} \underline{\text{film}}: & 25°C \xrightarrow{\sim 10°C/min} 300°C \xrightarrow{10°C/min} T_f, t_f \xrightarrow{3°C/min} 100°C, \text{tube cooled in air} \\ \underline{\text{sulfur}}: & 25°C \xrightarrow{\sim 6°C/min} \quad\quad 185°C, t_S \quad\quad \uparrow S \text{ furnace stopped, } N_2 \text{ flow started} \end{cases}$$
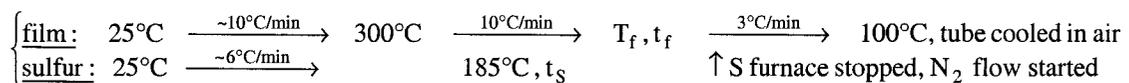
where T_f and t_f are the temperature of the film during the dwell and the duration of the dwell, respectively, and t_S is the time the sulfur was maintained at 185 °C. As indicated on the program above, the sulfur reaches 185 °C at the same time the film reaches 300 °C and the sulfur vapor generation is stopped when the film starts to cool down. This is achieved by removing the brass extension that heats the part of the annealing tube where the sulfur source is located.

Because of imperfect control over the Sb:Pb stoichiometric ratio in the as-deposited layered precursor films, only a few precursor films yielded pure plagionite group phases. Results should be read with this in mind and are, therefore, only partial.

264

Indeed, each annealing temperature and duration could not be performed for each precursor film (*i.e.* for each of the four plagionite phases) and for each of the precursor film types (*i.e.* thick or thin, 15 or 5 repeat units). Nevertheless, trends in film morphology, crystallinity and composition (pinholes, grain size, phase purity, depletion) can be observed.

First, long (135 minutes at 400 °C) and hot (500 °C for 20 minutes) annealings of thick precursor films yielded films severely antimony-depleted with poor morphologies. Also, it was observed that for Pb-rich phase (*i.e.* semseyite) the minimum temperature required to obtain films with satisfactory morphologies, crystallinities and compositions from thick precursor films is higher (400 °C *vs.* 350 °C) than the temperature required for Sb rich phases (*i.e.* plagionite). This suggests that the ease of nucleation and crystal growth increase with the antimony content of the plagionite phase. In addition, determining the appropriate duration of the high temperature dwell has to be done by a trial and error method, as antimony depletion compete with phase nucleation and growth. A minimum duration is required to obtain satisfactory film morphology and crystallinity, but if it is too long, too much antimony may be lost. Moreover, thicker precursor films logically require longer annealing times. Thus, for the thick precursor films for semseyite, heteromorphite and plagionite, the best results were obtained with annealings at 400 °C for 50 minutes, despite potential improvements at 350 °C. For the thin precursor films for plagionite and fülöppite, the best results were obtained at 350 °C for 2 hours. 2 hours may seem long, but was necessary to sufficiently deplete the very

265

antimony rich precursor films. Moreover, annealings at 400 °C for 30 minutes lead to satisfactory results as well. Evidences for the above trends are detailed below.

- Annealing at 400 °C:

Annealings at 400 °C for 45 or 50 minutes of thick (15 repeat units) precursor films for semseyite, heteromorphite and plagionite were performed. No significant differences could be noticed in terms of film morphologies between 45 and 50 minute annealings. Nevertheless, the film XRD pattern matched the reference XRD patterns slightly better with films annealed for 50 minutes. This was especially noticeable with the precursor films #28. These semseyite, heteromorphite and plagionite films have been presented earlier. Concerning the thin (5 repeat layers) precursor films, annealings at 400 °C for 15 and 30 minutes were performed. Annealings at 400 °C for 30 minutes yielded films with satisfactory morphologies, crystallinities and compositions for plagionite (Sb:Pb = 1.37 from precursor film #32_a) and fülöppite (Sb:Pb = 2.74 from precursor film #32_c).

Lastly, long (135 minutes) annealings at 400 °C have also been performed for thick (15 repeat layers) precursor films. Regardless of the starting composition, films were converted to semseyite, as major antimony depletion occurred, and no positive effect on the crystallite size could be observed. This result shows how important it is to find the appropriate duration for the high temperature dwell in order to maintain or, minimize changes to, the as-deposited layered precursor film composition; this is necessary to produce the preparation of the targeted plagionite phases.

266

- Annealings at 300 °C and 350 °C:

Thick precursor films (film #28_d) that yield plagionite films have also been annealed at 300 °C for 90 minutes and 350 °C for 60 and 120 minutes. The crystallinity of the films annealed at 300 °C for 90 minutes was poor by XRD (weak signal and broad peaks), suggesting that 300 °C is not high enough for the preparation of plagionite films with short annealing times; however, films suffered little or no antimony depletion. Similar observations have been made for thin precursor films (film #32_a) that yield plagionite annealed at 300 °C for 90 minutes.

Cross sectional SEM images of the thick precursor films annealed at 350 °C for 60 minutes featured smaller grains, while those of the films annealed at 350 °C for 120 minutes featured more sharp edges, suggesting larger grain sizes and increased crystallinity overall. It is interesting to note that films from both 60 and 120 minute 350 °C annealings have similar XRD peak widths and intensities, and WDX composition (Sb:Pb = 1.44 and 1.49, respectively). Moreover, thin precursor films (films #32_a and #32_b) that yield plagionite phase films have also been annealed at 350 °C for 120 minutes. The thin films obtained featured good morphology (smooth, sharp edges at the cross sectional fracture), good crystallinity (pattern agreed with plagionite phase) and were 15 at. % antimony poor (Sb:Pb = 1.36) and 12 at. % antimony rich (Sb:Pb = 1.79) relative to the ideal composition for plagionite, respectively.

Thick precursor films of semseyite (films #28_c and #28_b) were also annealed at 350 °C for 120 minutes. The crystallinity of the resultant films was poor; XRD peaks

267

were weak and broad, while cross-sectional SEM images featured small and poorly defined grains (no sharp and extended edges could be seen on the fracture). This suggests that, contrary to what has been observed for plagionite precursor films, 350 °C is not high enough for the preparation of semseyite films with adequate crystallinity, even with 2 hour long reaction times.

Lastly, because of deposition variability, the only layered precursor films appropriate for the synthesis of fülöppite thin films was a thin layered precursor film (5 repeat layers, film #32_c). Films annealed at 400 °C for 30 minutes featured 50 nm voids and 10 μm wide rough areas on the surface. Films annealed at 350 °C for 120 minutes yielded fülöppite thin films with good morphologies, crystallinities and compositions, as described in Section 6.4.1.d.

- Annealing at 500 °C:

Annealings at 500 °C for 20 minutes were performed for both thick and thin layered precursor films. At this temperature, major antimony depletion was observed. According to WDX data, the overall antimony depletion (see equation 6.7) for the thick precursor films ranged from 25 at. % to 61 at. %, yielding Sb:Pb stoichiometric ratio for the annealed films of 0.52 to 0.74, which is even smaller than the Sb:Pb ratio of boulangerite (Sb:Pb = 0.8): a lead rich dry phase stable at 500 °C. Thin precursor films were completely antimony depleted by WDX after annealing. The films obtained from thick precursor were continuous and smooth, with mirror-like surfaces. However, top-surface and cross-sectional SEM images show that films were a little porous. The films

268

obtained from thin precursor were discontinuous, featuring 1 to 10 μm holes. Unfortunately, for technical reasons (the XRD instrument was shut down for relocation), no XRD data were collected for these films. Regarding the film morphologies and, more significantly, the film compositions, the film probably contains PbS, which is not suitable in our quest for the preparation of light absorbing Pb-Sb-S ternary compounds. Heating at 500 °C for 20 minutes is definitely too long.

6.5.2 Preclusion of hydrogen

To show that our method precludes hydrogen incorporation, it is necessary to identify the possible sources of hydrogen that may exist during our thin-film process.

a)   *The glass substrates:* just before being loaded into our UHV system, the substrates are cleaned in IPA and blown dry with compressed N_2. This is one of the standard UHV-compatible cleaning methods. Substrates are then pumped down over night to 10^{-9} Torr, before being transferred into the deposition chamber. No significant amounts of hydrogen or water are present.

b)   *Film deposition:* deposition takes place in a deposition chamber pumped with a cryo-pump to a base pressure of high 10^{-9} Torr − low 10^{-8} Torr. This is an ultra high vacuum environment, and therefore no significant amounts of hydrogen or water vapor are present. The deposition plasma is established using high purity Ar gas, again no significant amounts of hydrogen or water vapor are present.

269

c) *Sample transfer:* After deposition and before annealing, samples are rapidly transferred in air, at this stage there is the possibility for adsorption of a water monolayer on the surface of the film. Nevertheless, that monolayer does not represent a significant amount of water nor hydrogen compared to the ~1 μm thick precursor film.

d) *Sample storage:* Samples are stored in a dry glove-box, with a controlled N_2 atmosphere. Once again, no significant amounts of hydrogen or water vapor are present.

e) *Sample annealing:* Finally, before annealing, elemental sulfur (stored in the glove-box) and samples are placed in a tube that is evacuated to 10^{-3} Torr and back-filled with high purity N_2, this purge process is performed 5 times. A final evacuation brings the tube to a pressure of 10^{-3} Torr, just before starting the annealing. Thus, the only residual gas that should be present is N_2. In the worst case scenario a monolayer of water would be adsorbed on the film at step *c)*, that monolayer would be desorbed rapidly during the first stage of the annealing (temperature ramp to 400 °C).

Therefore, our PVD precursor film deposition followed by annealing under sulfur vapor precludes the incorporation of significant amounts of hydrogen into our films.

6.5.3 Metastability of the plagionite group phases

As described in Chapter 5, metallic Pb-Sb co-sputtered and layered (S-free) precursor films were also annealed using conditions similar to those described previously. This approach is similar to the thin-film synthesis of $CuIn(Se,S)_2$ [30,31]

270

from chalcogenization of Cu-In metallic precursors. In contrast to the sulfur-containing layered precursor films, the metal precursor films yielded rough films with poor morphology. Moreover, they rarely produced phase-pure films. Films annealed at 375 °C for up to 3 h contained a mixture of a binary phase and a ternary phase, and films annealed at 400 °C for 1 h contained a mixture of one of the plagionite group phases and one of the low temperature phases of the Pb-Sb-S phase diagram evaluated using "dry" solid state syntheses [32]. WDX data on as-deposited and annealed films showed that metal precursor films, unlike sulfur containing layered precursor films, usually suffered significant Sb depletion during annealing. Thus, the incorporation of sulfur into the precursor film is critical for obtaining ternary, phase-pure films without significant depletion of Sb. The growth of phase-pure films with good morphology was possible because the Sb:Pb ratio was largely preserved and shorter annealing times were required.

Short duration reactive annealing of layered precursor films exclusively yielded plagionite group phases, indicating that plagionite group phases easily nucleate under these annealing conditions. As our growth method can not enable hydrogen incorporation into the films, it is very unlikely that the plagionite group phase occurrence depends on the presence of hydrogen, as hypothesized by Garvin [14]. Also, a review of the crystallographic density shows that these phases are slightly less dense than the low temperature phases [32,33] boulangerite, robinsonite and zinkenite, and that they are denser than the higher temperature phases that have been reported. As plagionite group phases failed to appear in the Pb-Sb-S phase diagram established from

271

traditional solid state reactions [32], their low density as well as several experimental observations described hereafter suggest that they may be metastable phases.

Annealing of plagionite group compound thin films at 400 °C under 1 atm of Ar for 12 h induced decomposition to a mixture of phases including PbS along with loss of Sb_2S_3. Neither plagionite nor semseyite were stable at 400 °C for long periods, confirming previous reports [14,15]. Furthermore, Robinson produced semseyite, plagionite, and fülöppite from aqueous solutions at temperatures between 340 °C and 435 °C [15] whereas Garvin investigated the phase diagram to temperatures as low as 300 °C using dry synthesis, and KCl-LiCl and NH_4Cl-LiCl fluxes and obtained none of the plagionite group phases [14]. Perhaps significantly, Garvin's reactions were all maintained at temperature for at least 7 days and then quenched, while Robinson's reactions were maintained at the maximum temperature for at most 24 hours and then slowly cooled to room temperature over 2-10 days, enabling successive phases to deposit in layers during slow cooling.[15]

Taken collectively with our results, it appears that formation of the plagionite phases requires short reaction times at temperatures below 435 °C, enabled in our case by intimate mixing of the Pb, Sb, and S in the precursor films. The plagionite group phases are also relatively scarce in nature [14]. All these observations suggest that plagionite phases are likely to be metastable. Indeed, our novel thin-film approach to synthesize lead antimony sulfides may favor the synthesis of metastable phases, as moderate annealing temperatures and durations are required to interdiffuse reactants that

are in close proximity, similar to other thin film syntheses producing metastable phases [34].

6.6   Optical properties of thin films of Plagionite group phases

Optical characterization of the films presented in Table 6.2 have been performed. Thus, Figures 6.17, 6.16, 6.18 and 6.19 gather the optical data for the thin films of semseyite, heteromorphite, plagionite and fülöppite, respectively. Figures 6.17.a, 6.16.a, 6.18.a and 6.19.a shows the optical transmittance and near-normal reflectance spectra as well as the corrected transmittance spectra of thin films of the four plagionite group phases thin-films. The corrected transmittance for reflection losses at the air-film interface is calculated using the following equation:

$$T_c = T/(1-R)^2 \qquad\qquad (6.7)$$

The absorption coefficients α of the films have been calculated using the relation [35]:

$$\alpha = \frac{1}{d}\,\ln\!\left[\frac{(1-R)^2}{T}\right] = \frac{1}{d}\,\ln\!\left[\frac{1}{T_c}\right] \qquad\qquad (6.8)$$

where T and R are, respectively, the transmittance and the reflectance values, and where d is the film thickness in cm, evaluated from high magnification cross-section SEM images. Energy dependence of the absorption coefficients is shown in Figures 6.17.b, 6.16.b, 6.18.b and 6.19.b. Moreover, for semiconductors, $(h\nu\alpha)$ is proportional to $(h\nu - E_g)^{1/n}$ where E_g and $n = 2$, $\frac{2}{3}$, $\frac{1}{2}$ or $\frac{1}{3}$ for, respectively, direct allowed, direct forbidden, indirect allowed or indirect forbidden optical transition [36]. Thus, a plot of $(h\nu\alpha)^n$ vs. $(h\nu)$ yielding a straight line enables the band gap value and nature to be determined from the intercept with the photon energy axis. Good straight-line fits were usually obtained

273

for n = ⅔ and n = 2, indicating direct forbidden and a direct allowed transitions between the valence and the conduction band, which corroborates the large absorption coefficient values obtained. These results are presented in Figures 6.17.c, 6.16.c, 6.18.c and 6.19.c for n = 2 and Figures 6.17.d, 6.18.d and 6.19.d for n = ⅔. Table 6.4 gathers the optical characterization of the films of plagionite group phases presented in Table 6.2. Therefore, for each plagionite phase Table 6.4 recalls the actual film stoichiometry obtained from WDX, the precursor film and the annealing conditions that yielded this phase. Moreover, for each plagionite group phase film, Table 6.4 gives the film thickness in nanometers used to calculate the absorption coefficient, the absorption coefficient α in cm^{-1} at energies greater than the band gap energy (*i.e.* 2.5 or 2.9 eV), and the band gap energy values in the case of a direct allowed transition or a direct forbidden transition.

Table 6.4. Results for thin films of plagionite group phases

Phase - Film stoichiometry	Precursor film - Annealing conditions	Thick. (nm)[1]	α (cm^{-1})	E_g (eV) dr. al.[2]	E_g (eV) dr. fr.[3]	E_g (eV) litt.[4]	Figures
Semseyite $Pb_{8.6}Sb_{7.6}S_{21.7}$	28_c 400 °C - 50 min.	867	7.2×10^4 (5)	1.88	**1.67**	1.50	6.17, 6.8, 6.9.
Heteromorphite $Pb_{6.9}Sb_{8.2}S_{18.9}$	27_a 400 °C - 50 min.	1511	2.4×10^4 (5)	**1.52**	N/A	1.41	6.16, 6.10, 6.11.
Plagionite $Pb_{5.2}Sb_{7.3}S_{17.4}$	28_d 400 °C - 50 min.	744	1.2×10^5 (5)	**1.82**	1.60	1.53	6.18, 6.12, 6.13.
Fülöppite $Pb_{2.9}Sb_{7.7}S_{15.4}$	32_c 350 °C - 120 min.	330	2.8×10^5 (6)	2.22	**1.87**	1.63	6.19, 6.14, 6.15.

Notes: (1) Thick. = Thickness,

(2) dr. al. stands for direct allowed transition,

(3) dr. fr. stands for direct forbidden transition,

(4) lit. = literature,

(5) absorption coefficient α at 2.5 eV,

(6) absorption coefficient α at 2.9 eV.

274

a)   *Absorption coefficient*

As shown in Table 6.4, all thin films of the plagionite group phases have high absorption coefficient values, comprised between 2.4×10^4 and 2.8×10^5 cm^{-1}. These phases are, therefore, strongly absorbing, suggesting a direct transition between the valence and the conduction bands. As mentioned in Chapter 1, direct band gap semiconductors have higher absorption coefficients; for instance, GaAs, which is a direct band gap semiconductor, has an absorption coefficient of 1×10^5 cm^{-1} at 2.5 eV, whereas Si, which is an indirect semiconductor has an absorption coefficient of 3×10^3 cm^{-1} at 2.5 eV [37]. Moreover, it is hard to say that one compound is more absorbing than the other given the results presented in the Table 6.4, but one may say that one film with a given thickness is more absorbing than another. Indeed, it seems that the absorption coefficient depends on the film thickness; thus, thin films (~300 nm) are more absorbing than thick film (~1500 nm). This observation can be related to the value of the reflectance in the high energy region (E > E$_g$): thin films lead to higher values of reflectance (~30 %) whereas thicker films lead to smaller values of reflectance (~10 %); thus, according to formula (6.8), the larger R is, the larger $(1-R)^2$ and, therefore, the larger the absorption coefficient. This fluctuation in reflectance value may come from slight differences in the top surface morphology. For the 700 to 800 nm, absorption coefficient values around 1×10^5 cm^{-1} are observed regardless of the phase (*i.e.* plagionite or semseyite).

275

b)   Nature of the direct transition: allowed or forbidden

For all the optical data collected, plots of $(h\nu\alpha)^n$ *vs.* $(h\nu)$, with n = 2, $\frac{2}{3}$, $\frac{1}{2}$ or $\frac{1}{3}$ were graphed to estimate the quality of the straight-line fit; if a good fit is achieved then the band gap nature can be determined from the value of n and the value of the band gap from the intercept with the photon energy axis. Good straight-line fits were never obtained with n = $\frac{1}{2}$ or $\frac{1}{3}$, but could be found for n = $\frac{2}{3}$ or n = 2, meaning direct forbidden or direct allowed transitions between the valence and the conduction band, respectively; this result is in agreement with the high values of the absorption coefficient described earlier. Thus, as shown in Table 6.4, for all the phases except heteromorphite both allowed and forbidden transitions could be derived. Nevertheless, the quality of the straight-line fit is not necessary the same for both transition types.

Heteromorphite thin films were only infrequently obtained and the optical data could not be collected right away (PerkinElmer instrument arrived in late March 2006); the film that could be characterized was four months old and was probably coated with an oxide layer, affecting its optical characteristics (for instance, the observed reflectance was only ~10 %). Despite the lower quality of optical data, an estimate of the band gap can be given. Considering the transmission spectra (Figure 6.16.a), one can see that the absorption edge goes from 1.60 eV to 1.80 eV, the plot of $(h\nu\alpha)^2$ *vs.* $(h\nu)$ (Figure 6.16.c) lead to a straight line fit over 33 nm (*i.e.* 33 points) with a linear regression coefficient of 0.9993, yielding a direct allowed band gap of 1.52 eV. This value is ~0.1 eV smaller than the beginning of the absorption edge. Thus, the optical data obtained for this

276

heteromorphite thin film indicate it is a direct band gap semiconductor with a direct allowed transition of 1.5 to 1.6 eV between the valence and the conduction bands.

a)

b)

c)
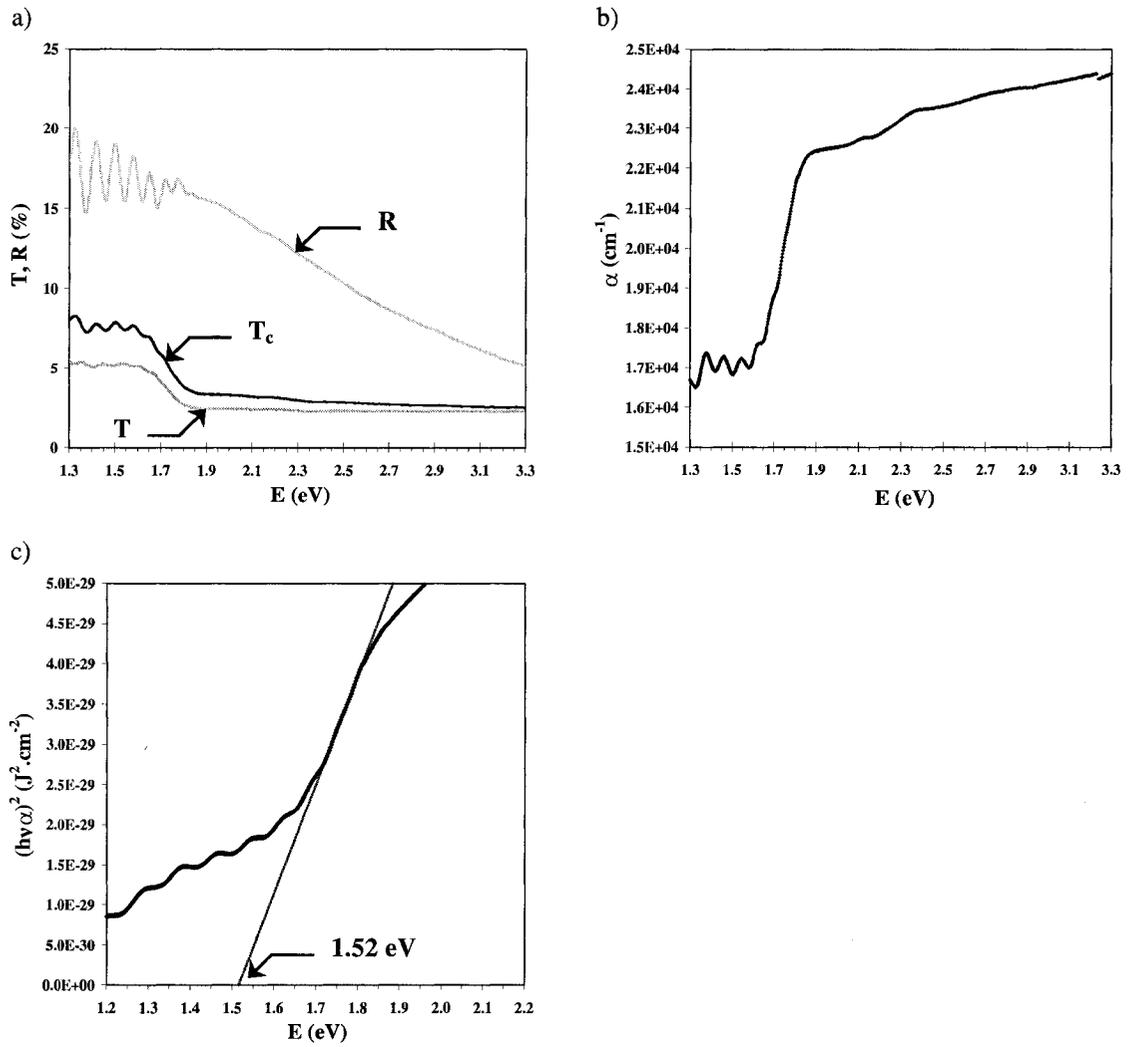
Figure 6.16. Optical characterization of a heteromorphite ($Pb_7Sb_8S_{19}$) thin-film: a) optical transmittance (T), reflectance (R) and corrected transmittance (T_c) sprectra, b) absorption coefficient (α) and c) direct allowed optical band gap extrapolation from $(h\upsilon\alpha)^2$ vs. E.

277
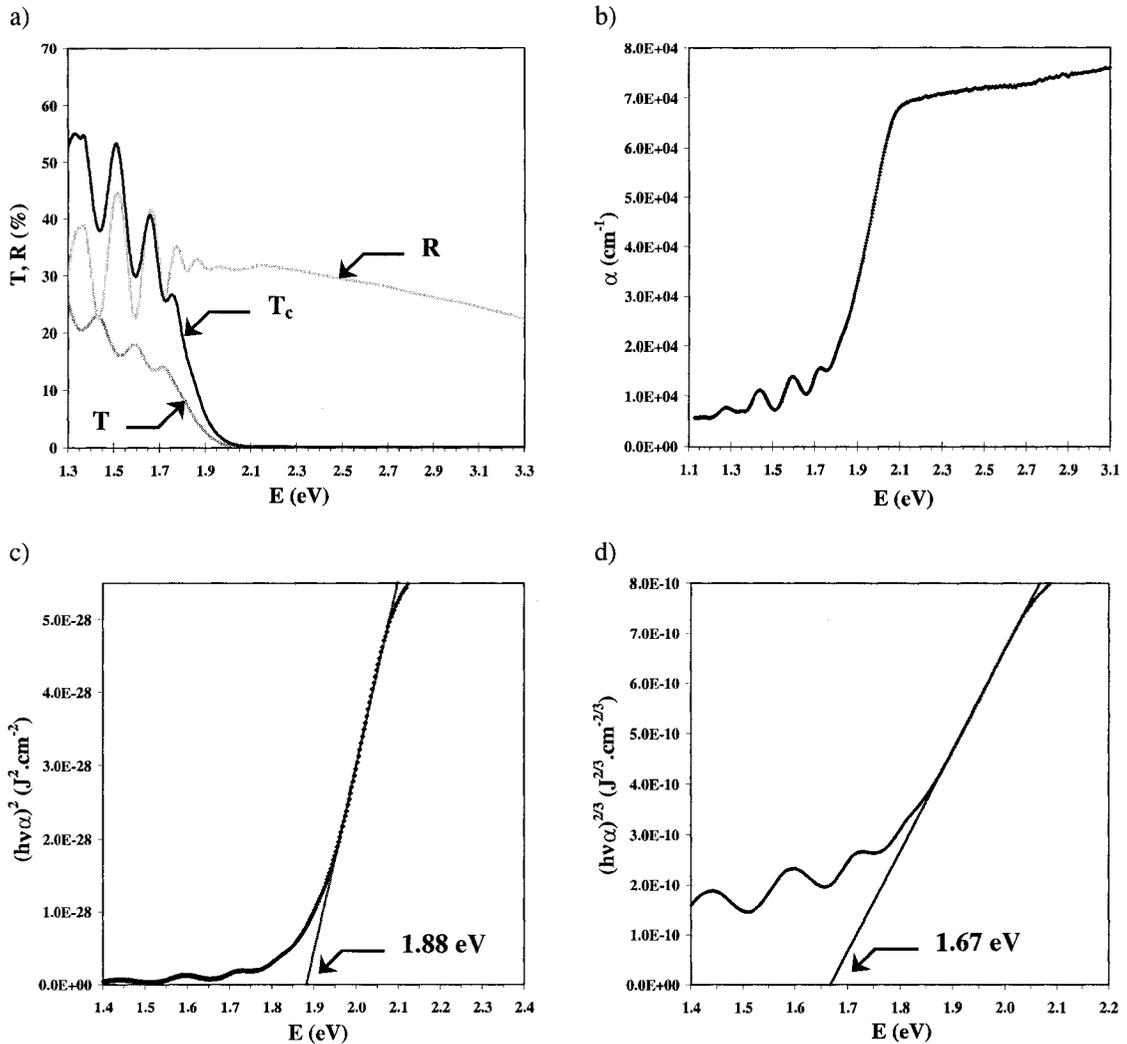
Figure 6.17. Optical characterization of a semseyite ($Pb_9Sb_8S_{21}$) thin-film: a) optical transmittance (T), reflectance (R) and corrected transmittance (T_c) sprectra, b) absorption coefficient (α), c) direct allowed optical band gap extrapolation from $(h\upsilon\alpha)^2$ vs. E, and d) direct forbidden optical band gap extrapolation from $(h\upsilon\alpha)^{2/3}$ vs. E.

For semseyite films (Figure 6.17), the plot of $(h\upsilon\alpha)^{2/3}$ vs. (hv) (Figure 6.17.d) yields a 1.67 eV direct forbidden band gap; whereas, the plot of $(h\upsilon\alpha)^2$ vs. (hv) (Figure 6.17.c) yields a 1.88 eV direct allowed band gap. A better straight line fit was obtained for the direct forbidden transition compared to the direct allowed transition. Indeed, in the direct-forbidden case, the straight line fit is obtained over 50 nm (*i.e.* 50 points) with

278

a linear regression coefficient of 0.9997, whereas in the direct-allowed case, the straight-line fit is steeper and obtained over 42 nm (*i.e.* 42 points) with a linear regression coefficient of only 0.998. Considering the direct-forbidden case, the derived optical band gap energy corresponds to the beginning of the increase in absorption of the corrected transmittance spectrum. Considering the direct-allowed case, the intercept with the photon energy axis yields a band gap energy that is close to the 100 % absorption onset. Similar results have been obtained for other semseyite films. Thus, from the optical data obtained from various semseyite thin films, semseyite is a direct band gap semiconductor with a forbidden transition of 1.7 eV between the valence and the conduction bands.

For plagionite films (Figure 6.18), the plot of $(h\nu\alpha)^{2/3}$ vs. $(h\nu)$ (Figure 6.18.d) yields a 1.60 eV direct forbidden band gap; whereas, the plot of $(h\nu\alpha)^{2}$ vs. $(h\nu)$ (Figure 6.17.c) yields a 1.82 eV direct allowed band gap. A better straight line fit was obtained for the direct allowed transition compared to the direct forbidden transition. Indeed, in the direct-allowed case, the straight line fit is obtained over 36 nm (*i.e.* 36 points) with a linear regression coefficient of 0.9992, whereas in the direct-forbidden case, the straight-line fit is obtained over 39 nm (*i.e.* 39 points) with a linear regression coefficient of only 0.9987. Considering the direct-allowed case, the intercept with the photon energy axis yields a band gap energy that is close to the 100 % absorption onset. Thus, from the optical data presented here, plagionite is a direct band gap semiconductor with an allowed transition of 1.8 eV between the valence and the conduction bands. It is interesting to note that for other plagionite thin films with stoichiometry shifted from the

279

ideal plagionite composition (*i.e.*15 at. % antimony poor (Sb:Pb = 1.36) and 12 at. %

antimony rich (Sb:Pb = 1.79)) a forbidden transition of 1.8 eV was derived.
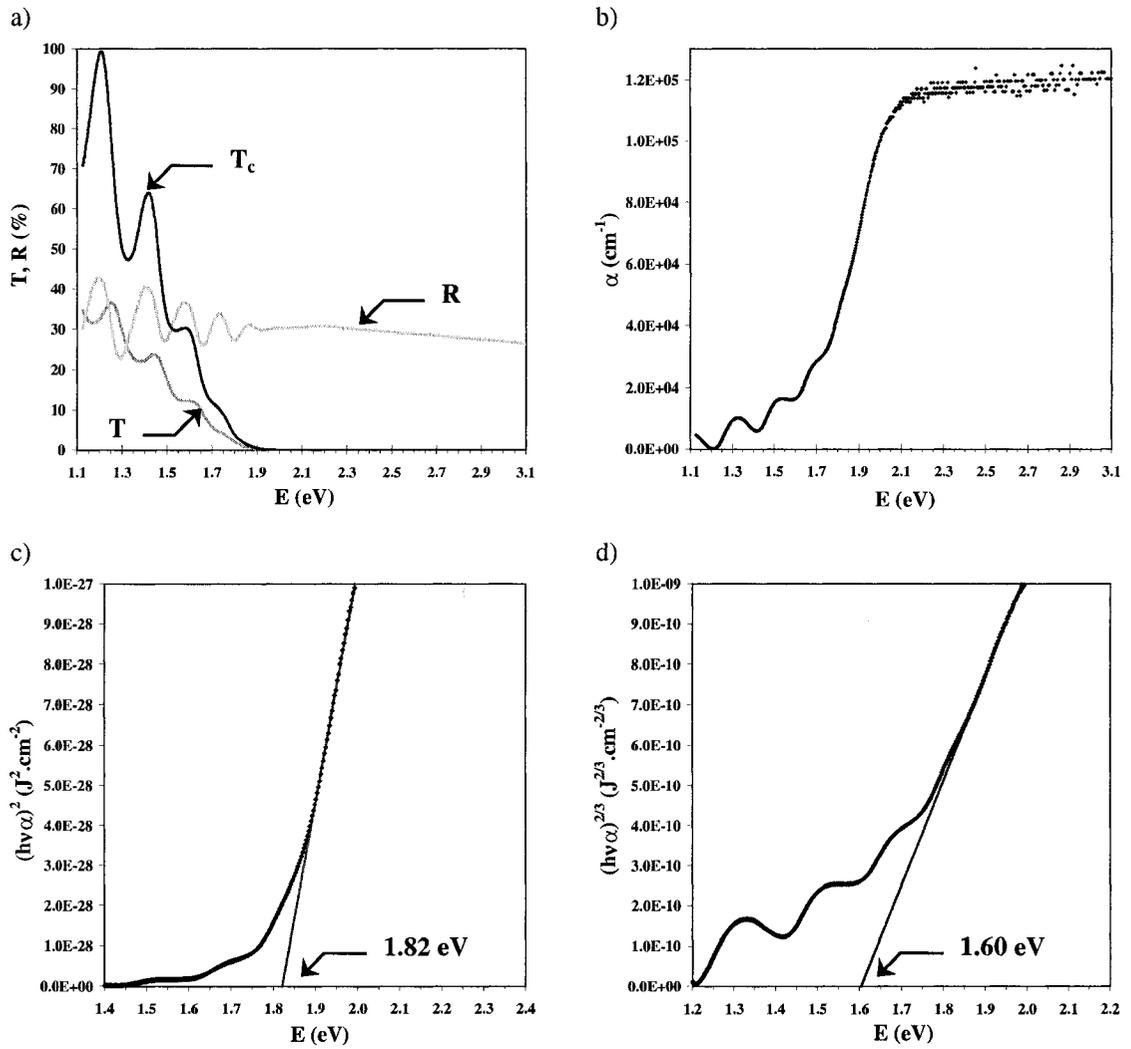
Figure 6.18. Optical characterization of a plagionite ($Pb_5Sb_8S_{17}$) thin-film: a) optical transmittance (T), reflectance (R) and corrected transmittance (T_c) sprectra, b) absorption coefficient (α), c) direct allowed optical band gap extrapolation from $(h\upsilon\alpha)^2$ vs. E, and d) direct forbidden optical band gap extrapolation from $(h\upsilon\alpha)^{2/3}$ vs. E.

280
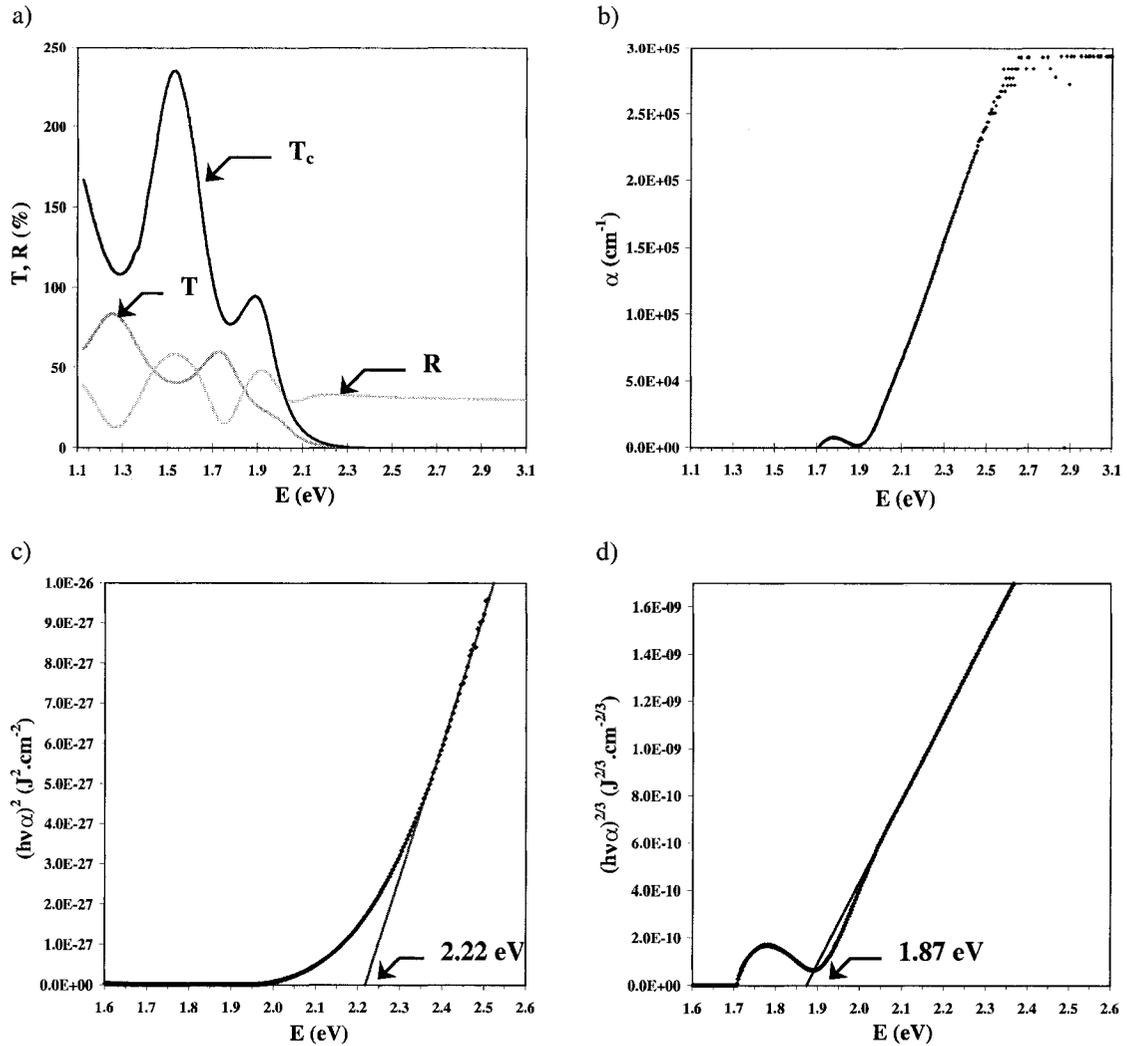
Figure 6.19. Optical characterization of a fülöppite ($Pb_3Sb_8S_{15}$) thin-film: a) optical transmittance (T), reflectance (R) and corrected transmittance (T_c) sprectra, b) absorption coefficient (α), c) direct allowed optical band gap extrapolation from $(h\upsilon\alpha)^2$ vs. E, and d) direct forbidden optical band gap extrapolation from $(h\upsilon\alpha)^{2/3}$ vs. E.

For fülöppite films (Figure 6.19), the plot of $(h\upsilon\alpha)^{2/3}$ vs. (hv) (Figure 6.19.d) yields a 1.87 eV direct forbidden band gap; whereas, the plot of $(h\upsilon\alpha)^2$ vs. (hv) (Figure 6.19.c) yields a 2.22 eV direct allowed band gap. A better straight line fit was obtained for the direct forbidden transition compared to the direct allowed transition. Indeed, in the direct-forbidden case, the straight-line fit is obtained over 70 nm (i.e. 70 points) with

281

a linear regression coefficient of 0.99997, whereas in the direct-allowed case, the straight-line fit is obtained over 35 nm (*i.e.* 35 points) with a linear regression coefficient of only 0.997. Considering the direct-forbidden case, the derived optical band gap energy corresponds to the beginning of the increase in absorption of the corrected transmittance spectrum. Considering the direct-allowed case, the intercept with the photon energy axis yields a band gap energy that is close to the 100 % absorption onset. Moreover, some Urbach tailing can be observed in Figure 6.19.c as the experimental curve is quite distant from the linear regression straight-line at energies below ~2.35 eV. Urbach tailing would suggest a defect-rich direct band gap semiconductor with trap states located within the band gap involving some band edge tailing [38]. Thus, from the optical data presented here, fülöppite is a direct band gap semiconductor with a forbidden transition of 1.9 eV between the valence and the conduction bands.

c)   *Band gap values*

The band gap values that we observed were significantly higher than the one reported in the literature for mineralogical samples [5,6]: approximately 0.2 eV larger for semseyite, 0.1 to 0.2 eV larger for heteromorphite, and lastly 0.3 eV larger for plagionite and fülöppite. Boldish *et al.* performed diffuse reflectance spectroscopy on crushed mineralogical samples of semseyite, plagionite and fülöppite; the band gap value was then determined via direct extrapolation of the absorption edge. Lomelino *et al.* derived the band gap of heteromorphite from the photoconductivity threshold observed on a mineralogical sample. Some of the differences observed between our thin film values and the mineralogical sample values may arise from the different techniques

282

used to obtain the band gap values. Also, as mentioned earlier in the XRD data description section, slight crystallographic and compositional differences between the mineralogical samples studied by Boldish *et al.* or Lomelino *et al.* and our thin-film samples may explain the difference in the reported band gap values. Indeed, crystallographic and compositional differences would affect the band structure and alter the band gap. Although wider than the optimal 1.4 eV, the band gap values obtained for the various phases are promising and might be lowered by improving the thin-film composition and crystallinity. Most of the films have been obtained sulfur-rich and/or antimony-poor, this stoichiometric deviation and subsequent defects in the crystal structure may well induce an increase in the band gap value.

6.7   Conclusions

WDX analyses of as-deposited crystalline PbS and amorphous (Sb,S) layered precursor films demonstrated some variability in the as-deposited Sb:Pb ratio, despite careful control of the deposition parameters, this phenomenon is believed to be due to evolutionary changes on the surface of the Sb_2S_3 target as it ages. Despite this lack of precise control over the as-deposited Sb:Pb ratio, crystalline PbS and amorphous (Sb,S) layered precursors successfully yielded thin-film of the four plagionite group phases: semseyite, heteromorphite, plagionite and fülöppite.

Studies of the annealing parameters showed that for the thick precursor films for semseyite, heteromorphite and plagionite, the best results were obtained with annealings at 400 °C for 50 minutes; for the thin precursor films for plagionite and fülöppite, the

283

best results were obtained at 350 °C for 2 hours. The different behavior exhibited during reactive annealing of the co-sputtered metal precursor films (Chapter 5) and of the layered precursor films demonstrated that the incorporation of sulfur into the precursor film is essential to prepare ternary phase-pure films with good morphology. Moreover, films of the plagionite group phases were preferentially obtained with our thin-film growth process, indicating that the presence of hydrogen is not necessary for their occurrence and suggesting their metastability.

Thus, sulfurization of the unique crystalline PbS and amorphous (Sb,S) layered precursor films yielded smooth, continuous and phase-pure films of the plagionite group phases. Optical measurements indicated that films of the plagionite group phases have strong absorption coefficients ($\sim 10^5$ cm^{-1}). In addition, they showed that semseyite and fülöppite are direct band gap semiconductors with a forbidden transition of 1.7 eV and 1.9 eV, respectively, and that heteromorphite and plagionite are direct band gap semiconductors with allowed transition of 1.5 eV and 1.8 eV, respectively.

6.8   References

[1]   D. Bonnet, P. Meyers, J. Mater. Res. 13 (1998) 2740.

[2]   M.A. Green, K. Emery, D.L. King, Y. Hisikawa, W. Warta, Progress in Photovoltaics 14 (2006) 45.

[3]   B.A. Andersson, Progress in Photovoltaics 8 (2000) 61.

[4]   H. Dittrich, D.J. Vaughan, R.A.D. Pattrick, S. Graeser, M. Lux-Steiner, R. Kunst, D. Lincot, in: W. Freiesleben (Ed.), Proceedings of the 13th European

Photovoltaic Solar Energy Conference, Nice, France, October 23-27, 1995, p.1299.

[5]   T.F. Lomelino, G. Mozurkewich, Am. Mineral. 74 (1989) 1285.

[6]   S.I. Boldish, W.B. White, Am. Mineral. 83 (1998) 865.

[7]   A. Luque, A. Marti, in: S.S. Hegedus, A. Luque (Eds.), Handbook of Photovoltaic Science and Engineering, John Wiley and Sons Ltd., Chichester, UK, 2003.

[8]   H. Dittrich, K. Herz, in: R.D. Tomlinson, A.E. Hill, R.D. Pilkington (Eds.), Ternary and Multinary Compounds: Proceedings of the 11th International Conference on Ternary and Multinary Compounds, Salford, UK, September 8-12, 1997 Inst. Phys. Conf. Ser. 152 (1997) 293.

[9]   J.L. Jambor, Mineral. Mag. 37 (1969) 443.

[10]   S.-A. Cho, B.J. Wuensch, Nature 225 (1970) 444.

[11]   B.J. Wuensch, Acta Crystallogr., Sect. B: Struct. Sci. B30 (1974) 2935.

[12]   B.J. Wuensch, in: J.M. Cowley (Ed.) International Conference on Modulated Structures, Kailua Kona, Hawaii, U.S.A., 1979, AIP Conference Proceedings 53 (1979) 337.

[13]   M.Y. Versavel, J.A. Haber, Chem. Commun. (2006) 3543.

[14]   P.L. Garvin, Neues Jahrb. Mine. Abh. 118 (1973) 235.

[15]   S.C. Robinson, Econ. Geol. 43 (1948) 293.

[16]   Y. Noda, K. Masumoto, S. Ohba, Y. Saito, K. Toriumi, Y. Iwata, I. Shibuy, Acta Crystallogr., Sect. C: Cryst. Struct. Commun. C43 (1987) 1443.

[17] Powder Diffraction File, International Center for Diffraction Data, Newton Square, PA, 2002, Card 65-135.

[18] H. Swanson, Tatge, National Bureau for Standards, Circ. 539 vol. 1 (1953) 34.

[19] Powder Diffraction File, International Center for Diffraction Data, Newton Square, PA, 2002, Card 4-686.

[20] D.M. Mattox, Handbook of Physical Vapor Deposition (PVD) Processing: Film Formation, Adhesion, Surface Preparation and Contamination Control, Noyes Publications, Westwood, NJ, 1998.

[21] Powder Diffraction File, International Center for Diffraction Data, Newton Square, PA, 2002, Card 22-1130.

[22] A. Edenharter, Z. Kristallogr. 151 (1980) 193.

[23] Powder Diffraction File, International Center for Diffraction Data, Newton Square, PA, 2002, Card 83-1428.

[24] Powder Diffraction File, International Center for Diffraction Data, Newton Square, PA, 2002, Card 73-1112.

[25] A. Edenharter, W. Nowacki, Zeitschrift fur Kristallographie, Kristallgeometrie, Kristallphysik, Kristallchemie 142 (1975) 196.

[26] Powder Diffraction File, International Center for Diffraction Data, Newton Square, PA, 2002, Card 65-2330.

[27] B. Meyer, Chem. Rev. 76 (1976) 367.

[28] K.C. Mills, Thermodynamic Data For Inorganic Sullphides, Selenides and Tellurides, Butterworth and Co Ltd, London, 1974.

286

[29] G.L. Miessler, D.A. Tarr, Inorganic Chemistry, Pearson Education Inc., Upper Saddle River, NJ, 2004.

[30] C. Guillén, J. Herrero, Sol. Energy Mater. Sol. Cells 73 (2002) 141.

[31] M. Kemell, M. Ritala, M. Leskelä, Crit. Rev. Solid State Mater. Sci. 30 (2005) 1.

[32] A. Kitakaze, A. Sugaki, H. Shima, Mineralogical Journal 17 (1995) 282.

[33] B. Salanci, Neues Jahrb. Mine. Abh. 135 (1979) 315.

[34] M.D. Hornbostel, E.J. Hyer, J. Thiel, D.C. Johnson, J. Am. Chem. Soc. 119 (1997) 2665.

[35] J.I. Pankove, Optical Processes in Semiconductors, Prentice-Hall Inc., Englewood Cliffs, NJ, 1971.

[36] R.A. Smith, Semiconductors - 2nd edition, Cambridge University Press, Cambridge, NY, 1978.

[37] J.L. Gray, in: S.S. Hegedus, A. Luque (Eds.), Handbook of Photovoltaic Science and Engineering, John Wiley and Sons Ltd., Chichester, UK, 2003.

[38] H.J. Möller, Semiconductors for Solar Cells, Artech House, Boston, MA, 1993.

287

Chapter 7: Concluding Remarks and Future Directions

The work described in this thesis is the first work performed using the custom built ultra high vacuum deposition system described in Chapter 1. As one may expect with such a versatile system and given the difficulties encountered with the transfer and substrate stage sub-systems and later with the vacuum pumps, getting the system up and running smoothly required a lot of time and effort. In addition, when we produced our first Hf-Zr-Sb films, the XRD diffractometer was also newly installed and, unfortunately, required several debugging operations. I am grateful for the opportunity I had to attend a D8 instrument operation training class at the Bruker AXS Inc. facility in Madison, WI, therefrom, progressively building up the experience and technical skills required to efficiently operate the instrument and to explore its diverse capabilities. Lastly, the UV-VIS spectrometer and its specular reflectance attachment only arrived at the beginning of 2006, towards the end of my experimental work. Starting the group projects both scientifically and technically from "ground zero" was challenging and difficult at the time, but truly enriching and plentiful of valuable lessons about combinatorial techniques and about the design and maintenance of complex vacuum deposition facilities.

In this context, I began working on the first project that is described later in Appendix 2. This combinatorial project aimed to discover new crystal structures in the Hf-Zr-Sb phase diagram. Unfortunately, because this project involved volatile, refractory and/or oxophilic elements, employed high temperatures and utilized our

288

deposition system, which was not designed to produce wide composition-spread gradient libraries, this project proved to be very difficult to handle. As a final remark, I would like to say that, by inexperience, we started directly our investigation using a combinatorial approach; it would have been wiser first to test our experimental techniques and our infrastructure capabilities with a film composed of a carefully chosen single composition of hafnium, zirconium and antimony.

Nevertheless, during the first project we implemented a reliable film deposition rate calibration method. Thus, the X-ray reflectometry technique successfully yielded satisfactory determination of the deposited film thicknesses for hafnium, zirconium and antimony, and later, for amorphous antimony sulfide. Given our experimental set-up, the determination of film thickness of 50 to 100 nm may be achieved accurately, 75 nm being optimal. Because of smoothness requirements on the film for X-ray reflectometry, lead deposition was, nevertheless, successfully calibrated by weigh measurement of lead films, assuming the bulk density.

The development of the synthesis of lead antimony sulfide thin films also lead to the preparations of PbS (galena) films and, more significantly, of Sb_2S_3 (stibnite) films. Similar to the outcome with the ternary phases, annealing antimony metal precursor films in sulfur vapor had limited successes, while the amorphous Sb_2S_3 precursor films obtained by RF-sputtering of an Sb_2S_3 target proved to yield superior films. Thus, part of this work is the first report of the preparation of amorphous and polycrystalline antimony sulfide (Sb_2S_3) thin films from RF-sputtering of an Sb_2S_3 target and

subsequent annealing at 400 °C in sulfur vapor. It yielded smooth and compact semiconductor films of amorphous and crystalline Sb_2S_3 with strong absorption coefficients and direct band gaps.

In an effort to prepare polycrystalline films of lead antimony sulfides, sputtered metallic Pb-Sb precursor films were used. The sulfurization procedure attempted first was based on annealing the precursor films in a H_2S environment, as it was successfully reported for $CuInS_2$ [1-3]. Yielding rough and discontinuous films, this rather long procedure was inefficient and poorly suited to the Pb-Sb-S film preparation. A second annealing procedure that allows higher experimental throughput was, therefore, implemented. Precursor films were annealed in elemental sulfur vapor generated from elemental sulfur. From this approach, we gained insight into the behavior and the reactivity of the metallic Sb-Pb co-sputtered films in sulfur vapor. For films made of 30 at. % lead and higher, it was observed that the inevitable initial formation of PbS was detrimental. Indeed, it decreased the overall reactivity of the film, causing preferential re-evaporation of the antimony over ternary phase growth, negatively impacted the morphology of the films. All of the films, regardless of the starting composition, obtained by this preparation route suffered important composition changes (mostly antimony depletion) and, therefore, did not have the crystallinity (purity) or morphology meeting the requirements for their integration into thin film solar cells as light absorbers.

A more successful approach was to replace the metallic Pb-Sb precursor films with sulfur-containing precursor films; these crystalline PbS and amorphous (Sb,S)

290

layered precursor films were prepared by cycled RF-sputtering of Sb_2S_3 and DC-sputtering of lead. Despite a lack of precise control over the as-deposited Sb:Pb ratio, the annealing in sulfur vapor of these layered precursor films successfully yielded thin-films of the four plagionite group phases: semseyite ($Pb_9Sb_8S_{21}$), heteromorphite ($Pb_7Sb_8S_{19}$), plagionite ($Pb_5Sb_8S_{17}$) and fülöppite ($Pb_3Sb_8S_{15}$). The different behaviors exhibited during reactive annealing of the co-sputtered metal precursor films (Chapter 5) and of the sulfur containing layered precursor films (Chapter 6) demonstrated that the incorporation of sulfur into the precursor film is essential to prepare ternary phase-pure films with good morphology. Indeed, the initial presence of sulfur in the precursor increased its overall reactivity, thereby decreasing the extent of antimony depletion. In addition, films of the plagionite group phases were preferentially obtained with our thin-film growth process. This indicates that the presence of hydrogen is not necessary for their occurrence, as previously hypothesized, and suggests that they are metastable. Sulfurization of the crystalline PbS and amorphous (Sb,S) layered precursor films yielded smooth, continuous and phase-pure films of the plagionite group phases, with appropriate optical properties. In other words, they possess direct band gaps ranging from 1.5 eV to 1.9 eV and strong absorption coefficients.

However, the electrical properties of these films are not suitable, at this stage, as films proved to be highly resistive. Indeed, their electrical properties could not be determined by regular van der Pauw or four-point probe methods due to their high resistivity [4] nor by a guarded van der Pauw system, which allows for measurement of semiconductors with resistivities greater than 10^7 Ω and smaller than 10^{12} Ω [5]. Thus,

as-annealed films are highly resistive; this may be due to some crystal defects and the small crystallite size. Therefore, before any attempt to integrate the films into a solar cell, electrical properties of films of lead antimony sulfides need to be improved. To achieve this goal, one should improve the crystallinity of the films; the number of crystal defects should be minimized, and the crystallite grain size should be increased from their current 100 nm width.

To improve the structural and, thereby, electrical properties of the film, it is first highly desirable to gain control over the as-deposited Sb:Pb of the layered PbS and amorphous (Sb,S) in order to ensure a more reproducible process. As the deposition rate variability is most likely due to evolutionary changes in the Sb_2S_3 target, lowering the RF-power (*i.e.* the energy) applied to the target will allow more efficient cooling of the target and reduce its temperature, thereby decreasing the extent of the surface changes (cracks, soot, recrystallization...). Changing the power applied to the target will necessarily require new calibration experiments for the cycled sputtering of Sb_2S_3 and Pb in order to determine the Sb:Pb stoichiometric ratios of the as-deposited layered films and to evaluate the reproducibility of the process. Thus, once the optimal annealing conditions are found, control over the initial Sb:Pb ratio will be extremely useful to fine-tune the final film composition in order to precisely control the stoichiometry of the lead antimony sulfide phases and, thereby, potentially limit the amount of crystalline defects.

Despite the fairly large number of annealing conditions that have been tested for the crystalline PbS and amorphous (Sb,S) layered precursor films, none yielded large

292

crystallites, one of the conditions required to potentially improve the electrical properties of the films. Thus, it may be useful to attempt the conditions described below.

- A true three-zone tube furnace should be purchased and used to gain precise control over the sulfur source temperature. Thus, it would not only increase the reproducibility of the annealing process, but also allow for the investigation of a broader range of conditions for the sulfur source ramp rate and maximum temperature. Therefore, it would be possible to vary the partial pressure of the sulfur as a function of the film temperature.

- Rapid thermal processing has proven to be successful for the preparation of $CuInS_2$ [6,7]. During this process, elemental sulfur and precursor film are heated very rapidly (10 °C/s) to 600 °C, kept at this temperature for only a few minutes (~2 min.) and then cooled down rapidly (~3 min) to 100 °C. This process requires state-of-the-art equipment; special lamp or inductive heating elements capable of fast heat-up rates and reproducible and stable control of the high temperature must be used.

- The crystalline PbS and amorphous (Sb,S) precursor films have not been annealed under $H_2S_{(g)}$. Thus, a starting point would be to anneal the precursor films at temperatures higher than 400 °C for short periods of time, in a tube furnace back-filled with $H_2S_{(g)}$, as early results for annealing of metallic Sb-Pb precursor films under $H_2S_{(g)}$ showed a tendency to yield large crystals. This process requires the capability of safely and precisely control the pressure (~5 mTorr) of H_2S in the annealing tube.

293

- The repeat layer thicknesses of the precursor films were maintained in the range of 40 to 80 nm, without notable changes. Nevertheless, one may consider either decreasing or increasing these. Indeed, by having a near intimate mixing situation or, on the contrary, a diffusion couple-like situation, the reaction pathway may be affected and thereby modifying the phases that are nucleated and their morphology. One should bear in mind that both plagionite-like and acicular lead antimony sulfide phases may be considered potential solar absorbers for thin film solar cells.

- Sulfur-containing precursor films showed better behavior upon annealing in sulfur vapor than metallic Sb-Pb precursor films. These precursor films were obtained by cycled Sb_2S_3 and Pb sputtering, but they may also be obtained by sequential or simultaneous sputtering or evaporation of PbS and Sb_2S_3. Indeed, as most of the lead antimony sulfide phases belong to the PbS-Sb_2S_3 joint, it would be interesting to start with these two binaries to have initial, overall and sulfur compositions as close as possible to those of the target phases. Sputtering PbS requires the purchase of a lead sulfide target, which we were unsuccessful in obtaining. Quotes were hard to get and expensive. Delivered targets contained significant and detrimental amounts of lead metal, lead sulfate and/or elemental sulfur, arising from the inadequate PbS powder hot pressing. A more promising process would be the sequential or co-evaporation of PbS and Sb_2S_3, providing that they don't decompose during evaporation, as evaporation is known to generally yield larger crystal grains. One should note that co-evaporation is not possible with our deposition system.

294

As a final remark, I would like to briefly mention that once lead antimony sulfide films are obtained with appropriate morphology, crystallinity, and optical and electrical properties, it will then be necessary to integrate these films into thin film solar cells. A good starting point would probably be with the well-known architecture of CIGS solar cells, *i.e.* SnO_2:F/ZnO:Al/CdS/absorber/Mo. Also, the original and ultimate goal of our research was to combinatorially investigate several device architectures. Using a set of quaternary fractal masks, one may deposit as many as 64 different architectures on a 2 in. × 2 in. substrate, exploring various combinations of back-contacts, buffer layers, heterojunction couples and front contacts for a given absorber. One should not forget that each layer and each material will require its own development stage to achieve suitable characteristics before its use in a combinatorial strategy.

References

[1]   H.J. Lewerentz, Sol. Energy Mater. Sol. Cells 83 (2004) 395.

[2]   T. Nakabayashi, T. Miyazawa, Y. Hashimoto, K. Ito, Sol. Energy Mater. Sol. Cells 49 (1997) 375.

[3]   M. Gossla, H. Metzner, H.-E. Mahnke, Thin Solid Films 387 (2001) 77.

[4]   D.K. Schröder, Semiconductor Material and Device Characterization, Wiley, New York, NY, 1990.

[5]   P.M. Hemenger, Rev. Sci. Instrum. 44 (1973) 698.

[6]   R. Scheer, R. Klenk, J. Klaer, I. Luck, Solar Energy 77 (2004) 777.

[7]   R. Klenk, *et al.*, Sol. Energy Mater. Sol. Cells 49 (1997) 349.

Appendix 1: Preparation of PbS (Galena) Thin-films

This Appendix reports experimental details for the of thin film preparation of PbS (galena). This information was collected during the combinatorial annealings described in Chapter 5.

A1.1 Thin-film deposition and annealing

In our effort to develop a preparation for Pb-Sb-S ternary phase thin films, antimony (see Chapter 4) and lead precursor films have been prepared in order to synthesis stibnite (Sb_2S_3) and galena (PbS). Films of lead were sputtered onto pre-cleaned glass substrates. The lead films presented in Table A1.1 gave the most significant results.

Table A1.1. Lead precursor films

Film	Power	Time	Rotation speed	Thickness (nm)
A	50 W	46'	10 s/rev	~1000
B	10 W	285'	10 s/rev	~1000
C	10 W	20'	2 s/rev	~100

Films were prepared by magnetron sputtering a lead metal target (Kurt J. Lesker, 99.999 %) with an argon pressure of 667 (±3) mPa. As usual, the substrate was continuously rotated during deposition; however, the speed was increased from 10 s/rev (usual set-up) to 2 s/rev, in order to decrease the roughness of the as-deposited films.

Several annealing experiments have been carried out on sputtered precursor films of lead. Table A1.2 gathers the different annealing parameters.

296

Table A1.2. Annealing parameters

Ann#	Film	T_S max	Rate (°C/min)	T_1 (°C)	Rate (°C/min)	T_2 (°C)	Rate (°C/min)
01	A	160 °C	13.5	160 °C (2h30)	Tube removed	-	-
02	A	200 °C	13.5	200 °C (2h)	Tube removed	-	-
03	A	250 °C	14	250 °C (1h30)	Tube removed	-	-
04	A	300 °C	14.5	300 °C (1h)	Tube removed	-	-
05	A	300 °C	13.5	160 °C (2h)	14	300 °C (2h)	Furnace Opened
06	A	235 °C	13.5	160 °C (2h)	14	300 °C (4h)	~ 3 →160 °C
07	A	135 °C	18.3	300 °C (45')	16.7	350 °C (1h45)	~ 3 →215 °C
08	A	185 °C	27.5	300 °C (30')	18.8	375 °C (2h30)	~ 3 →192 °C
09 N_2 atm	A	185 °C	23.3	375 °C (3h)	< 5	220 °C (1h30)	~ 3 →100 °C
10 N_2 atm	C	185 °C	13	400 °C (30')	3.0 →100 °C	-	-
11	C	185 °C	13	400 °C (30')	3.0 →100 °C	-	-
12	C	185 °C	13	400 °C (30')	3.0 →100 °C	-	-
13 (40)	C	185 °C	13	400 °C (50')	3.0 →100 °C	-	-

Annealings #01 to #05 and #06 were performed, respectively with the following set-ups: #01 to #05: boat with sulfur located in the same furnace as the film, and #06: boat with sulfur located in a separate furnace. All the other annealings were performed with the previously described sulfur boat located in a heated brass extension that is attached to the tube at the end of the main furnace. Except for annealings #09 and #10, for which the

297

annealing tube was back-filled with N_2 at atmospheric pressure, all annealing experiments were performed after evacuation of the annealing tube.

A1.2 Results

a) As-deposited films

As deposited films are made of crystalline lead. Regardless of the deposition conditions, films are deposited with a preferred orientation in the (111) direction as shown in Figure A1.1, which represents a typical XRD pattern for an as-deposited lead films.
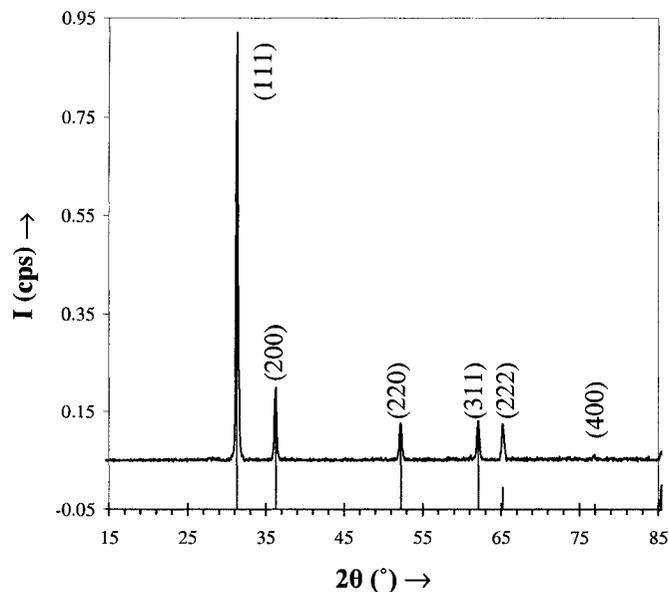
Figure A1.1. XRD pattern of an as-deposited lead film (film C in Table A1.1).

As deposited films of lead are usually rough, with micron high crystallites on top of the film base as shown in Figures A1.2.a and A1.2.b. This phenomenon was observed both for films of types A and B (see Table A1.1), which were deposited with different powers (50 W and 10 W, respectively).

298

a)   b)
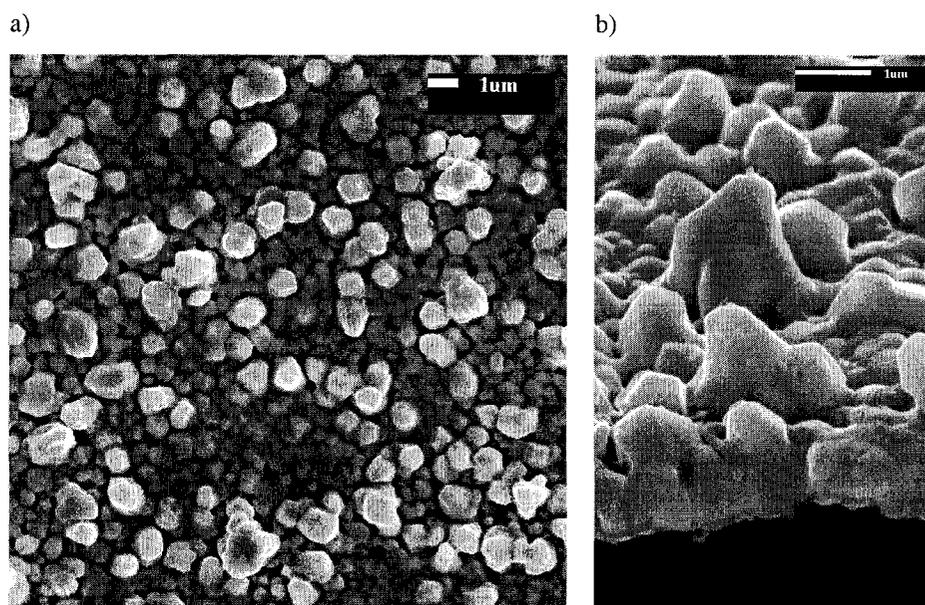
Figure A1.2. SEM images of an as-deposited lead film (film A in Table A1.1): a) top-surface image and b) tilt view of the cross-section.

However, it has been noticed that increasing the rotation speed of the substrate during deposition decreases the film roughness (no formation of the 1 μm high crystallites). This phenomenon may be seen in Figures A1.3.a and A1.3.b, showing the morphology of film C, previously described in Table A1.1. The film is made of 100 nm high, 1 to 3 micron long crystalline islands. The film is not completely continuous with 20 nm "canyons" between the islands; longer deposition times are necessary to coalesce the islands together.

a)   b)   c)
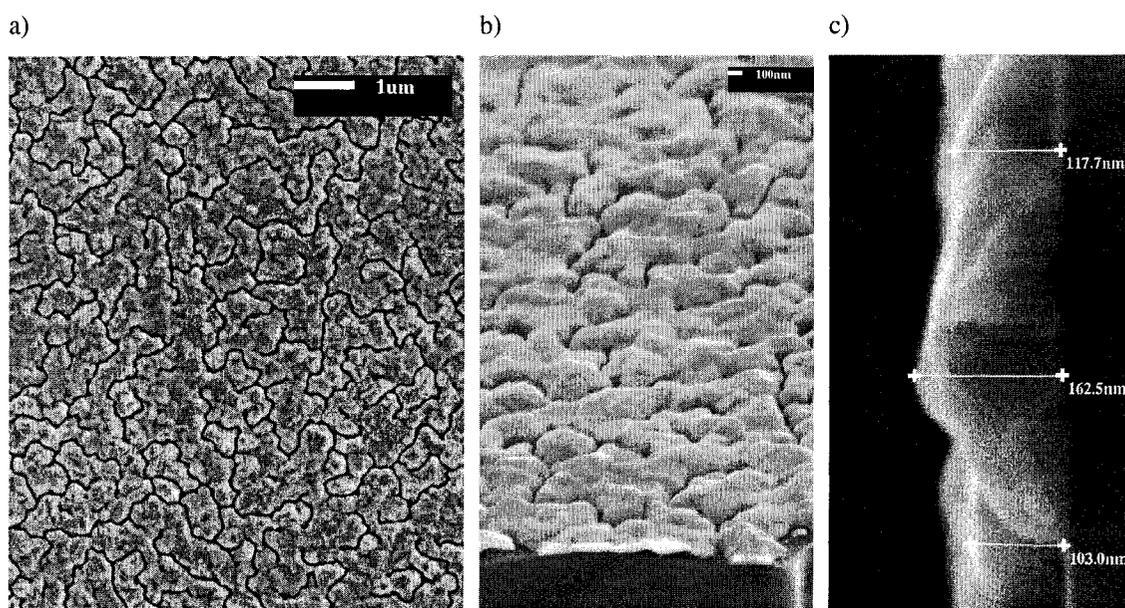
Figure A1.3. SEM images of an as-deposited lead film (film C in Table A1.1): a) top-surface image, b) tilt view of the cross-section and c) cross-sectional image.

b)   PbS (galena) thin film obtained from annealing in sulfur vapor

All the annealing conditions presented here yielded the conversion of the as-deposited lead precursor film into films of lead sulfide. Except for annealings #01 and #02, the conversion was complete, as no sign of lead could be detected by XRD. This is shown in Figure A1.4, which is the XRD pattern of the film obtained from annealing #04 in Table A1.2. In the cases of annealings #01 and #02, only traces of lead could be detected from very weak (111) peaks. In addition, WDX data on the PbS (galena) thin films consistently yielded sulfur-rich films with the Pb:S ration ranging from 45:55 to 50:50. No sign of texture was observed by XRD. The absence of texture was confirmed by the morphology of the films as shown below.

300
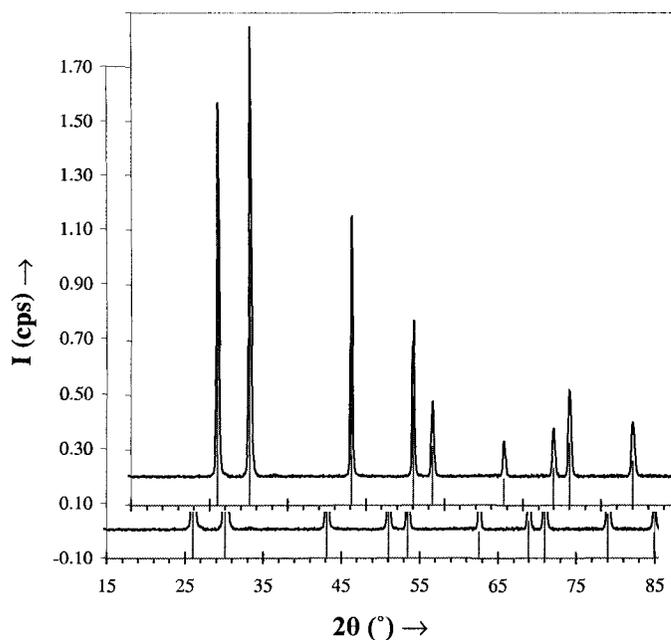
Figure A1.4. XRD pattern of galena film (film A in Table A1.1 obtained from annealing #04 in Table A1.2).

Considering annealings #01, #02, #03 and #04, one notices that with increasing temperatures (160 °C, 200 °C, 250 °C, 300 °C) the degree of agglomeration of the particles increases significantly, whereas the particle size increases only slightly (~0.1 to 0.2 μm), as shown in Figures A1.5.a, A1.5.b, A1.5.c and A1.5.d. Thus, upon annealing #01 (160 °C for 150 minutes), a porous and powdery PbS film was obtained, whereas annealing #04 (300 °C for 60 minutes) produced a very rough film with up to one micron aggregates. Thus, temperature mostly affects the film micron-scale morphology and has no or little influence regarding the grain size. Also, providing that the reaction time is long enough, Pb films can be fully converted into PbS films under sulfur vapor even at temperatures as low as 160 °C.

301

a)   b)

c)   d)
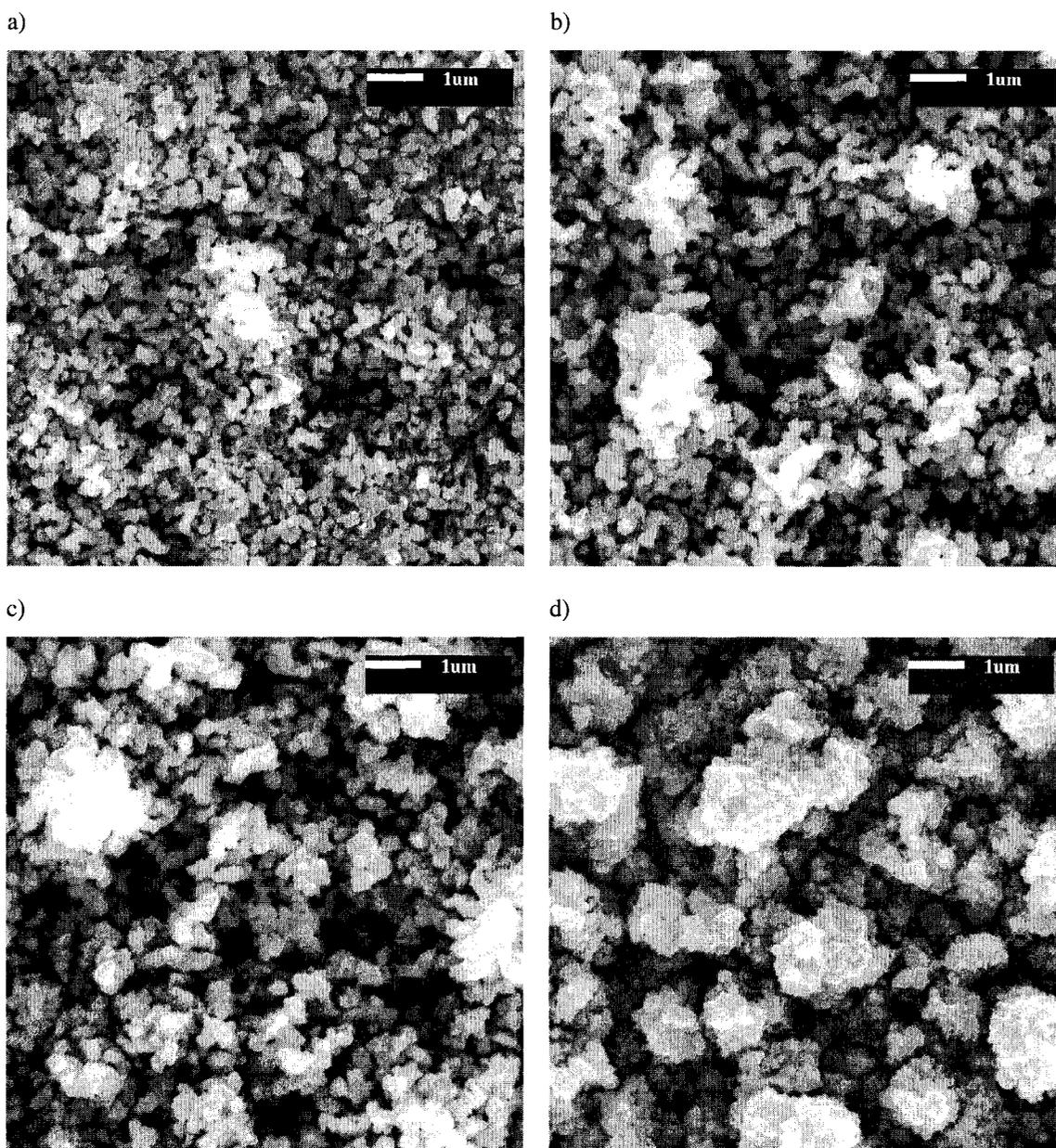
<u>Figure A1.5.</u> Top surface SEM images of lead precursor (film A in Table A1.1) annealed at a) 160 °C, b) 200 °C, c) 250 °C and d) 300 °C (*i.e.* annealings #01, #02, #03 and #04 in Table A1.2).

The annealing programs #01, #05 and #06 all contained a two-hour dwell at 160 °C followed by a dwell at 300 °C of varying time (0h, 2h, and 4h). SEM images of the films obtained are shown in Figures A1.5.a, A1.6.a and A1.6.b. Comparing the morphology of the PbS films obtained from annealings #01, #05 and #06, one notices

302

that the particles size remains approximately the same, but that the degree of agglomeration increases with the duration of the 300 °C dwell. Thus, annealing #06 lead to a film with an even and continuous film base (or background) featuring 1 to 2 micron aggregates on top. During the first dwell at low temperature, the Pb film is converted into a uniform and powdery PbS film (despite the fact that the as-deposited Pb film is dense and present micron scale lumps). Its morphology is then transformed during the second dwell at 300 °C.

a)   b)
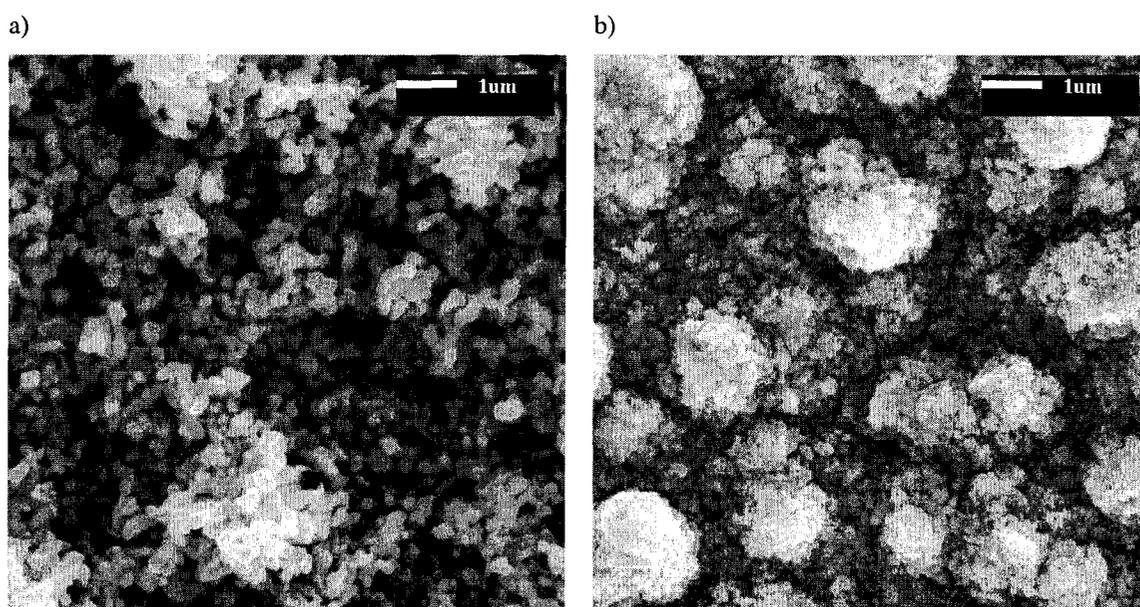
Figure A1.6. Top surface SEM images of lead precursor (film A in Table A1.1) annealed at 160 °C for 2h and then at 300 °C for a) 2h and b) 4h (*i.e.* annealings #05 and #06 in Table A1.2).

The annealing programs #04, #07 and #08 all contain a first short dwell at 300 °C (1h, 45', 30') followed by a dwell at higher temperature (350 °C – 105 minutes for annealing #07, 375 °C – 150 minutes for annealing #08). SEM images of these films are shown in Figures A1.5.d, A1.7.a and A1.7.b. Although similar, some differences can be noticed between the morphologies of these three films.

303

- Aggregates obtained with annealing programs #07 and #08 are larger than those obtained with annealing program #04, which confirms that the degree of aggregation increases with time and temperature.

- Films obtained with annealing programs #04 and #08 seem to have deeper cavities, whereas the films obtained via annealing #07 has a more continuous base. The origins of the cavities may be different in the cases of annealings #04 and #08. Indeed, in the case of annealing #04, one could say that the aggregation phenomenon is incomplete, whereas in the case of annealing #08, it could be in an advanced stage during which the vertical growth of the aggregates occurs at the expense of the film base.

- Lastly, cracks can be observed on films obtained via annealings #07 and #08. Thus, higher temperatures and longer annealing times may degrade the film adhesion properties.

a)

b)
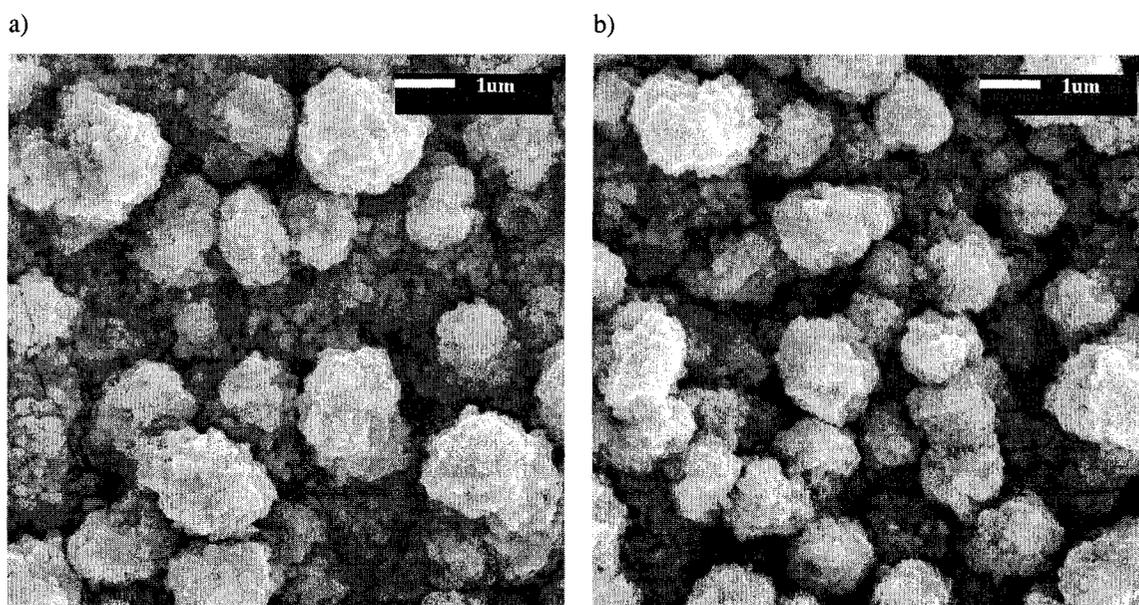
Figure A1.7. Top surface SEM images of lead precursor (film A in Table A1.1) annealed shortly at 300 °C and then at a) 350 °C for 105 minutes and b) at 375 °C for 150 minutes (*i.e.* annealings #07 and #08 in Table A1.2).

304

Looking at the SEM images, one notices that the film obtained via annealing #09 (Figure A1.8) looks somewhat different from the others: the film is not powdery and features terraces rather than lumps and cavities, with a more or less continuous base. This film was annealed at 375 °C for 3 hours and then at 220 °C for 90 minutes, but perhaps more importantly, during this annealing the pressure in the annealing tube was different, as the tube was back-filled with N_2 to atmospheric pressure before annealing. Thus, the increased pressure in the tube may prevent the vertical growth of aggregates and favor growth parallel to the substrate.
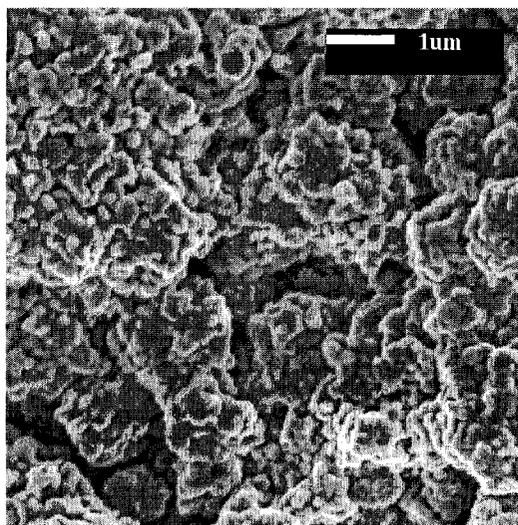
Figure A1.8. Top surface SEM images of lead precursor (film A in Table A1.1) annealed at 375 °C for 3h and 220 °C for 1h30 with the annealing tube back-filled with N_2 (*i.e.* annealing #09 in Table A1.2).

Finally, considering annealings #10, 11 and 12 of the thinnest as-deposited lead precursor films (*i.e.* type C in Table A1.1). Very similar morphologies were obtained regardless of the reaction conditions: evacuated or N_2 filled tube, duration of the 400 °C dwell. Representative morphology is shown in Figures A1.9.a, A1.9.b and A1.9.c. Films are quite smooth with 200 to 400 nm aggregates of small grains (~50 nm) and with pores smaller than 100 nm. As shown in Figure A1.9.c, the base of the film looks dense.

305
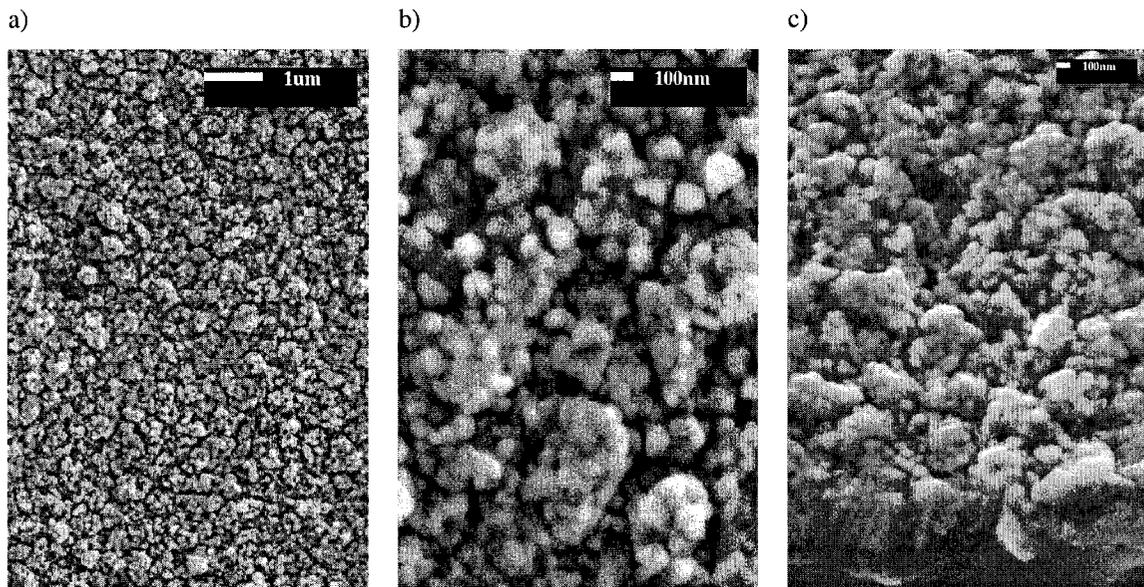
Figure A1.9. SEM images of lead precursor (film C in Table A1.1) annealed shortly at 400 °C for 50 min. (*i.e.* annealing #12 in Table A1.2): a) and b) top-surface images and c) tilt view of the cross-section.

A1.3 Conclusions

Fully converting Pb into PbS is easily accomplished by reaction of a Pb film with sulfur vapor. However, obtaining smooth films composed of large crystals is challenging. Typically, films are obtained slightly sulfur rich. As annealing temperatures and times increase, films go from powdery to rough with aggregates on top of a uniform base, to very rough with aggregates, cavities and cracks. Performing the annealing experiments under an atmospheric pressure of N_2 seemed to prevent the vertical growth of the aggregates in the case of thick (1000 nm) lead precursor films. Lastly, the deposition of smooth, thin (100 nm) lead films and their conversion into continuous PbS thin films with moderate roughness was achieved. The growth of large grains of PbS has not been possible, one explanation for this may be the relatively high melting point of lead sulfide (1114 °C).

306

Appendix 2: Combinatorial Investigation of the Hf-Zr-Sb Ternary Phase Diagram

A2.1 Introduction

Ternary and binary picnides of the group 4-transition metals exhibit a remarkably complex structural chemistry that is still not fully elucidated. Many of these compounds have been envisaged as possible hosts for diverse interstitial chemistries [1]. Probably the best known antimonides are the filled skutterudites LnM_4Sb_{12} (Ln = lanthanoid: Zr, Hf, Nb, Ta, Mo, ..., M = Fe, Co, Ni, ...), as some of these compounds are small band-gap semiconductors with outstanding electrical properties [2]. Thus, Kleinke and co-workers, for instance, are exploring early-transition-metal antimonides (such as zirconium antimonides) with the long-term goal of discovering antimony atom substructures in semiconducting antimonides comparable to the one found in the skutterudites [3,4]. Moreover, the binary zirconium-antimony phases are still not fully elucidated and the characterization of this system is far from complete as shown in Figure A2.1 representing the Zr-Sb phase diagram [5,6], despite thorough investigations from Corbett and co-workers [7,8]. To date, the binary hafnium antimonides are not well investigated, and most of these binaries have been characterized by comparison with analogous zirconium antimonides and not from single crystal data; indeed, Hf_3Sb, α-HfSb, β-HfSb and $HfSb_2$ seem isostructural to the corresponding zirconium compounds, but other zirconium antimonides, such as Zr_2Sb have, for now, no known counterpart in the Hf-Sb systems [9]. Thus, the Zr-Sb and Hf-Sb binary system are still very interesting for solid-state chemists.

307
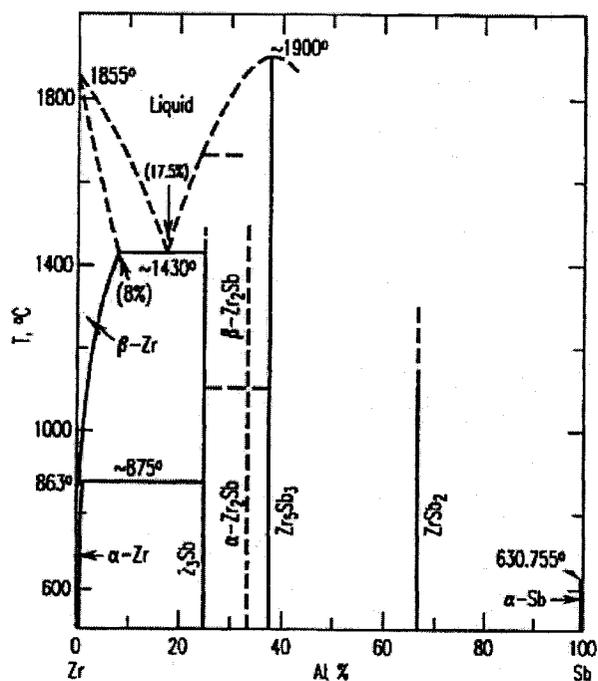
Figure A2.1. Zr-Sb binary phase diagram (from reference [6]).

In addition, the formation of ternary compounds between hafnium, zirconium and antimony is anticipated, especially at high temperatures (T ≥ 100 °C). Indeed, similarly to what has been observed by Franzen and coworkers for Nb-Ta-S and Nb-Ta-P phases [10], cationic Differential Fractional Site Occupancy (DFSO) may occur for Hf-Zr-Sb, leading to the formation of new ternary compounds. The three criteria for a cationic DFSO-stabilized compound are (i) that all metal sites are fractionally occupied by mixtures of atoms, (ii) which are fixed at each site but vary from site to site, and (iii) that the compound possesses a structure that is unknown in the parent binary systems [10-12]. While in most cases mixing related metal atoms just leads to the formation of solid solutions, mixed occupancy factors can favor structural complexity through diversity of metal atom sites. This is observed in phases prepared at high temperatures,

308

when the configurational entropy plays a major role in the stability, and when distinct differences in bonding, even minor, between the different metals become important.
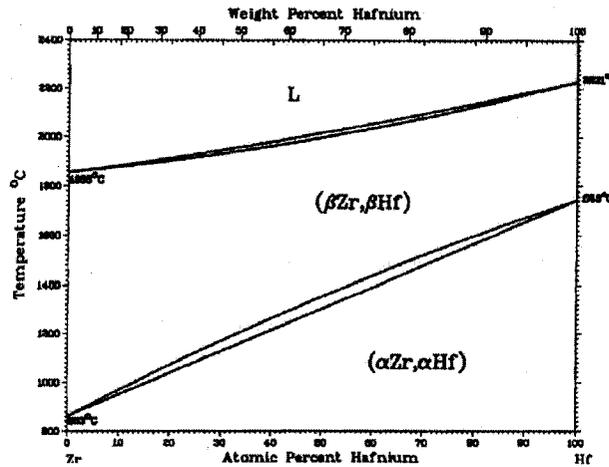
Figure A2.2. Zr-Hf binary phase diagram (from reference [13]).

Zirconium and hafnium are transition-metal atoms that form solid solutions, as shown in their phase diagram in Figure A2.2. More importantly, zirconium and hafnium are closely related metals due to the lanthanoid contraction. Thus, zirconium and hafnium have similar covalent radii of 160 pm and 159 pm, respectively. Moreover, their Pauling electronegativities only differ by 0.1, zirconium and hafnium's electronegativities are 1.4 and 1.3, respectively. However, similar to the case of Nb and Ta, slight differences between zirconium and hafnium may occur, yielding a difference in metal-metal bond energies: for instance, tantalum forms stronger metal-metal bonds than does niobium [10]. The first consequence of the difference in metal-metal bonding is that the ternary phase is stabilized relative to the stoichiometric mixture of the binary structures with the same metal ratio on the metal atom sites (i.e. alloy with random site occupancy). Therefore, the ternary phases are stabilized relative to the pure binary

309

phases by the configurational entropy [10]. The second consequence is the DFSO, or in other words: the more highly metal-metal bonded sites tend to be preferentially occupied by the more efficient metal-metal bonding element (*i.e.* Ta) [10]. Similarly to what has been observed with Nb and Ta, this phenomenon may yield new ternary compounds of Hf-Zr-Sb which are entropically stabilized relative to the stoichiometric mixture of the pure binaries and energetically differentiated from solid solutions of the binaries by DFSO. The high temperature stabilities of the ternary results from the entropic stabilization and the structural differentiation is driven by the differential metal-metal bond [10]. Compounds stabilized by DFSO include, for instance, Hf_6TiSb_4 [14], $Zr_{1-x}Ti_xSb$ [15], $Nb_{1.72}Ta_{3.28}S_2$, $Nb_{0.95}Ta_{1.05}S_2$, $Nb_{4.92}Ta_{6.08}S_4$ and $Nb_{6.74}Ta_{5.26}S_4$, $Zr_{6.45}Nb_{4.55}P_4$ or $Hf_{5.08}Mo_{0.92}P_{3.8}$ [11].

As mentioned in the previous chapters, preparations of compound thin films may include co-deposition or sequential deposition of the constituent elements of the compound. These precursor films are then annealed. For the combinatorial deposition of thin films, both co- and sequential deposition may be used. For instance, co-deposition usually takes advantage of the geometry of the sources relative to the deposition area: for a given source, the geometry spreads the material flux, *i.e.* the deposition rate, over the substrate area, yielding non-uniform deposition film thicknesses. Regarding our system geometries and capabilities, co-deposition can not be used to deposit composition gradients since our system is specifically designed to yield uniform deposition over the 5 cm × 5 cm deposition area. Thus, sequential deposition must be used. Deposition of multilayer films as precursors to new compounds has, for instance,

310

been studied extensively by Johnson and coworkers [16,17]. Their first approach is to sequentially deposit ultra-thin elemental layers with a modulation thickness of 20 to 80 Å, a situation similar to the first combinatorial strategy described below in Section A2.3. In these conditions, the reaction is not limited by the slow rate of mass transfer as in traditional solid-state chemistry. Indeed, as the constituents are in close proximity the diffusion of reactant may occur completely before nucleation of phases at the layer interfaces occurs, yielding an amorphization of the precursor prior to the nucleation of the phases, as shown in Figure A2.3. The sequential deposition of ultra-thin elemental layers allows for the control of the reaction pathway, and because the diffusion rate does not need to be increased the reaction temperatures may be kept lower. Therefore, this method can potentially yield metastable phases [18-21].

Superlattice   Amorphous   Crystalline
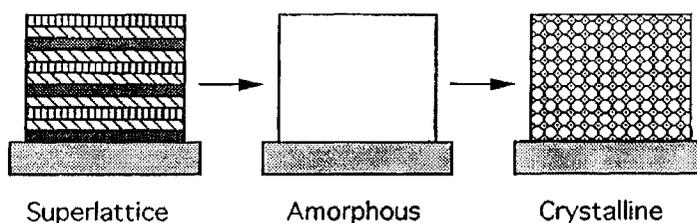
Figure A2.3. Schematic of the evolution of a modulated elemental reactant containing elemental layers below the critical thickness for interfacial nucleation as a function of temperature (from reference [16]).

The other situation is when the modulation sequence becomes larger and the interdiffusion does not occur or is incomplete. In this case, nucleation of binary phases takes place at the interfaces, and binary phases and then ternary phase grow from these interphases by diffusion of the reactants. This is most likely the case in the second strategy described below, where the repeat distance was set to be around 500Å. This range of thicknesses and even thicker have, for instance, been successfully used to prepare composite photoluminescent materials combinatorially [22]. Comprehensive

311

reviews of the increasingly important role of combinatorial chemistry in the search of new inorganic materials include references [23-27]. Derived from the combinatorial research in the pharmaceutical area, the modern era of combinatorial materials chemistry started in the 1990s at the Lawrence Berkeley National Laboratory [28]. The concept has been validated for solid-state applications by the successful discovery of new optical, dielectric and magnetic materials [25,29] from phase diagram mapping. As each deposition system and target system under investigation have their own requirements and constraints on geometry and compatible deposition techniques, despite some basic masking method (*e.g.* quaternary fractal masks, or linear wedge tools), strategies have to be developed and fine tuned for the specific project and equipment.

Because of the potential for new ternary phases of hafnium, zirconium and antimony stabilized by DFSO, especially at high temperatures, the combinatorial phase diagram mapping of this system is particularly interesting. In this chapter, two different combinatorial strategies are described, each of which was implemented in an effort to map the Hf-Zr-Sb phase diagram. The aim of a combinatorial strategy is to be able to prepare phases from a large number of compositions, with a high throughput, that includes both the synthesis and the characterization steps. To achieve this, our combinatorial deposition system includes the possibility of using various sets of five shadow masks and possesses a wedge tool for preparation of linear gradients. Particularly interested in the crystal structure of the prepared films, data collection on both the X-ray diffraction instruments and the electron microprobe can be automated for pre-set points, thus offering the potential for high-throughput characterization.

312

A2.2 Deposition techniques

In order to prepare films with composition gradients of hafnium, zirconium and sulfur, it was necessary to know quite precisely the deposition rate of thin films. Because of sublimation and subsequent inadequate control on the deposition rate, antimony can not be e-beam evaporated in our deposition system, as previously mentioned in Section 5.2. Therefore, antimony was DC sputtered with an applied power of 25 W and an argon 1.33 ($\pm$0.03) Pa (~10 mTorr). Use of the wedge tool in the deposition strategies also limits the possibilities in terms of deposition techniques. Only e-beam evaporation, which in our system yields a flux normal to the substrate, and sputtering from magnetron #1, which directly faces the wedge tool, are appropriate for use with the wedge tool. In the first combinatorial strategy described below, a set of masks is used to select the regions of the substrate on which the sputtered antimony was deposited, while the wedge tool was used as the mask for the remaining elements (hafnium and zirconium). In the second combinatorial strategy described below, the wedge tool was used for all three elements; as antimony must be sputtered, therefore, using magnetron #1, the two remaining elements (hafnium and zirconium) have to be evaporated. Calibrations of the deposition rates for e-beam evaporation of zirconium and hafnium and for sputtering of antimony have been performed and are described in Chapter 3, Sections 3.3 and 3.4.1. The combinatorial deposition of multilayered Hf-Zr-Sb films were, therefore, planed taking into account:

- a 96 % tooling factor for hafnium deposition monitored on the FTM,

- an 82 % tooling factor for zirconium deposition monitored on the FTM,

313

- a 0.70 Å/s deposition rate for DC sputtered antimony with an applied DC power of 25 W and plasma pressure of ~1.33 Pa.

The two strategies described in this section lead to the deposition of 66 different compositions of zirconium, hafnium and antimony, which correspond to the 66 compositions necessary to map the phase diagram with an increment of 10 at. % as shown in Figure A2.4, with the 3 pure elemental compositions, 27 binary compositions and 36 ternary compositions.
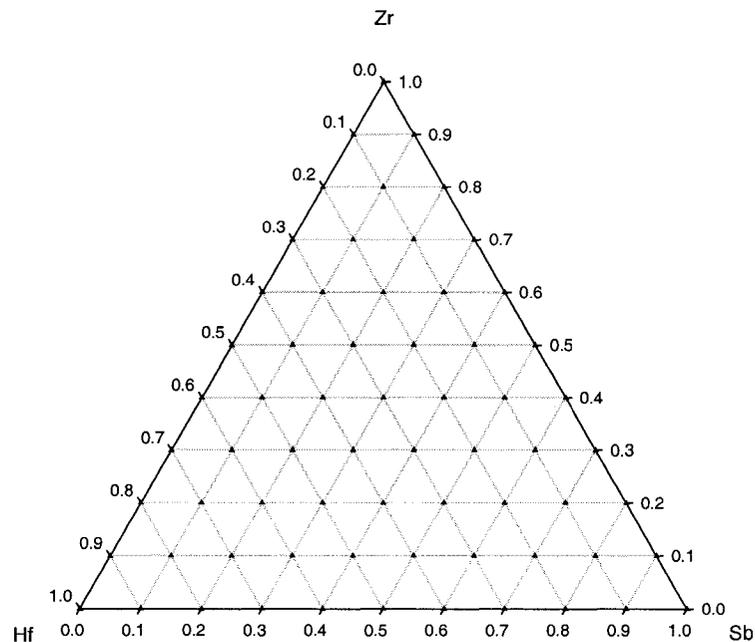
Figure A2.4. Ternary composition diagram for zirconium, hafnium and antimony with a 0.1 (*i.e.* 10 at. %) increment.

A2.3 Strategy using both shadow masks and the wedge tool

a)   Description

The first approach that was developed is based on depositions of antimony, hafnium and zirconium on selective areas, which is obtained using a set of 5 masks for

314

the sputtered antimony, and the step-by-step retraction of the wedge tool for evaporated zirconium and hafnium. The masks and the substrate map of the deposited array of films are shown in Figure A2.5. This is achieved with a particular deposition sequence, which is repeated enough times to produce the layered precursor film with the desired total thickness. In the description of the sequence below, t_{Sb} represents the time necessary to deposit the same number of antimony atoms as the number of zirconium and hafnium atoms contained in the thicknesses d_{Zr} and d_{Hf} deposited over an arbitrary surface unit. These parameters may be called control parameters, as the sputtering of antimony is controlled with the deposition time once calibrated for set plasma and power conditions, and as the evaporation of zirconium and hafnium is controlled with the actual deposited thickness measured by the film thickness monitor. Note that the film thickness monitor automatically closes the substrate shutter once the programmed thickness is reached. The deposition sequence is the following:

- first, the diagonal antimony gradient is deposited using successively mask B during 1 t_{Sb}, mask E during 2 t_{Sb}, mask C during 4 t_{Sb} and finally mask D during 4 t_{Sb}.

- second, the zirconium gradient is deposited with mask A in place, while retracting the wedge tool in 10 steps every d_{Zr}.

- last, the horizontal hafnium gradient is deposited with mask A in place and the substrate and mask assembly rotated 90° with respect to the wedge tool; the wedge tool is then retracted in 10 steps every d_{Hf}.

315
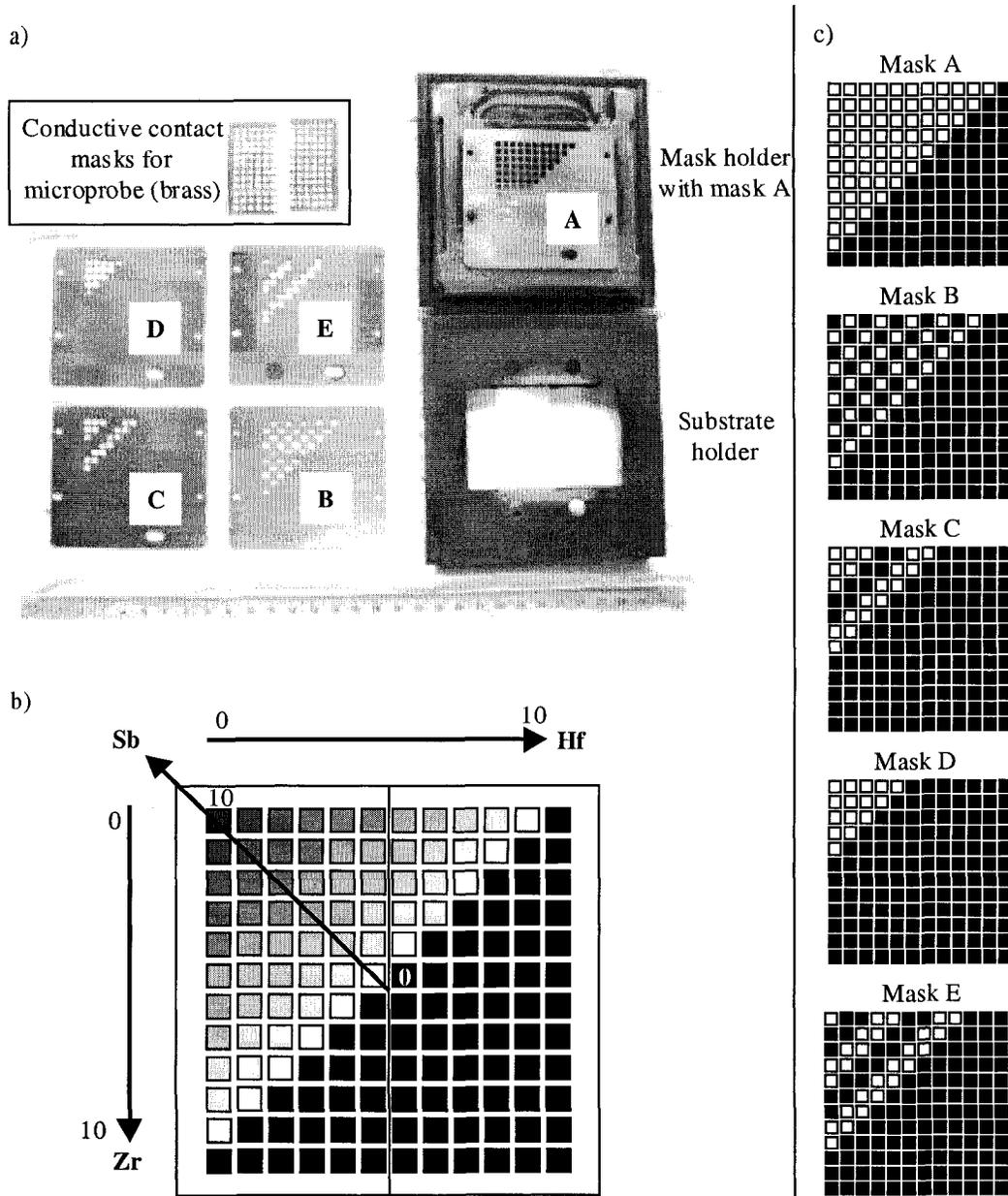
Figure A2.5. Schematic of the first combinatorial strategy implemented for the Hf-Zr-Sb phase diagram mapping: a) and c) set of shadow masks used for the deposition and b) map of the substrate after deposition.

b)   Deposition and annealing parameters

The three control parameters are calculated according to the approximate desired repeat layer thickness and the results of the calibrations recalled in Section A2.2. Thus, assuming the bulk densities for the as-deposited films, which is a reasonable assumption

316

according to the simulation results obtained from the calibration experiments, one can

calculate the mass deposited on an arbitrary unit of surface set to 1 cm^2 (m in g/cm^2):

$$m = \rho \times d \times 10^{-8} \qquad\qquad (A2.1)$$

Here, m is the deposited mass in grams, ρ is the material density in g/cm^3 and d is the

thickness in Å; 10^{-8} relates the Å to the cm. Hence, the deposited thickness on this

surface equals:

$$d = 10^8 \times \frac{m}{\rho} = 10^8 \times \frac{n \times M}{\rho} \qquad\qquad (A2.2)$$

Here, M is the element molar mass in g/mol and n is an arbitrary number of moles

deposited on 1 cm^2 (n in mol/cm^2). For antimony, the deposition time t_{Sb} in seconds can

be calculated according to the deposition rate R_{Sb} in Å/s:

$$t_{Sb} = \frac{d}{R} = 10^8 \times \frac{n \times M_{Sb}}{\rho_{Sb} \times R_{Sb}} \qquad\qquad (A2.3)$$

Table A2.1 Determination of d_{Zr}, d_{Hf} and t_{Sb} for an overall repeat layer thickness of 100 Å

	Zr	Hf	Sb
M (g/mol)	91.22	178.49	121.75
ρ (g/cm^3)	6.49	13.1	6.68
R (Å/s)	-	-	0.70
n (mol/cm^2)	0.66×10^{-8}	0.66×10^{-8}	0.66×10^{-8}
d (Å)	9	9	12
t (s)	-	-	17

To have a repeat layer thickness of approximately 100 Å, each deposition step should

deposit approximately 10 Å of material, as each cell on the substrate receives an overall

number of ten depositions. If the arbitrary number of moles deposited on 1 cm^2, n, is set

to 0.66×10^{-8} mol/cm^2, then, as shown in Table A2.1, d_{Zr} and d_{Hf} equal 9 Å, while d_{Sb}

equals 12 Å, which is deposited in 17 seconds at a rate 0.70 Å/s.

317

Thus, the following deposition sequence is performed:

- first, the diagonal antimony gradient is deposited using successively mask B for 17 seconds, mask E for 34 seconds, mask C for 68 seconds and finally, mask D for 68 seconds, with a plasma pressure of 10 mTorr and an applied DC power on the antimony target of 25 W,

- second, the vertical zirconium gradient is deposited with mask A in place, while retracting the wedge tool in 10 steps, with 9 Å of zirconium deposited at each step,

- last, the horizontal hafnium gradient is deposited with mask A in place and the substrate and mask assembly rotated 90° with respect to the wedge tool; the wedge tool is then retracted in 10 steps, with 9 Å of hafnium deposited at each step.

This deposition sequence was repeated 20 times for an ~200 nm thick precursor film or 30 times for an ~300 nm thick precursor film. Indeed, 200 nm was determined to be the minimal thickness producing adequate diffracted x-ray signal intensities. The evaporation parameters during deposition of zirconium and hafnium are given in Table A2.2.

Table A2.2. Parameters recorded during the evaporation of zirconium and hafnium

Element	Current (Amps)	Pressure (Torr)	FTM deposition rate (Å/s)
Zirconium	0.180 – 0.230	low 10^{-9} – low 10^{-8}	0.3 ↔ 0.5
Hafnium	0.110 – 0.125	low 10^{-9} – mid 10^{-9}	0.4 ↔ 0.5

Once the 66 different multilayered precursor films were deposited, the substrate was transferred to the annealing chamber, while maintaining the film under a high

318

vacuum environment. The annealing chamber base pressure was ~9×10^{-8} Torr. Several annealing programs were performed, among them were programs with maximum temperature of 500 °C and 750 °C. The annealing at 500 °C for 150 minutes was performed according to the program shown in Figure A2.6 with an ~200 nm thick (20 repeat trilayers) precursor film. The first part of the annealing, during which the temperature is ramped up to 500 °C, was to enable the interdiffusion of the elemental layers, while the high temperature stage at 500 °C was intended to unable the nucleation and crystal growth of ternary Hf-Zr-Sb phases.
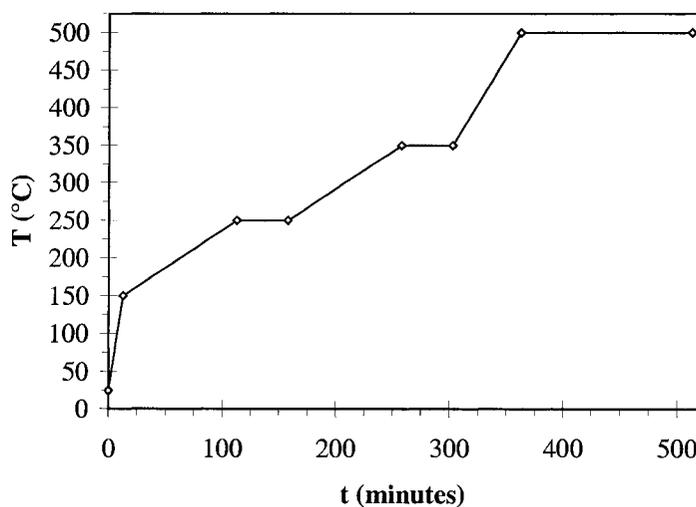
Figure A2.6. 500 °C annealing program.

The annealing at 750 °C for 180 minutes was performed according to the program shown in Figure A2.7 with an ~300 nm thick (30 repeat tri-layers) precursor film. The first part of the annealing, during which the temperature is ramped up to 750 °C, was intended to enable the interdiffusion of the elemental layers. Temperatures were decreased during the first part relative to the 500 °C program, in an effort to limit antimony depletion while intermixing the precursor film constituents. Also, in an effort

319

to produce a partial pressure of antimony to reduce the rate of antimony sublimation, ~2 μm of antimony were deposited on the half of the substrate that did not have the multilayered films. The high temperature stage at 750 °C was intended for the nucleation and crystal growth of the ternary Hf-Zr-Sb phases.
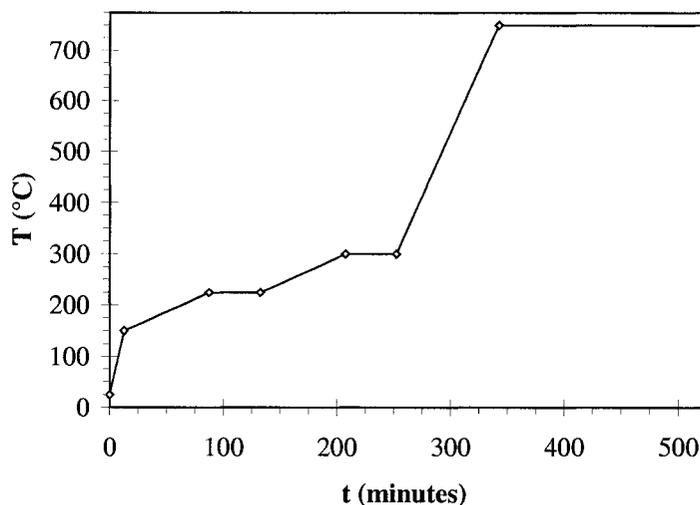
Figure A2.7. 750 °C annealing program.

Once annealed, XRD data were collected from $2\theta = 3°$ to $2\theta = 110°$. This was achieved in four steps or snap shots: the detector, located at ~15 cm from the goniometer center, is positioned successively at $2\theta = 20°$, $45°$, $70°$ and $95°$, while the sample is rotated by an angle θ from $3°$ to $17°$, from $15.5°$ to $29.5°$, from $28°$ to $42°$ and from $40.5°$ to $54.5°$, respectively. Each detector position was held for 240 seconds. Lastly, the data collection was automated using a routine similar to the one shown in Appendix 3, which contained the command to collect an additional fourth frame. This routine was launched once the 66 cell coordinates (x,y,z) had been determined and entered into the XRD collection software. Finally, once collected, the frames were integrated using another routine, which produced the conventional I *vs.* 2θ diffraction powder patterns,

320

that were then studied and matched to the reference patterns available in the JCPDS database, using EVA software from Bruker AXS Inc.

Finally, as described in Section 2.2.3, elemental compositions of the 66 cells were determined from WDX data. To avoid charging in the electron microprobe, a brass contact mask was applied to the substrate. These masks are shown in Figure A2.5.a. This proved to be efficiently and avoided having to apply a chromium or carbon coating onto the film. Indeed, initially we intended to reuse the films for other annealing runs, at higher temperatures, for instance, in order to map the ternary phase diagram.

c)   Results

This combinatorial strategy successfully yielded the 500 °C ternary phase diagram presented in Figure A2.8. Six distinct domains may be seen. First, a domain where the film was completely lost, corresponding to the six compositions richest in antimony, indicating that antimony sublimed during the annealing. Second, a large domain with an antimony content less than 35 at. % remained amorphous or, more correctly, nanocrystalline with broad peaks corresponding to hafnium (PDF card #38-1478 [30,31]) or zirconium (PDF card #65-3366 [32,33]) (002l) and (101) reflections. This demonstrates that the interdiffusion of the zirconium, hafnium and antimony layers was successful; however, the high temperature dwell at 500 °C for 150 minutes was not hot and/or long enough to nucleate any ternary phases. The other intermediate domains contain crystalline phases.

321
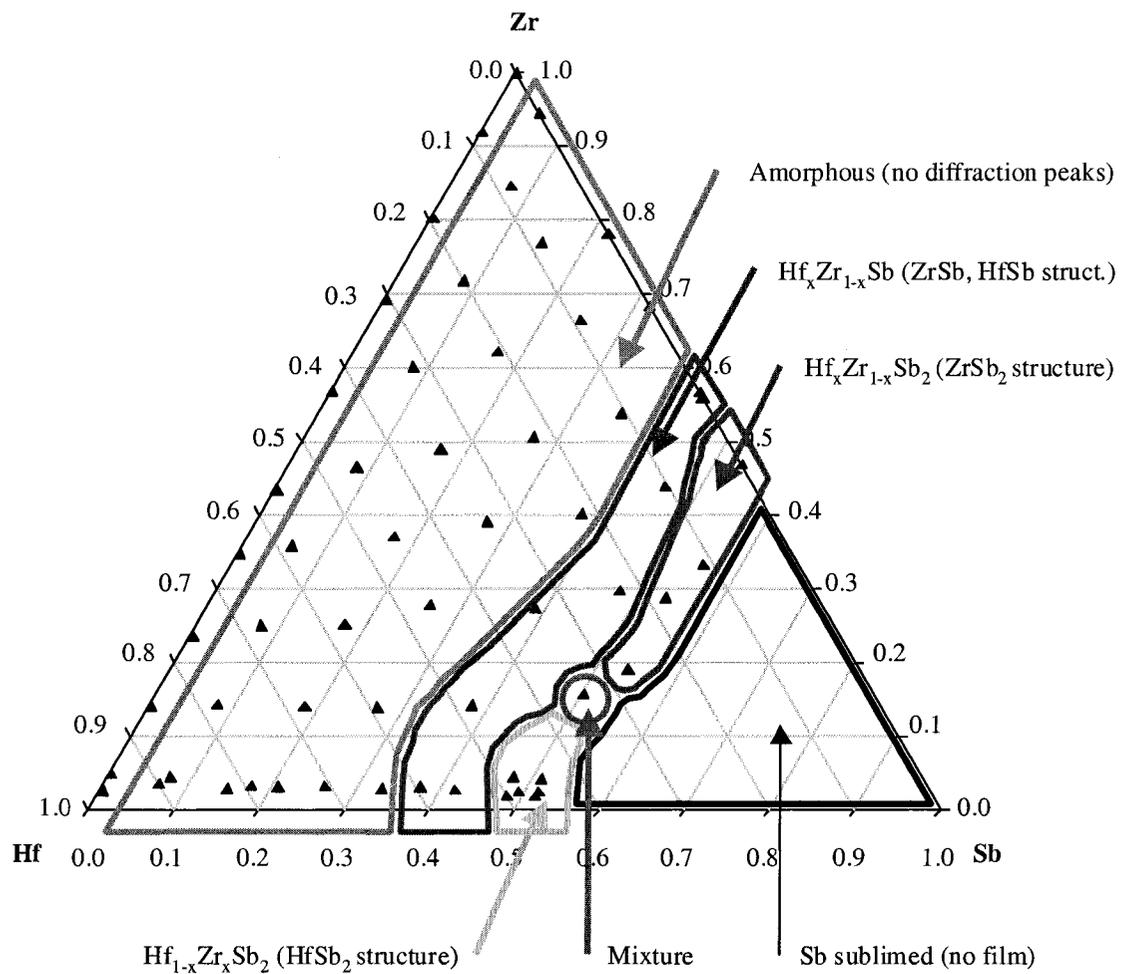
Figure A2.8. Hf-Zr-Sb phase diagram obtained from annealing at 500 °C for 150 minutes of the 66 cell multilayered metallic precursor film.

As shown in Figure A2.8, a large domain is made of HfSb-like or ZrSb-like (PDF card #44-1316 [7,34]) phases for an antimony composition 38 to 49 at. %. This area is therefore made of a solid solution of $Hf_xZr_{1-x}Sb$ ($0 < x < 1$), with a continuum of hafnium and zirconium substitution. XRD patterns for these domains are shown in Figure A2.9.

322
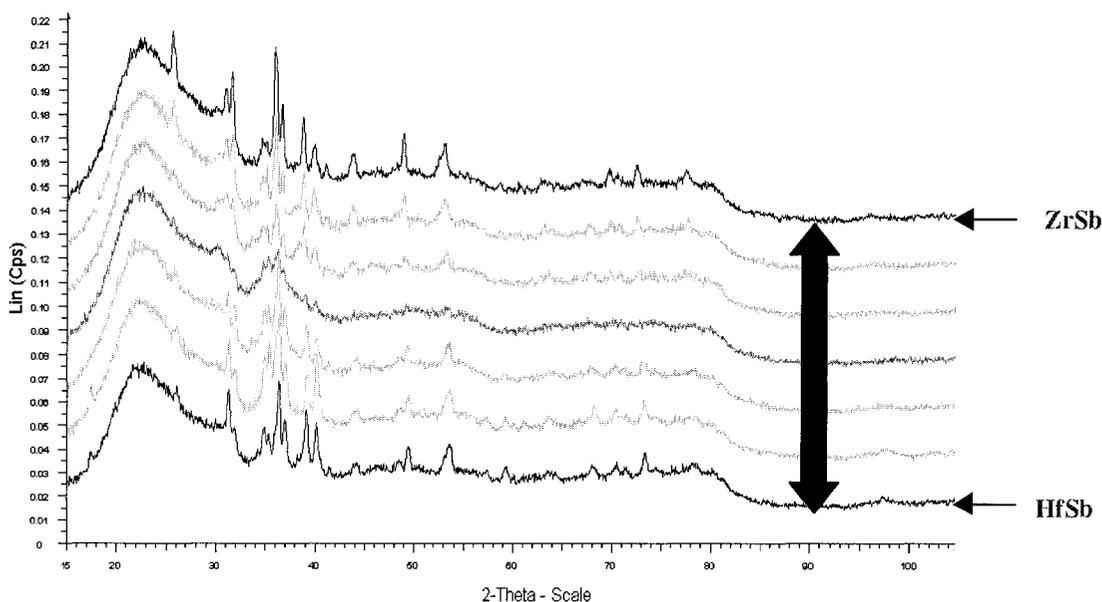
Figure A2.9. XRD patterns for the $Hf_xZr_{1-x}Sb$ domain.

Similarly, a domain with an $HfSb_2$-like phase (JCPDS card #89-2236 [35,36]) and a domain with a $ZrSb_2$-like phase (JCPDS card #89-2235 [35,37]) may be observed, XRD patterns for these domains are shown in Figure A2.10. For $Hf_xZr_{1-x}Sb_2$, the hafnium content is less than 30 at. %, while the antimony content is around 55 at. %. For $Hf_{1-x}Zr_xSb_2$, the zirconium content is less than 10 at. %, while the antimony content is around 50 at. %. Lastly, one may notice a single data point at 50 at. % of antimony, 15 at. % of zirconium and 35 at. % of hafnium. The phase at this point could not be determined, due to a poorly resolved powder pattern: this may be a new phase or a mixture of the phases previously mentioned.

323
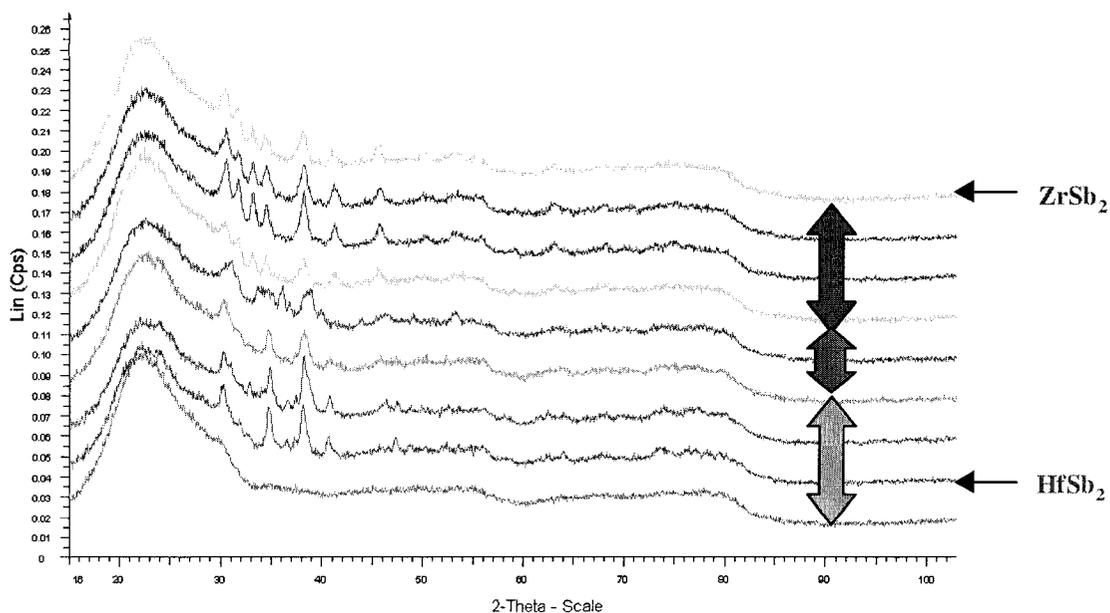
Figure A2.10. XRD patterns for the $Hf_xZr_{1-x}Sb_2$ and $Hf_{1-x}Zr_xSb_2$ domains.

In Figure A2.8, the ternary compositions indicated are the compositions established from WDX data. As one notices, $HfSb_2$ or $ZrSb_2$-like phases should correspond to an antimony composition of 67 at. %, but, as already indicated, a 50 at. % was determined, the antimony depletion may explain the differences that can be seen between the actual XRD patterns and the reference patterns for $HfSb_2$ and $ZrSb_2$: including peak shifts, relative intensity shifts and extra peaks, as shown in Figure A2.11. For HfSb and ZrSb-like phases, the antimony composition should be around 50 at. %, but the antimony composition determined from WDX data was around 45 at. %, again the film was antimony poor, however the stoichiometry shift in this case is not as dramatic.

324
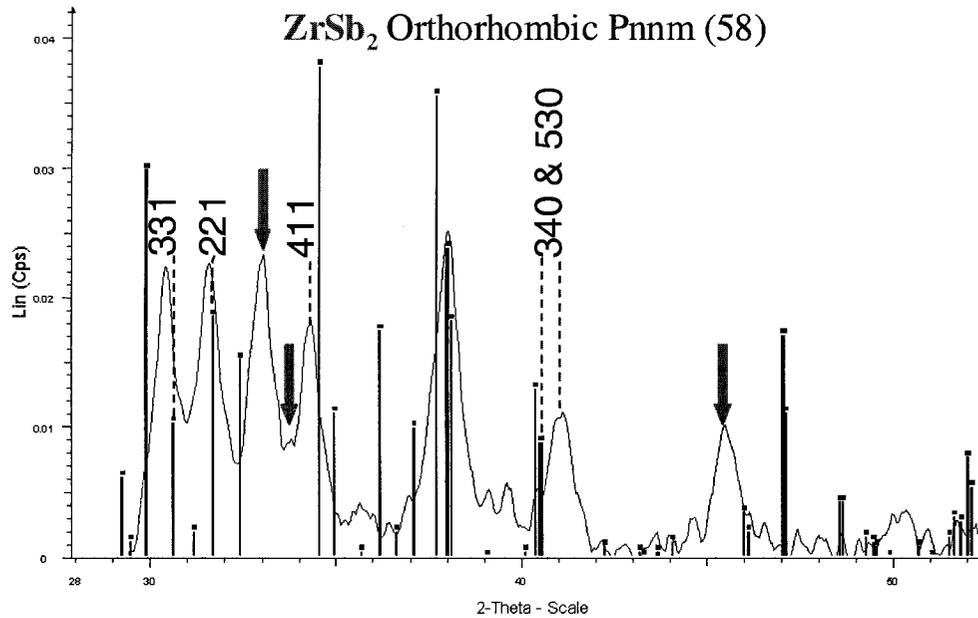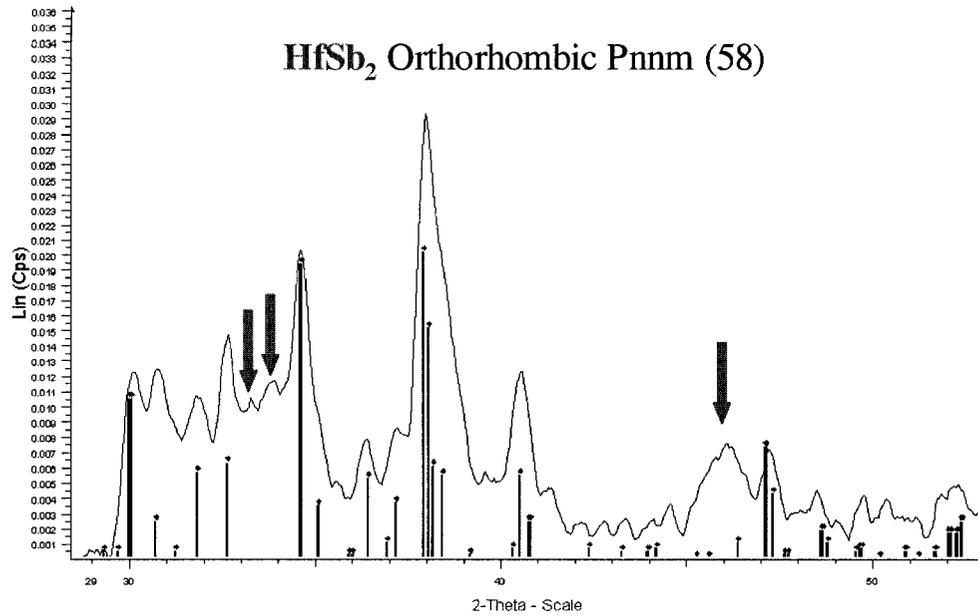
Figure A2.11. Expanded XRD patterns for the $HfSb_2$ and $ZrSb_2$ domains, with the respective PDF cards.

Also, the XRD patterns collected on Zr-Hf, Zr-Sb and Hf-Sb tie-lines for the library annealed at 500 °C were graphed as shown in Figures A2.12, A2.13 and A2.14, respectively. Thus, in Figure A2.12, the Zr-Hf tie line is presented and shows the zirconium-hafnium solid solution shown in the phase diagram, Figure A2.2. Indeed, the evolution from pure zirconium to pure hafnium is clear, especially the intensity

evolution of the (002) and (101) reflections, and also the peak position shifts; one may

especially notice the (102) and (103) reflections position displacement, as the d-spacings

of these reflection decrease from pure zirconium to pure hafnium, the Bragg angles (θ)
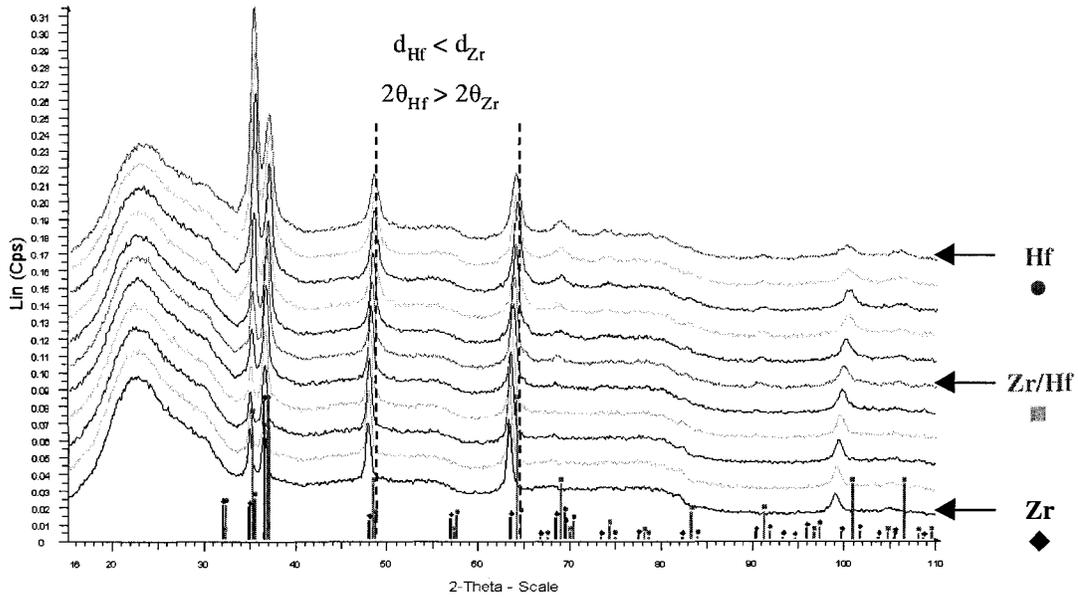
increases.

Figure A2.12. XRD patterns collected on Zr-Hf tie-line.
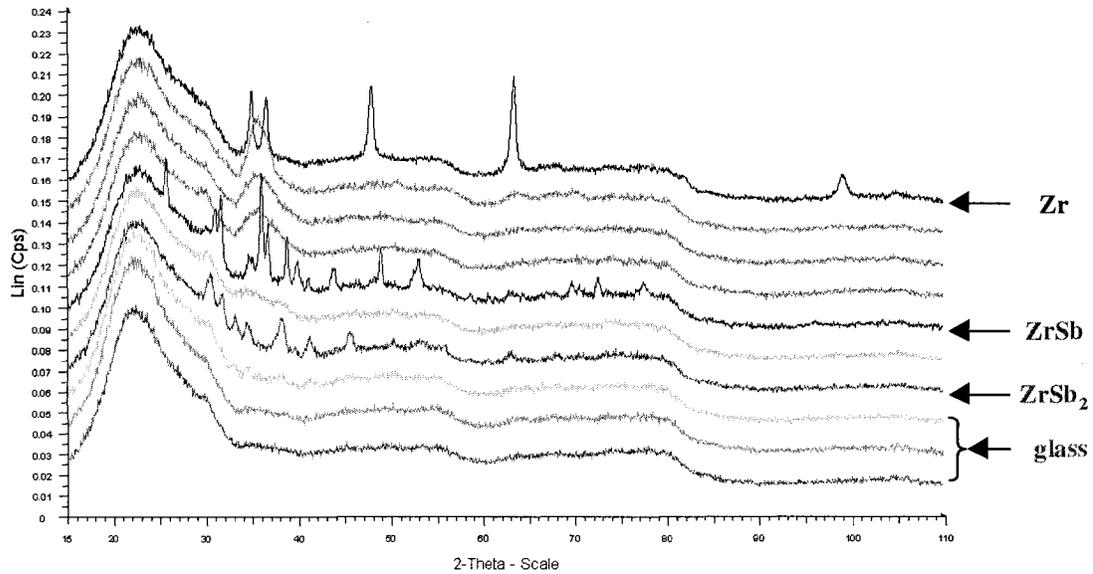
Figure A2.13. XRD patterns collected on Zr-Sb tie-line.

326

The Zr-Sb (Figure A2.13) and the Hf-Sb (Figure A2.14) tie lines show, as the antimony content decreases, the phase evolution from the 1:2 phase to the 1:1 phase to the nanocrystalline domain and eventually to pure zirconium or hafnium.
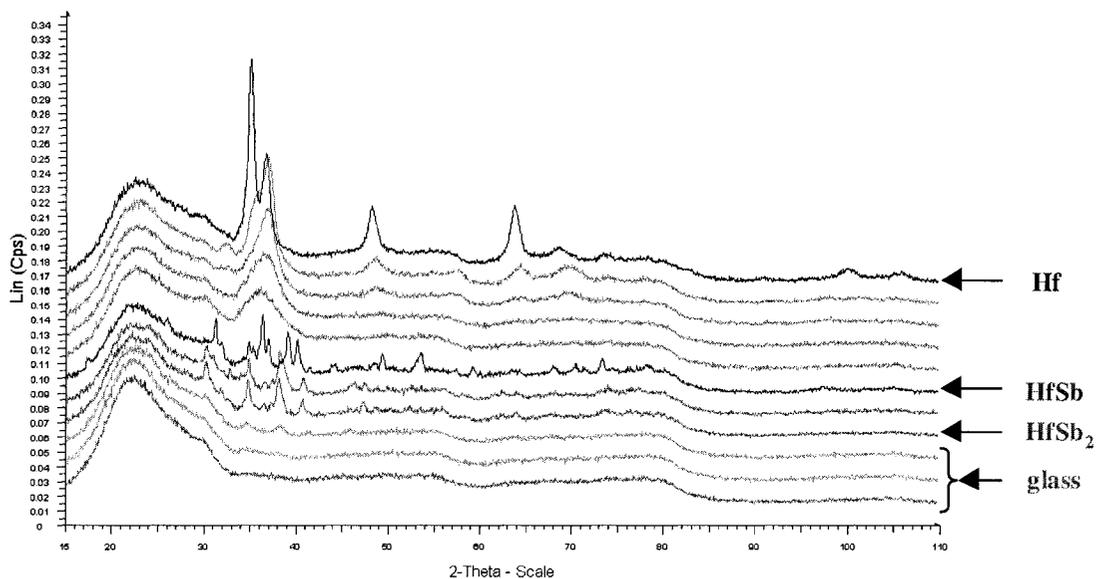
Figure A2.14. XRD patterns collected on Hf-Sb tie-line.

Annealing at 750 °C yielded only nearly complete antimony depletion and oxidation of the film. Indeed, regardless of the starting composition, after annealing at 750 °C, the 66 cells contained less than 1 at. % antimony and between 60 and 90 at. % oxygen. Moreover, XRD data showed the formation of monoclinic ZrO_2 and HfO_2. The only source of oxygen is the oxygen contained in the fused silica (SiO_2) substrate, since the film was kept under high vacuum from deposition to the end of the annealing. Therefore, the incorporation of oxygen into the film must have occurred through oxygen migration from the substrate to the film, while heated at 750 °C.

327

d)   *Critique*

Thus, despite successful interdiffusion of the elemental reactant layers and subsequent nucleation leading to a map of the ternary phase diagram at 500 °C, showing domains with continuous substitution of zirconium and hafnium, this first approach revealed experimental and practical issues, such as the tediousness of the deposition process, the antimony depletion and the oxygen migration from the fused silica substrate at high temperatures.

The aim of any combinatorial strategy is to increase the experimental throughput to increase the chance of discoveries. This first combinatorial strategy successfully yielded the preparation of a large number (66) of distinct compositions of Hf-Zr-Sb at once with a repeated sequence of 6 distinct operations – 4 masked antimony depositions, 1 zirconium gradient and 1 hafnium gradient – instead of 165 with a non combinatorial approach. However, the benefit of the investigation of a large number of phases at once did not overcome the time-consuming deposition process, and high throughput was therefore not really achieved, as the number of annealing conditions that could be tried remained too low. Indeed, to deposit the 66 cells and obtain precursor films with sufficient overall thicknesses, 20 to 30 repeats of the tri-layer deposition sequence was necessary. Each of these sequences demands a real deposition time comprised between 2 and 2.5 hours. This duration includes the effective deposition times, the pump-down periods between antimony sputtering (Ar plasma) and zirconium and hafnium evaporation (high vacuum), and the mask changes between antimony sputtering. The mask change steps not only require the motion of the substrate/mask assembly from the

328

deposition chamber to the load/lock chamber, but also require a pump-down of the deposition chamber to a high vacuum pressure similar to the one in the load/lock and central distribution chambers. In addition, one should know that these films were the first deposited with the system, which at the time was not running entirely smoothly; thus, down times to repair the fork transfer system and other mechanical problems greatly increased the time required for each library deposition. Thus, the 20-repeat film required nine working days to deposit, which was improved to ten working days for the 30-repeat film. In addition, the sequence requires the constant attention and action of the operator. Every 0.5 to 1.5 minutes a task must be manually performed, making that method tedious and long in the absence of full automation of the deposition system (a feature not available with our system). Lastly, one should add the time required to set-up the XRD and WDX instruments and then collect the data, and, probably, more significantly, the time spent to gather and sort the results in a comprehensive way.

As described earlier, under the annealing conditions that could be experimentally accessed, films suffered major and even complete antimony depletion. Antimony is a volatile element that generates high vapor pressures; therefore, in a hot vacuum environment antimony sublimes. The annealing chamber with its large volume and cold water-cooled walls does not allow the antimony partial pressure to build up to saturated levels. The antimony continuously re-evaporates and recondenses on the cold walls of the chamber. The only possible way to mitigate the rate of antimony sublimation in the chamber was by back-filling the annealing chamber with an inert gas, such as Argon. This was attempted without success: the antimony depletion was not prevented.

Finally, the last experimental issue concerns the oxygen migration from the fused silica substrate into the film during higher temperature annealing; this requires the use of a different substrate chemically inert to reaction with hafnium and zirconium during high temperature annealing of Hf-Zr-Sb layered precursor films. This issue is addressed below.

A2.4   Strategy using only the wedge tool

The second approach taken was developed in order to address the defects experienced with the first approach. Thus, the deposition strategy was changed to avoid long and tedious deposition times, the substrate material was changed in order to avoid oxygen migration from the substrate, and the annealing procedure was changed to limit antimony depletion.

a)   *Deposition: description and parameters*

The selective depositions of antimony, hafnium and zirconium over 66 different cells, necessary to map the phase diagram with an increment of 10 at. %, may be acieved using the wedge tool with the substrate in three positions that are 120° apart. To accommodate the deposition chamber geometry and dimension, a new wedge tool had to be designed and manufactured. The new wedge tool is 7 cm long instead of 3 cm long. Prior to the actual deposition, the wedge tool linear zero and height zero have to be determined; a conductivity tester lights up when the wedge tool and the substrate platen are in contact. A schematic of this combinatorial strategy is presented in Figure A2.15.

330

a)

b)

| Loading | Sb deposition | Zr deposition | Hf deposition |
| $\alpha = 0°$ | $\alpha = 90°$ | $\alpha = 210°$ | $\alpha = 330°$ |
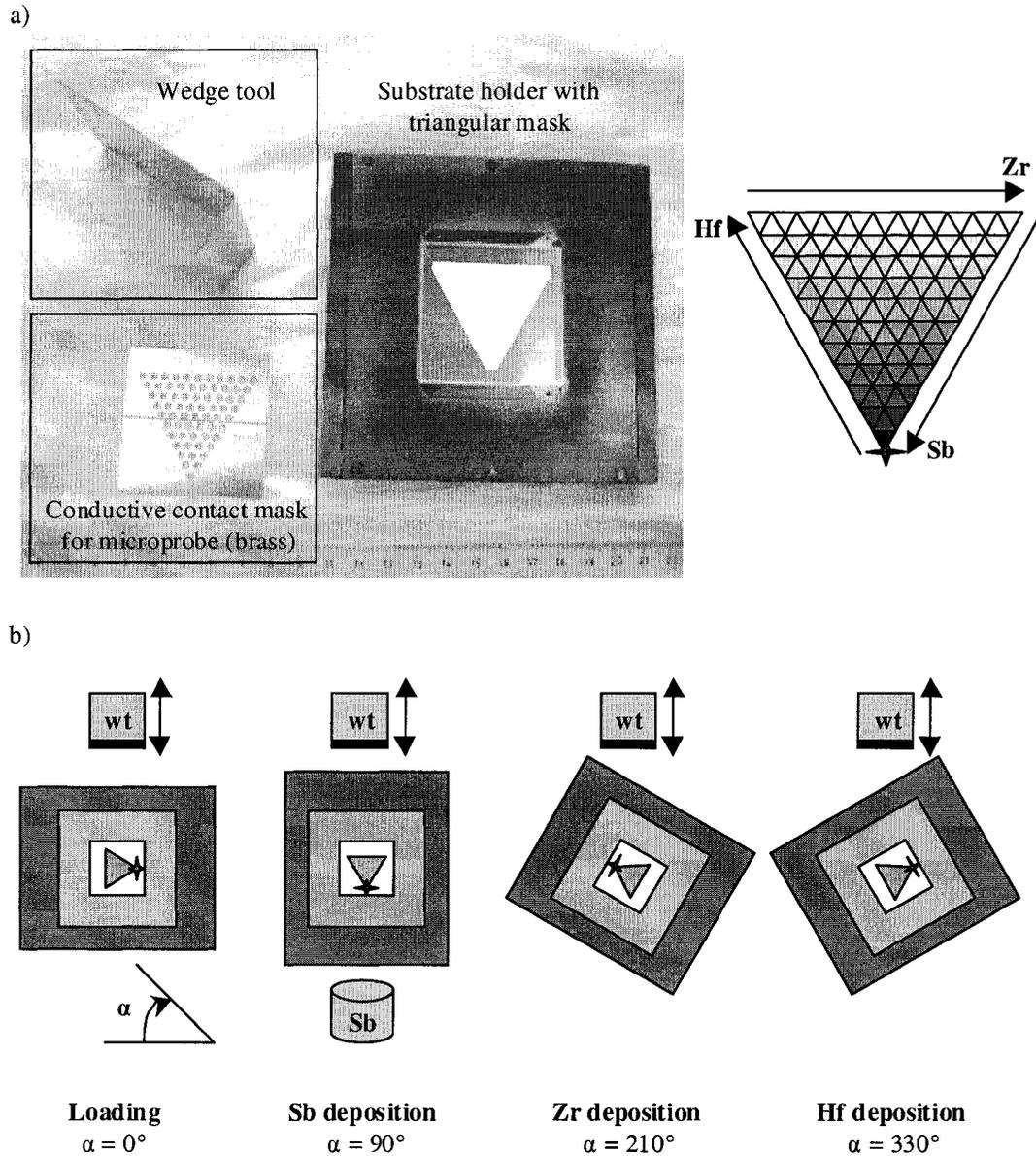
Figure A2.15. Schematic of the second combinatorial strategy implemented for the Hf-Zr-Sb phase diagram mapping: a) substrate holder and tool required, map of the substrate after deposition and b) schematic of the deposition sequence.

In the description below, t_{Sb} represents the time necessary to deposit the same number of antimony atoms as the number of zirconium and hafnium atoms contained in the thicknesses d_{Zr} and d_{Hf}. These parameters are the control parameters. The deposition sequence (Figure A2.15.b) for a repeat layer is:

331

- first, the antimony gradient is deposited with the sample at an angle of 90° with respect to the loading direction, so that the antimony target placed in magnetron #1 faces the wedge tool; the wedge tool is then retracted every t_{Sb} in 10 steps,

- then, the zirconium gradient is deposited with the sample at an angle of 210°, the wedge tool is then retracted in 10 steps every d_{Zr},

- lastly, the hafnium gradient is deposited with the sample at an angle of 330°, the wedge tool is then retracted in 10 steps every d_{Hf}.

Thus, only using the wedge tool is a nice way to create ternary composition gradients, without long and tedious mask changes. Because antimony can not be evaporated with the electron-beam evaporator, both sputtering and electron-beam evaporation had to be used, increasing the overall time to deposit the combinatorial precursor film, as it requires the deposition chamber to be pumped down between sputtering (Ar plasma) and evaporation (UHV conditions). In addition, to further increase the experimental throughput, the number of repeat units (*i.e.* number of trilayers) was decreased, therefore, it is necessary to increase the thickness of each layer to maintain the total film thickness. Thus, trilayers 50 to 70 nm thick were deposited rather than ~10 nm thick tri-layer used in the previously described combinatorial approach. A longer interdiffusion dwell during the annealing program was necessary, as the elements are now further apart and need to diffuse over longer distances. However, the larger thicknesses of the trilayers significantly decreased the deposition time and,

332

meanwhile, increase the overall precursor film thickness, which improved the XRD signal to noise ratio.

Similar to what was described earlier for the first strategy, the three control parameters were calculated according to the approximate desired repeat layer thickness and the results of the calibrations recalled in Section A2.2. As a higher deposition rate was required for antimony, a quick mass calibration for an applied power of 65 W and a plasma pressure of ~1.33 Pa was performed, it yielded a rate of 1.9 Å/sec. Again, assuming the bulk densities for the as-deposited films, one can calculate the mass deposited on an arbitrary unit of surface set to 1 cm^2 (m in g/cm^2), the deposited thickness on this surface, and for antimony, the deposition time t_{Sb} in seconds, according to equations (A2.1), (A2.2) and (A2.3). In order to have a repeat layer thickness of approximately 500 Å, each deposition step should yield the deposition of approximately 50 Å of material, as each cell on the substrate receives an overall number of ten depositions. If the arbitrary number of moles deposited on 1 cm^2, n, is set to 3.9×10^{-8} mol/cm^2, then, as shown in Table A2.3, d_{Zr} and d_{Hf} equal 54 Å, while d_{Sb} equals 71 Å which were deposited in 37 s at a rate 1.9 Å/s.

Table A2.3. Determination of d_{Zr}, d_{Hf} and t_{Sb} for an overall repeat layer thickness of ~500 Å

	Zr	Hf	Sb
M (g/mol)	91.22	178.49	121.75
ρ (g/cm^3)	6.49	13.1	6.68
R (Å/s)	-	-	1.9
n (mol/cm^2)	3.9×10^{-8}	3.9×10^{-8}	3.9×10^{-8}
d (Å)	54	54	71
t (s)	-	-	37

333

Thus, the following deposition sequence is performed: for the antimony gradient, the wedge tool is retracted one step every 37 seconds in 10 steps, while for the zirconium and hafnium gradients, the wedge tool is retracted in 10 steps as soon as 54 Å of zirconium and hafnium are deposited. This deposition sequence was repeated 14 times for an overall precursor film thickness of ~770 nm, or 9 times for an overall precursor film thickness of ~500 nm. The evaporation parameters during deposition of zirconium and hafnium are given in Table A2.4:

Table A2.4. Parameters recorded during the evaporations of zirconium and hafnium

Element	Current (Amps)	Pressure (Torr)	FTM deposition rate (Å/s)
Zirconium	0.290 – 0.340	mid 10^{-8} – mid 10^{-7}	~2 ↔ ~3
Hafnium	0.190 – 0.215	mid 10^{-9} – mid 10^{-8}	~2 ↔ ~3

b)   Substrate choice

To prevent oxygen diffusion from the quartz substrate observed for annealing at temperatures higher than 750 °C with the first combinatorial approach, the substrate material was changed. Two solutions were considered: the use of a buffer layer between the fused silica and the Hf-Zr-Sb film or the use of a different substrate. The first solution was not chosen, since it would require a period of time to develop a new thin-film growth process, without guaranteeing its effectiveness. Indeed, it can take several experiments to develop a process to grow a good quality film in a reproducible manner. Thus, for practical and time considerations, wee decided to use a different substrate. The selection criteria for the substrate are described below.

334

First, the substrate should be stable at high temperatures (up to 1000 °C), in other words, there should not be any reaction with Zr, Hf or Sb, and the material should not undergo a phase transformation. Thus, a crystalline substrate of a refractory material would be one of the best candidates. Second, the ideal case is to have an oriented single crystalline substrate (wafer) that creates poles during XRD collection. Poles can be easily distinguished from the film diffraction pattern, this is even easier with a cubic or hexagonal phase, as they yield fewer reflections. Orientation is not detrimental, indeed epitaxial growth is unlikely and texturing of the product films that might be induced can be addressed; one should note that thanks to the area detector used to collect the X-ray patterns, texture can be detected, if present. In addition, these types of substrates usually have very smooth surfaces. Lastly, the practical handling of substrates, both during preparation and characterization, limits the workable substrate dimensions to 1 in. × 2 in. size. This substrate size does not require any dicing or any adjustments to the system design, as the annealing enclosure (see details below) and the microprobe stage can accommodate substrates that are smaller than 1 in. × 4 in.

Hence, there are several refractory materials such as sapphire (Al_2O_3), aluminum nitride (AlN), boron carbide (B_4C), boron nitride (BN), magnesium oxide (MgO), silicon carbide (SiC), titanium carbide (TiC), titanium diboride (TiB_2), titanium dioxide (TiO_2), yttrium oxide (Y_2O_3) and zirconia (ZrO_2). Among them, few crystallize in cubic phases (MgO, TiC, Y_2O_3, ZrO_2). Alumina (sapphire, *i.e.* corundum phase) is commonly used as a crucible for solid state synthesis, as it is very stable. Although it crystallizes in a hexagonal phase, it is a material of interest for several applications and some wafer

335

vendors can provide sapphire wafers. MgO or the other cubic materials that were mentioned are much harder to obtain as 1 in. ×2 in. wafers. Because of the requirements enumerated previously, the only substrates that could be purchased were Al_2O_3 (sapphire) single crystalline and polycrystalline 1 in. × 2 in. wafers from Valley Design, Corp. (Santa Cruz, CA). The single crystalline sapphire 1 in. ×2 in. substrates were used to prepare the films that yielded the results described below.

c)   Annealing set-up

In an effort to prevent the sublimation or re-evaporation of antimony during annealing, a sealed and uniformly heated enclosure was conceptualized, in order to prevent condensation of antimony on cold surfaces. The schematic of the annealing vessel and related set-up is shown in Figure A2.16. The assembly is four parts made of fused silica: the female and male parts of the vessel with ¼ in. OD extensions and two supports to hold the sealed vessel in place in the furnace. As detailed later, the vessel is loaded under nitrogen, it is then evacuated and sealed off using the ¼ in. OD extension located on the right-hand side on the schematic in Figure A2.16. Also, to generate antimony vapor inside the vessel and therefore reduce the antimony depletion in the film, excess antimony was added in the tube during loading, prior to sealing. Specifically, a 100 mg antimony pellet was sealed in the vessel; according to Table A2.5, it should be sufficient to saturate the ~10^{-4} m^3 annealing vessel, assuming the perfect gas law given in equation (A2.4).

$$m = \frac{PV}{RT} M \tag{A2.4}$$

336

here, m is the mass in g, P is the partial vapor pressure of antimony in Pa at the temperature T in Kelvin, V is the vessel volume in m^3, R is the universal gas constant $R = 8.31447$ J.mol^{-1}.K^{-1} and M is the molar mass in g.mol^{-1}. Partial pressure and temperature are obtained from Figure 2.1.

Table A2.5. Antimony partial vapor pressure as a function of temperature and the mass required to fill the annealing tube to the equilibrium vapor pressure

T (°C)	P (Torr)	P (Pa)	m (g)
227	10^{-10}	1.3×10^{-8}	3.9×10^{-14}
327	4×10^{-7}	5.3×10^{-5}	1.3×10^{-10}
427	10^{-4}	1.3×10^{-2}	2.8×10^{-8}
527	10^{-2}	1.3	2.4×10^{-6}
627 (mp)	10^{-1}	1.3×10^{1}	2.2×10^{-5}
727	1	1.3×10^{2}	2.0×10^{-4}
1227	10^{2}	1.3×10^{4}	1.3×10^{-2}

As described previously, the annealing chamber, part of the combinatorial deposition system, does not allow us to control the antimony depletion occurring during annealing; in addition, films oxidize quite easily forming zirconium oxide and hafnium oxide. Therefore, annealing need to be performed in a tube furnace and films should not be in contact with any source of oxygen during the transfer process. Thus, to transfer the precursor films from the deposition chamber to the annealing enclosure, while maintaining an oxygen-free environment, a plexiglass glove-box was custom-made and sealed to the system load/lock chamber. This allows the transfer of the precursor film from the substrate holder into a portable dessicator with a manual vacuum pump (Fisherbrand Desi-Vac Container) in a nitrogen environment. When the dessicator is evacuated, it can maintain a pressure of ~0.5 atm for more than 24 hours. It is then

337

opened in another nitrogen glove-box, where the film is placed in the annealing vessel and connected to an evacuation assembly. The annealing vessel and the evacuation assembly (valve closed) are removed from the glove-box and connected to a rotary vacuum pump. The ¼ in. OD quartz tube extending from the male joint of the annealing vessel is then sealed with a hydrogen-oxygen torch. The sealed vessel is then placed into the tube furnace as shown in Figure A2.16.
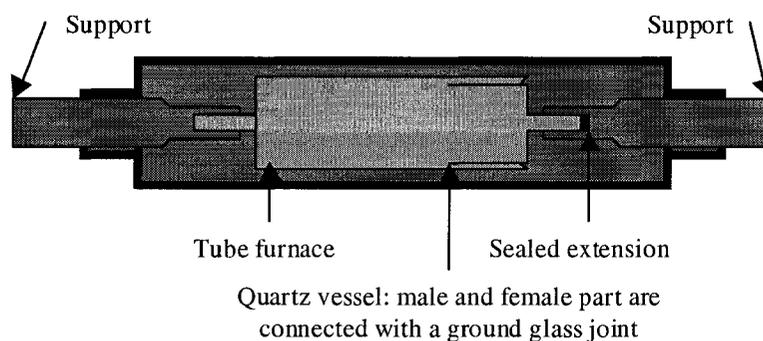

Figure A2.16. Schematic of the annealing enclosure.

Films were annealed according to programs displayed in Figure A2.17.
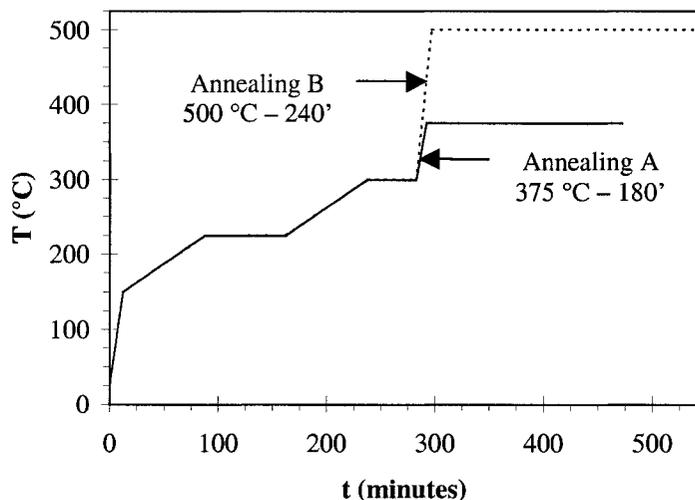
Figure A2.17. Annealing programs.

338

The annealings at 375 °C and 500 °C were performed with the antimony rich halves of a 14-repeat layer and a 9-repeat layer precursor film, respectively.

a)

b)
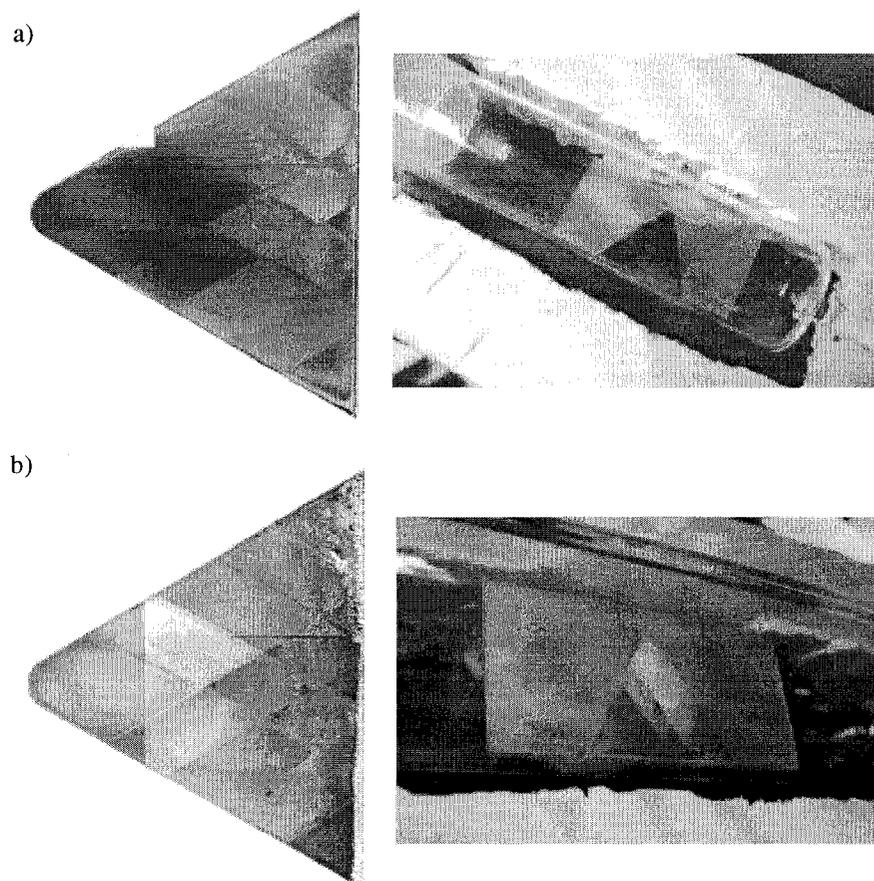
Figure A2.18. Pictures of the films after annealings (the left hand-side apexes represent the antimony rich cell, the steps of the hafnium and zirconium gradients can also be clearly seen) and pictures of the films in the annealing enclosure: film obtained from a) annealing A and b) annealing B.

Once annealed, XRD data were collected, as described previously, using a routine similar to the one shown in Appendix 3, which contained the command to collect a total of four frames. This routine was launched once the 21 cells (x,y,z) coordinates have been determined using the diffractometer video camera images, shown in Figure A2.18. Positions were then entered into the XRD collection software. Finally, once collected, the frames were integrated using another routine, which lead to the

339

conventional I *vs.* 2θ diffraction powder patterns, that were then studied and matched to the reference patterns available in the PDF database, using EVA software from Bruker AXS Inc. Finally, as described in Section 2.2.3, elemental compositions of the 21 cells were determined from WDX data. To avoid charging in the electron microprobe, a brass contact mass was applied to the substrate (shown in Figure A2.15.a).

d)   *Results and discussion*

Photographs of the antimony-rich parts of the films that were annealed according to the annealing programs A and B shown in Figure A2.17 are shown in Figures A2.18.a and A2.18.b. WDX data showed that an antimony gradient was produced and maintained during the annealing. Therefore, the annealing vessel successfully maintained a high vapor pressure of antimony that prevented antimony depletion from the film. The absence of cold re-condensation areas and the possibility of adding antimony into the vessel are believed to be the key factors explaining the absence of antimony depletion in the film. However, this annealing method could not prevent the oxidation of the film and Sb_2O_3 was observed along with some ZrO_2 and HfO_2. Oxygen migration from the sapphire Al_2O_3 substrate is considered an unlikely source of oxygen, as alumina boat are used for traditional solid state chemistry shake-and-bake synthesis, because of their stability. Other sources of oxygen include poor sealing of the annealing vessel and possible leakage at the ground glass joint. Indeed, despite the evacuation of the tube, upon cooling after the high temperature dwell, the residual pressure inside the annealing vessel should decrease, and the difference on pressure with the outside atmosphere may favor the entry of air into the annealing vessel. In addition, the ground

340

glass joint may expand upon heating, while it may contract upon cooling. These distortions of the joint may enable air to leak into the tube.

Lastly, the deposition process, was not only able to create the desired hafnium-zirconium-antimony gradient, but was also efficient in terms of the overall deposition time. This combinatorial deposition strategy increased the potential experimental throughput; indeed, the repeated sequence only contained 3 distinct operations: one gradient for each of the three elements obtained by the step-by-step retraction of the wedge tool. This is better than our first strategy that required six operations and better than a non-combinatorial approach, which would require 165 operations. In addition to the reduced number of operations, this second strategy limited the number of pump-downs and time-consuming substrate and mask transfers by avoiding the use of fractal shadow masks during the antimony deposition. One should remember that changing a fractal deposition shadow mask requires the pump down of the deposition chamber (which contains argon to sustain the plasma) prior to opening the gate valve between the deposition chamber and the central distribution (high vacuum environment). Thus, once loaded in the deposition chamber, the substrate and triangular mask assembly stays in the deposition chamber and is just rotated with respect to the wedge as described earlier. Each deposition sequence only requires one pump-down phase: a significant improvement compared to the four pump-down phases required for the first combinatorial strategy. Moreover, the thicknesses of the repeat trilayers were increased from 100 Å (first strategy) to 500 Å (second strategy), decreasing the number of deposition sequences that are required, while increasing the precursor film overall

341

thickness. Thus, to deposit the 66 cells and obtained precursor films with sufficient overall thicknesses, 9 to 14 repetitions of the tri-layer deposition sequence were necessary. Each of these sequences demands a real deposition time between 45 minutes and one hour. This duration includes the effective deposition times, and the pump-down period between antimony sputtering (Ar plasma) and zirconium and hafnium evaporation (high vacuum). Thus, the 14-repeat films were deposited in two working days and the 9-repeat films were deposited in one working day. These time-lines are more appropriate and bearable, knowing that the deposition requires that every 0.5 to 1.5 minutes a task is manually performed. The use of the wedge tool and shadow masks, in conjunction with the need to use both sputtering and e-beam evaporation capabilities and the necessity to have small repeat trilayers could be accommodated thanks to this second strategy. However, this strategy still requires the constant attention of an operator.

A2.5   Conclusions and future directions

The two different combinatorial strategies that were implemented did not produce that were the initial goal of the project. For conventional combinatorial approaches, films are deposited with automated processes in a few hours, our experimental throughput remained far from that, since our system was not designed to deposit wide composition-spread ternary gradients. I realized the limitations of our deposition system, and inspired by the work of Dahn and coworkers [38,39] and Koinuma and co-workers [23], I suggested a possible upgrade to our deposition system that would enable composition-spread library with large gradient to be prepared using the three sputter guns. However, this would require significant effort to engineer and

342

machine a new substrate holder sub-assembly. Conceptually, the idea is to bring the substrates into close proximity to the sputter guns, which would be shadowed by gradient masks. The usual deposition platen, which hosts the regular substrate and mask holders, would be replaced by an alternative assembly adapted to the deposition chamber geometry. A schematic of the assembly may be found in Figure A2.19. This assembly would be made with eight arms terminated by substrate holders able to host 2 in. × 2 in. substrates and be rotated by 90° and then returned to their original position.
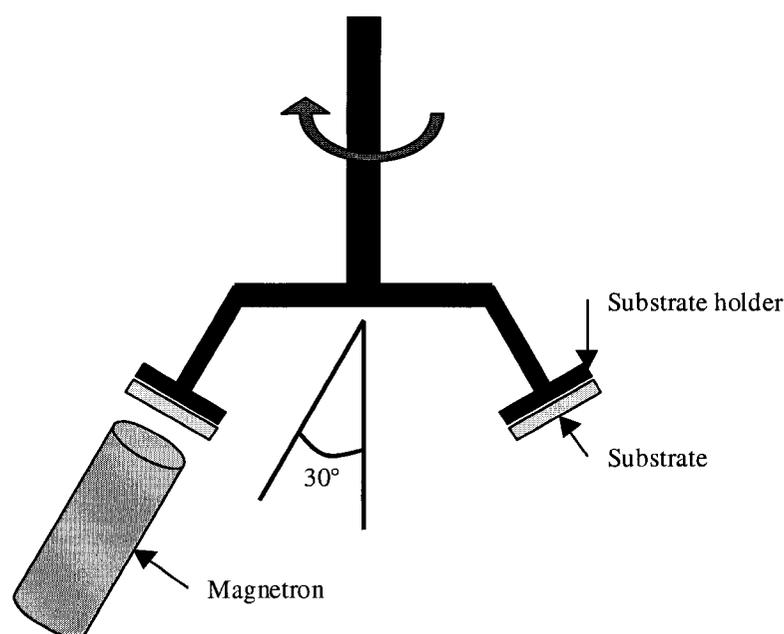
Figure A2.19. Schematic of the deposition sub-assembly.

Nevertheless, this project allowed us to debug the system and test its limitations and capabilities. Also, this project has been the occasion to develop small angle x-ray diffraction data collection and simulation, as well as the opportunity to implement combinatorial routines for regular powder pattern data collection with the newly arrived Bruker AXS D8 diffractometer (see Appendix 3). After the development of these strategies, we soon realized that the oxophilicity of zirconium and hafnium, the volatility

343

of antimony and the need for high annealing temperatures would pose very stringent experimental challenges; nevertheless, we were able to map the phase diagram at 500 °C.

A2.6 References

[1] J.D. Corbett, E. Garcia, Inorg. Chem. 27 (1988) 2353.

[2] N. Soheilnia, A. Assoud, H. Kleinke, Inorg. Chem. 42 (2003) 7319.

[3] I. Elder, C.-S. Lee, H. Kleinke, Inorg. Chem. 41 (2002) 538.

[4] H. Kleinke, Inorg. Chem. 40 (2001) 95.

[5] H. Okamoto, Journal of Phase Equilibria 14 (1993) 228.

[6] American Ceramic Society, Phase diagrams for Zirconium and Zirconia systems, American Ceramic Society, Westerville, OH, 1998.

[7] E. Garcia, J.D. Corbett, J. Solid State Chem. 73 (1988) 440.

[8] E. Garcia, J.D. Corbett, J. Solid State Chem. 73 (1988) 452.

[9] H. Kleinke, J. Alloys Compd. 270 (1998) 136.

[10] H.F. Franzen, M. Köckerling, Prog. Solid State Chem. 23 (1995) 265.

[11] H. Kleinke, H.F. Franzen, J. Am. Chem. Soc. 119 (1997) 12824.

[12] A. Tkachuk, A. Mar, Inorg. Chem. 43 (2004) 4400.

[13] K.P. Gupta, Journal of Phase Equilibria 22 (2001) 73.

[14] H. Kleinke, Inorg. Chem. 38 (1999) 2931.

[15] H. Kleinke, J. Am. Chem. Soc. 122 (2000) 853.

[16] M. Noh, C.D. Johnson, M.D. Hornbostel, J. Thiel, D.C. Johnson, Chem. Mater. 8 (1996) 1625.

[17] L. Fister, T. Novet, C.A. Grant, D.C. Johnson, Advances in the Synthesis and Reactivity of Solids 2 (1994) 155.

[18] A.L.E. Smalley, M.L. Jespersen, D.C. Johnson, Inorg. Chem. 43 (2004) 2486.

[19] J.R. Williams, D.C. Johnson, Inorg. Chem. 41 (2002) 4127.

[20] H. Sellinschegg, S.L. Stuckmeyer, M.D. Hornbostel, D.C. Johnson, Chem. Mater. 10 (1998) 1096.

[21] M.D. Hornbostel, E.J. Hyer, J. Thiel, D.C. Johnson, J. Am. Chem. Soc. 119 (1997) 2665.

[22] J. Wang, Y. Yoo, C. Gao, I. Takeuchi, X. Sun, H. Chang, X.-D. Xiang, P.G. Schultz, Science 279 (1998) 1712.

[23] H. Koinuma, I. Takeuchi, Nat. Mater. 3 (2004) 429.

[24] T.X. Sun, G.E. Jabbour, MRS Bulletin 27 (2002) 309.

[25] I. Takeuchi, R.B. van Dover, H. Koinuma, MRS Bulletin 27 (2002) 301.

[26] B. Jandeleit, D.J. Schaefer, T.S. Powers, H.W. Turner, W.H. Weinberg, Angew. Chem., Int. Ed. 38 (1999) 2494.

[27] J.N. Cawse, Account for Chemical Research 34 (2001) 213.

[28] X.-D. Xiang, X. Sun, G. Briceno, Y. Lou, K.-A. Wang, H. Chang, W.G. Wallace-Freedman, S.-W. Chen, P.G. Schultz, Science 268 (1995) 1738.

[29] X.-D. Xiang, Annual Review in Material Science 29 (1999) 149.

[30] H. MacMurdie, M. Morris, E. Evans, B. Paretzkin, W. Wong-Ng, Y. Zhang, Powder Diffr. 2 (1987) 46.

[31] Powder Diffraction File, International Center for Diffraction Data, Newton Square, PA, 2002, Card 38-1478.

[32]   Powder Diffraction File, International Center for Diffraction Data, Newton Square, PA, 2002, Card 65-3366.

[33]   R. Russel, J. Appl. Phys. 24 (1953) 232.

[34]   Powder Diffraction File, International Center for Diffraction Data, Newton Square, PA, 2002, Card 44-1316.

[35]   D. Eberle, K. Schubert, Zeitchrift für Metal Kunde 59 (1968) 306.

[36]   Powder Diffraction File, International Center for Diffraction Data, Newton Square, PA, 2002, Card 89-2236.

[37]   Powder Diffraction File, International Center for Diffraction Data, Newton Square, PA, 2002, Card 89-2235.

[38]   J.R. Dahn, S. Trussler, T.D. Hatchard, A. Bonakdarpour, J.R. Mueller-Neuhaus, K.C. Hewitt, M. Fleischauer, Chem. Mater. 14 (2002) 3519.

[39]   T.D. Hatchard, Ph.D. Thesis, Department of Physics, Dalhousie University, Halifax, NS, 2004.

Appendix 3: Routine for Combinatorial XRD Data Collection

This Appendix reports the script of the routine that was used to combinatorially collect three frames (2θ ranges of an XRD pattern) of any pre-set number of data points on the substrate (X, Y, Z coordinates). One should note that the lines starting with "!" are just informative, they do not imply any command.

```
! CombiCollect.slm: Combinatorial collection of XRD powder patterns
!    Created by: Matthieu on 27Feb04
!    Modified by: Matthieu on 02Jul06
!
! Function: this script file will collect 3 frames per pre-set point (at
! 2Theta=20°, 45° and 70°) then move to the next point.
!
! Requirements: this script assumes:
! - that the target list is already pre-set (the run # corresponds to the
!   data point #)
! - that a GADDS project has been opened
! - that the character in run # equals 2
! - that the base for the run # is 10
!
! Parameters to be implemented when launching the routine:
!   %1: exp# (experiment name, user's choice)
!   %2: Scantime (in seconds per frame)
!
! Variable:
!   N is a local variable, that corresponds to the run #. Its maximum value
!   (i.e. the number of data point to be collected) is entered between "" at
!   ('%N' <= ".."). Here it is 07.
!
!        1) routine introductory lines
#ON ERROR THEN BREAK
#LET %N= "01"
#WHILE ('%N' <= "07") DO
!
!        2) position at preset target, collect first frame and save the
!           frame in the opened project as exp#_xx_000.gfrm (xx=run #)
  SCAN /MULTITARGETS 1 /2THETA=20.0 /OMEGA=3 /PHI=0.000 /CHI=90 /AXIS=2-Om &
  /WIDTH=14 /SCANTIME=%2 '%1' /TITLE="solar cell" /SAMPLE="solar cell" &
  /NUMSAMPLE=0 /DISPLAY=15 /REALTIME /CLEAR /STARTRUN=%N /ENDRUN=%N &
  /MODE=scan /OSCILLATE=XY /AMPLITUDE=0.5
!
!        3) collect and save second frame (exp#_xx_001.gfrm)
  SCAN /SINGLERUN 1 /2THETA=45 /OMEGA=15.5 /PHI=0.000 /CHI=90 &
  /X=@5 /Y=@6 /Z=@7 /AXIS=2-Om /WIDTH=14 /SCANTIME=%2 &
  /TITLE="solar cell" /SAMPLE="solar cell" /NUMSAMPLE=0 &
  /NAME='%1' /RUN=@R /FRAMENO=001 /DISPLAY=15 &/REALTIME /CLEAR &
  /MODE=Scan /OSCILLATE=XY /AMPLITUDE=0.5
!
```

347

```
!          4) collect and save third frame (exp#_xx_002.gfrm)
 SCAN /SINGLERUN 1 /2THETA=70 /OMEGA=28 /PHI=0.000 /CHI=90 &
 /X=@5 /Y=@6 /Z=@7 /AXIS=2-Om /WIDTH=14 /SCANTIME=%2  &
 /TITLE="solar cell" /SAMPLE="solar cell" /NUMSAMPLE=0 &
 /NAME='%1' /RUN=@R /FRAMENO=002 /DISPLAY=15 /REALTIME /CLEAR &
 /MODE=Scan /OSCILLATE=XY /AMPLITUDE=0.5
!
!          5) move to the next data point
#INC %N
      #WEND
```

348

Appendix 4: Calculation of the Exact Relation for the Absorption Coefficient

This Appendix reports the calculation of the absorption coefficient, α. The absorption coefficient, α, of the films can be calculated from optical transmittance (T) and reflectance (R), using the equation (2.13):

$$T = \frac{(1-R)^2 e^{-\alpha d}}{1 - R^2 e^{-2\alpha d}}$$

then, the absorption coefficient, α, is given by equation (2.15):

$$\alpha = \frac{1}{d} \ln \left[\frac{(1-R)^2 + \sqrt{(2RT)^2 + (1-R)^4}}{2T} \right]$$

The calculation is given below:

$$T = \frac{(1-R)^2 e^{-\alpha d}}{1 - R^2 e^{-2\alpha d}}$$

$$T(1 - R^2 e^{-2\alpha d}) = (1-R)^2 e^{-\alpha d}$$

$$4T^2(1 - R^2 e^{-2\alpha d}) = 4T(1-R)^2 e^{-\alpha d}$$

$$(2RT)^2 e^{-2\alpha d} = 4T^2 - 4T(1-R)^2 e^{-\alpha d}$$

$$[(2RT)^2 + (1-R)^4]e^{-2\alpha d} = (2T)^2 - 2 \times 2T \times (1-R)^2 e^{-\alpha d} + [(1-R)^2 e^{-\alpha d}]^2$$

$$[(2RT)^2 + (1-R)^4]e^{-2\alpha d} = [2T - (1-R)^2 e^{-\alpha d}]^2$$

$$\sqrt{(2RT)^2 + (1-R)^4}\, e^{-\alpha d} = 2T - (1-R)^2 e^{-\alpha d}$$

$$e^{-\alpha d} = \frac{2T}{(1-R)^2 + \sqrt{(2RT)^2 + (1-R)^4}}$$

$$e^{\alpha d} = \frac{(1-R)^2 + \sqrt{(2RT)^2 + (1-R)^4}}{2T}$$

$$\alpha = \frac{1}{d} \ln \left[\frac{(1-R)^2 + \sqrt{(2RT)^2 + (1-R)^4}}{2T} \right]$$

349